

Numerical Prediction of Hydrodynamic Damping and Loads on a Floating Offshore Wind Turbine

Von der Fakultät für Ingenieurwissenschaften, Abteilung Maschinenbau und Verfahrenstechnik
der

Universität Duisburg-Essen
zur Erlangung des akademischen Grades

eines

Doktors der Ingenieurwissenschaften

Dr.-Ing.

genehmigte Dissertation

von

Simon Mewes (geb. Burmester)
aus
Winsen (Luhe)

Gutachter: Prof. Dr.-Ing. Bettar Ould el Moctar

Prof. Dr. Erin Bachynski-Polić

Tag der mündlichen Prüfung: 2. Juli 2021

Abstract

This thesis is aimed at reliable numerical predictions of hydrodynamic damping and loads on floating offshore wind turbines. Investigations of hydrodynamic damping and loads on a moored semi-submersible floater are presented using Reynolds-Averaged Navier-Stokes equations. The investigations include systematic verification studies comparing three discretisation error and uncertainty quantification methods on four different aspects of floating wind turbine simulations. These aspects are wave propagation, wave loads on a cylinder, surge decay motion of a semi-submersible, and a dynamic mooring model in surge decay motion. The discretisation error and uncertainty estimation approaches are based on Richardson extrapolation. Furthermore, a variety of different settings and models are studied to predict hydrodynamic damping, including temporal and spatial discretisation, wave radiation as well as turbulence and mooring models. For each model and numerical setting, the hydrodynamic damping in terms of the linear and quadratic component along with the flow field is analysed.

Zusammenfassung

Das Ziel dieser Arbeit ist die zuverlässige Vorhersage der hydrodynamischen Dämpfung und der Belastungen auf schwimmende Offshore-Windkraftanlagen mittels numerischer Methoden. Die hydrodynamische Dämpfung eines verankerten, schwimmenden Halbtauchers wird mit einem Reynolds-gemittelten Navier-Stokes Löser untersucht. Die Untersuchungen umfassen systematische Verifizierungsstudien, in denen drei Methoden zur Quantifizierung von Diskretisierungsfehlern und -unsicherheiten auf vier verschiedene Simulationsaspekte schwimmender Windkraftanlagen angewendet und miteinander verglichen werden. Diese Aspekte sind Wellenausbreitung, Wellenlasten auf einen Zylinder, Ausschwingversuch eines Halbtauchers in Längsrichtung (Wellen-/Windrichtung) und die Dynamik eines Verankerungsmodells für den gleichen Ausschwingversuch. Die Fehlerquantifizierungsmethoden beruhen auf der Richardson-Extrapolation. Darüber hinaus werden ver-

schiedene Modelle und Einstellungen zur Vorhersage der hydrodynamischen Dämpfung untersucht. Diese Modelle und Einstellungen beinhalten die räumliche und zeitliche Diskretisierung, die Wellenradiation sowie Turbulenz- und Verankerungsmodelle. Für jedes Modell und jede Einstellung wird die hydrodynamische Dämpfung in Bezug auf die lineare und quadratische Komponente und das Strömungsfeld analysiert.

Acknowledgements

First and foremost, I would like to acknowledge my PhD advisors Prof. Dr. Bettar Ould el Moctar and Dr. Guilherme Beleza Vaz. Their enthusiasm, guidance, critical reflection, motivation, and collaboration have helped me to conduct this work and to complete this thesis. In addition, I would like to thank Prof. Dr. Erin Bachynski-Polić for her interest and critical reflection of this work.

Furthermore, I am grateful for the financial, knowledge, and infrastructural support by the Maritime Research Institute Netherlands (MARIN) and the Institute of Ship Technology, Ocean Engineering and Transport Systems (ISMT) of the University of Duisburg-Essen. In particular, I would like to thank Sébastien Gueydon who pioneered my way to conduct research and aroused my interest in offshore renewable energies. I am also grateful for the comments, enriching discussions, and new ideas from Dr. Arjen Koop and Dr. Anand Ashok from MARIN as well as Guillermo Chillcce and Dr. Andreas Peters from ISMT. Moreover, I would like to express my gratitude to my colleagues at MARIN and at ISMT who discussed my work, encouraged me, and made my time there much more fun and enjoyable. At last, I would like to thank my parents and my wife Sina for their continuous support in the last years.

Declaration

Parts of the work described in this thesis were previously published in the following references of the author:

Burmester, S., Guerinel, M.: Calculations of Wave Loads on a Vertical Cylinder using Potential-Flow and Viscous-Flow Solvers. In *Proceedings of the 35th International Conference on Ocean, Offshore & Arctic Engineering, OMAE2016-54467*. Busan, Korea. 2016.

Burmester, S., Gueydon, S., Make, M.: Determination of Scaled Wind Turbine Rotor Characteristics from 3 Dimensional RANS Calculations. *Journal of Physics: Conference Series* 753, Munich, Germany. 2016.

Burmester, S., Vaz, G., Gueydon, S., el Moctar, O.: Surge Decay Simulations of a Semi-submersible Floating Offshore Wind Turbine. In *20th Numerical Towing Tank Symposium, NuTTS*. Wageningen, The Netherlands. 2017.

Burmester, S., Vaz, G., Gueydon, S., el Moctar, O.: Investigation of a Semi-Submersible Floating Wind Turbine in Surge Decay using CFD. *Ship Technology Research* 67, 2-14. 2020c.

Burmester, S., Vaz, G., el Moctar, O.: Towards Credible CFD Simulations for Floating Offshore Wind Turbines. *Ocean Engineering* 209, 107237. 2020a.

Burmester, S., Vaz, G., el Moctar, O., Gueydon, S., Koop, A., Wang, Y., Chen, H.C.: High-Fidelity Modelling of Floating Offshore Wind Turbine Platforms. In *Proceedings of the 39th International Conference on Ocean, Offshore & Arctic Engineering, OMAE2020-18913*. Fort Lauderdale, FL, USA. 2020b.

Mewes, S., Vaz, G., el Moctar, O.: On the Hydrodynamic Damping and Analysis of a Moored Floating Offshore Wind Turbine Using CFD. To be submitted to: *Renewable Energy*. 2022.

Contents

Abstract	i
Zusammenfassung	i
Acknowledgements	iii
Declaration	v
List of Figures	xii
List of Tables	xv
Abbreviations and Acronyms	xix
List of Symbols	xxi
1 Introduction	1
1.1 State of the Art	3
1.1.1 Experimental tests of floating wind turbines	3
1.1.2 Numerical simulations of floating wind turbines	6
1.1.3 Hydrodynamic damping of floating wind turbines	8
1.1.4 Novelties of this work	9
1.2 Motivation and Objectives	10
1.3 Structure of the Thesis	12
2 Theoretical Background	13
2.1 Hydrodynamic Damping	13
2.1.1 Damping components	13
2.1.2 Damping estimation tests	16
2.1.3 Damping function	18
2.1.4 Damping estimation methods	20
2.1.5 Equivalent linear damping	25
2.1.6 Comparison of the estimation methods	26
2.2 Governing Equations	27
2.2.1 Continuity equation	28
2.2.2 Momentum equation	28

2.2.3	Volume fraction transport equation	29
2.2.4	Inviscid flow equations	30
2.2.5	Integral form of the transport equations	30
2.3	Turbulence Modelling	31
2.3.1	Reynolds-Averaged Navier-Stokes equations	33
2.3.2	Shear Stress Transport turbulence model	34
2.3.3	KSKL turbulence model	36
2.3.4	Explicit Algebraic Reynolds Stress Model	36
2.4	Numerical Wave Tank	37
2.4.1	Wave theory	38
2.4.2	Wave absorption	39
2.4.3	Non-reflecting boundary condition	40
2.5	Rigid Body Motions	42
2.5.1	Rigid body equation of motion	42
2.5.2	Modification to the transport equations	43
2.6	Catenary Mooring Line Equation	44
2.6.1	Inelastic equations	46
2.6.2	Elastic equations	48
3	Numerical Methods	51
3.1	Discretisation Methods	51
3.1.1	Approximation of surface and volume integrals	52
3.1.2	Convection discretisation schemes	54
3.1.3	Total Variation Diminishing	55
3.1.4	Interface capturing schemes	55
3.1.5	Temporal discretisation	57
3.1.6	Algebraic system of equations	58
3.1.7	Boundary conditions	58
3.2	Solution of Navier-Stokes Equations	60
3.2.1	Linearisation of momentum equation	60
3.2.2	Pressure equation	61
3.2.3	Pressure velocity coupling	61
3.2.4	Solution algorithm	64
3.2.5	Iterative convergence	64
3.3	Coupling with Rigid Body Equations of Motion	65
3.3.1	Solution algorithm	66
3.3.2	Semi-implicit coupling schemes	66
3.4	Mooring Solver	68
3.4.1	Mooring model types	68
3.4.2	Dynamic mooring model	70
3.4.3	Coupling of fluid and mooring equations	73
3.5	Verification and Validation	73
3.5.1	Numerical Errors and Uncertainties	75
3.5.2	Approach by Eça and Hoekstra	76
3.5.3	Approach by Oberhagemann and el Moctar	79
3.5.4	Approach by Xing and Stern	80

3.5.5	Validation uncertainty	81
4	Wave Propagation and Loads	83
4.1	Wave Propagation	83
4.1.1	Test case description and numerical setup	83
4.1.2	Absorption zones	86
4.1.3	Wave propagation results	86
4.1.4	Iterative convergence	89
4.1.5	Discretisation errors	92
4.1.6	Stokes 5th order	96
4.2	Wave Loads	97
4.2.1	Test case description and numerical setup	97
4.2.2	Wave load results	100
4.2.3	Iterative convergence	104
4.2.4	Discretisation errors	105
4.2.5	Validation	111
4.3	Concluding Remarks on Waves and Wave Loads	111
5	Hydrodynamic Damping	115
5.1	Test Case Description	115
5.1.1	Semi-submersible and mooring layout	115
5.1.2	Numerical Setup	118
5.2	Discretisation Errors and Uncertainties	120
5.2.1	Viscous-flow simulations	121
5.2.2	Dynamic mooring model	130
5.3	Input Sensitivity	134
5.3.1	Initial displacement and release time	134
5.3.2	Restoring stiffness	137
5.4	Modelling Influence	141
5.4.1	Turbulence modelling	141
5.4.2	Free surface and motion coupling	145
5.4.3	Complete domain and motions	151
5.4.4	Dynamic mooring model	154
5.5	Validation	158
5.5.1	Initial six DOF displacement	158
5.5.2	Comparison with experiment	160
5.6	Concluding Remarks	162
6	Conclusions and Outlook	165
6.1	Summary	165
6.2	General Conclusions	166
6.3	Outlook	168

A Mooring Calculations	171
A.1 Time integration schemes	171
A.2 Drag and inertia on the mooring lines	172
A.3 Mooring characteristics	175
B Further Hydrodynamic Damping Investigations	179
B.1 Coupling schemes	179
B.2 Influence of Temperature	181
B.3 Motion coupling	181
C Interface Capturing Schemes	183
C.1 Numerical Simulations	183
C.2 Iterative Convergence	183
C.3 Wave Elevation and Loads	184
C.4 Flow Solution	184
C.5 Remarks	185
Bibliography	187

List of Figures

1.1	Floating foundation concepts for offshore wind turbines.	2
1.2	Aspects of floating wind turbine simulations with CFD.	11
2.1	Damping components of a semi-submersible floater.	14
2.2	Different oscillators with respective damping ratios.	19
2.3	Illustration of the PQ analysis method to obtain damping estimation coefficients.	23
2.4	Example of an optimised motion PQ analysis.	25
2.5	Comparison of the PQR and PQ analysis methods.	27
2.6	Relation between the earth-fixed and body-fixed coordinate system.	44
2.7	Catenary moorings with definitions.	45
2.8	Forces on a mooring element.	45
2.9	Definitions for a single moored vessel.	48
3.1	Detail of a 2D Cartesian grid with notation.	52
3.2	Grid cells at interface with notation, adapted from Klaij et al. (2018).	56
3.3	Sketch of the wave inflow boundary condition.	60
3.4	Differences of the mooring model types.	69
3.5	Principle of lumped mass model.	70
3.6	General simulation procedure of a moored floating structure with moving grids.	74
4.1	Grid and domain setup for the wave propagation test case.	84
4.2	Grid topology of a coarse grid with wave elevation.	85
4.3	Wave reflection coefficient as a function of the absorption coefficient.	87
4.4	Wave elevation for a selection of 15 simulations.	87
4.5	Wave heights for a selection of 15 simulations.	88
4.6	Air volume fraction for wave propagation.	89
4.7	Residuals for the wave propagation test case at the end of each time step for three grids.	90
4.8	Residuals of the vertical component of the velocity in the domain for the wave propagation test case.	91
4.9	Residuals averaged over time for different convergence criteria.	92
4.10	Discretisation error and uncertainty estimation using the approach by Eça and Hoekstra (2014) for the mean wave height H_{wmean}	93

4.11 Comparison of results for extrapolated grid and time step independent solution of the mean wave height $H_{w,mean}$ for the three discretisation error estimation approaches.	95
4.12 Comparison of numerical with analytical result for test case one.	97
4.13 Computational domain for test case two with grid from different views.	99
4.14 Wave loads F_x on the cylinder for 25 simulations with different grids and time steps.	101
4.15 Free surface around cylinder.	102
4.16 x component of velocity at free surface around cylinder.	103
4.17 Example of iterative convergence for test case two.	104
4.18 Velocity residuals in z direction in the domain for test case two.	104
4.19 Residuals averaged over time for different convergence criteria for test case two.	105
4.20 Discretisation error and uncertainty estimation using the approach by Eça and Hoekstra (2014) for the mean of the wave load height F_x	106
4.21 Comparison of results for extrapolated grid and time step independent solution for the mean oscillation height of the wave load $F_{x,h,mean}$ using the method by Oberhagemann and el Moctar.	108
4.22 Comparison of results for extrapolated grid and time step independent solution using the three approaches for test case two.	110
4.23 Comparison of numerical and experimental results of wave loads F_x for test case two including uncertainty bars.	112
5.1 Drawing of the semi-submersible at model scale.	116
5.2 Mooring setup for the semi-submersible at model scale.	117
5.3 Initial mooring line configuration.	118
5.4 Computational domain including boundaries for the surge decay simulations.	119
5.5 Grid topology for surge decay simulation presented for the coarse grid.	120
5.6 Courant numbers around the floater for verification studies.	122
5.7 Surge decay motion x for 18 simulations.	123
5.8 Results of the hydrodynamic damping analysis using the optimised motion PQ method for different grids and time steps.	124
5.9 Examples of iterative convergence for the surge decay simulations.	125
5.10 The residuals for air volume fraction for the surge decay simulations.	126
5.11 Residuals averaged over time for different convergence criteria for the surge decay simulations.	126
5.12 Comparison of results for different convergence criteria of the surge decay simulations.	127
5.13 Discretisation error and uncertainty estimation using the approach by Eça and Hoekstra (2014) for the oscillation height of the surge decay simulations.	128

5.14 Comparison of results for extrapolated grid and time step independent solution for second oscillation height H_2 using the three different approaches for the surge decay simulations.	129
5.15 Time history of 11 selected surge decay simulations	132
5.16 Surge decay time history of simulations with different initial release time instances.	135
5.17 Surge decay time history and PQ analysis of simulations with different initial displacements.	136
5.18 Surge decay time history of simulations with different stiffness properties.	138
5.19 Velocity magnitude of several numerical simulations with symmetric domain and different restoring stiffness.	139
5.20 Contour of $Q = 0.5 \text{ s}^{-2}$ around the floater for several numerical simulations with symmetric domain.	140
5.21 Surge decay time history of simulations with different turbulence modelling approaches.	142
5.22 Wave elevation as a function of time for different turbulence modelling approaches.	143
5.23 Vorticity around the floater for different turbulence modelling approaches.	144
5.24 Contour of $Q = 0.5 \text{ s}^{-2}$ around the floater for different turbulence modelling approaches.	146
5.25 Surge decay time history of simulations with and without free surface, and with and without wave absorption.	147
5.26 Surface elevation in the domain for two simulations with and without absorption zone.	148
5.27 Velocity magnitude of several numerical simulations with symmetric domain for investigations of the wave radiation effects.	149
5.28 Contour of $Q = 0.5 \text{ s}^{-2}$ around the floater for several numerical simulations with symmetric domain.	150
5.29 Surge decay time history of simulations with motion coupling.	152
5.30 Results for surge decay time history of simulations with different computational domains.	153
5.31 PQ diagram for simulations with different computational domains.	154
5.32 Vortices around the floater for symmetric and full domain.	154
5.33 Results for surge decay time history of simulations with dynamic mooring model.	157
5.34 PQ diagram for simulations with different dynamic mooring models.	158
5.35 Results for surge decay time history of simulations with dynamic mooring model and 6 displacement.	159
5.36 Results for surge decay time history compared with experiment. . .	161
A.1 Time history second-order Runge-Kutta and fifth-order Cash-Karp scheme.	172
A.2 Mooring tension in line 1 as a function of surge displacement for different normal drag coefficients.	173

A.3	Mooring tension in line 1, 2 and 3 as a function of surge displacement for different tangential drag coefficients.	174
A.4	Mooring tension in line 1 as a function of surge displacement for different normal inertia coefficients.	175
A.5	Mooring tension in line 1, 2 and 3 as a function of surge displacement for different submerged weight values.	176
B.1	Comparison of results for two different coupling schemes.	180
B.2	Comparison of results for two different coupling frequencies and two different maximum outer-loop iterations.	180
B.3	Motion coupling for 6 DOF simulations.	182
C.1	Residuals for the volume fraction c in L_2 norm of the different in- terface capturing schemes.	184
C.2	Wave elevation along the x axis for the different interface capturing schemes.	185
C.3	Wave loads on the cylinder for the different interface capturing schemes.	185
C.4	Air volume fraction of the wave for four different interface capturing schemes.	186

List of Tables

2.1	PQ analysis comparison between different methods.	27
2.2	Coefficients for $k - \omega$ SST turbulence model.	35
2.3	Coefficients for KSkl turbulence model.	36
2.4	Constants for $k - \omega$ TNT EARSM model.	37
3.1	Segregated solution algorithm for unsteady flows (Klaij and Vaz, 2017).	65
3.2	Solution algorithm with predictor and corrector step for coupling with structural equation of motion	67
4.1	Wave characteristics.	83
4.2	Computational domain for wave propagation test case.	84
4.3	Grid definitions for test case one. The values tabulated are valid for refinement box A relative to the wave.	85
4.4	Theoretical CFL numbers for test case one. The time steps are defined as a ratio of the wave period $T_p = 1.711\text{ s}$, i.e. $T_p/280$ is a coarse and $T_p/1200$ a fine time step.	86
4.5	Influence of the iterative convergence criterion on the wave propagation.	92
4.6	Results for discretisation error and uncertainty estimation by Eça and Hoekstra (2014) for $H_{w_{mean}}$	94
4.7	Results for discretisation error and uncertainty estimation for $H_{w_{mean}}$ using the approach by Oberhagemann and el Moctar (2019) . . .	96
4.8	Results for discretisation error and uncertainty estimation for $H_{w_{mean}}$ using the approach by Xing and Stern (2010).	96
4.9	Wave characteristics for the wave load test case.	98
4.10	Computational domain for test case two.	98
4.11	Grid definitions for test case two.	100
4.12	Theoretical CFL numbers for test case two.	100
4.13	Influence of the iterative convergence criterion on the wave loads. . .	106
4.14	Results for discretisation error and uncertainty estimation for different sets of grids and time steps for the mean of the wave load height $F_{x,h_{mean}}$ using the approach by Eça and Hoekstra (2014) . .	107

4.15 Results for discretisation error and uncertainty estimation for the mean of the wave load height $F_{x,hmean}$ using the approach by Oberhagemann and el Moctar (2019).	109
4.16 Results for discretisation error and uncertainty estimation for the mean of the wave load height $F_{x,hmean}$ using the approach by Xing and Stern (2010).	111
5.1 Main particulars of the floating wind turbine system.	116
5.2 Linearised stiffness properties of the mooring system.	116
5.3 Mooring characteristics as given by Gueydon (2016).	117
5.4 Grid topology for surge decay simulations.	120
5.5 Grid definitions for surge decay simulations.	121
5.6 Theoretical CFL numbers for surge decay simulations.	121
5.7 Results for discretisation error and uncertainty estimation using the approach by Eça and Hoekstra (2014) of the surge decay simulations.	127
5.8 Results for discretisation error and uncertainty estimation for H_2 using the approach by Oberhagemann and el Moctar (2019).	129
5.9 Results for discretisation error and uncertainty estimation for H_2 using the approach by Xing and Stern (2010).	129
5.10 Semi-submersible model in aNySIM as given by Gueydon (2016).	131
5.11 Results for discretisation error and uncertainty estimation using the approach by Eça and Hoekstra (2014) for five different parameters of the mooring simulations.	132
5.12 Results for discretisation error and uncertainty estimation for different parameters using the approach by Oberhagemann and el Moctar (2019) for mooring simulations.	133
5.13 Results for discretisation error and uncertainty estimation for different parameters using the approach by Xing and Stern (2010) for the mooring simulations.	133
5.14 Hydrodynamic damping comparison of simulations with different input parameters.	135
5.15 Hydrodynamic damping values for simulations with different turbulence modelling approaches.	142
5.16 Hydrodynamic damping comparison of simulations with and without free surface.	148
5.17 Hydrodynamic damping comparison of simulations with symmetric and full domain.	155
5.18 Characteristics of the final mooring system.	156
5.19 Hydrodynamic damping comparison of simulations with lumped-mass mooring model.	156
5.20 Hydrodynamic damping comparison between numerical simulation and experiment.	162
A.1 Characteristics of the new mooring system.	177

B.1 Damping differences between two different coupling frequencies and two different maximum outer-loop iterations.	181
C.1 Average amount of outer-loop iterations per time step for different interface capturing schemes.	184

Abbreviations and Acronyms

ABM2	Second-order Adams-Bashforth-Moulton
BC	Boundary Condition
BDF2	Second-order backward differencing
BEMT	Blade-Element-Momentum theory
CFD	Computational Fluid Dynamics
CFL	Courant-Friedrichs-Lowy
COG	Centre of gravity
CPU	Central Processing Unit
CV	Control volume
DB	Double Body
DNS	Direct Numerical simulation
DOF	Degrees-of-freedom
DST	Development Centre for Ship Technology and Transport Systems
DTU	Technical University of Denmark
EARSM	Explicit Algebraic Reynolds Stress Model
EAWE	European Academy of Wind Energy
EH	Eça and Hoekstra
EWEA	European Wind Energy Association
FD	Finite Difference
FE/FEM	Finite Element Method
FOWT	Floating Offshore Wind Turbine
FVM	Finite Volume Method
HAWT	Horizontal Axis Wind Turbine
HIL	Hardware In the Loop
HPC	High Performance Computing
IEA	International Energy Agency
ITTC	International Towing Tank Conference
KSKL	$k - \sqrt{kL}$
LCOE	Levelised Cost of Energy
LES	Large Eddy Simulation
LID	Large negative Initial Displacement
LM	Lumped Mass
MARIN	Maritime Research Institute Netherlands
MSWT	MARIN Stock Wind Turbine
MVG	Moving-grid formulation

NREL	National Renewable Energy Laboratory
NRBC	Non-Reflecting Boundary Condition
NS	Navier-Stokes
OC3	Offshore Code Comparison Collaboration
OC4	Offshore Code Comparison Collaboration Continued
OC5	Offshore Code Comparison Collaboration Continued, with Correlation
OeM	Oberhagemann and el Moctar
PWI	Pressure Weighted Interpolation
QSM	Quasi-static Mooring model
QUICK	Quadratic Upwind Interpolation for Convective Kinematics
RANS	Reynolds-Averaged Navier-Stokes
RANSE	Reynolds-Averaged Navier-Stokes equations
ReFRESCO	Reliable & Fast RANS Equations solver for Ships and Constructions Offshore
RK	Runge-Kutta
RWT	Reference Wind Turbine
SIL	Software In the Loop
SIMPLE	Semi-Implicit Method for Pressure Linked Equations
SST	Shear Stress Transport
TLP	Tension-leg platform
TNT	Turbulent/Non-Turbulent
TVD	Total Variation Diminishing
URANS	Unsteady Reynolds-Averaged Navier-Stokes
VAWT	Vertical axis wind turbine
VOF	Volume of Fluid
WEC	Wave energy converter
wFreeS	With free surface
XMF	Extensible Modelling Framework
XS	Xing and Stern

List of Symbols

Label	Description	Unit
Latin		
A	Matrix of linear equation system	[⁻¹]
\hat{A}	Approximation of A	[⁻¹]
a	Extra Reynolds stress anisotropy tensor	[\cdot]
C	Restoring or stiffness matrix	[N/m, N m/rad]
D	Mechanical damping matrix	[N s/m, N m s/rad]
G	Gradient matrix	[\cdot]
I	Identity matrix	[\cdot]
M	Mass matrix	[kg, kg m ²]
Q	Advection and diffusion matrix	[\cdot]
R_{xyz}	Transformation matrix	[\cdot]
S_t	Strain rate tensor	[1/s]
T	Stress tensor	[N/m ²]
\vec{a}	Acceleration vector	[m/s ²]
\vec{e}	Eccentricity vector	[m]
\vec{f}_a	Added body force vector/source term for wave absorption	[Pa/m]
\vec{f}_b	Body force vector	[Pa/m]
\vec{f}_C	Restoring force vector	[N, N m]
\vec{f}_D	Mechanical damping force vector	[N, N m]
\vec{f}_{Dr}	Drag force vector	[N]
\vec{f}_{d_i}	Mooring damping force vector per lumped node <i>i</i>	[N]
$\vec{f}_{external}$	External mooring force vector	[N]
\vec{f}_H	Hydrodynamic force vector	[N, N m]
$\vec{f}_{internal}$	Internal mooring force vector	[N]
\vec{f}_M	Inertia force vector	[N]
\vec{f}_s	Surface force vector	[Pa/m]
\vec{f}_{st_i}	Mooring stiffness force vector per lumped node <i>i</i>	[N]

¹Depends on ϕ

Label	Description	Unit
\vec{g}	Gravitational acceleration vector	[m/s ²]
\vec{h}	Coefficient matrix to solve equation of motion	[kg, kg m ² ,N, N m, m/s, rad/s]
$\vec{k}_1, \dots, \vec{k}_1$	Runge-Kutta scheme coefficient vectors	[m/(s ²), m/(s ³)]
\vec{n}	Normal vector of a surface	[·]
\vec{n}_{f_i}	Normal vector of CV face i	[·]
\vec{n}_I	Interface normal vector	[·]
\vec{q}_ϕ	General source term vector	[·]
\vec{r}	Residual of linear equation system	[·]
\vec{r}_u	Residual of momentum equation	[·]
\vec{S}_{f_i}	Surface area vector of face i	[m ²]
\vec{v}	Velocity vector	[m/s]
\vec{v}^*	Velocity prediction vector	[m/s]
\vec{v}'	Velocity correction vector	[m/s]
\vec{v}_G	Grid velocity vector	[m/s]
\vec{x}	Space vector	[m,rad]
$\dot{\vec{x}}$	Velocity vector	[m/s,rad/s]
$\ddot{\vec{x}}$	Acceleration vector	[m/s ² , rad/s ²]
\vec{x}_{CD}	Vector connecting cell centres of C and D	[m]
\vec{x}_P	Space vector in body fixed coordinate system	[m]
\vec{x}'_0	Space vector between earth fixed and body fixed coordinate system	[m]
\vec{x}'_p	Resultant space vector between \vec{x}_P and \vec{x}'_0	[m]
\vec{y}	Coefficient vector for time integration	[m/s,m/s ²]
A	Cross-sectional area of mooring line	[m ²]
$B(\dot{x})$	Hydrodynamic damping function of \dot{x}	[Ns/m, N ms]
B_1	Linear damping coefficient	[Ns/m, N ms]
$B_{1,eq}$	Equivalent linear damping coefficient	[Ns/m, N ms]
B_2	Quadratic damping coefficient	[Ns ² /m ² , N ms ²]
B_3	Cubic damping coefficient	[Ns ³ /m ³ , N ms ³]
B_{crit}	Critical damping coefficient	[Ns/m, N ms]
C	Stiffness or restoring	[N/m]

Label	Description	Unit
C_{55}	Stiffness component of pitch	[N m/rad]
C_A	Added mass coefficient	[\cdot]
C_a	Ratio between horizontal tension T_H and submerged weight w	[m]
C_D	Drag coefficient	[\cdot]
C_{D_n}, C_{D_t}	Normal and tangential drag coefficient	[\cdot]
$C_{Dk\omega}$	Turbulence model coefficient	[\cdot]
$C_{D\omega}$	Turbulence model coefficient	[\cdot]
CFL	Courant number or Courant-Friedrichs-Lowy number	[\cdot]
C_{it}	Outer-loop convergence criterion	[\cdot]
C_M	Inertia coefficient	[\cdot]
C_{Mn}, C_{Mt}	Normal and tangential inertia coefficient	[\cdot]
C_r	Wave reflection coefficient	[\cdot]
C_α	EARSM turbulence model coefficient	[\cdot]
$C_{\alpha 1}, C_{\alpha 2}$	$k - \omega$ SST turbulence model coefficients	[\cdot]
C_β	EARSM turbulence model coefficient	[\cdot]
$C_{\beta 1}, C_{\beta 2}$	$k - \omega$ SST turbulence model coefficients	[\cdot]
C_μ	Turbulence model coefficient	[\cdot]
D	Diameter	[m]
E	Elastic Young's modulus	[N/m ²]
E_u	Euler number	[\cdot]
F_1, F_2	Blending function	[\cdot]
F_r	Froude number	[\cdot]
F_s	Safety factor for discretisation uncertainty estimation	[\cdot]
F_x	Wave load in x direction	[N]
$F_{x,hmean}$	Mean oscillation height of wave load in x direction	[N]
G	Constant obtained to solve auxiliary function	[\cdot]
H, H_{2nd}	First and second order Sommerfeld operator	[\cdot]
H_2, H_3	Oscillation height of second (2) and third (3) oscillation cycle	[m]
H_w	Wave height	[m]
$H_{w,min}$	Minimum wave height of a time history	[m]
$H_{w,max}$	Maximum wave height of a time history	[m]
$H_{w,mean}$	Mean wave height of a time history	[m]
K_C	Keulegan-Carpenter number	[\cdot]
L_0	Characteristic length	[m]
L_{vK}	von Kármán length scale	[m]
M	Structural and added mass	[kg]
N_{cells}	Number of cells or CVs	[\cdot]
N_f	Number of faces per CV	[\cdot]
N_t	Number of time steps	[\cdot]
P	Convergence ratio between observed and theoretical order, used in Xing and Stern approach	[\cdot]

Label	Description	Unit
P_k	Turbulence model production term for k	[\cdot]
\tilde{P}_k	Modified turbulence model production term for k	[\cdot]
Q	Q -criterion, imbalance between the magnitude of vorticity and strain rate, used for vortex identification	[$1/\text{s}^2$]
Q_C	Source terms of cell C	[$^{-1}$]
R	Convergence ratio	[\cdot]
R_e	Reynolds number	[\cdot]
$S_1(\dots), S_2(\dots)$	Least-squares function for 1 st and 2 nd order convergence used in Oberhagemann and el Moctar approach	[$^{-1}$]
S_f	Cell face surface area	[m^2]
S_{t_M}	Strain rate magnitude	[$1/\text{s}$]
$S_{RE}^w(\dots)$	Weighted least-squares function used in Eça and Hoekstra approach	[$^{-1}$]
S	Surface	[m^2]
T	Mooring line tension	[N]
T_n	Natural period	[s]
T_p	Wave period or oscillation period	[s]
T_{pmean}	Mean of wave period or oscillation period	[s]
T_{LPmean}	Mean of wave load period	[s]
T'	Mooring line tension including submerged weight contribution	[N]
T_0	Mooring line tension at touch-down point	[N]
T_H	Horizontal component of mooring line tension	[N]
T_{ref}	Reference period	[s]
T_Z	Vertical component of mooring line tension	[N]
$U_{EXP}(\phi)$	Experimental uncertainty of given quantity ϕ	[$^{-1}, \%$]
$U_{FS}(\phi)$	Discretisation uncertainty for ϕ used for Xing and Stern approach	[$^{-1}, \%$]
$U_{INP}(\phi)$	Input uncertainty of given quantity ϕ	[$^{-1}, \%$]
$U_{NS}(\phi)$	Numerical simulation uncertainty of given quantity ϕ	[$^{-1}, \%$]
$U_V(\phi)$	Validation uncertainty of given quantity ϕ	[$^{-1}, \%$]
U_ϕ	Uncertainty of given quantity ϕ	[$^{-1}, \%$]
$U_{LSQth}(\phi_i)$	Discretisation uncertainty for ϕ of simulation i used for Oberhagemann and el Moctar approach	[$^{-1}, \%$]
V	Volume	[m^3]
W_B	Work done by damping force	[J]
X	Surge motion	[m]
$X(t_i)$	Oscillation amplitude/peak at time instant t_i	[m]
a, a_1, a_2	Discretisation error coefficients used by Oberhagemann and el Moctar approach	[\cdot]
a_1	Turbulence model coefficient	[\cdot]
c	Volume fraction	[\cdot]
c_1, c_2, c_3	Time integration coefficients	[\cdot]

Label	Description	Unit
c_f	Geometric interpolation factor	[\cdot]
c_w	Wave celerity	[m/s]
c_{w1}, c_{w2}	Wave celerity for first and second order Sommerfeld function	[m/s]
d_t	Distance to nearest wall	[m]
$f(\dots)$	Function to solve initial value problems	[\cdot]
f_b	Body force function for wave absorption	[1/s]
f_{max}	Wave absorption coefficient	[\cdot]
f_n, f_t	Hydrodynamic forces normal (n) and tangential (t) to the mooring line	[N/m]
g	Gravitational acceleration, vertical/third component of gravity vector	[m/(s ²)]
h	Relative grid spacing used for Eça and Hoekstra approach	[\cdot]
h	Water depth	[m]
k	Turbulent kinetic energy	[N m/kg]
k_w	Wave number	[rad/m]
L_t	Turbulent length scale	[m]
l	Total mooring line length between fairlead and anchor	[m]
l_s	Mooring line length between fairlead and touch down point	[m]
m	Number of current iteration	[\cdot]
n	Number of current time step	[\cdot]
n_d	Number of spatial dimensions	[\cdot]
p	Pressure	[Pa]
p	Linear damping estimation coefficient	[\cdot]
p'	Pressure correction	[Pa]
p_{dyn}	Dynamic pressure	[Pa]
q	Quadratic damping estimation coefficient	[1/m, 1/rad]
r	Cubic damping estimation coefficient	[1/m, 1/rad]
r	General refinement factor	[\cdot]
r_n	Normalised residual	[\cdot]
r_{L_2}	L_2 residual norm or root-mean-square of the residuals	[\cdot]
r_{L_∞}	L_∞ residual norm or maximum value of the residuals	[\cdot]
r_x, r_y, r_z	Refinement factor in x, y, z	[\cdot]
r_{xx}, r_{yy}, r_{zz}	Radius of gyration around x, y, z	[m]
s	Mooring line coordinate	[m]
t	Time	[s]
t_i	Relative time step or instant of time	[\cdot]
u_0	Characteristic flow velocity	[m/s]
u, v, w	Vector components of velocity in x, y, z	[m/s]

Label	Description	Unit
u_{dyn}	One-dimensional velocity component	[m/s]
u_i	Vector components of velocity in x, y, z	[m/s]
\hat{u}_i	Theoretical wave orbital velocity components in x, y, z	[m/s]
v_M	Magnitude of velocity vector	[m/s]
v_t	Turbulence velocity scale	[m/s]
w	Submerged weight per unit length	[N/m]
w_i	Weights for least-squares method	[‐]
x, y, z	Cartesian coordinates	[m]
\dot{x}, \ddot{x}	1 st and 2 nd temporal derivative of x or velocity and acceleration in x	[m/s, m/s ²]
x', y', z'	Cartesian coordinates for earth-fixed coordinate system	[m]
x_b	Location of the absorption zone	[m]
x_i	Cartesian coordinates	[m]
x_i	Oscillation amplitude	[m]
x_{c_i}	Location of cell centre	[m]
x_{f_i}	Location of face centre	[m]
y^+, y_{max}^+	Non-dimensional wall distance and its maximum value	[‐]

Greek

ϱ	Relaxation matrix	[‐]
τ	Viscous stress tensor	[N/m ²]
τ_R	Reynolds stress tensor	[N/m ²]
$\vec{\kappa}$	Velocity vector for equation of motion	[m/s, rad/s]
$\vec{\phi}$	Vector of ϕ values at cell nodes	[‐ ¹]
$\vec{\Omega}_v$	Vorticity vector	[1/s]
α	Discretisation error coefficient	[‐ ¹]
α_t	Temporal discretisation error coefficient	[‐ ¹]
α_x	Spatial discretisation error coefficient	[‐ ¹]
Γ	Diffusivity of ϕ	[m ² /s]
Δp	Pressure difference	[Pa]
Δt	Time step	[s]
$\Delta V, \Delta V_c$	Volume of respective CV	[m ³]
Δx	Typical grid cell spacing or typical grid cell spacing in x	[m]
Δy	Typical grid cell spacing in y	[m]
Δz	Typical grid cell spacing in z	[m]
Δ_ϕ	Data range parameter for discretisation uncertainty estimation	[‐ ¹]
Λ_i	Logarithmic decrement of oscillation i	[‐]
Λ_{pmean}	Mean of positive (p) and negative (n)	

Label	Description	Unit
$\Lambda_{n_{mean}}$	logarithmic decrement	[\cdot]
δ	Error	[$^{-1}$]
$\delta_1, \delta_2, \delta_{12}$	Error estimators	[$^{-1}$]
δ_{RE}	Error obtained by Richardson extrapolation	[$^{-1}$]
β	Blending factor for Refrics	[\cdot]
β	Sarpkaya's frequency parameter	[\cdot]
β^*	Turbulence model coefficient used for $k - \omega$ SST and EARSM	[\cdot]
ϵ	Turbulence dissipation rate	[m^2/s^3]
ϵ_{CO}	Comparison error	[$^{-1}, \%$]
ϵ_d	Discretisation error	[$^{-1}, \%$]
ϵ_I	Input error	[$^{-1}, \%$]
ϵ_{it}	Iterative error	[$^{-1}, \%$]
ϵ_M	Modelling error	[$^{-1}, \%$]
ϵ_{NS}	Numerical simulation error	[$^{-1}, \%$]
ϵ_{ro}	Round-off error	[$^{-1}, \%$]
ϵ_{st}	Statistical error	[$^1, \%$]
ϵ_T	Total computational error	[$^{-1}, \%$]
ζ	Free surface elevation or wave elevation	[m]
$\zeta_1, \zeta_2, \zeta_3$	KSKL turbulence model coefficients	[\cdot]
ζ_a	Wave amplitude	[m]
ζ_D	Critical damping ratio	[$\%$]
η_{ob}	Observed order of convergence	[\cdot]
η_{obt}	Observed temporal order of convergence	[\cdot]
η_{obx}	Observed spatial order of convergence	[\cdot]
η_{th}	Theoretical order of convergence based on order of approximation	[\cdot]
θ	General angular integration variable	[rad]
θ_{ps}	Phase shift	[rad]
κ	von Kármán constant	[\cdot]
λ	Scaling factor	[\cdot]
λ_b	Bulk or volume viscosity	[Pa s]
λ_w	Wave length	[m]
μ	Dynamic viscosity	[$N s/m^2$]
μ_a	Dynamic viscosity of air	[$N s/m^2$]
μ_t	Turbulent or eddy viscosity	[$N s/m^2$]
μ_w	Dynamic viscosity of water	[$N s/m^2$]
ν	Kinematic viscosity	[m^2/s]
ξ	Stretched mooring line length	[m]
ρ	Density	[kg/m^3]
ρ_a	Density of air	[kg/m^3]
ρ_w	Density of water	[kg/m^3]
ϱ_u, ϱ_p	Relaxation parameter for velocity and pressure	[\cdot]

Label	Description	Unit
σ_d	EARSM turbulence model coefficient	[\cdot]
σ_k	Turbulence model coefficient used for KSKL and EARSM	[\cdot]
σ_{k1}, σ_{k2}	$k - \omega$ SST turbulence model coefficients	[\cdot]
σ_{RE}^w	Weighted standard deviation for uncertainty estimation	[$^{-1}$]
σ_Φ	KSKL turbulence model coefficient	[\cdot]
σ_ω	EARSM turbulence model coefficient	[\cdot]
$\sigma_{\omega1}, \sigma_{\omega2}$	$k - \omega$ SST turbulence model coefficients	[\cdot]
Υ	Non-dimensional scalar grid refinement ratio used for Oberhagemann and el Moctar approach	[\cdot]
ϕ	Given quantity	[$^{-1}$]
$\bar{\phi}$	Mean value of ϕ	[$^{-1}$]
$\dot{\phi}$	1 st temporal derivative of ϕ	[$^{-1}$]
$\ddot{\phi}$	2 nd temporal derivative of ϕ	[$^{-1}$]
$\nabla\phi$	Gradient of ϕ	[$^{-1}$]
ϕ_0	Exact or extrapolated value of given quantity	[$^{-1}$]
ϕ_1, ϕ_2, ϕ_3	Given quantity of simulation with fine, medium and coarse resolution	[$^{-1}$]
ϕ_c	Cell centre value of ϕ	[$^{-1}$]
ϕ_{cD}, ϕ_{cU}	Cell centre value of ϕ downstream and upstream of given location	[$^{-1}$]
ϕ_{fi}	Value of ϕ of cell face i	[$^{-1}$]
ϕ_i	Given quantity of i^{th} simulation	[$^{-1}$]
ϕ^m	Value of ϕ at iteration m	[$^{-1}$]
ϕ_n	Value of ϕ at time step n	[$^{-1}$]
ϕ_{ref}	Reference value of ϕ	[$^{-1}$]
ϕ_{vp}	Velocity potential	[m^2/s]
φ	Mooring line angle w.r.t horizontal	[rad]
φ_0	Mooring line angle w.r.t horizontal at touch-down point	[rad]
φ_n	Angle between \vec{n}_I and \vec{x}_{CD}	[rad]
φ_{prop}	Angle between wave propagation direction and domain boundary	[rad]
φ_w	Mooring line angle w.r.t horizontal at free surface	[rad]
ω	Specific turbulence dissipation	[$1/\text{s}$]
ω_d	Damped oscillation frequency or observed oscillation frequency	[rad/s]
ω_n	Natural frequency or eigenfrequency	[rad/s]
ω_w	Wave frequency	[rad/s]

1. Introduction

The nuclear disasters in Fukushima and Chernobyl led to public concerns in several nuclear powered countries (Bauer et al., 2018) and were followed by increased awareness of the evident climate change. Starting in 2010, political decisions of many industrial countries aimed at a transition from fossil to renewable energy as its sustainable use is seen as an important approach to mitigate climate change and to meet the energy demand of future generations (Owusu and Asumadu-Sarkodie, 2016).

In the offshore energy sector, the major renewable sources may be found in wind, wave, current, solar and thermal energy. Wind technology as a whole is the oldest and furthest developed technology in the renewable industry (Andersen, 2016). The onshore wind market is well established and many turbines were built in the past (Komusanac et al., 2020). The offshore wind market, however, just started in 1991 with its first wind farm inaugurated 2.5 km off the coast in Denmark (Burton et al., 2011). Nevertheless, a steady increase of the offshore wind market may be observed over the past two decades (European Wind Energy Association, 2011). In 2019, about 10 % of the new installations worldwide were erected offshore. These new installations accumulated to a total energy capacity of more than 6.1 GW. Globally, this was the peak for the wind energy market (Lee and Zhao, 2020). As locations close to shore are limited and the wind blows more steadily further offshore, the average distance to shore and water depth of new installations continue to grow (Ramírez et al., 2020). For deep waters exceeding 50 – 60 m, floating support structures for wind turbines become attractive alternatives to the current monopile or jacket type bottom-fixed foundations (van Kuik and Peinke, 2016).

At steep coasts such as in China, Japan, Norway, Portugal, Spain, the United Kingdom, the United States of America, France, etc. the water depth increases quickly and reduce significantly the amount of accessible wind resources with bottom-fixed foundations. Hence, several concepts of floating foundations for wind turbines were and are currently developed, tested, and analysed. These concepts originate mostly from the oil and gas industry. Sketches for the most frequently encountered concepts are illustrated in Figure 1.1. Commonly, these floating concepts are categorised based on their principle to achieve static stability (Butterfield et al., 2005, Andersen, 2016) by ballast, mooring line tension, or buoyancy. The spar buoy achieves static stability due to ballast. These platforms lower the centre of gravity below the centre of buoyancy by additional ballast. In this way, a restoring moment arises when the platform is not in equilibrium. Tension-leg platforms (TLP)

obtain their stability owing to the mooring line tension. Their centre of gravity lies above the centre of buoyancy, which may lead to unstable configurations without moorings. The taut mooring system provides the righting moment using fairleads at off-axis locations. Semi-submersibles and barge type floaters acquire stability by buoyancy. These floaters distribute buoyancy to different elements piercing the free surface at locations outside of the centre turbine tower axis. Thus, the righting moment arises due to eccentric buoyancy changes. The mooring system of semi-submersibles and barges are used mainly for stationkeeping but depending on the design might contribute to the stability of the platform. Furthermore, hybrid concepts exist using a combination of these principles.

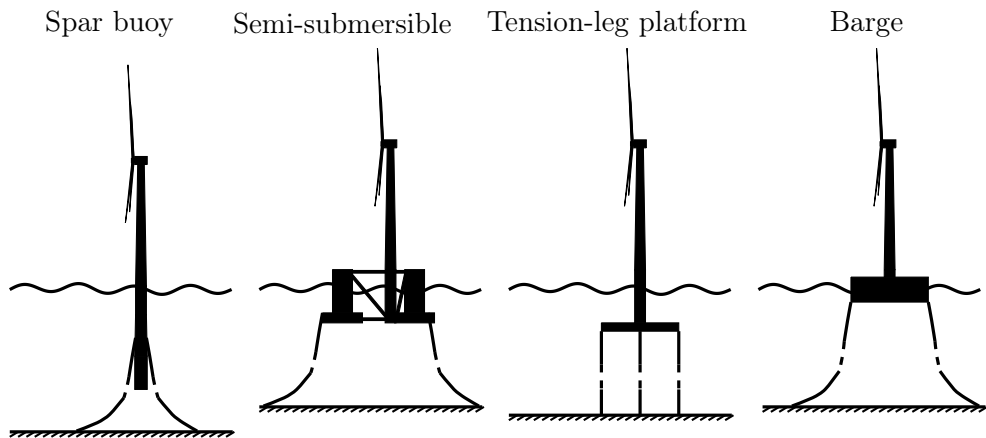


Figure 1.1: Floating foundation concepts for offshore wind turbines (not drawn to scale).

The advantages of floating wind turbines are, amongst others, that they provide access to greater wind resources further offshore, may be standardised for a whole wind park, enable access to areas with difficult soil conditions, and are less visible from shore (Cordle and Jonkman, 2011, Gueydon and Fernandes, 2013). They operate, however, in very complex environmental conditions. The main loads acting on the floating system by the environment originate from wind, wave, and current. Furthermore, the aero- and hydrodynamic interaction is very complex, and only a few commercially applied systems exist to date.

Floating wind turbine concepts utilise mostly horizontal axis, three-bladed, upstream wind turbines. In the late 1970s and early 1980s vertical axis wind turbines (VAWT) were also investigated for onshore applications (Burton et al., 2011). As these types of turbines are aerodynamically less efficient, and thus, have larger costs of energy than horizontal axis wind turbines (HAWTs), they were disregarded for onshore sites and subsequently also for offshore locations. For floating offshore wind turbines (FOWTs), VAWTs reveal some important advantages for the dynamic behaviour of the floating system (e.g. lower heeling moment, lower centre of gravity, etc.). Moreover, because of the larger dynamic stability, smaller, and consequently, cheaper floaters might be possible. VAWTs are also insensitive to the wind direction. Therefore, also VAWTs are considered for the ongoing de-

velopment of several floating wind turbine concepts (Cruz and Atcheson, 2016). More details on the advantages of VAWTs may be found in Borg et al. (2014). However, this is out of the scope of this thesis.

The first floating wind park, called Hywind Scotland, uses a spar buoy floater and a HAWT, and is connected to the grid in Scotland since October 2017 (Rummelhoff, 2017). In December 2019, the first turbine of the WindFloat Atlantic wind farm got grid connected in Portugal (Skopljak, 2020). The wind turbine foundation belongs to the semi-submersible types of floaters (see Figure 1.1). Currently, 70 % of all installed wind turbines mounted on floating foundations are located in Europe. Moreover, Ramírez et al. (2020) predicted a strong increase of floating wind turbine installations for the next three years. In their report, six new European projects were listed in France, the United Kingdom, and Norway. Two of these six projects make use of semi-submersible type floaters, two of tension-leg platforms (TLPs), one of spar buoys, and one of barge type configurations. Thus, semi-submersibles are used in most ongoing commercial projects in Europe (Lemmer, 2018). These numbers and fast developments show that the amount of new concepts and participants are growing, and that many floating wind turbine concepts are getting market-ready.

Nevertheless, there are still relatively few experiences with FOWTs. Therefore, the research community needs to fill the knowledge gaps. The European Academy of Wind Energy (EAWE) formulated “long-term research challenges in wind energy” (van Kuik and Peinke, 2016). These challenges are manifold and range from societal and economic aspects via environmental, structural and material, control, electromechanical, reliability and design methods issues to aerodynamic and hydrodynamic problems. The challenges specified for the hydrodynamics of floating wind turbines include reliable prediction of viscous damping, accurate modelling of mooring line dynamics, and verification and validation protocols for numerical tools. These hydrodynamic aspects are addressed in the research studies conducted in this thesis.

1.1 State of the Art

Experiments and numerical simulations are two approaches to fill knowledge gaps on the dynamics of floating wind turbines. One of the major problems to be addressed by the research community is to predict hydrodynamic damping accurately and reliably. This requires, however, an accurate prediction of hydrodynamic loads and surrounding flow field. A brief review on the current state of the art for experiments, numerical simulations, and hydrodynamic damping of floating wind turbines is given in the following.

1.1.1 Experimental tests of floating wind turbines

Physical model tests of floating wind turbines are important to gain experience on, amongst others, its aero- and hydrodynamics. Experimental data are needed to understand the physical phenomena around these relatively new floating structures for all load conditions to be expected and to validate numerical simulation tools

(Müller et al., 2014). At model scale, these experiments are associated with lower costs, require less resources, reduce risks, allow more detailed measurements, and the environmental conditions can be better controlled than at full scale. As experiments of floating wind turbines involve aerodynamics and hydrodynamics with different scaling laws, model testing is not straightforward. When geometrical similarity is to be achieved between full and model scale, aero- or hydrodynamics may be scaled by the laws of Froude or Reynolds. Froude's scaling law is applied, if viscous effects are negligible and gravity effects are dominating. This is mostly the case with hydrodynamic flows involving a free surface. In contrast, Reynolds' scaling law is used if viscous effects dominate. Thus, for experiments at model scale and constant viscosity, either Froude or Reynolds scaling law can be followed. However, using Froude's law and geometrical scaling with a factor of λ results in an approx. $\lambda^{1.5}$ times smaller Reynolds number at model scale (Chakrabarti, 1998). If the flow regime changes, e.g. from turbulent to laminar, due to the Reynolds number mismatch, the load ratio between aerodynamics and hydrodynamics differ compared to the ratio at full scale. In addition, also the aerodynamic performance of the turbine changes. In experiments with Froude scaled conditions at MARIN (Maritime Research Institute Netherlands), lower aerodynamic loads on the scaled turbine, and therefore, lower thrust and power were measured (Make and Vaz, 2015).

Thrust, torque, and power of the turbine are dominant quantities for the dynamic behaviour of the floating wind turbine. They influence aerodynamic damping and contribute to the dynamic stability of the whole system. Hence, research institutes investigating floating wind turbines at model scale try to find work-around solutions by either coupling a numerical code with the experiment in real time, see e.g. Sauder et al. (2016), Hall and Goupee (2018) and Bayati et al. (2018), or by performance matching of the turbine, see e.g. Martin et al. (2012), de Ridder et al. (2014) and Bredmose et al. (2017). Müller et al. (2014) presents an extensive review of the different methods to perform experiments of floating wind turbines. This was extended by Gueydon et al. (2020), who discusses the benefits and drawbacks of each testing technique in great detail. Hardware-in-the-loop (HIL) or Software-in-the-loop (SIL) methods use numerical tools to calculate loads or motions in real-time and apply them experimentally on the investigated structure by robots (Bayati et al., 2018), ducted fans (Azcona et al., 2014) or cables (Sauder et al., 2016, Hall and Goupee, 2018). The majority of the SIL methods apply Blade-Element-Momentum theory (BEMT) to obtain the loads on the turbine (Gueydon et al., 2020). BEMT codes are preferred because of their computational speed and widespread use. Then, the scaling effects due to the Froude-Reynolds dissimilarity may be neglected but the investigation of aero- and hydrodynamic interaction effects are limited to the capabilities of the numerical tools and their coupling schemes, i.e. considering the gyroscopic momentum of the floating turbine and its aerodynamic torque is problematic (Müller et al., 2014). Moreover, the numerical tools used to represent the missing physical effects need to be verified and validated.

Geometrical scaling of the turbine in Froude scaled conditions results in smaller Reynolds numbers, and lower power and thrust (Martin et al., 2012, de Ridder

et al., 2014, Gueydon et al., 2020). An improved model testing technique uses increased wind velocities which results in larger drag coefficient while the lift does not change. As a consequence, the thrust shifts to smaller relative rotations (tip speed ratio) and the power remains small or might become negative. Therefore, a common method is the so-called performance matching which refers to down scaling the turbine and altering the geometry to achieve the same performance coefficients in Froude scaled conditions as at full scale. Thrust has a larger influence on the dynamic behaviour of the floating turbine than torque. As a result, the main objective for performance matching is the slope of the thrust force w.r.t. the tip speed ratio and the thrust coefficient. Hence, performance matching allows to study aero- and hydrodynamic interaction effects but geometrical similarity cannot be kept. This process might also result in different mass distributions, which influence the natural frequencies of the system. In addition, performance matching of the turbine is more expensive than other techniques and limits the investigation to the available redesigned rotors. Two examples of performance-matched wind turbines are the MARIN Stock Wind Turbine (MSWT) and the 1/60 scale DTU 10 MW reference wind turbine (DTU 10 MW RWT). The former model was designed to match the performance coefficients of the NREL 5 MW baseline turbine at full scale (Martin et al., 2012, de Ridder et al., 2014) and the latter the DTU 10 MW RWT at full scale (Bredmose et al., 2017). Details of NREL's 5 MW baseline turbine may be found in the publication by Jonkman et al. (2009) and of the DTU 10 MW RWT in the work by Bak et al. (2013). Further examples are given by Gueydon et al. (2020).

Summarising the different experimental techniques, model tests with HIL or SIL methods provide thrust forces and properties of the dynamic behaviour of the full system. Performance matched wind turbines aim at correct thrust and power prediction, and allow for more detailed studies of the flow around the rotor and of special aero- and hydrodynamic coupling effects (Müller et al., 2014). Further investigations, such as comparison between the different techniques and to measurements at full scale, are required to improve experimental procedures.

Floating wind turbines utilise mostly horizontal axis wind turbines. The floater concepts, however, are more diverse as depicted in Figure 1.1. To reflect this diversity, the DeepCwind consortium performed physical tests of three different floating foundations with NREL's 5 MW turbine at scale 1/50 (Goupee et al., 2012, Koo et al., 2012). The foundations were chosen to be a spar type, a semi-submersible, and a TLP floater. Furthermore, the floating wind turbine concepts Hywind, Windfloat, Gicon SOF, GustoMSC Tri-floater, Fukushima Project were tested experimentally by, amongst others, Cermelli et al. (2009), Myhr et al. (2011), Adam et al. (2014), Huijs et al. (2014) and Chujo et al. (2013).

Many more model tests on floating wind turbines may be found in the publications of e.g. Müller et al. (2014), Stewart and Muskulus (2016) and Gueydon et al. (2020). These publications depict that model testing of FOWTs is difficult and possesses many uncertainties involving the accurate aerodynamic modelling in Froude scaled conditions and the accurate mooring modelling. Therefore, more knowledge and experience is required to optimise and standardise experimental testing procedures. As Gueydon et al. (2020) demonstrated, comparison between different test

techniques to obtain knowledge and confidence is important to proceed and improve model testing of floating wind turbines. In addition, so far, model test data are rarely given with error and uncertainty estimates. In fact, none of the experiments on floating wind turbines cited here provides errors and uncertainties. An extensive attempt was undertaken by Robertson et al. (2020a) for a test campaign using the DeepCwind semi-submersible without a turbine connected. They performed uncertainty quantification studies using also a large amount of numerical simulations to assess the input uncertainties. The uncertainties obtained, however, do not include all uncertainty sources which are obligatory for formal validation of numerical tools.

1.1.2 Numerical simulations of floating wind turbines

Next to model testing of floating wind turbines, also numerical simulations provide further insights in the dynamic behaviour of the whole system. Nowadays, numerical simulation tools assist in the design and analysis of these floating offshore structures. Many possible scenarios may be simulated in advance to understand physical effects and to reduce safety factors and risks. Their increased use will ultimately help to drive down the costs in order to compete with other energy sources (Cordle and Jonkman, 2011). To simulate floating wind turbines, the tools need to account for aero- and hydrodynamics, body motions, structural elasticity, dynamic mooring loads, and control algorithms. Currently, most simulation tools make use of potential flow based methods for hydrodynamics, Blade-Element-Momentum theory (BEMT) for aerodynamics, and lumped-mass (LM) or finite element methods (FEM) for mooring dynamics and structural elasticity (Cordle and Jonkman, 2011, Davidson and Ringwood, 2017, Robertson et al., 2017b). Due to their long term usage in the industry, these tools have gained experience and trust in the past. As there is generally lower influence of viscosity at full scale hydrodynamics and in wave-related phenomena, and potential-flow based simulations are less costly and fast, these tools are often used in the design and even in the analysis of floating and bottom-fixed offshore wind turbines.

To gain more experience and to increase knowledge transfer on potential-flow based solvers, the International Energy Agency wind (IEA wind) initiated several cooperative offshore code comparison projects. The OC3 (Offshore Code Comparison Collaboration) and OC4 (Offshore Code Comparison Collaboration Continued) projects were aimed at code-to-code comparisons to investigate modelling differences. Participants of both projects used low-fidelity potential-flow based methods. The results of these projects, however, did not provide details on the most accurate approaches. To overcome this limitation, physical test data was provided to the participants of OC5 (Offshore Code Comparison Collaboration Continued, with Correlation) to validate² their lower-fidelity numerical simulation tools. In this study, the results were not compared to higher-fidelity viscous-flow solvers. The test data was provided for model and full scale as well as for fixed and floating wind applications. In the second phase, a semi-submersible floating wind turbine

²This is not equivalent to validation as defined in this thesis.

was simulated in calm water, in waves, and in combined wind and wave conditions. A major outcome of phase II of the OC5 project was that potential-flow based methods cannot accurately represent the oscillatory motions of the floater excited around the low-frequent natural frequencies of the moored floater. It was suspected that viscous loads not accounted for were the reason for this discrepancy. These results were published recently by Robertson et al. (2017b).

At Froude scaled conditions, i.e. at lower Reynolds numbers, floating wind turbine models experience larger viscous loads. These conditions cause earlier flow separation and radial flow on the turbine blades. The input data of BEMT codes, at full scale usually provided by potential-flow codes, need to be optimised to accurately predict the dynamics caused in Froude scaled flow conditions (Burmester et al., 2016). In fact, Make et al. (2015) demonstrated the significance of the input optimisation to account for radial interaction of the flow. For this purpose, several common optimisation methods exist to calculate the angle of attack from three-dimensional flow data (Guntur and Sørensen, 2014). These methods, however, were used for steady wind conditions, which are seldom encountered in real sea environments. Furthermore, large pitch motion of the floating foundations lead to unsteady cases in which the wind turbine interacts with its own wake. In the work of Tran et al. (2014), this condition was investigated by prescribing a sinusoidal pitch motion of the floater. The comparison between Reynolds-Averaged Navier-Stokes (RANS) and BEMT simulations demonstrated that the latter simulations are not capable of predicting the aerodynamics accurately. In fact, the results of the BEMT simulations depicted overestimated turbine power and thrust values. Nowadays, performing accurate simulations of floating wind turbines is also possible by the use of high-fidelity viscous-flow solvers. These solvers allow the analysis of the important viscous loads on the floater. Moreover, the complex aerodynamic effects of unsteady turbine pitching, and the interaction of aero- and hydrodynamics may be investigated. The implementation of rigid body motion solvers for six degrees-of-freedom (DOF) in combination with overset, deforming, and/or moving grid techniques has enabled the simulation of floating wind turbines with spinning turbine rotors on moving floaters. Liu et al. (2017), Liu and Xiao (2019) and Tran and Kim (2016) demonstrated that it is possible to use RANS codes for the simulation of floating wind turbines. In these studies, a RANS solver utilising the finite volume method (FVM) was successfully coupled to mooring and structural simulation tools to investigate the NREL 5 MW wind turbine mounted on top of the OC4 DeepCwind semi-submersible floater at full scale. Details on the OC4 DeepCwind system are given in Robertson et al. (2014). The results of these RANS-based simulations were compared to widely used engineering tools relying on potential flow and BEMT. The comparison revealed good agreement for various parameters investigated. Another, similar study was documented in Zhang and Kim (2018) using the OC5 characteristics for the semi-submersible floating wind turbine at full scale. They focused their research on the prediction of wind and wave excited motions with CFD (Computational Fluid Dynamics). In wave excited motions when inertia forces dominate, Froude scaling is appropriate for the output data. Therefore, their results showed good agreement for the motions in surge and heave.

In the work of Borisade et al. (2016) and Quallen et al. (2014), the hydrodynamics of floating wind turbines were investigated in detail. They studied various effects, such as different design considerations and moorings, on the dynamic behaviour of a barge and a spar type floater. In both cases, the flow solution around the floaters and turbine were scrutinised which presents another advantage of using CFD. Besides, as Make and Vaz (2015) and Borisade et al. (2016) presented, also scale effects on the turbine and floater due to Froude scaling may be analysed using these high-fidelity tools. Further investigations on aero- and hydrodynamics of floating wind turbines were conducted, see e.g. Benitz et al. (2015), Beyer et al. (2013, 2015), Bozonnet and Emery (2015), Benitz (2016) and Li et al. (2012). Nematbakhsh et al. (2015) investigated a floating wind turbine on a TLP foundation. They found good agreement of potential-flow and viscous-flow solvers for applications in which linear effects dominate. Large discrepancies were observed for decay simulations and for the surge motion. Nematbakhsh et al. (2015) also found accurate predictions of natural periods with coarse grids, and the requirement for finer spatial discretisation to predict hydrodynamic damping. This finding is also corroborated by the results of this thesis.

The use of CFD as an engineering tool, however, requires verification and validation studies involving error and uncertainty quantification. Error and uncertainty quantification is seldom observed in experiments as well as numerical simulations. For the case of a wave energy converter (WEC), another device from the offshore renewable energy industry, Wang et al. (2018) demonstrated that thorough error and uncertainty quantification is possible also for complex engineering applications. Another verification study on floating wind turbine applications was recently published by Wang et al. (2020b). Verification studies for CFD simulations of floating wind applications are a step towards the fulfilment of the long-term research challenges of EAWE and part of the work of this thesis.

1.1.3 Hydrodynamic damping of floating wind turbines

Floating offshore wind turbines (FOWTs) experience a very complex mix of wind, waves, and current loads. Many different concepts of floater and mooring configurations exist (examples are in Figure 1.1) to accommodate these loads. Each concept needs to guarantee safety and cost efficiency which may both be controlled by hydrodynamic damping. Hydrodynamic damping refers to the decrease of motion amplitude of an oscillating body over time by loads acting in anti-phase to its velocity (Sarpkaya, 2010). This can be revealed by a decay test. In general, damping refers to the dissipation of energy owing to oscillatory motions. Damping restricts, reduces or prevents the system from motions. Thereby, the kinetic energy of the moving system is transformed into radiated waves, heat and disturbance of the flow field. Hydrodynamic damping was investigated by various researchers, see e.g. Himeno (1981), Handschel et al. (2015), Piehl (2016), Wassermann (2017). Their research in hydrodynamic damping is focused on ships and on roll motions. Roll motions may be critical for cargo and passenger ships. The former might lead to the loss of goods and the latter to sea sickness. Nevertheless, there are also many studies on hydrodynamic damping of floating offshore structures (ITTC,

2014). For instance, a decay test of a semi-submersible was investigated using CFD by Rosetti et al. (2016). Pistidda et al. (2012) performed CFD simulations to assess hydrodynamic damping of a barge floater. They compared their results to experimental data and found underestimated quadratic damping and slightly overestimated linear damping.

Offshore platforms for the oil and gas industry are usually single-item designs, whereas FOWT and WEC concepts are meant for series production, and therefore, are more cost sensitive (Cruz and Atcheson, 2016). FOWTs and WECs are two types of floating systems designed to operate in very energetic environmental conditions. WECs are designed to be excited at or close to their natural frequencies. In contrast, FOWTs need to ensure strong dynamic stability in order to reduce loads on the turbine and tower. Strong dynamic stability also yields to better power predictions (Karimirad and Moan, 2010) and to increased safety of the floating system. Hence, it is important to analyse hydrodynamic damping of floating wind turbines. Furthermore, accurate assessment of hydrodynamic damping enables correct prediction of the motions of the floating system. Numerical simulations of floating wind turbines with high-fidelity viscous-flow solvers allow to investigate many different factors influencing the hydrodynamic damping. In the studies of Nematbakhsh et al. (2015), Rivera-Arreba et al. (2019), and Robertson et al. (2017b) hydrodynamic damping of floating wind turbines was investigated with RANS-based and potential-flow based methods, respectively. In Froude scaled conditions, viscous damping, i.e. the contributions of skin friction, pressure drag, and eddy making, adds a major component to the total hydrodynamic damping. This damping component may be investigated and analysed by viscous-flow solvers and underlies scaling effects. Nematbakhsh et al. (2015) and Rivera-Arreba et al. (2019) performed decay simulations of floating wind turbines and demonstrated a large impact of the numerical discretisation on the damping but did not quantify the effect. Thus, hydrodynamic damping predictions with CFD suffer from large dependencies on the spatial and temporal discretisation. CFD simulations using coarse grids and time steps include large numerical diffusion. This diffusion acts as additional numerical damping and might lead to a good agreement with the measured data which is misleading as large numerical errors remain. Therefore, verification and validation studies are important to reduce these errors. In this thesis, the numerical damping was quantified in terms of linear and quadratic damping coefficients, and discretisation errors were estimated. Additionally, the influence of several numerical and physical factors on the hydrodynamic damping were studied. These studies will assist in the accurate and reliable prediction of viscous damping of floating platforms for wind turbines. Thus, they are inline with the aforementioned long-term research challenges defined by EAWE (van Kuik and Peinke, 2016) and new to the existing research on wind turbine floaters.

1.1.4 Novelties of this work

In this thesis, the hydrodynamic side of a semi-submersible floating wind turbine was investigated using a RANS based CFD solver. Therefore, CFD simulations were performed for the wave propagation of a regular wave, wave loads on a cylin-

der, and surge decay simulations of a semi-submersible floater. Additionally, surge decay simulations were computed using a dynamic mooring model. For validation purposes, extensive verification studies for CFD simulations of the described floating wind applications were performed within this work. These systematic investigations included the comparison of three different discretisation error and uncertainty estimation methods. Furthermore, the work was focused on the investigation of hydrodynamic damping of a semi-submersible floating wind turbine platform. Different influencing factors, numerical and physical, were analysed in detail and their contribution to the damping highlighted. These detailed studies are new to the existing research on floating wind turbines.

1.2 Motivation and Objectives

Further research is required to support the emerging FOWT industry to gather knowledge and experience. Consequently, risks and safety factors may be reduced and designs of the floating structures optimised. This will ultimately help to drive down the costs in order to compete with the established bottom-fixed offshore wind turbines. Experimental model tests in research facilities and numerical simulations with viscous flow solvers are known to be two appropriate methods to achieve this goal. Numerical simulations benefit from the possibility to compute solutions at different scales and to be able to analyse the flow field in detail. However, verification and validation studies are required in order to use CFD in a reliable manner for engineering applications. These studies need to be performed on all relevant flow parameters. Thus, for FOWTs this includes, amongst others, lift and drag on the wind turbine blades, deformation of and loads on the structure, motions of the floater involving the assessment of hydrodynamic damping, wave propagation, current interaction, and mooring line forces (see Figure 1.2). The sensitivity to different numerical schemes, turbulence models, and the coupling with different models/tools, such as mooring models, or structural deformation and rigid body motion solvers, also need to be studied in order to achieve confidence and credibility.

Safety and efficiency of floating wind turbines are key requirements to be maintained when driving down the costs. These may be governed by dynamic stability. A major contributor to dynamic stability is the damping of the floating system, i.e. aero- and hydrodynamic damping. Therefore, the work of this thesis is aimed at reliable numerical predictions of hydrodynamic damping and loads on a moored floating offshore wind turbine. Hydrodynamic damping generally consists of wave radiation, skin friction, eddy making and lift, and (for a moored floater) drag of the mooring lines (Himeno, 1981, Wassermann, 2017). These components may be categorised in potential and viscous damping. The latter necessitates the application of viscous-flow solvers. Additionally, these damping components are a simplification for the different effects originating from the pressure and velocity field. Pressure and velocity may be calculated by CFD tools and are dependent on temporal and spatial discretisation, turbulence modelling, mooring modelling, free surface representation, coupling between different motion degrees-of-freedom,

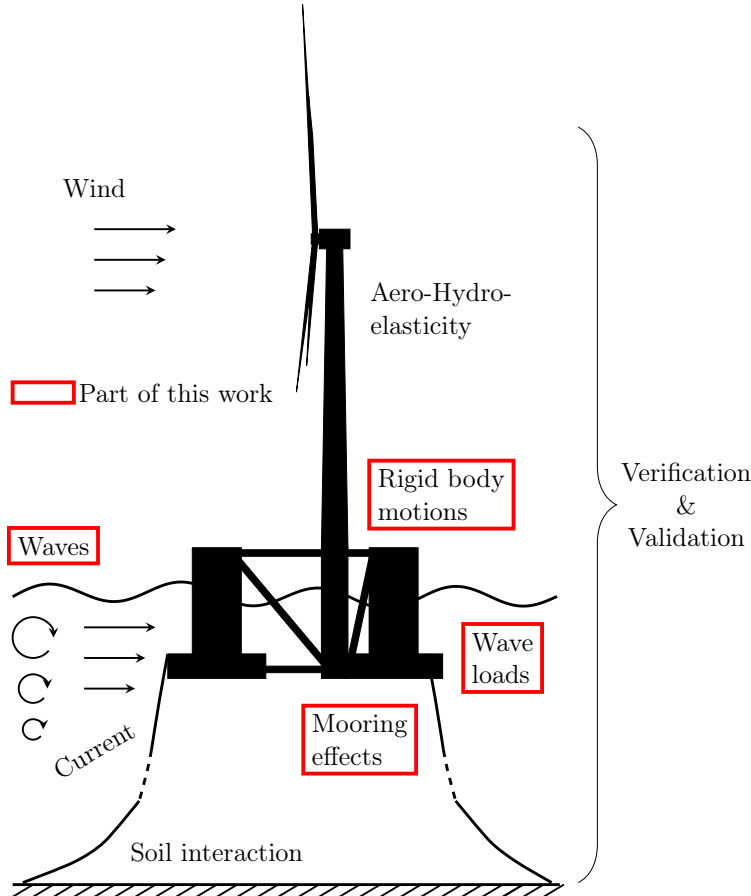


Figure 1.2: Aspects of floating wind turbine simulations with CFD. The red boxes mark aspects investigated in this thesis.

and different numerical schemes. The impact of these effects on hydrodynamic damping and the flow field were analysed in this thesis.

Furthermore, extensive verification studies were conducted on different aspects of FOWT simulations. These aspects are wave propagation, wave loads, rigid body motions, and mooring line dynamics (see Figure 1.2). For each test case, discretisation errors and uncertainties were obtained by three different established techniques, which rely on the Richardson extrapolation and were published by Eça and Hoekstra (2014), Oberhagemann and el Moctar (2019) and Xing and Stern (2010). For the approach by Oberhagemann and el Moctar (2019), a new discretisation uncertainty estimate was developed and tested against these four aspects. The differences between these methods are due to assumptions on the extrapolation, and differences in the error and uncertainty calculation procedure. The results of each approach were compared to each other, and their use and applicability were scrutinised. Thus, this work provides a way to gain confidence and credibility in CFD simulations of FOWTs.

As semi-submersibles are used in most ongoing floating wind turbine projects (Lemmer, 2018, Ramírez et al., 2020), this research work is also focused on a semi-

submersible floating foundation. Experimental data of the OC5 DeepCwind floating system were available for decay motions of all six degrees-of-freedom (Goupee et al., 2014, Robertson et al., 2017b). The two most problematic degrees-of-freedom for a semi-submersible floating wind turbine are the surge and pitch motions as the turbine might interact with its own wake. Since pitch undergoes large restoring forces owing to hydrostatic loads and surge restoring forces originate solely due to the mooring system, accurate representation of the surge motion is a major challenge for numerical simulations of FOWTs. Therefore, the work of this thesis was focused on the surge decay motion of the OC5 DeepCwind semi-submersible. The work also provides a path for further research as shown by Wang et al. (2019, 2020b) and Wang et al. (2020a).

1.3 Structure of the Thesis

At first, theoretical background on hydrodynamic damping, governing equations, turbulence modelling, waves, rigid body motions, and catenary mooring equations is provided in Chapter 2. Chapter 3 describes the numerical methods including discretisation and integration schemes, boundary conditions, pressure and velocity coupling, free surface treatment, coupling with structural equations of motion and mooring models. The chapter ends with a detailed description on verification and validation procedures. Subsequently, Chapter 4 contains the verification and validation studies on and results of wave propagation and wave loads on a vertical surface piercing cylinder. Three error and uncertainty quantification methods were applied to these FOWT simulation aspects. Chapter 5 starts with a description of the OC5 semi-submersible and the mooring set-up. Then, studies to estimate the discretisation errors are followed by investigations of the hydrodynamic damping, with increasing complexity. The chapter concludes with a full domain simulation coupled with a dynamic mooring model is validated against experimental data. In Chapter 6, the thesis is summarised, major conclusions are drawn, and an outlook regarding further work in this field is provided.

The appendices are dedicated to further details on mooring calculations (Appendix A), investigations with the OC5 semi-submersible (Appendix B), and a study on different interface capturing schemes for the wave load test case (Appendix C).

2. Theoretical Background

This chapter is dedicated to theoretical background on hydrodynamic damping and the sets of fundamental formulations required to investigate influencing parameters on the damping. At first, the concept of hydrodynamic damping is explained. Furthermore, different testing techniques are detailed to obtain hydrodynamic damping from motion decay tests. Then, a set of fundamental formulations is given. These are governing equations of viscous flows, RANS turbulence models, rigid body motion equations, and the catenary mooring equations.

2.1 Hydrodynamic Damping

Hydrodynamic damping arises due to loads from the surrounding fluid on the moving body. Thus, the total hydrodynamic damping force may be decomposed as integrated pressure and shear stress on the wetted surface of the floater. The pressure and shear stresses are influenced by wave radiation, eddy making and lift, skin friction and pressure drag. Thereby, shear stress is caused by skin friction and is a consequence of the velocity gradient in the proximity of the surface and the viscosity of the fluid. The pressure loads arise because of radiated waves, eddies, and pressure drag. The pressure drag is a consequence of pressure differences between upstream and downstream side of the moving floater. Moreover, energy losses in the boundary layer, vortices, and flow separation contribute to the pressure loads and affect the pressure drag. These effects prevent the pressure to rise up to the stagnation pressure as predicted by ideal flow theories (Bertram, 2012). The pressure drag is influenced by the shape of the oscillating floater, i.e. the pressure dependent damping contribution reduces for more streamlined forms.

2.1.1 Damping components

The wave radiation, eddy making and lift, skin friction and pressure drag damping components are used from engineering perspective in the literature (Himeno, 1981, Handschel et al., 2015, Piehl, 2016, Wassermann, 2017). A contribution from mooring lines needs to be added for oscillatory motions of moored floating platforms (Webster, 1995). A similar component wise division of the hydrodynamic damping may also be found in ITTC (2011). These components are illustrated in Figure 2.1 and detailed in the following.

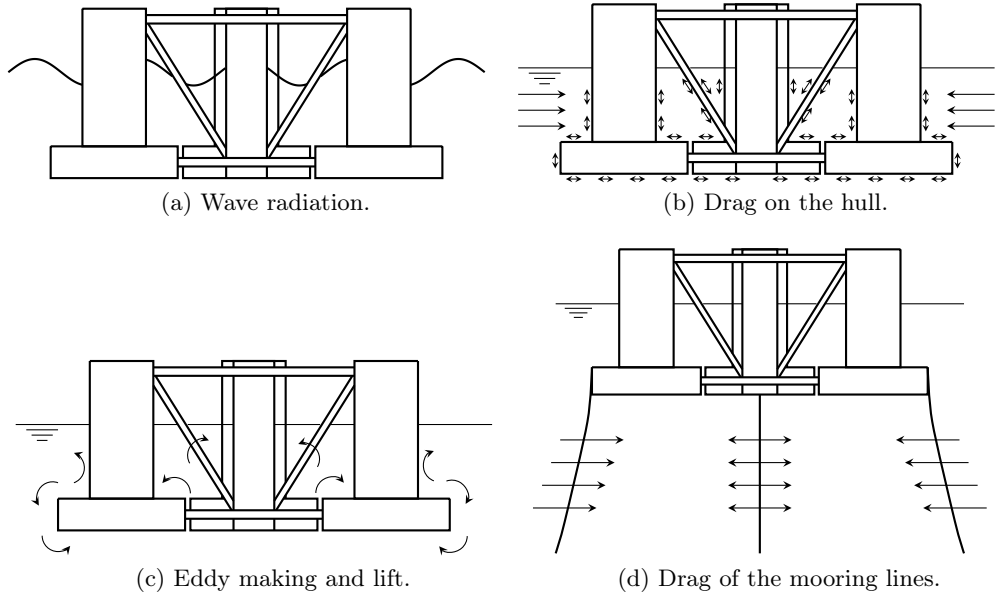


Figure 2.1: Damping components of a semi-submersible floater: wave radiation, drag on the hull, eddy making and lift, drag of the mooring lines.

Wave radiation occurs because of the motions of the oscillating system and the dynamic pressure field. A floater in motion radiates waves. This causes a loss of kinetic energy of the floater. This component also includes the interaction between waves and eddies and between waves and lift. However, this interaction is very small and consequentially the wave radiation component may be regarded as linear (Himeno, 1981). Wave radiation is characterised by the Froude number F_r :

$$F_r = \frac{u_0}{\sqrt{gL_0}} . \quad (2.1)$$

u_0 denotes the characteristic relative velocity between flow and floater, L_0 the characteristic length of the floater and g the gravitational acceleration. The Froude number is a non-dimensional measure of the relation between inertia and gravitational forces. Radiation of waves is directly related to the velocities of the oscillating floater. The wave radiation component vanishes for very small Froude numbers, i.e. very small velocities of the floater. Its value increases with Froude number up to a certain point forming a hump and decreasing above this number. The shape of this line depends on the geometry investigated. This damping component may be represented also with potential-flow methods. Nevertheless, higher-order wave radiation and interaction with eddies might occur that limit the accuracy by lower-fidelity methods.

Eddy making and lift damping occurs because of flow separation at the columns, braces, pontoons, and heave damping plates of the semi-submersible floater. Hence, potential flow based methods are not suited for the estimation of hydrodynamic damping if eddy creation is expected by the motion of the floater.

The heave damping plates at the lower end of the corner columns and the cross braces of the OC5 semi-submersible are designed to add damping and to disturb the flow by the creation of vortices. Lift damping and eddy creation are two connected effects distinguished in linear and non-linear damping, respectively. These damping components occur because of shed vortices and local pressure changes at the surface of the floater originating from vortices (Himeno, 1981, Wassermann, 2017). Eddy and lift damping is associated with the Euler number E_u and the Strouhal number S_t :

$$E_u = \frac{\Delta p}{\rho u_0^2} \quad \text{and} \quad (2.2)$$

$$S_t = \frac{f_{vs} L_0}{u_0}. \quad (2.3)$$

Δp is the pressure difference: $\Delta p = p_{st} - p_{st0}$, where p_{st} is the local static pressure and p_{st0} the free stream/initial static pressure. f_{vs} denotes the vortex shedding frequency. The Euler number provides a relation between pressure and inertia forces, its value being half of the pressure coefficient. The Strouhal number is a measure of oscillating flow mechanisms and represents the non-dimensional vortex shedding frequency.

Drag on the hull is composed of skin friction (shear) and pressure drag damping. Skin friction appears between the surface of the floater and the surrounding fluid if relative velocities are present. For small velocities, the shear stress occurs due to laminar flow while at higher velocities owing to turbulent flow. Thus, the skin friction depends on the viscosity of the fluid and the type of flow. This damping component depends on surface area, relative velocity between floater and fluid, surface roughness of the floater, and viscosity of the fluid. For slender bodies, the skin friction dominates the drag damping component. For bluff bodies such as cylinders, however, the pressure drag dominates. The pressure drag depends on the shape of the geometry, the relative velocity between body and fluid, and the density of the fluid. The drag damping is associated with the Reynolds number R_e , Keulegan-Carpenter number K_C , and Sarpkaya's frequency parameter β :

$$R_e = \frac{\rho u_0 L_0}{\mu} = \frac{u_0 L_0}{\nu}, \quad (2.4)$$

$$K_C = \frac{u_0 T_p}{L_0} \quad \text{and} \quad (2.5)$$

$$\beta = \frac{R_e}{K_C} = \frac{L_0^2}{\nu T_p}. \quad (2.6)$$

ρ denotes the fluid density, μ the dynamic viscosity, ν the kinematic viscosity, and T_p the oscillation period. The Reynolds number describes the ratio between inertia and viscous forces. The Reynolds number is used to predict the transition between laminar and turbulent flow. At model scale (using Froude scaling), the Reynolds number is smaller and the boundary layer, relative to the geometry, thicker compared to at full scale. These two conditions increase the skin friction

damping at model scale. At full scale, when Reynolds numbers are large and the boundary layer thinner relative to the geometry, the skin friction damping plays a minor role. Therefore, the relative hydrodynamic damping estimated at model scale is larger than the damping estimated at full scale for the same structure. The Keulegan-Carpenter number is a measure for the ratio between drag and inertia forces. For K_C values above unity as for the first oscillations of the OC5 semi-submersible in surge decay ($K_C \approx 4.2$), the pressure drag component dominates (Bearman and Russel, 1997). Sarpkaya's frequency parameter β was introduced in Sarpkaya (1976) and relates the Reynolds and Keulegan-Carpenter numbers.

Drag of the mooring lines is a viscous damping component similar to friction damping and eddy creation around the structure. Additional friction (pressure and shear) and eddies appear due to catenary moorings being towed along with the motions of the floater. As the motions of mooring lines are relatively large compared to their diameter, the pressure drag damping component dominates the mooring line damping (Bearman and Russel, 1997). This additional damping is represented as drag coefficient in the mooring model. This damping component is purely quadratic with respect to the relative velocity between fluid and object as Morison's drag force depends also on the square of the velocity. The drag varies with the Reynolds and Keulegan-Carpenter numbers.

The hydrodynamic damping may be assessed using special designed tests and a suitable estimation technique. In the following sections, several tests are highlighted, parameters are defined, and estimation methods are detailed to analyse influencing factors on the damping. Moreover, the estimation method applied in this thesis is further highlighted.

2.1.2 Damping estimation tests

According to Wassermann (2017), there are four different testing techniques to estimate the hydrodynamic damping of a floating vessel (ship or offshore structure). These testing techniques are:

- Decay motion test
- Harmonic excited motion
- Harmonic forced motion
- Non-harmonic excited motion

These motion tests are detailed in the following.

Decay motion test also called extinction test or simply decay test is a simple technique and less expensive than the other methods. The floater is initially displaced by a certain distance or angle and released to oscillate with decaying motion amplitudes. In model test basins, no excitation facility is needed to perform these tests. Damping coefficients for various amplitudes are measured with a single initial

displacement (excitation) of the floater. This technique saves measurement and/or simulation time. As the floating vessel oscillates freely after release, coupling between different degrees-of-freedom can be investigated. However, large oscillation amplitudes cannot be studied with this technique. During the first oscillation the fluid flow is not fully developed as the test starts from (or close to) calm water conditions. This technique is widely applied also for the estimation of the correct mass distribution. A few examples of decay tests are given in Schmitke (1978), Irvine et al. (2005), Aloisio and Di Felice (2006) and Piehl (2016) for experiments and in Nematbakhsh et al. (2015), Robertson et al. (2017b), Rivera-Arreba et al. (2019), Robertson et al. (2020b) and Tran and Kim (2015) for numerical simulations of floating wind turbines.

Harmonic excited motion is obtained by e.g. shifting weights between different defined locations within the floater or by rotating flywheels. Because of the change of mass distribution the floater starts to oscillate. This technique allows to obtain damping also for larger oscillations. Coupling between different degrees-of-freedom can also be investigated. Predefined oscillating forces and moments may also be taken to study motions in the vertical plane.

Harmonic forced motion means to prescribe the oscillating motion of the floater in calm water. The floater follows a fixed trajectory. Harmonic forced motion does not allow to investigate coupling between different degrees-of-freedom. This technique also requires special equipment to apply accurate forces on the floater. Nevertheless, the harmonic motion tests can establish steady periodic signals which enables to investigate and estimate statistical errors. Here, the motion time history and the reaction loads (forces and moments) of the fluid are measured to estimate the damping (Piehl, 2016).

Non-harmonic excited motion can be obtained by e.g. waves that excite the floater. Then, random logarithmic decrements may be selected to calculate the damping, see Kölling et al. (2014). The damping for several different amplitudes and frequencies may be estimated. Yet, this method is very uncommon for the investigation of hydrodynamic damping of a floating vessel as it requires complicated post-processing methods and is difficult to be reproduced.

The most used method for experiments and the most employed method for the numerical simulation of floating wind turbines is the decay motion test. Furthermore, the OC5 DeepCwind semi-submersible was tested with moored decay motion tests. Therefore, the time trace of the decaying oscillations are of interest. One objective of the current work was to reproduce the decay motions of the experiments with numerical simulations. Hence, the investigation focused on the quantification of the physical and numerical influences on the hydrodynamic damping. For this reason, it is crucial to look at the motion time history and at quantifiable damping values. Several estimation methods exist to obtain values for the hydrodynamic damping. Some methods are explained in the following section.

2.1.3 Damping function

The damping test type predefines the corresponding estimation method. Excited or forced motion tests include additional periodic/non-periodic forces on the right-hand side of the equation of motion. Thus, the motion time traces may not be utilised alone for the damping estimation. For decay motion tests, the oscillation system reduces to inertia, damping, and restoring terms which enables the usage of motion time traces. The equation of motion for a one DOF system may be written as (Himeno, 1981):

$$M\ddot{x} + B(\dot{x}) + C(x) = 0 . \quad (2.7)$$

M represents the mass of the system including structural and added mass, $B(\dot{x})$ the damping function and $C(x)$ the restoring function. x is the motion variable, \dot{x} the first and \ddot{x} the second time derivative representing the velocity and acceleration of the system, respectively. For more than one DOF, x becomes the state vector \vec{x} of the system. Equation (2.7) holds for decay motions without external exciting forces or moments. Here, $C(x)$ is the total restoring force/moment originating from the hydrostatics and mooring system. For small motion amplitudes and simple mooring configurations (e.g. spring type taut moorings), the restoring may be assumed linear and represented by C . For a floating wind turbine, the damping function $B(\dot{x})$ includes contributions originating from the hydrodynamics of the floater, the aerodynamics of the turbine and tower, and structural components such as the mooring lines or other mechanical connections. For the numerical simulations of this thesis, the damping contribution due to the aerodynamics was neglected as the turbine did not rotate during the surge decay experiments. Then, the damping function may be obtained as a series expansion of \dot{x} and $|\dot{x}|$:

$$B(\dot{x}) = B_1\dot{x} + B_2\dot{x}|\dot{x}| + \dots . \quad (2.8)$$

Here, B_1 and B_2 are the linear and quadratic damping coefficients. This series expansion is a simplification as the series is truncated after the second term. For the floating wind turbine system investigated, the first and second order damping coefficients may be assumed sufficiently accurate to represent the motions of the platform as shown by Gueydon (2016), Robertson et al. (2017b). Several ways to represent the total damping of the system exist: equivalent linear damping and linear and quadratic damping. At first, the concept using a linear damping coefficient is shown to represent the total damping (equivalent linear damping) of the system.

Linear damping assumes a linear damping coefficient representing the total damping of the system. This damping coefficient has a linear relation with the velocity. If Equation (2.7) is divided by the mass M , then it may be simplified to:

$$\ddot{x} + \frac{B}{M}\dot{x} + \frac{C}{M}x = 0 . \quad (2.9)$$

Introducing the natural frequency ω_n and the damping ratio ζ_D as:

$$\omega_n = \sqrt{\frac{C}{M}} \quad \text{and} \quad \zeta_D = \frac{B}{2\sqrt{MC}} \quad (2.10)$$

yields:

$$\ddot{x} + 2\zeta_D \omega_n \dot{x} + \omega_n^2 x = 0 . \quad (2.11)$$

The damping ratio and the natural frequency (eigenfrequency) are important quantities for the dynamics of a general oscillating system. The floating system is usually designed not to operate in sea conditions with excitation loads close to the natural frequency (wave energy converters are typical exceptions). ζ_D denotes the ratio between actual B and critical damping $B_{crit} = 2\sqrt{MC}$. This ratio is taken to categorise oscillations in terms of damping as follows:

- $\zeta_D < 0$ the oscillation is unstable
- $0 < \zeta_D < 1$ the oscillation is weakly damped
- $\zeta_D = 1$ this condition depicts critical damping (limit case)
- $\zeta_D > 1$ there is no oscillation. Asymptotic approach to centre of oscillation for $t \rightarrow \infty$.

Figure 2.2 shows examples for different oscillating systems.

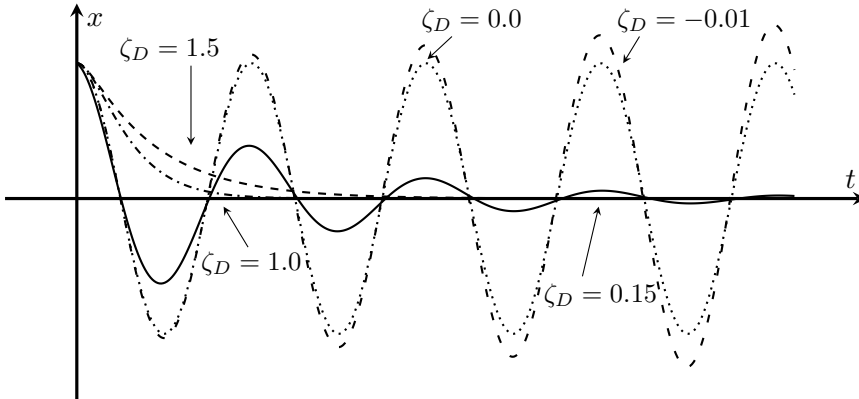


Figure 2.2: Different oscillators with respective damping ratios (attenuation factors) ζ_D . The solid line represents a typical decay motion with $\zeta_D = 0.15$, the dotted line an undamped system $\zeta_D = 0.0$, the dash-dotted line critical damping $\zeta_D = 1.0$, the densely dashed line strong damping $\zeta_D = 1.5$, and the loosely dashed line an unstable oscillator $\zeta_D = -0.01$.

The decay tests of a moored semi-submersible floater fall in the category of a weakly damped oscillator ($0 < \zeta_D < 1$). Therefore, just this case is regarded hereinafter.

Equation (2.11) is linear and can be solved with an analytical initial function of the form (Gross et al., 2006):

$$x(t) = Ge^{-\zeta_D \omega_n t} \cos(\omega_d t - \theta_{ps}) . \quad (2.12)$$

G is a parameter defined by the initial conditions, e.g. $x(t = 0)$ and/or $\dot{x}(t = 0)$. θ_{ps} represents a phase shift needed in case the decay does not start at a positive

maximum. The damped or observed oscillation frequency ω_d for a linear and weakly damped system is defined as:

$$\omega_d = \omega_n \sqrt{1 - \zeta_D^2} . \quad (2.13)$$

Thus, the observed oscillation frequency is not the natural frequency. In many cases, however, the damping ratio ζ_D is very small and the natural frequency may be approximated from the observed frequency. Nevertheless, the accuracy of the damping estimation method determines also the accuracy of the natural frequency estimated. The linear damping ratio of the OC5 semi-submersible system is in the order of 0.1–3% and the quadratic of 3.9–42.4% (Robertson et al., 2017a). Hence, the linear damping assumption is not valid for the investigated floating system.

Linear and quadratic damping adds a second damping coefficient B_2 to the equation of motion. This allows to include effects related with the square of the velocity. These effects arise mostly owing to viscosity in the flow (Himeno, 1981) which is often called “viscous damping” in the literature. It refers to the hydrodynamic loads and defined damping components arising from eddy making, skin friction, pressure drag, and drag of the mooring lines, see Section 2.1.1. The equation of motion for systems with linear and quadratic damping components in decay tests may be written as:

$$M\ddot{x} + B_1\dot{x} + B_2\dot{x}|\dot{x}| + Cx = 0 . \quad (2.14)$$

This equation disregards motion coupling. The term $\dot{x}|\dot{x}|$ ensures orientation of the damping inline with the motion of the floater. No analytical solution exists for quadratic and higher-order damping functions. Therefore, numerical methods are required to approximate the solution and to obtain reliable damping values. Several available methods utilise least-squares fitting of an n^{th} order function and/or the PQ method by van der Vegt (1984).

Linear, quadratic and cubic damping and higher-order damping ensure a more accurate representation of the hydrodynamic damping. It adds additional terms to the equation of motion. For linear, quadratic and cubic damping coefficients, the equation reads:

$$M\ddot{x} + B_1\dot{x} + B_2\dot{x}|\dot{x}| + B_3\dot{x}^3 + Cx = 0 . \quad (2.15)$$

The third-order damping coefficient depends on the cubic of the velocity \dot{x}^3 . The combination of linear and cubic damping is often used for the estimation of ship roll damping. An estimation method for linear, quadratic and cubic damping coefficients is given in the following.

2.1.4 Damping estimation methods

In this subsection, estimation methods are given for linear, quadratic, and cubic damping. Linear damping may be obtained by fitting an analytical first-order

damping function to the time history or estimating the logarithmic decrement. For linear and quadratic damping the PQ method may be applied and for linear, quadratic, and cubic damping the PQR method is valid.

Linear damping In case the decay motion signal is assumed to be linear, Equation (2.12) may be fitted to the data. For the fit, standard procedures such as least-squares may be used. Another method originates from the logarithmic decrement. This method is applicable only for weakly damped systems. From Equation (2.12), for two succeeding amplitudes one has:

$$\frac{X(t_i)}{X(t_i + T_d)} = e^{\zeta_D \omega_n T_d} \quad (2.16)$$

Here, $X(t_i)$ is the oscillation peak at the time t_i of cycle i and T_d is the damped oscillation period, i.e. $T_d = \frac{2\pi}{\omega_d}$. Assuming $T_d \approx T_n$ for small $\zeta_D \ll 1$ and

$$\Lambda_i = \log \left(\frac{X(t_i)}{X(t_{i+1})} \right), \quad (2.17)$$

the damping ratio may be estimated with:

$$\zeta_D = \frac{1}{2\pi} \Lambda. \quad (2.18)$$

This method needs to be applied to both the positive and negative oscillation peaks.

PQ method The PQ analysis was provided by van der Vegt (1984). This method relies on the energy loss in an oscillation cycle and equates it with the work done by the damping force on the floater.

The damping in decaying oscillations is assumed to be equal to the loss of kinetic and potential energy of the system. The loss of energy ΔE in a decay oscillation cycle i may be written as (Jaouën et al., 2019):

$$\begin{aligned} \Delta E_i &= \Delta E_{kin,i} + \Delta E_{pot,i} \\ &= \frac{1}{2} M \dot{x}_i^2 - \frac{1}{2} M \dot{x}_{i+1}^2 + \frac{1}{2} C x_i^2 - \frac{1}{2} C x_{i+1}^2. \end{aligned} \quad (2.19)$$

$\Delta E_{kin,i} = E_{kin,i} - E_{kin,i+1}$ denotes the loss of kinetic energy and $\Delta E_{pot,i} = E_{pot,i} - E_{pot,i+1}$ the loss of potential energy within one oscillation cycle. The decay amplitudes are given with x_i and x_{i+1} and their derivatives with respect to time \dot{x}_i and \dot{x}_{i+1} denote the respective velocity. Since the velocity is zero at the amplitudes i and $i + 1$, the loss of energy simplifies to:

$$\begin{aligned} \Delta E_i &= \frac{1}{2} C (x_i^2 - x_{i+1}^2) \\ &= \frac{1}{2} C (x_i + x_{i+1})(x_i - x_{i+1}) \\ &= C \bar{x}_i \Delta x_i. \end{aligned} \quad (2.20)$$

$\bar{x}_i = \frac{1}{2}(x_i + x_{i+1})$ is the average of two succeeding amplitudes and $\Delta x_i = x_i - x_{i+1}$ their difference. Using Equation 2.10 for a weakly damped oscillatory system, this equation reads:

$$\Delta E_i = M\omega_n^2 \bar{x}_i \Delta x_i . \quad (2.21)$$

The damping force F_B for decay motion with linear and quadratic damping may be written as:

$$F_B = B_1 \dot{x} + B_2 \dot{x} |\dot{x}| . \quad (2.22)$$

The work done by this damping force W_B during one oscillation cycle is given by (Jaouën et al., 2019):

$$\begin{aligned} W_{B,i} &= \int_{t_i}^{t_{i+1}} (B_1 \dot{x} + B_2 \dot{x} |\dot{x}|) \dot{x} dt \\ &= B_1 \int_{t_i}^{t_{i+1}} \dot{x}^2 dt + B_2 \int_{t_i}^{t_{i+1}} |\dot{x}| \dot{x}^2 dt . \end{aligned} \quad (2.23)$$

x is a function of time, i.e. $x(t)$. For the time interval $[t_i, t_{i+1}]$, $x(t)$ may be approximated by $x(t) = \bar{x}_i \cos(\omega_n t)$. Then, the velocity $\dot{x}(t)$ becomes $\dot{x}(t) = -\omega_n \bar{x}_i \sin(\omega_n t)$. Introducing these two expressions in the damping work equation above yields:

$$\begin{aligned} W_{B,i} &= \omega_n^2 \bar{x}_i^2 B_1 \int_{t_i}^{t_{i+1}} \sin^2(\omega_n t) dt \\ &\quad + \omega_n^3 \bar{x}_i^3 B_2 \int_{t_i}^{t_{i+1}} |\sin(\omega_n t)| \sin^2(\omega_n t) dt \\ &= \omega_n \pi \bar{x}_i^2 B_1 + \frac{8}{3} \omega_n^2 \bar{x}_i^3 B_2 . \end{aligned} \quad (2.24)$$

The time interval $[t_i, t_{i+1}]$ is equal to the oscillation period T_p and is approximately equal to the natural period T_n for weakly damped systems. As the energy loss in one oscillation cycle arises from the work done by the damping force, the equations (2.20) and (2.24) may be equated:

$$\begin{aligned} \Delta E_i &= W_{B,i} \\ C \bar{x}_i \Delta X_i &= \omega_n \pi \bar{x}_i^2 B_1 + \frac{8}{3} \omega_n^2 \bar{x}_i^3 B_2 . \end{aligned} \quad (2.25)$$

Dividing this equation by C and \bar{x}_i^2 delivers an expression used for the PQ analysis:

$$\begin{aligned} \frac{\Delta x_i}{\bar{x}_i} &= \frac{\pi \omega_n}{C} B_1 + \frac{8}{3} \frac{\omega_n^2 \bar{x}_i}{C} B_2 \\ \frac{\Delta x_i}{\bar{x}_i} &= p + q \bar{x}_i . \end{aligned} \quad (2.26)$$

The p and q damping estimation coefficients are given by:

$$p = \frac{\pi \omega_n}{C} B_1 = \frac{2\pi^2}{T_n C} B_1 \quad \text{and} \quad q = \frac{8}{3} \frac{\omega_n^2}{C} B_2 = \frac{32}{3} \frac{\pi^2}{T_n^2 C} B_2 . \quad (2.27)$$

Thus, the linear B_1 and quadratic damping coefficients B_2 may be obtained as follows:

$$B_1 = p \frac{T_n C}{2 \pi^2}, \quad B_2 = 3q \frac{T_n^2 C}{32 \pi^2}. \quad (2.28)$$

This method relies on successive amplitudes to determine the relative decrement and the mean of two succeeding amplitudes of the decay test. This new data is taken to make a new diagram. Subsequently, a line is fitted through these data points using least-squares to obtain the intercept (p -value) and the slope (q -value) as one can see from Equation (2.26). In Figure 2.3 the decrement of motion amplitude as a function of the mean motion amplitude is plotted for an example decay simulation.

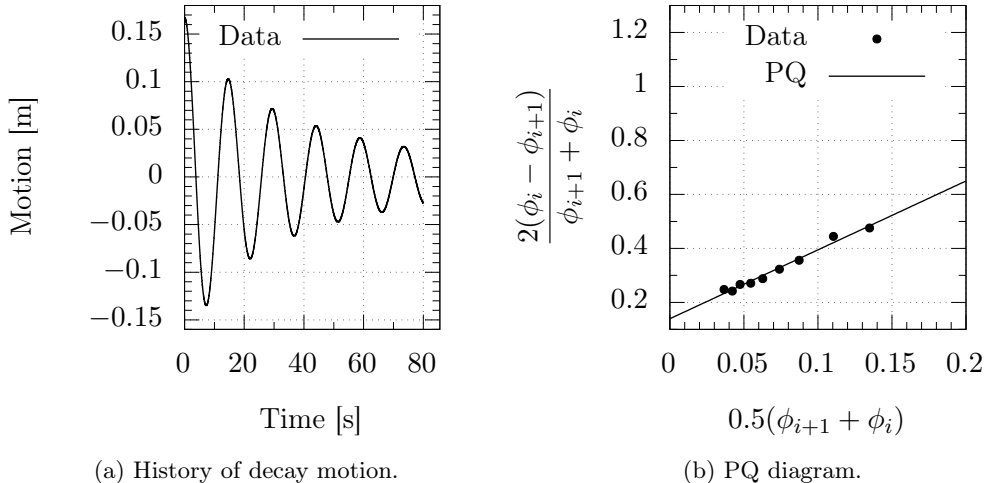


Figure 2.3: Illustration of the PQ analysis method to obtain damping estimation coefficients. x_i denotes the current motion amplitude

The diagram on the right-hand side of Figure 2.3 is used to obtain the linear and quadratic damping coefficients B_1 and B_2 using Equation (2.28). The PQ method is more accurate for small coupling with other degrees-of-freedom (DOF). More details on this procedure may be found also in Journée and Massie (2001), Weller (2012), Burmester et al. (2020c), Jaouën et al. (2019), and Wang et al. (2019).

PQR method In case a damping model with linear and quadratic coefficients does not provide satisfactory results, a cubic coefficient of the form $B_3 \dot{x}^3$ may be added to the damping force. The work done by this damping force becomes

(Jaouën et al., 2019):

$$\begin{aligned} W_{B,i} &= \int_{t_i}^{t_{i+1}} (B_1 \dot{x} + B_2 \dot{x} |\dot{x}| + B_3 \dot{x}^3) \dot{x} \, dt \\ &= \omega_n \pi \bar{x}_i^2 B_1 + \frac{8}{3} \omega_n^2 \bar{x}_i^3 B_2 + B_3 \omega_n^4 \bar{x}_i^4 \int_{t_i}^{t_{i+1}} \sin^4(\omega_n t) \, dt \\ &= \omega_n \pi \bar{x}_i^2 B_1 + \frac{8}{3} \omega_n^2 \bar{x}_i^3 B_2 + \frac{3}{4} \pi \omega_n^3 \bar{x}_i^4 B_3 . \end{aligned} \quad (2.29)$$

Analogue the lines of the derivation for the linear and quadratic damping, the damping work is equated with the loss of energy:

$$C \bar{x}_i \Delta X_i = \omega_n \pi \bar{x}_i^2 B_1 + \frac{8}{3} \omega_n^2 \bar{x}_i^3 B_2 + \frac{3}{4} \pi \omega_n^3 \bar{x}_i^4 B_3 . \quad (2.30)$$

This equation is again divided by C and \bar{x}_i^2 which yields:

$$\begin{aligned} \frac{\Delta x_i}{\bar{x}_i} &= \frac{\pi \omega_n}{C} B_1 + \frac{8}{3} \frac{\omega_n^2 \bar{x}_i}{C} B_2 + \frac{3}{4} \frac{\pi \omega_n^3}{C} \bar{x}_i^2 B_3 \\ \frac{\Delta x_i}{\bar{x}_i} &= p + q \bar{x}_i + r \bar{x}_i^2 . \end{aligned} \quad (2.31)$$

This procedure adds a third damping estimation coefficient r to the equation. Note that the estimated values for p and q may be different to those by the PQ method. The cubic damping coefficient B_3 and the estimation coefficient r may be obtained by:

$$r = \frac{3}{4} \frac{\pi \omega_n^3}{C} B_3 = 6 \frac{\pi^4}{T_n^3 C} B_3 \quad \text{and} \quad (2.32)$$

$$B_3 = r \frac{T_n^3 C}{6 \pi^4} . \quad (2.33)$$

In the following, this technique is called PQR method to distinguish the third-order damping estimation from the second-order procedure (PQ method).

A major drawback of the presented PQ and PQR methods is the dependence on the motion amplitudes. For many cases, only a few oscillations are available to determine the hydrodynamic damping. For this reason, these methods are not very robust.

Optimised motion PQ method To improve the PQ method, a spring-mass-damper system as given by Equation (2.14) is fitted to the original decay signal using the simplex algorithm by Nelder and Mead (1965). In this way, all points of the decay can be exploited which means many more data points than for the previous methods which leads to a more robust method. The amplitudes of this second-order damping model are taken to obtain the PQ diagram. Subsequently, the same steps as for the PQ method are followed and the linear and quadratic damping coefficients may be calculated using Equation (2.28).

This method was implemented in a code and made available in form of a tool called TyDox by MARIN (Burmester et al., 2020c).

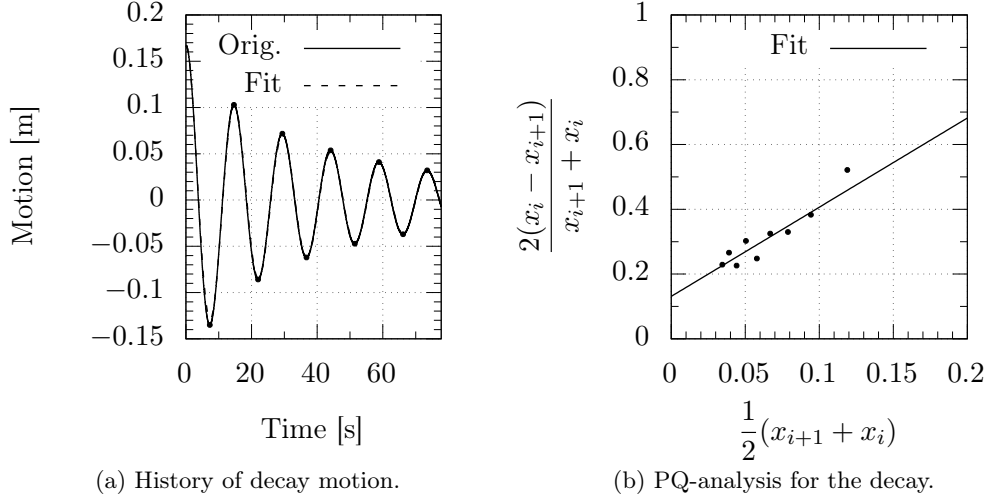


Figure 2.4: Example of an optimised motion PQ analysis.

2.1.5 Equivalent linear damping

This approach assumes that the work done by an equivalent linear damping force is equal to the work done by linear, quadratic and n^{th} order damping force components (Jaouën et al., 2019). Hence, an equivalent linear damping coefficient $B_{1,\text{eq}}$ may be estimated. An harmonic oscillation $x(t)$ with a constant amplitude of the form:

$$x(t) = x_0 \cos(\omega_n t) \quad (2.34)$$

is required to derive an expression for the equivalent linear damping. The work done by the equivalent linear damping force $W_{B_{L,\text{eq}}}$ reads:

$$\begin{aligned} W_{B_{1,\text{eq}}} &= \int_{t_0}^{t_0+T_n} F_{B_{1,\text{eq}}}(t) \dot{x}(t) dt \\ &= \int_{t_0}^{t_0+T_n} B_{1,\text{eq}} \dot{x}^2(t) dt \\ &= B_{1,\text{eq}} \int_{t_0}^{t_0+T_n} \dot{x}^2(t) dt . \end{aligned} \quad (2.35)$$

The equivalent linear damping force is given with: $F_{B_{1,\text{eq}}}(t) = B_{1,\text{eq}} \dot{x}(t)$. $\dot{x}(t)$ is the derivative of Equation (2.34). Then, Equation (2.35) becomes:

$$W_{B_{1,\text{eq}}} = \omega_n \pi x_0^2 B_{1,\text{eq}} . \quad (2.36)$$

The work done by the linear and quadratic damping force is defined as:

$$W_{B_{1,2}} = \int_{t_0}^{t_0+T_n} F_{B_{1,2}}(t) \dot{x}(t) dt = \omega_n \pi x_0^2 B_1 + \frac{8}{3} \omega_n^2 x_0^3 B_2 . \quad (2.37)$$

Assuming that the work done by the linear and quadratic damping force equates the work done by the equivalent linear damping force delivers an expression for the linear equivalent damping coefficient:

$$B_{1,eq} = B_1 + \frac{16x_0}{3T_n} B_2 . \quad (2.38)$$

This expression depends on the linear and quadratic damping coefficients estimated beforehand. For an additional cubic damping coefficient, the corresponding damping work $W_{B_{1,2,3}}$ reads:

$$W_{B_{1,2,3}} = W_{B_{1,2}} + W_{B_3} = \omega_n \pi x_0^2 B_1 + \frac{8}{3} \omega_n^2 x_0^3 B_2 + \frac{3}{4} \pi \omega_n^3 x_0^4 B_3 . \quad (2.39)$$

The corresponding equivalent linear damping coefficient follows with:

$$B_{1,eq} = B_1 + \frac{16x_0}{3T_n} B_2 + \frac{3\pi^2 x_0}{T_n^2} B_3 . \quad (2.40)$$

The equivalent linear damping coefficient may also be expressed as a ratio of the critical damping using following equation:

$$\zeta_D = \frac{B_{1,eq}}{B_{crit}} \quad \text{with} \quad B_{crit} = 2\sqrt{MC} . \quad (2.41)$$

M is the total mass consisting of structural and added mass. C denotes the linearised stiffness coefficient. The equivalent linear damping was already published in Himeno (1981). More details may also be found in Jaouën et al. (2019) and Piehl (2016). In case the equivalent quadratic damping is desired, the equivalent quadratic damping force $F_{B_{2,eq}}$ needs to be integrated (as in Equation (2.35)) and equated to the work done by the linear and quadratic (and cubic) damping force. Then, the procedure is the same as shown above.

2.1.6 Comparison of the estimation methods

Figure 2.5 shows a comparison of the PQR method to the PQ method for the same example decay simulation with free surface as in Figure 2.3.

The fits are almost on top of each other and differences are hardly visible. In the PQ diagram the differences are better to observe. The estimated equivalent linear damping $B_{1,eq}$ values are listed in Table 2.1 for comparison.

The largest differences were obtained between the PQ and the PQR method. These methods differed by 10.3% in estimated equivalent linear damping. The differences to the optimised motion PQ method reduce to 4.2% in equivalent linear damping. Thus, different hydrodynamic damping values may be obtained depending on the method adopted. This comparison was done for a 1 DOF simulation. Differences in equivalent linear damping of 6.8% between PQ and PQR and of 1.2% between PQ and optimised motion PQ method may be determined for the experiments underlying to the numerical investigations of this thesis. In the experiments, the studied floater may move in all 6 degrees-of-freedom. Since the optimised motion

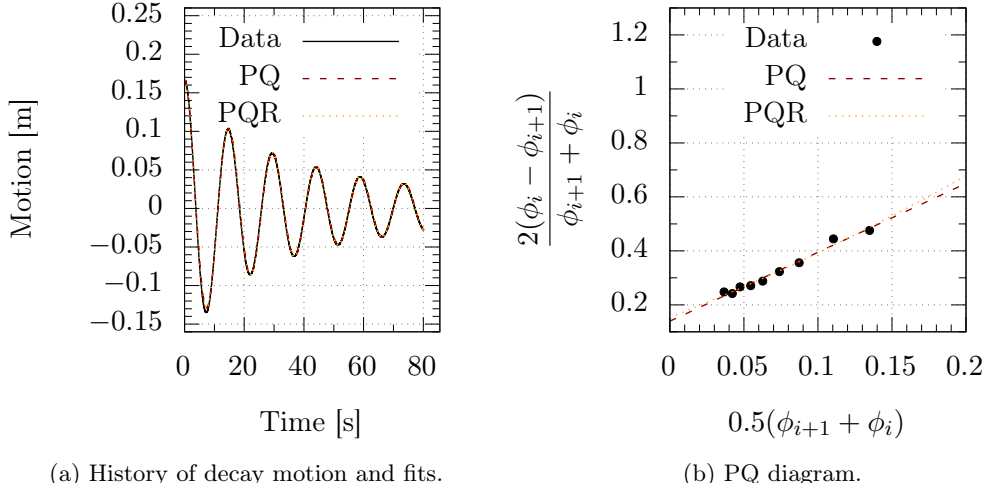


Figure 2.5: Comparison of the PQR and PQ analysis methods to obtain damping estimation coefficients. x_i denotes the current motion amplitude

Table 2.1: PQ analysis comparison between different methods based on the results shown in the figure 2.3 - 2.5. The methods are compared based on the calculated equivalent linear damping coefficient $B_{1,eq}$ and the oscillation period.

Damping parameters	PQ method	Optimised motion PQ method	PQR method
T_p , [s]	14.681	14.674	14.681
$B_{1,eq}$, [N s/m]	14.235	14.865	15.878

PQ method is more robust than the other two methods, the hydrodynamic damping for each numerical simulation was estimated with this technique for all further calculations and studies presented in this thesis. Nevertheless, the results and discussion may be influenced by the estimation method applied as the results may differ. Different publications and authors may as well use different procedures. Therefore, comparison between different publications is difficult.

2.2 Governing Equations

The flow of fluids is described based on the continuity and momentum equations. In the absence of sources or sinks, the continuity equation states that the mass of a fluid flow is neither created nor destroyed. The momentum equation, often referred to as Navier-Stokes equations, follows from Newton's second law of motion. The momentum of a flow is changed by the actions of forces on the flow. In addition, a transport equation for two-phase flows is needed, if free surface problems, such as waves, are investigated. This equation is the volume fraction transport

equation and originates from the Volume-of-Fluid (VOF) method. These governing equations in incompressible form are discretised based on the finite volume method (FVM). The CFD solver employed is called ReFRESCO. More details on the CFD solver may be found in Klaij et al. (2018) and Vaz et al. (2009), and on the governing equations may be found in e.g. Moukalled et al. (2016) and Ferziger and Perić (2002). The discretisation process is detailed in Chapter 3.

2.2.1 Continuity equation

A right-handed Cartesian coordinate system with x , y and z axes is assumed. The continuity equation in differential form reads:

$$\frac{\partial \rho}{\partial t} + \nabla \cdot (\rho \vec{v}) = 0 . \quad (2.42)$$

Here, \vec{v} denotes the velocity vector with (u, v, w) or u_i vector components, ρ the density and t the time. The gradient of a quantity is represented by the nabla operator ∇ and together with the dot-product \cdot it forms the divergence of a quantity. The flows, considered in this thesis, may be treated incompressible. Hence, there are no density changes along a trajectory over time, i.e. $\frac{D\rho}{Dt} = 0$. Then, the continuity equation for a single phase flow may be simplified to:

$$\nabla \cdot \vec{v} = 0 . \quad (2.43)$$

This equation states that the velocity field is divergence free. However, there can be density changes in the domain owing to multiphase flows. Consequently, another transport equation is required.

The mass conservation equation (2.42) in Cartesian components may also be written as:

$$\frac{\partial \rho}{\partial t} + \frac{\partial(\rho u_i)}{\partial x_i} = 0 . \quad (2.44)$$

u_i are the Cartesian components ($i = 1, 2, 3$) or ($i = x, y, z$) of the velocity vector \vec{v} and x_i the Cartesian coordinates. For simplification, the methods and schemes addressed in this work are described using the equations for incompressible, single-phase flows. Nevertheless, for the calculations of this thesis the homogeneous VOF approach including density variations in space is used to model multiphase flows.

2.2.2 Momentum equation

In the original sense, only the momentum equations represent the Navier-Stokes (NS) equations. In differential and vectorial form, this equation is defined as follows (Moukalled et al., 2016, Klaij et al., 2018):

$$\frac{\partial}{\partial t} (\rho \vec{v}) + \nabla \cdot \{\rho \vec{v} \vec{v}\} = -\nabla p + \nabla \cdot \boldsymbol{\tau} + \rho \vec{g} . \quad (2.45)$$

p denotes the pressure. The only body force, \vec{f}_b , considered originates from the gravitational acceleration vector \vec{g} . The surface forces include the pressure gradient

∇p and the divergence of the viscous stress tensor $\nabla \cdot \boldsymbol{\tau}$. For a Newtonian fluid, the viscous stress tensor reads:

$$\boldsymbol{\tau} = \mu \left(\nabla \vec{v} + (\nabla \vec{v})^T \right) + \lambda_b (\nabla \cdot \vec{v}) \mathbf{I} . \quad (2.46)$$

The superscript T represents the transpose of a vector or matrix. μ denotes the dynamic viscosity. λ_b is the bulk viscosity and defined as $\lambda_b = -\frac{2}{3}\mu$. \mathbf{I} denotes the unit tensor of size (3×3) . Following the continuity equation, the term $\nabla \cdot \vec{v}$ equals zero. Thus, the viscous stress tensor may be simplified to:

$$\boldsymbol{\tau} = \mu \left(\nabla \vec{v} + (\nabla \vec{v})^T \right) . \quad (2.47)$$

In Cartesian notation, the momentum equation (2.45) becomes (Ferziger and Perić, 2002):

$$\frac{\partial(\rho u_i)}{\partial t} + \frac{\partial(\rho u_j u_i)}{\partial x_j} = -\frac{\partial p}{\partial x_i} + \frac{\partial \tau_{ij}}{\partial x_j} + \rho g_i . \quad (2.48)$$

g_i is the i th component of the gravity vector pointing in the same direction as x_i .

2.2.3 Volume fraction transport equation

For the two-phase flow simulations, the homogeneous Volume-of-Fluid (VOF) method is used, which is utilised as depicted in Klaij et al. (2018). The VOF method belongs to the interface capturing methods. As opposed to the interface tracking methods using boundary-fitted grids, these methods enable the generation of fixed (non-adaptive) grids that extend beyond the free surface. The VOF method was firstly introduced by Hirt and Nichols (1981). The homogeneous approach models the multiphase flow by adopting a single continuum fluid, in which the density ρ and viscosity μ can vary in space and time for incompressible flows. The following equations give the density and viscosity for two different phases (water and air):

$$\rho = \rho_a c + (1 - c) \rho_w , \quad \mu = \mu_a c + (1 - c) \mu_w . \quad (2.49)$$

The subscript w and a represent the material properties of water and air, respectively. c denotes the volume fraction and ranges from $c = 0$ to $c = 1$. A value of $c = 0$ means that the cell or control volume (CV) is filled entirely by water and $c = 1$ entirely by air. Therefore, c is also termed air volume fraction in this thesis. Due to this approach, the momentum and continuity equations may be applied for the mixture. The volume fraction transport equation for incompressible fluids reads:

$$\frac{\partial c}{\partial t} + \nabla \cdot (c \vec{v}) = 0 . \quad (2.50)$$

A critical part of this equation is the discretisation of the convective term $\nabla \cdot (c \vec{v})$. Higher order schemes are required to reduce artificial mixing of the phases and to sharpen the interface. More explanation and details may be found in Klaij et al. (2018).

2.2.4 Inviscid flow equations

There are two special cases of the Navier-Stokes equations that need to be highlighted. These two cases are represented by the Euler equation and the potential-flow theory. Both equations neglect viscous effects in the flow. For many flows of practical interest, viscous effects are of minor interest. In inviscid flows, no tangential forces (shear stresses) exist, i.e. for hydrodynamic damping investigations the skin friction component is missing, and the damping component owing to eddies is not realistically represented.

Euler equation: Neglecting the viscosity in the governing equations results in the Euler equations. The continuity equation is identical to Equation (2.42), but the momentum equation becomes:

$$\frac{\partial}{\partial t} (\rho \vec{v}) + \nabla \cdot \{\rho \vec{v} \vec{v}\} = -\nabla p + \rho \vec{g}. \quad (2.51)$$

These equations disregard any skin friction as inviscid flow cannot stick to walls (Ferziger and Perić, 2002). Vorticity in the flow, however, can occur but only because of numerical inputs, sharp edges, and low grid quality.

Potential flow: Furthermore, if the flow may be assumed irrotational, i.e. the curl of the velocity vector is zero: $\nabla \times \vec{v} = 0$, then the flow may be expressed via a velocity potential ϕ_{vp} . The velocity vector follows as gradient of the velocity potential:

$$\vec{v} = \nabla \phi_{vp}. \quad (2.52)$$

The pressure p follows from substitution of the velocity in the momentum equation (Equation (2.45)). For unsteady and incompressible flows, the pressure follows from Bernoulli's equation:

$$\frac{p}{\rho} + gz + \frac{\partial \phi_{vp}}{\partial t} + \frac{1}{2} |\nabla \phi_{vp}|^2 = f(t) \quad (2.53)$$

z denotes the vertical distance to the free surface with negative values below still water line, see Figure 2.7. $f(t)$ is a time dependent function and constant for stationary flows. This equation states that the energy at any location in the flow is constant. The equation is valid for earth fixed coordinate systems. The potential flow theory leads to D'Alembert's paradox, i.e. a body in potential flow experiences neither drag nor lift. In Section 2.4.1, boundary conditions of the velocity potential are given to derive the required analytical kinematics for wave generation purposes.

2.2.5 Integral form of the transport equations

As the transport equations are solved in a finite volume framework, the integral form of the transport equations is required. The general procedure to obtain the integral form is given first before it is applied to the continuity and momentum

equations.

For an arbitrary quantity ϕ , the generic transport equation reads:

$$\underbrace{\frac{\partial}{\partial t} \rho \phi}_{\text{unsteady term}} + \underbrace{\nabla \cdot (\rho \phi \vec{v})}_{\text{convective term}} = \underbrace{\nabla \cdot (\Gamma \nabla \phi)}_{\text{diffusion term}} + \underbrace{\vec{q}_\phi}_{\text{source term}} . \quad (2.54)$$

Here, Γ is the diffusivity of ϕ and \vec{q}_ϕ a general source term. Owing to the second derivative of ϕ in the diffusion term, this equation is a second order differential equation. Integrating this equation over a control volume (CV) delivers the integral form:

$$\frac{\partial}{\partial t} \int_V \rho \phi \, dV + \int_V \nabla \cdot (\rho \vec{v} \phi) \, dV = \int_V \nabla \cdot (\Gamma \nabla \phi) \, dV + \int_V \vec{q}_\phi \, dV . \quad (2.55)$$

Using Gauss divergence theorem, the divergence terms are eliminated and the equation becomes:

$$\frac{\partial}{\partial t} \int_V \rho \phi \, dV + \oint_S (\rho \phi \vec{v} \cdot \vec{n}) \, dS = \oint_S (\Gamma \nabla \phi) \cdot \vec{n} \, dS + \int_V \vec{q}_\phi \, dV . \quad (2.56)$$

\vec{n} represents the normal vector of a CV pointing outwards. This form is the conservative form of the integral equations. This procedure results in volume and surface integrals that require approximations. Approximation schemes to solve volume and surface integrals are provided in Chapter 3.

For completeness, the Gauss divergence theorem may be applied also to the continuity and momentum equations to obtain their integral form. The continuity equation yields:

$$\frac{\partial}{\partial t} \int_V \rho \, dV + \int_S (\rho \vec{v} \cdot \vec{n}) \, dS = 0 . \quad (2.57)$$

The continuity equation states that the net flow across any control volume is zero, if no sources or sinks are present. As the change in mass in a control volume is equal to the net flux of mass through the faces, the mass inside a control volume is conserved. Therefore, the continuity equation is also called mass conservation equation.

The integral form of the momentum equation reads:

$$\frac{\partial}{\partial t} \int_V \rho \vec{v} \, dV + \int_S \rho \vec{v} \vec{v} \cdot \vec{n} \, dS = \int_S \mathbf{T} \cdot \vec{n} \, dS + \int_V \rho \vec{f}_b \, dV . \quad (2.58)$$

\mathbf{T} denotes the stress tensor and consists of pressure and viscous stress:

$$\mathbf{T} = -p \mathbf{I} + \boldsymbol{\tau} . \quad (2.59)$$

The divergence of the stress tensor equals the surface forces.

2.3 Turbulence Modelling

Turbulent flows are encountered in most engineering applications. They are three-dimensional and highly unsteady. The flow involves eddies in a broad range of

different scales. Thereby, the larger eddies break up into smaller ones dissipating the energy of the flow. The smallest turbulent eddies are characterised by the Kolmogorov micro length and time scales (see e.g. Moukalled et al. (2016)). Simulation and modelling of turbulent flows may be conducted by Direct Numerical Simulations (DNS), Large Eddy Simulations (LES), Hybrid/Bridging methods (also termed Scale Resolved Simulations) or Reynolds-Averaged Navier-Stokes (RANS). The first is the most accurate approach to simulate turbulence. For DNS, the turbulent kinetic energy is resolved and the accuracy of these simulations depends solely on the numerical discretisation. All eddies are resolved, but the simulations are computationally demanding. Large Eddy Simulations use a low-pass filter so that large scale turbulent structures are resolved down to local grid size and turbulent structures smaller than this grid size are modelled with a turbulence model. As a rule of thumb by Pope (2000), 80% of the turbulent kinetic energy should be resolved. Hence, LES is less demanding than DNS, but also less accurate. In many flow cases, both techniques, DNS and LES, are still very costly. Another approach relies on Hybrid/Bridging methods. Flow scales not amenable to modelling are resolved. The remaining turbulent scales are modelled by turbulence models (Pereira, 2018). Famous representatives of these approaches are Detached Eddy-Simulation, Very Large-Eddy Simulation, Scale-Adaptive Simulation, and Partially-Averaging Navier-Stokes equations. The most popular approach at the moment is based on Reynolds averaging of the Navier-Stokes equations. In fact, all transport equations are Reynolds-averaged. All turbulent effects are modelled by turbulence models. The accuracy of this approach depends on the turbulence model. Thus, the constraint on the resolution is reduced compared to the DNS and LES approaches, but at the cost of less accurate representation of turbulence in the flow.

The decay simulations of this thesis were performed at model scale Reynolds numbers of $R_e < 3.1 \cdot 10^4$. The fluid flow at this Reynolds number is turbulent. As the investigations involve oscillatory motions which involves varying velocities of the floater, transition between laminar and turbulent flow regimes may occur in several cycles. In Rosetti and Vaz (2017), transition modelling of moving cylinders was investigated. They found that the moving cylinder “filters” most of the higher-order turbulent effects. Hence, numerical simulations using Reynolds-Averaged Navier-Stokes equations were assumed sufficiently accurate for the decay simulations of a semi-submersible floating wind turbine. The turbulence model, however, influences the creation, existence, dissipation and destruction of vortical structures, which in turn affects the hydrodynamic damping. Therefore, three RANS turbulence models were compared in this thesis. These turbulence models are the $k - \omega$ Shear Stress Transport, the $k - \sqrt{k}L$, and the $k - \omega$ Explicit Algebraic Reynolds Stress Model. The SST model by Menter et al. (2003) is widely adopted for maritime applications, see e.g. Make and Vaz (2015), Tran and Kim (2015), Rosetti and Vaz (2017), Wang et al. (2018), Zhang and Kim (2018), Jiang et al. (2020). However, in the free-surface simulations of this thesis better iterative convergence was observed for the $k - \sqrt{k}L$ turbulence model by Menter and Egorov (2006). Furthermore, the EARSM model accounts for anisotropic turbulent flows and a non-linear relation between strain rate and Reynolds stresses, see Pereira (2018),

Pereira et al. (2021). This section details the Reynolds averaging process and these turbulence models. More details regarding turbulence and turbulence models may be found in e.g. Ferziger and Perić (2002), Moukalled et al. (2016), Pereira (2018) and Pereira et al. (2021).

2.3.1 Reynolds-Averaged Navier-Stokes equations

The Reynolds-averaging of the Navier-Stokes equations means that the time dependent quantities of the flow $\phi(\vec{x}, t)$ are replaced by a mean field $\bar{\phi}(\vec{x}, t)$ and a statistical fluctuation quantity $\phi'(\vec{x}, t)$ owing to turbulence:

$$\phi(\vec{x}, t) = \bar{\phi}(\vec{x}, t) + \phi'(\vec{x}, t) . \quad (2.60)$$

\vec{x} designates the space vector consisting of (x, y, z) or (x_1, x_2, x_3) components. For unsteady flow problems, the mean field quantity is obtained by ensemble averaging over N identical realisations:

$$\bar{\phi}(\vec{x}, t) = \lim_{N \rightarrow \infty} \frac{1}{N} \sum_{i=1}^N \phi(\vec{x}, t) . \quad (2.61)$$

The mean of the statistical fluctuation quantity is $\bar{\phi}'(\vec{x}, t) = 0$. Using Equation (2.60), the simplified continuity and momentum equations for an incompressible single phase flow are rewritten to:

$$\nabla \cdot (\rho \bar{v}) = 0 \text{ and} \quad (2.62)$$

$$\frac{\partial}{\partial t} (\rho \bar{v}) + \nabla \cdot \{\rho \bar{v} \bar{v}\} = -\nabla \bar{p} + \nabla \cdot (\bar{\tau} - \rho \bar{v}' \bar{v}') + \bar{f}_b . \quad (2.63)$$

\bar{f}_b represents the body forces. Then, there appear the so-called Reynolds stresses $\tau_R = -\rho \bar{v}' \bar{v}'$. These terms cannot be represented solely by the mean quantities. Thus, there are more unknowns than equations, i.e. the system of equations is not closed. Further equations are needed to obtain a solution for the Reynolds stresses. A popular approach relies on the Boussinesq approximation for linear eddy-viscosity based turbulence models:

$$\tau_R = -\rho \bar{v}' \bar{v}' = \mu_t \left(\nabla \bar{v} + (\nabla \bar{v})^T \right) - \frac{2}{3} \rho k \mathbf{I} = 2\mu_t \mathbf{S}_t - \frac{2}{3} \rho k \mathbf{I} . \quad (2.64)$$

The strain rate \mathbf{S}_t and its magnitude S_{t_M} are defined as:

$$\mathbf{S}_t = \frac{1}{2} \left(\nabla \bar{v} + (\nabla \bar{v})^T \right) , S_{t_M} = \sqrt{\mathbf{S}_t \cdot \mathbf{S}_t} . \quad (2.65)$$

The approximation or hypothesis by Boussinesq relies on the assumption that the effect of turbulence can be represented as an increased viscosity due to the turbulent or eddy viscosity μ_t . k denotes the turbulent kinetic energy and reads:

$$k = \frac{1}{2} \bar{v}' \cdot \bar{v}' . \quad (2.66)$$

The new Reynolds-Averaged Navier-Stokes (RANS) form of the momentum equation becomes:

$$\frac{\partial}{\partial t}(\rho \bar{v}) + \nabla \cdot \{\rho \bar{v} \bar{v}\} = -\nabla \bar{p} + \nabla \cdot \left[(\mu + \mu_t) \left(\nabla \bar{v} + (\nabla \bar{v})^T \right) \right] - \frac{2}{3} \nabla(\rho k) + \bar{f}_b . \quad (2.67)$$

The unknown eddy (turbulent) viscosity μ_t and the turbulent kinetic energy k are a result of the RANS turbulence models, here called turbulence models. The turbulent viscosity is generally considered to be proportional to a turbulence velocity scale v_t and a length scale L_t :

$$\mu_t = C_\mu \rho v_t L_t . \quad (2.68)$$

Here, $v_t = \sqrt{k}$ depends on the turbulent kinetic energy. C_μ is a dimensionless coefficient which is usually defined by the turbulence model used.

The models may be grouped into three main categories:

- Algebraic (zero-equation) models,
- One-equation models,
- Two-equation models.

The algebraic models can be applied for simple flows only. They make use of algebraic expressions for the turbulent viscosity. One-equation models require to solve one differential transport equation for the eddy viscosity. Two-equation models consist of two transport equations. Famous representatives of two-equation turbulence models are categorised as $k - \epsilon$, $k - \omega$ and $k - kL$. ϵ designates the turbulence dissipation rate of k originating from viscous stresses and ω the rate at which k is converted into internal thermal energy, also called specific dissipation. The two-equation models are widely adopted for industrial applications. Therefore, these turbulence models were applied also for the work of this thesis.

2.3.2 Shear Stress Transport turbulence model

As $k - \epsilon$ model better predict flows in the shear-layer and $k - \omega$ better in the boundary layer, Menter (1994) developed a RANS turbulence model that blends between the two approaches. It uses $k - \epsilon$ in the shear-layer and $k - \omega$ behaviour in the boundary layer. The blending model by Menter (1994) is called $k - \omega$ Shear Stress Transport turbulence model (SST). For this work, the improved version from 2003 was utilised as given in Menter et al. (2003). This model comes with two transport equations for k and ω , respectively:

$$\frac{\partial}{\partial t}(\rho k) + \nabla \cdot \{\rho \bar{v} k\} = \nabla \cdot \left[(\mu + \frac{\mu_t}{\sigma_k}) \nabla k \right] + S^k \text{ and} \quad (2.69)$$

$$\frac{\partial}{\partial t}(\rho \omega) + \nabla \cdot \{\rho \bar{v} \omega\} = \nabla \cdot \left[(\mu + \frac{\mu_t}{\sigma_\omega}) \nabla \omega \right] + S^\omega \quad (2.70)$$

with

$$S^k = \tilde{P}_k - \beta^* \rho \omega k , \quad S^\omega = C_\alpha \frac{\omega}{k} \tilde{P}_k - C_\beta \rho \omega^2 + 2(1 - F_1) \sigma_{\omega 2} \frac{\rho}{\omega} \nabla k \cdot \nabla \omega .$$

All coefficients are listed in Tab. 2.2 and estimated by a blend between subscript 1 and 2 as follows:

$$\phi = \phi_1 F_1 + \phi_2 (1 - F_1) .$$

Table 2.2: Coefficients for $k - \omega$ SST turbulence model (Menter et al., 2003).

a_1	$C_{\alpha 1}$	$C_{\alpha 2}$	$C_{\beta 1}$	$C_{\beta 2}$	β^*	σ_{k1}	σ_{k2}	$\sigma_{\omega 1}$	$\sigma_{\omega 2}$
0.31	0.5532	0.4403	0.075	0.0828	0.09	2.0	1.0	2.0	1.186

The blending function F_1 is defined as:

$$F_1 = \tanh \left(\min \left(\max \left(\frac{\sqrt{k}}{\beta^* \omega d_t}, \frac{500\nu}{d_t^2 \omega} \right), \frac{4\rho\sigma_{\omega 2} k}{C_{Dk\omega} d_t^2} \right) \right) .$$

$C_{Dk\omega}$ is calculated from:

$$C_{Dk\omega} = \max \left(2\rho\sigma_{\omega 2} \frac{1}{\omega} \nabla k \cdot \nabla \omega, 10^{-10} \right) .$$

d_t denotes the distance to the nearest wall. The modified production term \tilde{P}_k of the improved model from 2003 reads:

$$\tilde{P}_k = \min (\tau_{xy} \nabla \vec{v}, 10\epsilon) .$$

The principal turbulent shear stress τ_{xy} and the turbulent kinetic energy in the boundary layer are related by:

$$\tau_{xy} = \mu_t \vec{\Omega}_v = \rho \sqrt{\frac{\text{Production of } k}{\text{Dissipation of } k}} a_1 k .$$

a_1 is a coefficient and given in Tab. 2.2. The vorticity $\vec{\Omega}_v$ is defined as curl of the velocity vector, i.e.:

$$\vec{\Omega}_v = \nabla \times \vec{v} . \quad (2.71)$$

To avoid overproduction, the turbulent stresses are limited in the boundary layer (Pereira, 2018):

$$\mu_t = \frac{\rho a_1 k}{\max(a_1 \omega, S_{t_M} F_2)} .$$

F_2 is the second blending function in this model and given by:

$$F_2 = \tanh \left(\max \left[\frac{2\sqrt{k}}{\beta^* \omega d_t}, \frac{500\nu}{d_t^2 \omega} \right]^2 \right) .$$

In the following, this turbulence model is referred to as SST or SST 2003 model.

2.3.3 KSKL turbulence model

The KSKL ($k - \sqrt{k}L$) turbulence model is an advancement of Rotta's $k - kL$ model by Menter and Egorov (2006). The benefit over the $k - kL$ model lies in the simplification from a third to a second velocity derivative. This turbulence model formulates the first equation for the turbulent kinetic energy k and the second for $\Phi = \sqrt{k}L$:

$$\frac{\partial}{\partial t}(\rho k) + \nabla \cdot \{\rho \vec{v} k\} = P_k - C_\mu^{\frac{3}{4}} \rho \frac{k^2}{\Phi} + \nabla \cdot \frac{\mu_t}{\sigma_k} \nabla k \quad \text{and} \quad (2.72)$$

$$\frac{\partial}{\partial t}(\rho \Phi) + \nabla \cdot \{\rho \vec{v} \Phi\} = \frac{\Phi}{k} P_k \left(\zeta_1 - \zeta_2 \left(\frac{L}{L_{vK}} \right)^2 \right) - \zeta_3 \cdot \rho k + \nabla \cdot \frac{\mu_t}{\sigma_\Phi} \nabla \Phi. \quad (2.73)$$

The turbulent viscosity μ_t is defined as:

$$\mu_t = \nu_t \rho = \rho C_\mu^{\frac{1}{4}} \Phi. \quad (2.74)$$

ν_t is the turbulent kinetic viscosity. Here, the dimensionless coefficient is assigned with $C_\mu = 0.09$. L_{vK} designates the von Kármán length scale and is given by:

$$L_{vK} = \kappa \left| \frac{S_{tM}}{\vec{v}''} \right| \quad \text{with} \quad \vec{v}'' = |\nabla^2 \vec{v}|.$$

The von Karman length scale relies on the von Kármán constant $\kappa = 0.41$. The coefficients used are summarized in Tab. 2.3.

Table 2.3: Coefficients for KSKL turbulence model (Menter and Egorov, 2010).

ζ_1	ζ_2	ζ_3	σ_k	σ_Φ
0.8	1.47	0.0288	2/3	2/3

This turbulence model showed advantage in convergence of the residuals for free surface applications and less unrealistic eddy-viscosity compared to the $k-\omega$ SST 2003 model by Menter et al. (2003).

More details on this turbulence model may be found in Menter and Egorov (2006) and Menter and Egorov (2010).

2.3.4 Explicit Algebraic Reynolds Stress Model

The previously described RANS turbulence models rely on the Boussinesq hypothesis. This hypothesis sets the Reynolds stresses in linear relation to the strain rate. This is seldom observed in turbulent flows of practical interest. Therefore, an anisotropy tensor \mathbf{a} is added to compute the Reynolds stresses (see e.g. Pereira et al. (2017, 2021)):

$$\boldsymbol{\tau}_R = 2\mu_t \mathbf{S}_t - \frac{2}{3} \rho k \mathbf{I} - \mathbf{a} \mathbf{k}. \quad (2.75)$$

The anisotropy tensor \mathbf{a} depends on the strain rate tensor \mathbf{S}_t , the vorticity $\vec{\Omega}_v$, the turbulent kinetic energy k and the specific dissipation ω . Details on this model and

specifically the anisotropy tensor may be found in publications by Pereira (2018), Pereira et al. (2021), Wallin and Johansson (2000).

The $k - \omega$ Turbulent/Non-Turbulent model by Kok (2000) is the basis for this $k - \omega$ Explicit Algebraic Reynolds Stress Model (EARSM) (see e.g. Pereira et al. (2017), Pereira (2018), Pereira et al. (2021)). The transport equations for k and ω are given as follows:

$$\frac{\partial}{\partial t} (\rho k) + \nabla \cdot \{ \rho \vec{v} k \} = \nabla \cdot \left[(\mu + \frac{\mu_t}{\sigma_k}) \nabla k \right] + S^k \text{ and} \quad (2.76)$$

$$\frac{\partial}{\partial t} (\rho \omega) + \nabla \cdot \{ \rho \vec{v} \omega \} = \nabla \cdot \left[(\mu + \frac{\mu_t}{\sigma_\omega}) \nabla \omega \right] + S^\omega \quad (2.77)$$

with:

$$S^k = P_k - \beta^* \rho \omega k , \quad S^\omega = C_\alpha \frac{\omega}{k} P_k - C_\beta \rho \omega^2 + C_{D\omega} .$$

The cross-diffusion term $C_{D\omega}$ is defined as:

$$C_{D\omega} = \sigma_d \frac{\rho}{\omega} \max \{ \nabla k \nabla \omega , 0 \} .$$

The turbulent viscosity follows from:

$$\mu_t = C_\mu \frac{k \rho}{\beta^* \omega} . \quad (2.78)$$

The turbulence model coefficients are summarised in Tab. 2.4.

Table 2.4: Constants for $k - \omega$ TNT EARSM turbulence model (Kok, 2000).

C_α	C_β	β^*	κ	σ_d	σ_k	σ_ω
$\frac{C_\beta}{\beta^*} - \frac{\sigma_\omega \kappa^2}{\sqrt{\beta^*}}$	0.075	0.090	0.410	0.500	2/3	0.500

Compared to the previous two turbulence models, anisotropy and non-linear relation between Reynolds stress and strain rate are regarded. In the work of Pereira et al. (2019), the results of this turbulence model revealed a large dependency on the spatial discretisation. Moreover, larger vortical structures and smaller friction coefficients were obtained than for the SST 2003 model. These flow differences are expected to influence the hydrodynamic damping results.

A detailed comparison of these three RANS turbulence models may be found in Pereira et al. (2017).

2.4 Numerical Wave Tank

The simulations with free surface were modelled with wave boundary conditions for wave generation and absorption, see Section 3.1.7. The wave model used for the simulations was the Stokes 5th order formulation. In this section, basic assumptions to derive expressions for the Stokes 5th order wave model and absorption methods are detailed. Furthermore, a non-reflecting boundary condition of Sommerfeld type is explained (Sommerfeld, 1949).

2.4.1 Wave theory

The waves generated at the inlet boundary followed the Stokes 5th order formulation by Skjelbreia and Hendrickson (1960). Vaz et al. (2009) implemented this formulation according to the code provided by Lin (2008). Stokes waves as well as linear Airy waves are defined for irrotational inviscid flows. Consequentially, the basis is a velocity potential as given in Equation (2.52). This potential has to satisfy the Laplace equation:

$$\Delta \phi_{vp} = 0 \quad (2.79)$$

everywhere in the considered domain. Δ denotes the Laplace operator. The boundary conditions of the linear and Stokes wave theory are defined as (Faltinsen, 1990):

- The normal velocity on the sea bed must be zero:

$$\frac{\partial \phi_{vp}}{\partial z} = 0 \quad \text{for } z = -h . \quad (2.80)$$

h is the water depth and z the vertical coordinate measured from the calm water plane upwards, see Figure 2.7.

- No water particle can leave the free surface. This is known as the kinematic boundary condition. In Cartesian notation, this condition may be written as:

$$\frac{\partial \zeta}{\partial t} + \frac{\partial \phi_{vp}}{\partial x} \frac{\partial \zeta}{\partial x} + \frac{\partial \phi_{vp}}{\partial y} \frac{\partial \zeta}{\partial y} - \frac{\partial \phi_{vp}}{\partial z} = 0 \quad \text{on } z = \zeta(x, y, t) . \quad (2.81)$$

ζ denotes the free surface elevation.

- The pressure at the free surface must be equal to the constant atmospheric pressure. Using Bernoulli's equation for pressure (Equation (2.53)), the dynamic boundary condition for the velocity potential follows as:

$$g\zeta + \frac{\partial \phi_{vp}}{\partial t} + \frac{1}{2} \left[\left(\frac{\partial \phi_{vp}}{\partial x} \right)^2 + \left(\frac{\partial \phi_{vp}}{\partial y} \right)^2 + \left(\frac{\partial \phi_{vp}}{\partial z} \right)^2 \right] = 0 \quad \text{on } z = \zeta(x, y, t) . \quad (2.82)$$

For the linear Airy wave theory, a small wave steepness is assumed. Hence, the kinematic and dynamic boundary conditions may be linearised to:

$$\frac{\partial \zeta}{\partial t} = \frac{\partial \phi_{vp}}{\partial z} \quad \text{on } z = 0 , \quad (2.83)$$

$$g\zeta + \frac{\partial \phi_{vp}}{\partial t} = 0 \quad \text{on } z = 0 . \quad (2.84)$$

These two linearised conditions may be combined to the Cauchy-Poisson condition, which is written as (Hennig, 2005):

$$\frac{\partial^2 \phi_{vp}}{\partial t^2} + g \frac{\partial \phi_{vp}}{\partial z} = 0 \quad \text{on } z = 0 . \quad (2.85)$$

The velocity potential ϕ_{vp} for a linear wave follows with:

$$\phi_{vp}(t, x, z) = \frac{g\zeta_a}{\omega_w} \frac{\cosh[k_w(h+z)]}{\cosh(k_w d)} \cos(\omega_w t - k_w x) . \quad (2.86)$$

ζ_a denotes the wave amplitude, k_w the wave number, and ω_w the wave frequency. The wave elevation follows from the linearised dynamic condition:

$$\zeta(t, x) = \zeta_a \sin(\omega_w t - k_w x) . \quad (2.87)$$

Fluid particles are assumed to follow orbital trajectories. Expressions for orbital velocities are tabulated by Hennig (2005) and Faltinsen (1990). By Stokes expansion higher-order wave theories may be obtained. The expansion for the 5th order model results in a wave elevation with five components of the form:

$$\zeta(t, x) = \sum_{i=1}^5 C_i \sin[i(\omega_w t - k_w x)] . \quad (2.88)$$

The coefficients C_i and derivation of this wave equation may be found in Skjelbreia and Hendrickson (1960), Lin (2008) and Fenton (1985). Higher-order theories result in steeper waves with larger crests and shallower troughs than using Airy's linear approach. Therefore, the results of this theory become closer to real sea conditions. This 5th order model is applicable for deep and intermediate water depths (Lé Méhauté, 1976). As a consequence of the Laplace equation and boundary conditions, the wave model provides the surface elevation and velocity components. These velocity components decrease exponentially with water depths (vertical distance to the free surface).

2.4.2 Wave absorption

Wave reflection may arise from the open domain boundaries. These reflections change the upstream wave signal, and can cause large errors in the results. Consequently, undesired wave reflection needs to be minimised. In physical experiments, waves are usually damped by active or passive wave absorbers. In numerical simulations, waves can be damped by e.g. grid damping (numerical beaches by continuous increase of cell size towards respective domain boundary), beaches (slopes in the domain bottom as in experiments), active wave absorption techniques, solution-forcing or solver coupling, and additional body force terms (absorption zones or sponge layers) (Perić and Abdel-Maksoud, 2016). The most-widely used damping approaches are methods applying grid damping and using body forces in absorption zones. Perić and Abdel-Maksoud (2016) demonstrated that the performance of absorption zone techniques do not depend on grid, time step or discretisation schemes used, if the spatial and temporal discretisation is sufficiently fine. This is not the case for grid damping techniques. Then, wave absorption zones are beneficial and may be applied as shown by Rapuc et al. (2018) and Perić and Abdel-Maksoud (2018). Wave absorption is obtained by adding a source term to several or all governing equations. The absorption zone methods can be traced back to Israeli and Orszag (1981). The method used here is

comparable to the one proposed by Perić and Abdel-Maksoud (2018). However, it differs to the latter method by omitting body force functions in the volume fraction transport equation which was found unnecessary by Rapuc et al. (2018) and may impair iterative convergence. The momentum equation with added source term \vec{f}_a may be written as:

$$\frac{\partial}{\partial t} \rho \vec{v} + \nabla \cdot \{\rho \vec{v} \vec{v}\} = -\nabla p + \nabla \cdot \boldsymbol{\tau} + \rho \vec{g} + \vec{f}_a . \quad (2.89)$$

The added source term \vec{f}_a consists of a body force function f_b , the material density ρ and the difference between actual and theoretical orbital velocity. The source term acts in a plane in gravity direction:

$$f_{a_i} = \rho f_b (\hat{u}_i - u_i) . \quad (2.90)$$

u_i are the Cartesian components of the velocity vector. The theoretical initial wave orbital velocity components are given by \hat{u}_i . The body force function follows either a cosine or an exponential behaviour (Rapuc et al., 2018):

$$f_b = \frac{\frac{1}{T_{ref}} \cdot f_{max} (1 - \cos(\pi x_b))}{2} , \quad (2.91)$$

$$f_b = \frac{1}{T_{ref}} \cdot f_{max} \frac{e^{x_b^{3.5}} - 1}{e^1 - 1} . \quad (2.92)$$

T_{ref} is a reference period typically equal to the wave period and f_{max} the absorption coefficient. The body force function f_b is valid between two predefined ellipses perpendicular to the gravity. Inside the inner ellipse, the body force function is zero and waves may propagate freely. The inner ellipse gives the starting point for x_b . Increasing x_b towards the outer ellipse increases the body force function value according to the form (cosine or exponential) selected until it reaches its maximum. The benefit of using either of these functions is its smooth start at $x_b = 0$. This start reduces wave reflection from the beginning of the absorption zone. f_b is constant outside of the outer ellipse. The form of the ellipses can be changed from circular to almost rectangular. If the distance between the two ellipses is related to the wave length, f_{max} may be considered independent of the wave period (Rapuc et al., 2018).

2.4.3 Non-reflecting boundary condition

In addition, it is possible to apply non-reflecting boundary conditions (NRBCs). At these boundary conditions, certain predefined wave frequencies are not reflected. The boundary condition of Sommerfeld type (Sommerfeld, 1949) belongs to these NRBCs. In many publications, non-reflecting boundary conditions are also referred to as absorbing boundary conditions. It may be beneficial to use this condition in conjunction with the absorption zones described above. The NRBC relies on the Sommerfeld operator H :

$$H = \frac{\partial}{\partial t} + c \frac{\partial}{\partial x} . \quad (2.93)$$

Where, c denotes the wave celerity. Applying this operator to the wave velocity potential yields zero:

$$H\phi_{vp} = \left(\frac{\partial}{\partial t} + c \frac{\partial}{\partial x} \right) \phi_{vp} = 0 . \quad (2.94)$$

The linear wave velocity potential was given in Equation (2.86). The relation between the wave celerity c_w and the wave frequency reads:

$$c_w = \frac{\omega_w}{k_w} . \quad (2.95)$$

Replacing the fraction term in the velocity potential equation that depends on the vertical coordinate by

$$f(z) = \frac{\cosh(k_w(z+h))}{\cosh(k_w h)}$$

yields following expression:

$$H\phi_{vp} = \frac{g\zeta_a}{\omega_w} f(z) [-\omega_w + c_w k_w] \cos(k_w x - \omega_w t) = 0 . \quad (2.96)$$

The dynamic pressure p_{dyn} and velocity u_{dyn} for a 1D system are given by:

$$p_{dyn} = -\rho \frac{\partial \phi_{vp}}{\partial t} \quad \text{and} \quad u_{dyn} = \frac{\partial \phi_{vp}}{\partial x} . \quad (2.97)$$

Thus, applying the Sommerfeld operator on the pressure and velocity terms results in:

$$-\frac{p_{dyn}}{\rho} + c_w u_{dyn} = 0 . \quad (2.98)$$

This first-order version of Sommerfeld is accurate for waves propagating in normal direction to the boundary and for one phase velocity. Introducing φ_{prop} as the angle between wave propagation direction and domain boundary, the wave celerity may be adjusted with:

$$c_w = \frac{\omega_w}{k_w \cos(\varphi_{prop})} . \quad (2.99)$$

According to Veldman et al. (2016), the general representation of the Sommerfeld operator is:

$$\prod_i^P \left(\frac{\partial}{\partial t} + c_i \frac{\partial}{\partial x} \right) \phi_{vp} = 0 . \quad (2.100)$$

Here, P denotes the order of the boundary condition. The second-order Sommerfeld operator, H_{2nd} , is also implemented and reads:

$$H_{2nd}\phi_{vp} = \left(\frac{\partial}{\partial t} + c_{w1} \frac{\partial}{\partial x} \right) \left(\frac{\partial}{\partial t} + c_{w2} \frac{\partial}{\partial x} \right) \phi_{vp} = 0 \quad (2.101)$$

The advantage of this second-order operator lies in the second wave celerity, c_{w1} and c_{w2} , to be selected. The wave reflection reduces with the order of the Sommerfeld operator. The order of the Sommerfeld operator, however, also increases the order of the temporal and spatial derivates which leads to an increased computing

effort.

Waves propagating with the predefined celerity are not reflected. If the wave celerity is slightly above or below the defined value, the wave reflection is damped. The damping of the wave reflection reduces with difference to the predefined velocity. The boundary condition, on which Sommerfeld is applied, may be used for wave generation and absorption. For the linear case, the equations used at the boundary are Equation (2.93) for absorption alone, Equation (2.94) for wave absorption and generation, and solely the equations of the wave model for wave generation. More details may be found in Sommerfeld (1949), Veldman et al. (2016) and Wellens (2012).

2.5 Rigid Body Motions

The decay simulations were performed using a moving grid and domain around the floater. Therefore, the code was coupled with the rigid body equations of motion. This equation is required when bodies are moving and is detailed in Section 2.5.1. However, the computational grid has to be able to deal with this motion, see Section 2.5.2. Further details on the implementation and testing may be found in Rosetti (2015), Rosetti and Vaz (2017) and Vaz (2014).

2.5.1 Rigid body equation of motion

The rigid body equations of motion for an object enable the description of its attitude to external loads. Newton's second law is written as $\mathbf{M}\ddot{\vec{x}} = \vec{f}_{ext}$. The considered external loads \vec{f}_{ext} are the hydrodynamic force \vec{f}_H calculated by the RANS code, the restoring force \vec{f}_C , and the linear external damping force \vec{f}_D (originating, for instance, from mechanical components connected to the body). This leads to the total external loads, such as: $\vec{f}_{ext} = \vec{f}_H + \vec{f}_C + \vec{f}_D$. With a state vector for six degrees-of-freedom $\vec{x} = \{X_G, Y_G, Z_G, \Phi_G, \Theta_G, \Psi_G\}^T$, the dynamic equations are written as:

$$\mathbf{M}\ddot{\vec{x}} = \vec{f}_H + \vec{f}_C + \vec{f}_D \quad (2.102)$$

The forces \vec{f}_C and \vec{f}_D have the form:

$$\vec{f}_C = -\mathbf{C}\vec{x} \quad \text{and} \quad \vec{f}_D = -\mathbf{D}\dot{\vec{x}}$$

\mathbf{M} denotes the mass, \mathbf{D} the damping, and \mathbf{C} the stiffness/restoring matrix. The matrices \mathbf{M} and \mathbf{D} are positive and diagonal. As the body was assumed to be connected to the surroundings in such a way that the connection did not provide mechanical damping, the damping matrix was set to “zero”. Together, these equations form a second-order non-linear initial value problem. The problem is non-linear because the hydrodynamic forces, \vec{f}_H , keep a non-linear relation with \vec{x} via the NS equations. The coupling as applied in the CFD code is detailed in Section 3.3.

2.5.2 Modification to the transport equations

Rigid-body motions including translation and/or rotation of an object may be modelled with the following three approaches:

- Relative formulation or body-forces approach: The RANS equations are written and solved in the moving or relative reference frame. Extra volumetric terms or body forces have to be considered.
- Absolute formulation: The RANS equations are solved in the moving reference frame but written in terms of absolute or inertial reference frame quantities. Extra volumetric forces need to be accounted for in the momentum equations.
- Moving-grid formulation (MVG): The RANS equations are written and solved in the earth-fixed reference frame. Owing to the motion of the objects, the equations are inherently unsteady. This is also true for steady motions.

The decay simulations to investigate hydrodynamic damping applied the rigid-body motion equation with the moving-grid formulation. The mass and momentum conservation equations become:

$$\frac{\partial \rho}{\partial t} + \nabla \cdot \{\rho(\vec{v} - \vec{v}_G)\} = 0 , \quad (2.103)$$

$$\frac{\partial}{\partial t} (\rho \vec{v}) + \nabla \cdot \{\rho \vec{v}(\vec{v} - \vec{v}_G)\} = -\nabla p + \nabla \cdot \boldsymbol{\tau} + \rho \vec{g} . \quad (2.104)$$

The velocity of the body-fixed reference system is given by \vec{v}_G , but as rigid body motions are considered: $\nabla \cdot \vec{v}_G = 0$. In integral form, these equations read:

$$\frac{\partial}{\partial t} \int_V \rho \, dV + \int_S (\rho(\vec{v} - \vec{v}_G) \cdot \vec{n}) \, dS = 0 , \quad (2.105)$$

$$\frac{\partial}{\partial t} \int_V \rho \vec{v} \, dV + \int_S \rho \vec{v}(\vec{v} - \vec{v}_G) \cdot \vec{n} \, dS = \int_S \mathbf{T} \cdot \vec{n} \, dS + \int_V \rho \vec{f}_b \, dV . \quad (2.106)$$

Compared to the original conservation equations given in Section 2.2 only the convection term is altered. The relative velocity appears only in the convection term as the coordinate system is fixed (Ferziger and Perić, 2002). This applies also to all other transport equations. For any scalar ϕ , the generic transport or conservation equation reads:

$$\frac{\partial}{\partial t} (\rho \phi) + \nabla \cdot \{\rho \phi(\vec{v} - \vec{v}_G)\} = \nabla \cdot (\Gamma \nabla \phi) + \vec{q}_\phi . \quad (2.107)$$

The inertial or earth-fixed coordinate system is given by (x', y', z') and the body-fixed reference system by (x, y, z) as shown in Figure 2.6.

The vector \vec{x}'_p may be represented by:

$$\vec{x}'_p = \vec{x}'_0 + \mathbf{R}_{xyz} \vec{x}_p . \quad (2.108)$$

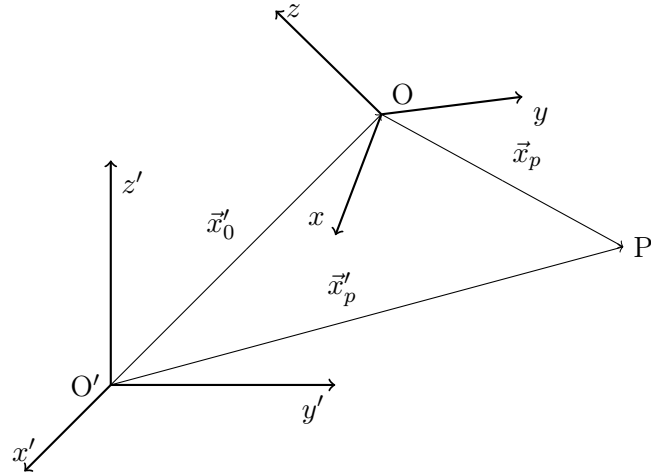


Figure 2.6: Relation between the earth-fixed O' (x', y', z') and body-fixed O (x, y, z) coordinate system, adopted from Rosetti (2015).

\mathbf{R}_{xyz} is the transformation matrix from body to earth fixed coordinate system. Deriving this equation with respect to time yields:

$$\dot{\vec{x}}'_p = \dot{\vec{x}}'_0 + \vec{\omega} \times \mathbf{R}_{xyz} \vec{x}_p + \mathbf{R}_{xyz} \dot{\vec{x}}_p \quad \text{with} \quad \vec{v}'_p = \dot{\vec{x}}'_p \quad \text{follows:} \quad (2.109)$$

$$\vec{v}'_p = \vec{v}'_0 + \vec{\omega} \times \mathbf{R}_{xyz} \vec{x}_p + \mathbf{R}_{xyz} \vec{v}_p . \quad (2.110)$$

$\vec{\omega}$ denotes the angular velocity. Assuming P being rigidly connected to the body-fixed coordinate system, the velocity of P is represented by $\vec{v}'_0 + \vec{\omega} \times \mathbf{R}_{xyz} \vec{x}_p$. Consequentially, \vec{v}_p is the velocity of P with respect to the body-fixed coordinate system. Hence, the velocity of the body-fixed reference system \vec{v}_G reads:

$$\vec{v}_G = \vec{v}'_0 + \vec{\omega} \times \mathbf{R}_{xyz} \vec{x}_p . \quad (2.111)$$

More details on coordinate system transformations may also be found in Chillcce and el Moctar (2018).

2.6 Catenary Mooring Line Equation

The semi-submersible floating wind turbine model studied was tested experimentally with a catenary mooring line system. Catenary mooring lines are characterised by, in general, a suspended line from the fairlead to the sea bed and some chain resting on it. There are multiple configurations with e.g. clamp weights and buoys that increase the complexity of this mooring configuration. However, no extra weights and floaters were attached to the mooring system used in this work (Robertson et al., 2017b). Figure 2.7 shows the schematic for one catenary mooring line. The respective coordinate system for the two-dimensional mooring line configuration consists of a horizontal coordinate x and a vertical coordinate z pointing upwards. The point of origin is set to the still water line and at the touch

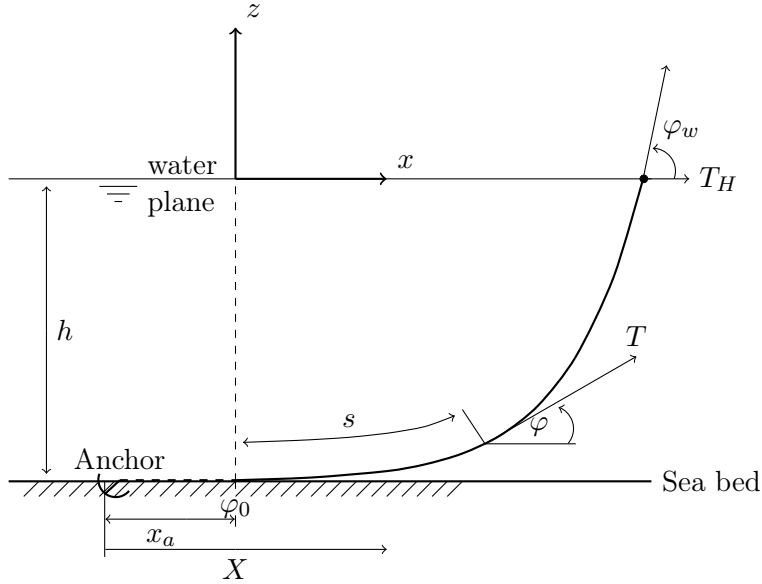


Figure 2.7: Catenary moorings with definitions, adapted from Faltinsen (1990). T denotes the tension in the mooring line, s the line length, h the water depth and φ the angle w.r.t the horizontal coordinate.

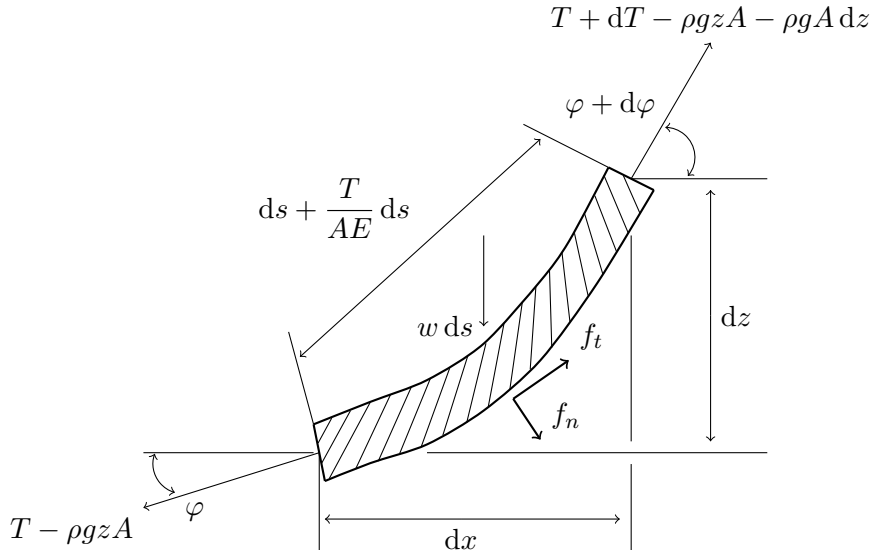


Figure 2.8: Forces on a mooring element, adapted from Faltinsen (1990). Here, ρ denotes the fluid density, w the submerged weight per unit length, A the cross-sectional area of the line, and E is the elastic (Young's) modulus. The forces f_t and f_n are mean hydrodynamic forces per unit length in tangential and normal direction, respectively.

down point. The location of this point changes with time as does the origin of the coordinate system.

The catenary equations for static moorings are derived based on the sketch shown in Figure 2.8. This figure shows a mooring line element with forces, angles, length and deformation definitions. The forces f_n and f_t are mean hydrodynamic forces per unit length in the normal and tangential direction of the mooring element, respectively. The density of the surrounding fluid (water) is given by ρ . w is the submerged weight per unit length, $A = D^2 \cdot \pi/4$ the cross-sectional area of the line with a diameter of D , T the tension in the mooring line with T_H being its horizontal component, and E the elastic (Young's) modulus. The buoyancy forces $-\rho g z A$ and $-\rho g z A - \rho g A$ arise owing to the submerged weight w .

Based on Figure 2.8, the equilibrium of forces is given by (Faltinsen, 1990):

$$dT - \rho g A z = \left[w \sin(\varphi) - f_t \left(1 + \frac{T}{AE} \right) \right] ds \quad (2.112)$$

$$T d\varphi - \rho g z A d\varphi = \left[w \cos(\varphi) - f_n \left(1 + \frac{T}{AE} \right) \right] ds . \quad (2.113)$$

These equations are non-linear and do not provide an explicit solution.

2.6.1 Inelastic equations

A simplification of the equations is adequate in many cases. The hydrodynamic forces f_t and f_n may be neglected for a static mooring line as well as the effect of elasticity. In addition, the submerged weight w is assumed constant along the line. This is not correct for real mooring lines consisting of different materials, e.g. metal chain and polymer rope. Yet, the material of the mooring lines used in the experiments and investigated in this thesis may be assumed homogeneous. Introducing $T' = T - \rho g z A$ yields:

$$dT' = w \sin(\varphi) ds \quad \text{and} \quad (2.114)$$

$$T' d\varphi = w \cos(\varphi) ds . \quad (2.115)$$

Division of these two equations reads:

$$\frac{dT'}{T'} = \frac{\sin(\varphi)}{\cos(\varphi)} d\varphi . \quad (2.116)$$

By integration, this equation becomes:

$$T' = T'_0 \frac{\cos(\varphi_0)}{\cos(\varphi)} . \quad (2.117)$$

φ_0 is defined as the angle at the touch down point of the mooring line and T_0 the corresponding mooring line tension, see Figure 2.7. Integration of Equation (2.115) results in:

$$s - s_0 = \frac{1}{w} \int_{\varphi_0}^{\varphi} \frac{T'_0}{\cos(\theta)} \frac{\cos(\varphi_0)}{\cos(\theta)} d\theta = \frac{T'_0 \cos(\varphi_0)}{w} [\tan(\varphi) - \tan(\varphi_0)] . \quad (2.118)$$

Here, θ is a general angular integration variable. With the relation $dx = \cos(\varphi) ds$, this equation may be rewritten to:

$$x - x_0 = \frac{1}{w} \int_{\varphi_0}^{\varphi} \frac{T'_0 \cos(\varphi_0)}{\cos(\theta)} d\theta = \frac{T'_0 \cos(\varphi_0)}{w} \left[\ln \left(\frac{1}{\cos(\varphi)} + \tan(\varphi) \right) - \ln \left(\frac{1}{\cos(\varphi_0)} + \tan(\varphi_0) \right) \right]. \quad (2.119)$$

In vertical direction, the relations $dz = \sin(\varphi) ds$ yields:

$$\begin{aligned} z - z_0 &= \frac{1}{w} \int_{\varphi_0}^{\varphi} \frac{T'_0 \cos(\varphi_0) \sin(\theta)}{\cos^2(\theta)} d\theta \\ &= \frac{T'_0 \cos(\varphi_0)}{w} \left[\frac{1}{\cos(\varphi)} - \frac{1}{\cos(\varphi_0)} \right]. \end{aligned} \quad (2.120)$$

In case of an angle at touch down point of $\varphi_0 = 0$, Equation (2.117) becomes:

$$T'_0 = T' \cos(\varphi). \quad (2.121)$$

The relation at the water plane for the horizontal component of the tension may be written as:

$$T_H = T \cos(\varphi_w). \quad (2.122)$$

If elasticity of the mooring lines is neglected, the Equations (2.121) and (2.122) under consideration of the definition $T' = T - \rho g z A$ yield the expression: $T'_0 = T_H$. The initial conditions are given with $x_0 = 0$, $z_0 = -h$ and $s_0 = 0$. Including Equation (2.119) into (2.118) and (2.120) eliminates the angle φ in these expressions with the use of sinh and cosh. Then, the resulting equations read:

$$s = \frac{T_H}{w} \sinh \left(\frac{w}{T_H} x \right) \quad \text{and} \quad (2.123)$$

$$z + h = \frac{T_H}{w} \left[\cosh \left(\frac{w}{T_H} x \right) - 1 \right]. \quad (2.124)$$

The mooring line tension T is found by combining the expression $T' = T - \rho g z A$ with the equations (2.120) and (2.121) (Faltinsen, 1990):

$$T = T_H + wh + (w + \rho g A)z. \quad (2.125)$$

The vertical component of the tension T_Z may be found by:

$$\begin{aligned} dT'_Z &= d(T' \sin(\varphi)) = dT' \sin(\varphi) + T' \cos(\varphi) d\varphi \\ &= w \sin^2(\varphi) ds + w \cos^2(\varphi) ds. \end{aligned}$$

This expression means $T'_Z = ws$, i.e. at the water plane:

$$T_Z = ws. \quad (2.126)$$

The location of the touch down point of the catenary mooring line is an important component for the tension in the line. In Figure 2.9, the length between fairlead

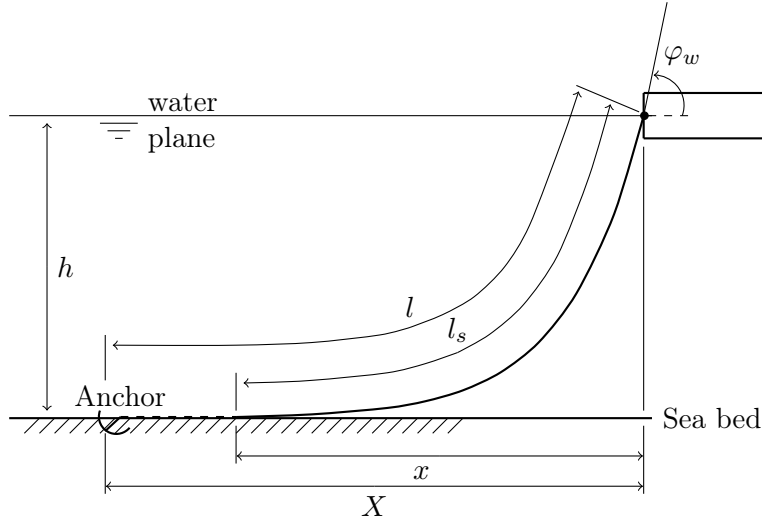


Figure 2.9: Definitions for a single moored vessel, adopted from Faltinsen (1990).

and touch down point is denoted with l_s and horizontally with x , the total line length between anchor and fairlead with l and horizontal distance with X .

The length l_s is given by:

$$l_s = C_a \sinh \left(\frac{x}{C_a} \right) \quad \text{with} \quad C_a = \frac{T_H}{w} . \quad (2.127)$$

This equation is equal to Equation (2.123). For $z = 0$, Equation (2.124) reads:

$$h = C_a \left[\cosh \left(\frac{x}{C_a} \right) - 1 \right] . \quad (2.128)$$

The total horizontal distance between anchor and fairlead follows from (Faltinsen, 1990):

$$X = l - h \left(1 + 2 \frac{C_a}{h} \right)^{\frac{1}{2}} + C_a \cosh^{-1} \left(1 + \frac{h}{C_a} \right) \quad \text{with} \quad C_a = \frac{T_H}{w} . \quad (2.129)$$

This procedure results in the solution for one mooring line. In general, floating structures are held in place by a spread mooring system. The studied semi-submersible floater was moored by three mooring lines with an angle of 120° between each. Hence, the mooring forces are not in-line with the overall Cartesian coordinate system. The forces need to be transferred from the mooring line coordinate system, which is 2D, into the surrounding 3D coordinate system to calculate the mooring line forces in horizontal and vertical direction at the fairleads. Therefore, the mooring tension forces of each line are multiplied with the angle and summed over the whole system to obtain the total mooring forces.

2.6.2 Elastic equations

In extreme conditions, such as the maximal displacements in a decay test, elasticity in the mooring line has to be considered to obtain a realistic model of the mooring

system. The equations (2.114) and (2.115) are still valid, since current forces are neglected. As $\varphi_0 = 0$ and $s_0 = 0$, Equation (2.121) holds and s follows from:

$$s = \frac{T'_0}{w} \tan(\varphi) . \quad (2.130)$$

A relationship between stretched, $d\xi$, and unstretched, ds , length of a line element is needed to calculate the horizontal and vertical coordinates. An approximation for this relationship is given by (Faltinsen, 1990):

$$d\xi = ds \left(1 + \frac{T}{AE} \right) . \quad (2.131)$$

The coordinates follow from:

$$\frac{dx}{ds} = \cos(\varphi) \left(1 + \frac{T}{AE} \right) \approx \cos(\varphi) \left(1 + \frac{T'}{AE} \right) = \cos(\varphi) + \frac{T'_0}{AE} \quad (2.132)$$

$$\frac{dz}{ds} = \sin(\varphi) \left(1 + \frac{T}{AE} \right) \approx \sin(\varphi) \left(1 + \frac{T'}{AE} \right) = \sin(\varphi) + \frac{w}{AE} s . \quad (2.133)$$

These approximations may be integrated until the fairlead. For simplification, the fairlead is assumed to be at $z = 0$. Integration of these equations yields:

$$h = \frac{T_H}{w} \left[\frac{1}{\cos(\varphi_w)} - 1 \right] + \frac{1}{2} \frac{w}{AE} l_s^2 \quad (2.134)$$

$$x = \frac{T_H}{w} \ln \left(\frac{\sqrt{(T_H^2 + T_Z^2)} + T_Z}{T_H} \right) + \frac{T_H}{AE} l_s . \quad (2.135)$$

The vertical tension T_Z may still be obtained by Equation (2.126), i.e. the unstretched length is $l_s = T_Z/w$. From these equations, the horizontal tension follows as:

$$T_H = \frac{T_Z^2 - \left(wh - \frac{1}{2} \frac{w^2}{AE} l_s^2 \right)^2}{2 \left(wh - \frac{1}{2} \frac{w^2}{AE} l_s^2 \right)} \quad \text{because} \quad \cos(\varphi_w) = \frac{T_H}{\sqrt{T_H^2 + T_Z^2}} . \quad (2.136)$$

The tension at the fairlead is simply a result of the Pythagorean theorem: $T = \sqrt{T_H^2 + T_Z^2}$. Then, the equations (2.134) - (2.136) may be adopted to obtain results for the elastic catenary equations. In offshore applications, the fairlead can be above or below the water plane. In the first case, the line segments above the water plane are solved with a different model neglecting the buoyancy of the line. Consequently, the input of the catenary mooring model requires the submerged weight w and dry mass m of the line. In the latter case, the hydrostatic correction forces cannot be neglected from the solution at the fairlead.

These elastic catenary equations were taken for the initial shape and loads of the mooring lines when coupled to the CFD solver. For the quasi-static approach, this system of equations is recalculated at each time step. More details on the different mooring models and its coupling with the CFD solver are given in Section 3.4.

3. Numerical Methods

This chapter details the numerical methods used to perform all simulations of this thesis. At first, integration and approximation schemes, and solution algorithms are given. They are followed by specifics on rigid body motion solvers and mooring modelling. Errors and uncertainties occur in numerical simulations. Therefore, this chapter ends with a detailed description of verification and validation including three different error and uncertainty estimation approaches.

3.1 Discretisation Methods

There exists no general analytic solution to the conservation equations given in Section 2.2. Therefore, the equations need to be approximated and discretised. In ReFRESCO, discretisation methods are based on a cell-centred, collocated arranged face-based Finite Volume Method (FVM). The FVM uses the integral form of the conservation equations as a starting point. The computational domain is discretised in a finite number of control volumes (CVs), also called cells, and the conservation equations are applied to each of these CVs (Ferziger and Perić, 2002). The values of variables are calculated at the central node of each cell. A detail of a typical Cartesian 2D grid with notation is given in Figure 3.1. The central nodes of each CV are indicated with points. The volume and surface integrals are approximated, and the variable values interpolated to obtain their values on cell faces. In addition to spatial discretisation, also temporal discretisation is needed, i.e. the total simulation time is discretised in a finite number of time steps. This discretisation of partial differential equations together with linearisations, relaxation and deferred corrections, leads to an algebraic system of equations. Apart from the continuity equation, the process is similar for each transport equation. Hence, it is exemplified by using a general transport equation. Most assumptions and discretisation schemes presented here are valid mostly for a second order unstructured FVM.

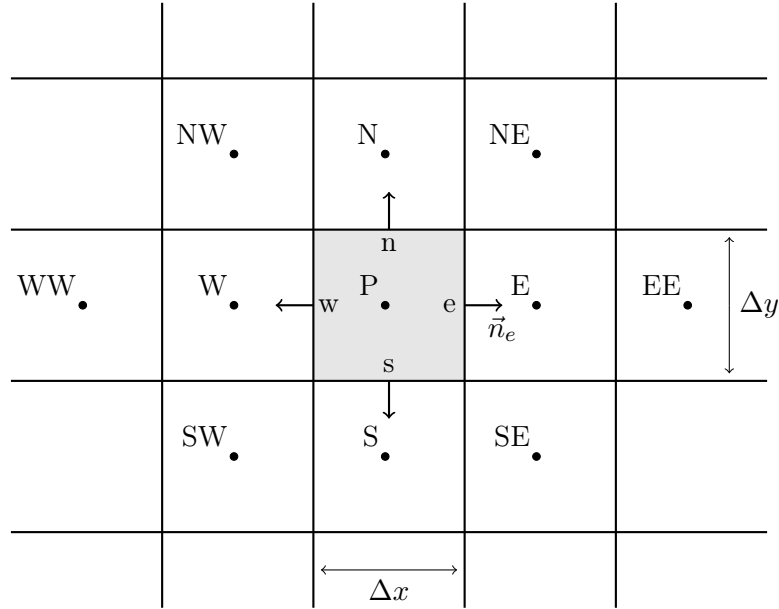


Figure 3.1: Detail of a 2D Cartesian grid with notation.

3.1.1 Approximation of surface and volume integrals

The finite volume method makes use of approximated volume and surface integrals for the convective and diffusive terms. The approximated integrals are given by:

$$\int_V \phi \, dV = \bar{\phi} \Delta V \approx \phi_c \Delta V \quad \text{and} \quad (3.1)$$

$$\int_S \phi \, dS \approx \sum_{i=1}^{N_f} \phi_{f_i} S_{f_i} . \quad (3.2)$$

ϕ expresses any of the terms defined in Equation (2.56), i.e. convection, diffusion or source term. The volume integral is replaced by the mean value $\bar{\phi}$ and the cell volume ΔV . Applying the midpoint rule allows to approximate the mean by the cell centre value ϕ_c of the integrand. This method is of 2nd order and piecewise constant.

The approximation of surface integrals requires summation over the faces of a cell using the face values ϕ_{f_i} times the face area S_{f_i} . In 2D, a cell in a Cartesian grid has $N_f = 4$ faces. These four faces are indicated with lower case letters around grid node P in Figure 3.1. For 3D grids with hexahedral cells, the number of faces expands to $N_f = 6$, if no hanging nodes are present.

Convection term: The convection term of the transport equations is a surface integral and follows the rule of Equation (3.2):

$$\oint_S (\rho \phi \vec{v} \cdot \vec{n}) \, dS \approx \sum_{i=1}^{N_f} (\vec{v}_{f_i} \cdot \vec{S}_{f_i}) \phi_{f_i} \rho_{f_i} . \quad (3.3)$$

Here, $\vec{S}_{f_i} = S_{f_i} \vec{n}_{f_i}$ denotes the surface area vector of a certain face i . In general, values at the centre of a control volume are known but values at the faces are unknown. Thus, the face values ϕ_{f_i} need to be interpolated based on the surrounding integration points. There are several interpolation methods available. In this context, these methods are called convection schemes and need to account for the parabolic behaviour of convection. Depending on their order of convergence, these methods can be categorised into linear, quadratic and higher-order accurate schemes. A few popular methods of these categories are upwind interpolation (first order), linear interpolation or central difference (second order), and quadratic upwind interpolation for convective kinematics (QUICK) scheme (third order for constant cell sizes). More details on schemes follow below. A higher-order scheme in combination with the second-order accurate midpoint-rule, however, results in second-order accuracy. Amongst all of the discretisation and interpolation schemes used, the lowest order method defines the convergence of the results with grid refinement.

Diffusion term: In the transport equations also the diffusion term is a surface integral and can be approximated in the following form:

$$\oint_S (\Gamma \nabla \phi) \cdot \vec{n} \, dS \approx \sum_{i=1}^{N_f} (\Gamma_{f_i} \nabla \phi_{f_i}) \cdot \vec{S}_{f_i} . \quad (3.4)$$

The challenge for discretisation of the diffusion term is the gradient of ϕ_{f_i} .

The gradients of cell centres are calculated using the Gauss-algorithm (Klaij and Vaz, 2017):

$$(\nabla \phi)_c \approx \frac{1}{\Delta V_c} \sum_{i=1}^{N_f} \vec{S}_{f_i} \phi_{f_i} . \quad (3.5)$$

ΔV_c is the cell volume. This means that gradients in cell centres require the face values of this quantity. These new face values are calculated based on an interpolation using cell centre values. The default scheme reads:

$$\phi_f = c_f \phi_{c_1} + (1 - c_f) \phi_{c_2} + \nabla \phi_f \vec{e} . \quad (3.6)$$

ϕ_{c_1} and ϕ_{c_2} represent the values of cell centres on each side of the cell face. The term $\nabla \phi_f \vec{e}$ is used for eccentricity correction with \vec{e} being the eccentricity vector. This vector may be found by orthogonal projection of the face centre location x_f on the straight line connecting the two adjacent cell centres. Then, the eccentricity vector reads:

$$\vec{e} = x_f - [c_f x_{c_1} + (1 - c_f) x_{c_2}] . \quad (3.7)$$

The gradient of the eccentricity term is taken from the previous iteration loop. The geometric interpolation factor c_f is defined as:

$$c_f = \frac{|x_{c_2} - x_f|}{|x_f - x_{c_1}| + |x_{c_2} - x_f|} . \quad (3.8)$$

Where, x_{c_i} denotes the location of the cell centre. This interpolation scheme may also be used to obtain gradients at faces (Klaij and Vaz, 2017):

$$(\nabla\phi)_f = c_f (\nabla\phi)_{c_1} + (1 - c_f) (\nabla\phi)_{c_2} . \quad (3.9)$$

3.1.2 Convection discretisation schemes

A few convection discretisation schemes are detailed here. These schemes are upwind interpolation, central difference approximation (linear interpolation) and QUICK. In this work, the upwind interpolation scheme was used as part of the hybrid scheme for the turbulence model transport equations and QUICK together with a limiter for the momentum equations.

Upwind interpolation: This scheme approximates face values by the nodal value upstream of the target face ϕ_{c_U} . Thus, for the target face and a structured grid ϕ_f holds:

$$\phi_f = \phi_{c_U} . \quad (3.10)$$

For the notation given in Figure 3.1 ϕ_e may be obtained by ϕ_P for a flow from left to right or by ϕ_E for a flow from right to left. This scheme is a first-order scheme.

Linear interpolation: For a Cartesian grid, linear interpolation between the two nearest nodes ϕ_{c_1} and ϕ_{c_2} yields:

$$\phi_f = \phi_{c_1} c_f + \phi_{c_2} (1 - c_f) \quad \text{with} \quad c_f = \frac{x_f - x_{c_2}}{x_{c_1} - x_{c_2}} . \quad (3.11)$$

As for the determination of face values for the diffusive term, c_f is interpolated based on the locations of the nodes and the cell face centre. This scheme is second-order accurate, but might produce oscillatory solutions. As this scheme corresponds to central difference approximation for finite difference methods, it is often named central difference scheme.

Hybrid scheme: In this thesis, the linear interpolation and upwind scheme were used as part of a hybrid scheme (Klaij and Vaz, 2017). This scheme blends between central differencing and first-order upwind using β :

$$\phi_f = (1 - \beta)\phi_{c_U} + \beta c_f \phi_{c_1} + \beta(1 - c_f) \phi_{c_2} + \beta \nabla \phi_f \vec{e} \quad \text{with} \quad 0 \leq \beta \leq 1 . \quad (3.12)$$

For $\beta = 0$, this scheme corresponds to the upwind interpolation scheme which was used for the convection terms of the turbulence model transport equations. This scheme is first order accurate and includes an additional term for eccentricity correction.

QUICK: The improvement of this scheme is to use a parabola instead of a straight line. Therefore, data from an additional point is required upstream of the target cell face. For a flow from left to right, the additional point is WW in Figure 3.1. The face value for a structured grid becomes:

$$\phi_f = \phi_{c_U} + c_{f1}(\phi_{c_D} - \phi_{c_U}) + c_{f2}(\phi_{c_U} - \phi_{c_{UU}}) . \quad (3.13)$$

Subscript c_U denotes the first nodal value upstream, c_{UU} the second upstream, and c_D the first downstream. The interpolation factors c_{f1} and c_{f2} are a function of the nodal and target cell face coordinates (Ferziger and Perić, 2002):

$$c_{f1} = \frac{(x_f - x_U)(x_f - x_{UU})}{(x_D - x_U)(x_D - x_{UU})} \quad \text{and} \quad c_{f2} = \frac{(x_f - x_U)(x_D - x_f)}{(x_U - x_{UU})(x_D - x_{UU})} . \quad (3.14)$$

In the solver, this scheme also accounts for unstructured grids and eccentricity, and is used together with a limiter. This limited QUICK scheme was applied to the momentum equations. The interested reader is referred to Klaij and Vaz (2017).

3.1.3 Total Variation Diminishing

These schemes are very commonly used for the interpolation of face values. The QUICK scheme was used as part of the Total Variation Diminishing (TVD) family. The idea of TVD is to reduce the total variation of the quantity ϕ defined by:

$$\text{TV}(\phi^n) = \sum_k |\phi_k^n - \phi_{k-1}^n| . \quad (3.15)$$

k denotes a grid point index. The reduction is obtained by limiting the flux of the quantity through the CV faces. The benefit of TVD schemes is its monotonicity, i.e. the solution is monotonic also for shocks, free surfaces or any other discontinuities. TVD schemes, however, reduce the order of approximation at discontinuities to yield monotonic solutions. More details on TVD may be found in Ferziger and Perić (2002).

3.1.4 Interface capturing schemes

Capturing the interface between two phases requires the usage of special schemes. Interface capturing schemes approximate the face values in the convection term of the volume fraction equation. These methods consist typically of three components (Klaij et al., 2018): a compressive scheme used in orthogonal direction to the interface, a high-resolution scheme for the other directions, and a blending function between both schemes. ReFRESCO's interface capturing scheme (Refrics) was applied for all simulations unless explicitly stated otherwise. This scheme is also part of the TVD class. For a uniform Cartesian grid as presented in Figure 3.1, face values may be obtained with (Klaij et al., 2018):

$$\phi_f = \phi_C + \frac{1}{2}\psi(r)(\phi_C - \phi_U) \quad \text{with} \quad r = \frac{\phi_D - \phi_C}{\phi_C - \phi_U} . \quad (3.16)$$

ϕ_C denotes the value of ϕ at node C. The corresponding U and D subscripts denote nodal values up- and downstream of C, respectively. The limiter function $\psi(r)$ reads:

$$\psi(r) = \frac{r + |r|}{1 + |r|}. \quad (3.17)$$

The smoothness of ψ enhances the convergence rate. This high-resolution scheme may be combined with the downwind scheme for sharpening:

$$\psi(r) = \max [0, \min (2r, 2)]. \quad (3.18)$$

This scheme is piece-wise linear. The blending function to combine both schemes depends on the direction normal to the interface. The normal direction is obtained by the gradient of the volume fraction c :

$$\vec{n}_I = \begin{cases} \frac{\nabla c}{\|\nabla c\|} & \text{if } \nabla c \neq 0 \\ \vec{0} & \text{else.} \end{cases} \quad (3.19)$$

The normal vector \vec{n} is defined at cell centres. It is a unit vector for $\nabla c \neq 0$. Then, the interface normal (not the face normal) between current cell C and downstream cell D may be obtained by geometric interpolation, see Figure 3.2.

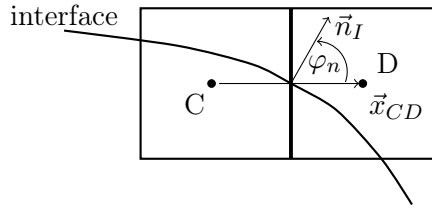


Figure 3.2: Grid cells at interface with notation, adapted from Klaij et al. (2018).

The angle φ_n between the interface normal \vec{n}_I and the vector connecting the two cell centres $\vec{x}_{CD} = \vec{x}_D - \vec{x}_C$ is given by:

$$\varphi_n = \arccos \left(\frac{\vec{n}_I \cdot \vec{x}_{CD}}{\|\vec{x}_{CD}\|} \right). \quad (3.20)$$

Then, the face value of quantity ϕ becomes (Klaij et al., 2018):

$$\phi_f = \beta \phi_{f_{compress}} + (1 - \beta) \phi_{f_{highres}} \quad \text{with} \quad \beta = \frac{\cos(2\varphi_n) + 1}{2}. \quad (3.21)$$

β is a factor that blends between the solution of the compressive $\phi_{f_{compress}}$ and high-resolution $\phi_{f_{highres}}$ schemes. For alignment of \vec{n}_I with \vec{x}_{CD} , β becomes one as $\varphi_n = 0$ and the compressive scheme is used. If the two vectors are perpendicular, i.e. $\varphi_n = \frac{\pi}{2}$, β is zero and the high-resolution scheme is used. ∇c becomes zero away from the interface and the method applies the high-resolution scheme as $\varphi_n = \frac{\pi}{2}$.

In Appendix C, a comparison of results for wave loads on a vertical cylinder applying different interface capturing schemes may be found. The other schemes are QUICK, High Resolution Interface Capturing (HRIC) by Muzaferija et al. (1999), and SuperBee by Roe (1985).

3.1.5 Temporal discretisation

In unsteady simulations, the transient/unsteady term in Equation (2.54) cannot be disregarded. Then, the equations become time dependent and need to be discretised in time. The unsteady numerical simulations of incompressible flows conducted in this thesis are elliptic in space and parabolic in time. The flow characteristics at a specific location in space influence the flow at other locations, but the current state just affects the future and has no impact on the past. Thus, the flow solution depends temporally only on the initialisation and boundary conditions. The time coordinate is treated linearly and can be divided into a finite number of time steps Δt . The time integration assumes the knowledge of the current state t_n of a quantity ϕ^n and aims to obtain the value of ϕ^{n+1} at the next time step t_{n+1} . Therefore, a number of schemes are available. They can be classified into explicit and implicit schemes as well as by their order of accuracy. Explicit schemes depend on previous time steps: $\phi^{n+1} = f(\phi^n, \phi^{n-1}, \phi^{n-2}, \dots)$, and implicit ones also on the following time step: $\phi^{n+1} = f(\phi^{n+1}, \phi^n, \phi^{n-1}, \dots)$. Introducing the one-dimensional Courant number (Courant-Friedrichs-Lowy) CFL:

$$\text{CFL} = \frac{u\Delta t}{\Delta x}, \quad (3.22)$$

delivers a stability criterion for time integration methods. Here, u denotes a one-dimensional velocity scalar and Δx the cell size in the corresponding direction. Explicit methods are stable for $\text{CFL} < 1$, while implicit methods are also stable for larger CFL numbers.

In the code used for this thesis, the implicit or backward Euler method:

$$\phi^{n+1} = \phi^n + f(t_{n+1}, \phi^{n+1})\Delta t \quad (3.23)$$

and the second-order backward scheme:

$$\phi^{n+1} = \frac{3}{4}\phi^n - \frac{1}{3}\phi^{n-1} + \frac{2}{3}f(t_{n+1}, \phi^{n+1})\Delta t \quad (3.24)$$

are available. For the cases investigated, the second-order backward scheme was applied for time integration. Nevertheless, the first order scheme is required for the first time step as no previous solution exist. Using a hybrid formulation of both schemes to discretise the unsteady term yields:

$$\frac{\partial}{\partial t} \int_V \rho\phi \, dV \approx \frac{c_1 (\rho_c \phi_c \Delta V)^{n+1} + c_2 (\rho_c \phi_c \Delta V)^n + c_3 (\rho_c \phi_c \Delta V)^{n-1}}{\Delta t}. \quad (3.25)$$

For the second-order backward scheme, also called three time level method, the coefficients are (Klaaij and Vaz, 2017): $c_1 = 1.5$, $c_2 = -2.0$, and $c_3 = 0.5$. They become $c_1 = 1.0$, $c_2 = -1.0$, and $c_3 = 0$ for the first order backward Euler scheme. The second-order backward scheme is a second-order accurate method and unconditionally stable. For the volume fraction transport equation, this scheme requires $\text{CFL} < \frac{1}{6}$ around the free surface for the convection scheme used to be TVD (Klaaij et al., 2018). This is more restrictive than for other schemes, e.g. the Crank-Nicolson scheme is unconditionally stable and already TVD for $\text{CFL} < \frac{2}{3}$. In case this Courant number requirement is not met, mass conservation might be affected, and thus, first order time integration schemes are used instead.

3.1.6 Algebraic system of equations

Summation of all flux approximations and source terms yields an algebraic equation that relates values of one control volume to values of the neighbouring CVs:

$$A_C \phi_C + \sum_{l=1} A_l \phi_l = Q_C . \quad (3.26)$$

C denotes the current grid cell, at which the partial differential equation is approximated. l is an index for the neighbour CVs. A_l are coefficients that depend on geometrical quantities, fluid properties, and variable values if the equations are non-linear (Ferziger and Perić, 2002). The terms with known variable values are stored in Q_C . This equation leads to an algebraic system in the form:

$$\mathbf{A} \vec{\phi} = \vec{q} \quad (3.27)$$

for the whole solution domain. \vec{q} contains all terms with known variables. \mathbf{A} is a square and sparse coefficient matrix, and $\vec{\phi}$ is a vector containing variable values at the cell nodes, e.g. velocities or pressures. The number of non-zero elements in each row of \mathbf{A} depends on the number of near neighbour cell values used for the approximation schemes. This matrix system of equations is closed by boundary conditions.

Matrices can be solved with many different methods. These methods are categorised in direct and iterative schemes. If the algebraic equation is non-linear, iterative methods must be used that involve an initial guess of the solution, linearisation of the equations for this solution, and improving the solution. This iterative process is repeated until convergence of the solution (Ferziger and Perić, 2002). Errors owing to the discretisation are expected to be larger than due to the iterative method. Besides, iterative methods are cheaper than direct schemes. This might change, however, if too many iterations are needed to solve the equations or if memory becomes cheaper. Nevertheless, iterative methods were used for the solution of the matrices. For iterative methods, Equation (3.27) becomes:

$$\mathbf{A} \vec{\phi}^m = \vec{q} - \vec{r}^m . \quad (3.28)$$

m denotes the number of iterations. Thus, a residual \vec{r} remains and introduces an error. This residual is minimised in an iterative process.

3.1.7 Boundary conditions

The procedure above yields a system of algebraic equations for each CV inside the computational domain. At the borders of the domain, boundary conditions are required to solve the equations. They can be divided in Dirichlet and Neumann boundary conditions or a combination of both named after Robin. The Dirichlet condition defines a value and the Neumann condition a gradient at the boundary faces. Physically, boundary conditions used in this thesis can be categorised as follows.

Inflow boundary condition: At the inlet or inflow boundary condition (*BCInflow*), all variables are prescribed either by constant values or by a user routine. These values are velocities \vec{v} , volume fraction c , and turbulent quantities such as k , ω , ϵ , and μ_t . This is defined as a Dirichlet condition. The pressure is extrapolated from the interior (Klaij and Vaz, 2017).

Outflow boundary condition: Cell centre values of the boundary cells at the outlet or outflow boundary condition (*BCOutflow*) substitute values at the boundary faces. This means that the values are obtained by zeroth order extrapolation. The variables to be extrapolated are pressure p , velocity \vec{v} , volume fraction c , turbulent kinetic energy k , eddy viscosity μ_t as well as ϵ and ω .

Pressure boundary condition: Pressure is prescribed as a constant or varying value for the complete pressure boundary (*BCPressure*). Velocities and other quantities are extrapolated from the interior as in the outflow boundary condition. Accordingly, many users term this boundary condition “Pressure outflow boundary condition”.

Wall boundary condition: At a wall boundary condition (*BCWall*), the velocity of the fluid is equal to the velocity of the wall (no-slip). The pressure follows from a Neumann condition. Except for the turbulent quantities ϵ and ω , Neumann conditions are used for all other variables: $\nabla\phi \cdot \vec{n} = 0$. A Neumann condition for ϵ and ω would yield unrealistic values, i.e. under determined and infinity. Therefore, these values follow from neighbouring cell centres of the boundary faces. For a slip-wall condition just the normal component of the velocity is given as equal to the wall velocity.

Symmetry boundary condition: The symmetry boundary condition (*BCSymmetry*) is in principle a slip wall boundary condition. The convective fluxes of all quantities are zero. The normal gradient of the velocity component tangential to the symmetry boundary is also zero. The turbulent quantities and volume fraction are extrapolated from interior cells.

Wave boundary condition: The wave boundary condition (*BCWave*) is an inlet/outlet boundary condition meant for wave generation and absorption. The velocity components and the volume fraction based on regular wave theories may be prescribed and wave reflection reduced owing to a Sommerfeld operator. Every boundary face at the inflow is assigned as follows (Vaz et al., 2009):

- Above the wave elevation, zero velocities are prescribed at the cell centres (apart from current, grid or boundary velocities) and every cell is full of air. Consequentially, every cell centre receives an air volume fraction of: $c = 1$.
- Below the wave elevation, each cell centre is assigned with velocities according to the wave theory adopted (here the Stokes 5th order model). The cells are

full of water. Hence, the volume fraction is set to: $c = 0$. A velocity according to a predefined current, or due to grid and boundary motions may be added.

Figure 3.3 illustrates this procedure on the domain boundary.

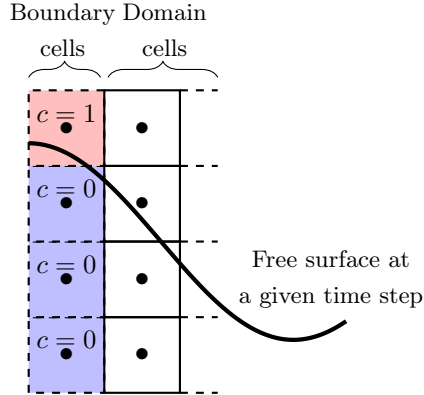


Figure 3.3: Sketch of the wave inflow boundary condition with grid, adapted from Vaz et al. (2009).

Details on regular water wave theories, on wave absorption, and on the non-reflecting boundary condition of Sommerfeld type is given in Section 2.4.

3.2 Solution of Navier-Stokes Equations

The methods presented in Section 3.1 may be applied for linear equations and lead to an algebraic equation system. The momentum equation, however, has a non-linear contribution in the convection term. For incompressible flows, there is no equation to compute the pressure field, and there is a strong coupling between pressure and velocity. This section deals with solution methods to these problems.

3.2.1 Linearisation of momentum equation

Problematic for the solution of the algebraic equations is the non-linear convection term of the momentum equation: $\rho \vec{v} \vec{v}$. This term is linearised using the Picard iteration approach. The mass flux is treated as known. Then, the non-linear convection term is approximated by:

$$(\rho \vec{v} \vec{v})^{m+1} \approx (\rho \vec{v})^m (\vec{v})^{m+1}. \quad (3.29)$$

The term $(\rho \vec{v})^m$ contains values of the previous m outer iteration. The current iteration is denoted with $m + 1$ in superscript. Similarly, the effective viscosity $\mu + \mu_t$ and the second contribution in the diffusion term are obtained from the previous iteration (Klaij and Vaz, 2017). Thus, this method replaces non-linear terms at $m + 1$ with corresponding terms at m until only linear terms are left. This procedure adds an additional iterative loop to the solution algorithm.

3.2.2 Pressure equation

The governing equations consisting of Equation (2.42) and (2.45) do not provide an independent equation for pressure. The momentum equation can be used to calculate velocities, but the continuity equation does not have a dominant variable in incompressible flows (Ferziger and Perić, 2002). Hence, a common approach is to combine the two equations and to take the divergence of the momentum equation:

$$\nabla \cdot \left(\frac{\partial}{\partial t} \rho \vec{v} + \nabla \cdot \{ \rho \vec{v} \vec{v} \} \right) = \nabla \cdot (-\nabla p + \nabla \cdot \boldsymbol{\tau} + \rho \vec{g}) . \quad (3.30)$$

The gradients of density and viscosity are assumed to be 'zero', i.e. $\nabla \mu = \nabla \rho = 0$. The divergence of the velocity vanishes $\nabla \cdot \vec{v} = 0$ (continuity equation for incompressible flows) and the equation becomes:

$$\nabla \cdot (\nabla \cdot \{ \rho \vec{v} \vec{v} \}) = \nabla \cdot (-\nabla p + \rho \vec{g}) . \quad (3.31)$$

Furthermore, the divergence of gravity is 'zero'. This leads to the Poisson equation for pressure in incompressible single-phase flows:

$$\Delta p = \nabla^2 p = \nabla \cdot (\nabla p) = -\nabla \cdot (\nabla \cdot \{ \rho \vec{v} \vec{v} \}) . \quad (3.32)$$

Δ is the Laplace operator. The pressure equation in Cartesian coordinates reads:

$$\frac{\partial}{\partial x_i} \left(\frac{\partial p}{\partial x_i} \right) = -\frac{\partial}{\partial x_i} \left(\frac{\partial(\rho u_i u_j)}{\partial x_j} \right) . \quad (3.33)$$

The discretisation of the Poisson equation has a couple of constraints to ensure mass conservation. The Laplace operator consist of a gradient and a divergence. The gradient results from the momentum and the divergence from the continuity equation. Consequently, the gradient needs to be discretised as in the momentum (Navier-Stokes) equation and the divergence as in the continuity equation. This is ensured by first discretising the momentum and continuity equation, and then, deriving the Poisson equation for pressure using these discretised forms. This adds another iterative loop.

3.2.3 Pressure velocity coupling

The variables of all scalars and the velocity are stored in a collocated arrangement at cell centroids. Then, in case of central differencing schemes being used for the momentum and pressure equations, spurious pressure oscillations may be visible in a so-called *checkerboard* pattern (Ferziger and Perić, 2002, Moukalled et al., 2016). Hence, the pressure weighted interpolation (PWI) method is used. This method was first introduced by Rhie and Chow (1983) and implemented for semi-implicit pressure linked algorithms by Miller and Schmidt (1988). In the PWI method, a pressure term is added to modify the interpolation of velocities at cell faces in the pressure correction equation. In principle, this method is a pseudo momentum equation that mimics the small pressure velocity coupling on staggered grids (Moukalled et al., 2016), where velocities are stored on cell faces. This new velocity

is used in the discretised continuity and momentum equations. More details on the implemented PWI methods may be found in Klaij and Vuik (2013).

The pressure velocity coupling may be done with several different algorithms. The coupling procedure used throughout this work is the Semi-Implicit Method for Pressure Linked Equations (SIMPLE) (see e.g. Klaij and Vuik (2013)). For the segregated solver of the pressure-velocity system, the SIMPLE algorithm uses a pressure-correction equation. Applying the PWI and Picard linearisation, the NS equation system has the form:

$$\begin{bmatrix} Q_1 & 0 & 0 & G_1 \\ 0 & Q_2 & 0 & G_2 \\ 0 & 0 & Q_3 & G_3 \\ D_1 & D_2 & D_3 & C \end{bmatrix} \begin{bmatrix} u_1 \\ u_2 \\ u_3 \\ p \end{bmatrix} = \begin{bmatrix} f_1 \\ f_2 \\ f_3 \\ g \end{bmatrix} \quad (3.34)$$

This system of equations can be written in the form of Equation (3.27) $\mathbf{A}\vec{\phi} = \vec{q}$:

$$\begin{bmatrix} \mathbf{Q} & \mathbf{G} \\ \mathbf{D} & \mathbf{C} \end{bmatrix} \begin{bmatrix} \vec{v} \\ p \end{bmatrix} = \begin{bmatrix} \vec{f} \\ g \end{bmatrix} . \quad (3.35)$$

\mathbf{Q} denotes the advection-diffusion, \mathbf{G} the gradient, \mathbf{D} the divergence and \mathbf{C} the stabilisation matrix originating from the PWI method (Klaij and Vaz, 2017). Thus, \mathbf{A} reads:

$$\mathbf{A} = \begin{bmatrix} \mathbf{Q} & \mathbf{G} \\ \mathbf{D} & \mathbf{C} \end{bmatrix} . \quad (3.36)$$

Derivation of SIMPLE: The velocity vector \vec{v} and the pressure p are assumed to be known at iteration m . Then, the prediction \vec{v}^* and the corrections \vec{v}' and p' may be defined as:

$$\vec{v}^{m+1} = \vec{v}^* + \vec{v}' \quad p^{m+1} = p^m + p' . \quad (3.37)$$

The velocity prediction \vec{v}^* does not satisfy the continuity equation, and is obtained by solving the momentum equation. The velocity prediction is obtained by solving:

$$\mathbf{Q}\vec{v}^* = \vec{f} - \mathbf{G}p^m . \quad (3.38)$$

This equation uses the pressure of the previous iteration m . For the current iteration, this equation becomes:

$$\mathbf{Q}\vec{v}^{m+1} = \vec{f} - \mathbf{G}p^{m+1} . \quad (3.39)$$

In addition, the mass equation must be satisfied:

$$\mathbf{D}\vec{v}^{m+1} + Cp^{m+1} = g . \quad (3.40)$$

The velocity correction equation follows from the subtraction of Equation (3.38) from (3.39) and multiplication of \mathbf{Q}^{-1} :

$$\vec{v}' = -\mathbf{Q}^{-1}\mathbf{G}p' . \quad (3.41)$$

Combining Equations (3.37) and (3.40) leads to the expression for the pressure correction (Klaij and Vuik, 2013):

$$(\mathbf{C} - \mathbf{D}\mathbf{Q}^{-1}\mathbf{G})p' = \vec{g} - \mathbf{D}\vec{v}^* - \mathbf{C}p^m . \quad (3.42)$$

On the left-hand side of this equation, the *Schur complement* of \mathbf{Q} in \mathbf{A} arises, i.e. $\mathbf{C} - \mathbf{D}\mathbf{Q}^{-1}\mathbf{G}$. The term \mathbf{Q}^{-1} is not available and not easily computed. Therefore, in SIMPLE an approximation of the following form is used:

$$\mathbf{Q}^{-1} \approx \text{diag}(\mathbf{Q})^{-1} . \quad (3.43)$$

Thus, \mathbf{Q}^{-1} is approximated by the inverse of the diagonal entries of \mathbf{Q} . Equation (3.38) is the standard SIMPLE type form. Here, the velocity correction form is applied instead (Klaij and Vuik, 2013):

$$\mathbf{Q}\vec{v} = \vec{r}_u^m . \quad (3.44)$$

These forms are equivalent, if the velocity residual \vec{r}_u equals zero as initial condition. The residual of the momentum equation is defined as: $\vec{r}_u^m = \vec{f} - \mathbf{Q}\vec{v}^m - \mathbf{G}p^m$. The relation of the correction equation is:

$$\vec{v}^* = \vec{v}^m + \vec{\tilde{v}} . \quad (3.45)$$

Then, as a final step the results for $\vec{\phi}$ are relaxed to improve convergence. The relaxation procedure for all quantities in $\vec{\phi}$ reads:

$$\vec{\phi}^{m+1} = \vec{\phi}^m + \boldsymbol{\varrho}\tilde{\mathbf{A}}^{-1}(\vec{q} - \mathbf{A}\vec{\phi}^m) . \quad (3.46)$$

$\tilde{\mathbf{A}}$ is an approximation of \mathbf{A} . The last term $\vec{q} - \mathbf{A}\vec{\phi}^m$ denotes the residuals \vec{r} . The relaxation matrix $\boldsymbol{\varrho}$ consists of velocity ϱ_u and pressure ϱ_p relaxation parameters:

$$\boldsymbol{\varrho} = \begin{bmatrix} \varrho_u \mathbf{I} & 0 \\ 0 & \varrho_p \mathbf{I} \end{bmatrix} .$$

\mathbf{I} denotes the unity matrix. Small values for the components of $\boldsymbol{\varrho}$ help to improve the robustness of a numerical simulation, but they also slow down the convergence. The resulting order to solve the pressure-velocity coupling reads (Klaij and Vuik, 2013, Klaij and Vaz, 2017):

1. Solve Equations (3.44) and (3.45) to obtain the velocity prediction \vec{v}^* based on values of previous iteration
2. Use the velocity prediction to obtain the pressure correction p' from Equation (3.42)
3. Compute the velocity correction \vec{v}' by using Equation (3.41)
4. Update the pressure and velocity with $p^{m+1} = p^m + \varrho_p * p'$ and $\vec{v}^{m+1} = \vec{v}^m + \varrho_v * \vec{v}'$

In addition to the shown explicit relaxation procedure, implicit relaxation may be applied. Implicit relaxation is independent on the explicit relaxation and is done to increase the diagonal dominance of the linear system shown in Equation (3.39) (Klaaij and Vuik, 2013):

$$\left(\mathbf{Q} + \frac{1 - \varrho_I}{\varrho_I} \text{diag}(\mathbf{Q}) \right) \vec{v}^{m+1} = \vec{f} + \left(\frac{1 - \varrho_I}{\varrho_I} \text{diag}(\mathbf{Q}) \right) \vec{v}^m - \mathbf{G} p^{m+1}. \quad (3.47)$$

ϱ_I is the implicit relaxation parameter. Implicit relaxation is an optional setting, but simplifies the solution procedure, and the residuals are not affected. Implicit relaxation updates the coefficient matrices to \mathbf{Q}_{ϱ_I} and \vec{f}_{ϱ_I} . Where, \vec{f}_{ϱ_I} reads:

$$\vec{f}_{\varrho_I} = \vec{f} + \left(\frac{1 - \varrho_I}{\varrho_I} \text{diag}(\mathbf{Q}) \right) \vec{v}^m. \quad (3.48)$$

The residual, however, stays:

$$\vec{r}_u^m = \vec{f} - \mathbf{Q} \vec{v}^m - \mathbf{G} p^m = \vec{f}_{\varrho_I} - \mathbf{Q}_{\varrho_I} \vec{v}^m - \mathbf{G} p^m.$$

Once this algorithm converges, i.e. the residual drops below a certain convergence criteria, the solver moves on to another iteration loop.

3.2.4 Solution algorithm

For unsteady simulations, the solution algorithm consists of three loops: time step, outer and inner iteration loops. The algorithm is detailed in Table 3.1. Each transport equation is solved segregated in an inner loop to compute the linear equations system until convergence is reached. Pressure and velocity are coupled using SIMPLE on outer loop level. Then, the quantities of the transport equations are relaxed as shown in Equation (3.46). The pressure and the velocity field obtained from the SIMPLE algorithm are used to compute the other transport equations. At last, the complete system is checked for convergence by a predefined residual level.

3.2.5 Iterative convergence

The residual, introduced in Equation (3.28), is a vector with values for each velocity component, for the pressure, and for all other equations solved in the iterative solution algorithm, e.g. volume fraction and turbulence quantities (turbulent kinetic energy and second variable if applicable). The residual is a measure of the imbalance of the algebraic equation. Usually, these residuals are presented in normalised form. In this thesis, the normalisation procedure is used as follows for any iteration m :

$$r_{n_{i,j}} = \frac{r_{res_{i,j}}}{A_{C_{i,j}} \phi_{ref_j}}. \quad (3.49)$$

The raw residual of quantity j per cell i is normalised by the diagonal component of \mathbf{A} , A_C , and the reference value ϕ_{ref} given. Thus, there are residuals for each control volume in the domain. Residual norms are a common way to stop iterative

Table 3.1: Segregated solution algorithm for unsteady flows (Klaij and Vaz, 2017).

Initialisation
Time step advancement $t \rightarrow t + \Delta t$
Start of outer loop iteration
SIMPLE algorithm
Solve momentum equation for velocity prediction
Inner loop to solve algebraic equation
Solve pressure correction equation
Inner loop to solve algebraic equation
Calculate velocity correction
Update pressure and velocity field
Solve equations of turbulence model
Inner loop to solve algebraic equation
Solve volume fraction transport equation
Inner loop to solve algebraic equation
Check for convergence according to criterion (Equation (3.50))
If not converged: \Rightarrow Advance outer loop.
Otherwise or if maximum number of outer loops reached
\Rightarrow Advance time
If maximum number of time steps reached
\Rightarrow Stop algorithm

loops and control convergence in the simulations. There are, amongst others, the L_2 and L_∞ norm. These norms per quantity j are defined as:

$$r_{L_2,j} = \sqrt{\frac{\sum_{i=1}^N r_{n_{i,j}}^2}{N}} \quad \text{and} \quad r_{L_\infty,j} = \max(|r_{n_{i,j}}|) . \quad (3.50)$$

The L_2 norm denotes the root-mean square (rms) and the L_∞ norm the maximum of all residuals in the domain. Then, an iterative convergence criterion is defined based on one of these residual norms. Then, this criterion is used to judge the iterative convergence of a simulation.

3.3 Coupling with Rigid Body Equations of Motion

For the decay simulations, the floater and domain were moved according to the solution of the rigid body equations of motion. Details on the equations and the grid motion are given in Section 2.5. In this section, the coupling between flow solution and rigid-body system is described and semi-implicit coupling schemes are given.

3.3.1 Solution algorithm

The exchange of information between flow solution and rigid-body system is done in the following:

- Forces and moments on the body by the fluid.
- Body motion and velocity.

This information is iteratively exchanged between fluid and structure side. The forces are a result of the integrated pressure and viscous loads over the surface of the body.

Explicit, implicit and semi-implicit coupling schemes exist. The advantages of the explicit schemes are an easy implementation and the low computer memory requirement. Nevertheless, explicit schemes may be unstable. Implicit schemes are more difficult to implement and require more computing time per time step. However, they are generally stable. In the present work, a semi-implicit coupling scheme was used consisting of a predictor-corrector step. The corresponding solution algorithm is given in Table 3.2. For this solution algorithm, the Adams-Bashforth scheme is applied as predictor and the Adams-Moulton scheme as corrector. The prediction takes place at the time-loop level and the correction at the outer iteration level. The outer loop frequency to execute the corrector step may be defined by the user. For the simulations of this thesis, the corrector step is called at each 10th outer loop iteration unless explicitly stated explicitly otherwise. A semi-implicit coupled scheme is employed to avoid numerical instabilities owing to low mass ratios and added-mass constraints. In addition, the second-order backward differencing (BDF2) scheme may be used as well. In this thesis, both schemes were compared to each other as most simulations of this thesis were performed using the BDF2 scheme, but most published work used the second-order Adams-Bashforth-Moulton (ABM2) scheme. These coupling schemes are detailed in the following.

3.3.2 Semi-implicit coupling schemes

To solve the non-linear initial value problem given in Equation (2.102), the formulation is rewritten to:

$$\dot{\vec{\kappa}} = \mathbf{M}^{-1}(\vec{f}_H - \mathbf{D}\dot{\vec{x}} - \mathbf{C}\vec{x}) \quad \text{with} \quad \dot{\vec{x}} = \vec{\kappa}. \quad (3.51)$$

\vec{x} and $\vec{\kappa}$ can be combined to: $\vec{\phi} = [\vec{\kappa} \ \vec{x}]^T$ and $\vec{h} = [\mathbf{M}^{-1}(\vec{f}_H - \mathbf{D}\dot{\vec{x}} - \mathbf{C}\vec{x}) \ \vec{\kappa}]^T$. These terms are used for the coupling scheme. These matrix equations are solved by:

$$\dot{\vec{\phi}} = \vec{h}(t, \vec{\phi}). \quad (3.52)$$

The Adams-Bashforth-Moulton scheme belongs to the family of multipoint methods (Ferziger and Perić, 2002). The second-order Adams-Bashforth scheme is used as predictor:

$$\vec{\phi}_0^{n+1} = \vec{\phi}^n + \frac{\Delta t}{2} [3f(t_n, \vec{\phi}^n) - f(t_{n-1}, \vec{\phi}_0^{n-1})]. \quad (3.53)$$

Table 3.2: Solution algorithm with predictor and corrector step for coupling with structural equation of motion, adapted from Rosetti (2015).

Time step advancement $t \rightarrow t + \Delta t$
Solve structure equation with predictor
Calculate grid velocity
Update grid position
Update velocity field and boundary conditions
Start of outer loop iteration
SIMPLE algorithm
Solve momentum equation for velocity prediction
Inner loop to solve algebraic equation
Solve pressure correction equation
Inner loop to solve algebraic equation
Calculate velocity correction
Update pressure and velocity field
Solve equations of turbulence model
Inner loop to solve algebraic equation
Solve volume fraction transport equation
Inner loop to solve algebraic equation
At each i^{th} outer loop iteration:
Solve structure equation with corrector
Calculate grid velocity
Update grid position
Update velocity field and boundary conditions
Check for convergence according to criterion (Equation (3.50))
If not converged: \Rightarrow Advance outer loop.
Otherwise or if maximum number of outer loops reached
\Rightarrow Advance time

The subscript 0 means the predictor step before the outer iterations m of each time step n with the corrector steps follow. The solution provides an initial guess for the time step $n+1$ to be used at the corrector step (Rosetti, 2015). The corrector step is based on the second-order Adams-Moulton scheme, which follows a trapezoidal rule of the form:

$$\vec{\phi}_m^{n+1} = \vec{\phi}_m^n + \frac{\Delta t}{2} \left[f(t_{n+1}, \vec{\phi}_m^{n+1}) + f(t_n, \vec{\phi}_m^n) \right]. \quad (3.54)$$

Both, the Adams-Bashforth and the Adams-Moulton scheme, may be substituted by the second-order backward differencing (BDF2) scheme for the predictor and corrector step. The BDF2 method reads:

$$\vec{\phi}_m^{n+1} = \frac{4}{3}\vec{\phi}_m^n - \frac{1}{3}\vec{\phi}_m^{n-1} + \frac{2}{3}\Delta t f(t_{n+1}, \vec{\phi}_m^{n+1}). \quad (3.55)$$

In case of either of the two methods, the first time step is computed using the first order Adams-Bashforth-Moulton schemes, i.e.:

$$\begin{aligned}\vec{\phi}_m^{n+1} &= \vec{\phi}^n + \Delta t f(t_n, \vec{\phi}^n) \quad \text{and} \\ \vec{\phi}_m^{n+1} &= \vec{\phi}^n + \Delta t f(t_{n+1}, \vec{\phi}^{n+1})\end{aligned}$$

These methods correspond to explicit and implicit Euler, respectively. These schemes are needed as no solution is available from the previous time steps. From the second time step onwards, the second order schemes are applied.

Some configurations of the corrector step may be specified by the user. The corrector may start at the first or i^{th} outer loop and may correct at each to i^{th} outer loops, where i may be any natural number without zero. In the current work, i was set to 10 for all surge decay simulations unless explicitly stated otherwise. For the corrector step, a convergence tolerance may be specified as well as a maximum number of iterations. Both values are stopping criteria for the corrector loop. The tolerance is an absolute value. It gives the estimated motion changes between two iteration loops. In this thesis, a tolerance of 10^{-5} with a maximum of 10 iterations was defined for all simulations unless stated otherwise.

The structural equation of motion may be coupled also with a mooring solver for simulations with restoring and external damping forces owing to mooring line equations. The obtained mooring loads are non-linear and provide a more realistic representation of the restoring \vec{f}_C and external damping forces \vec{f}_D .

3.4 Mooring Solver

The final simulations of this thesis involve RANS simulations coupled with a mooring solver to investigate the influence of moorings on the hydrodynamic damping. The mooring solver used is part of aNySIM-XMF. aNySIM-XMF is an in-house six-degrees-of-freedom multi-purpose time domain solver by MARIN (van den Berg and Pauw, 2018). It is utilised mostly for the simulation of offshore operations. Solely the mooring solver was used in this thesis. aNySIM-XMF is part of the Extensible Modeling Framework (XMF) which includes all time-domain simulation methods of MARIN. The version used in this thesis and coupled to ReFRESCO is xsimulation/4.1.

3.4.1 Mooring model types

Depending on their time dependence, mooring models can be categorised into three types. These models are static, quasi-static and dynamic moorings. In the following, these three models are described and differences are highlighted. The differences between these mooring model types are also illustrated in Figure 3.4.

Static mooring model: The procedure described in Section 2.6 provides the catenary equations for static moorings. Static mooring models are characterised by the following steps (Davidson and Ringwood, 2017):

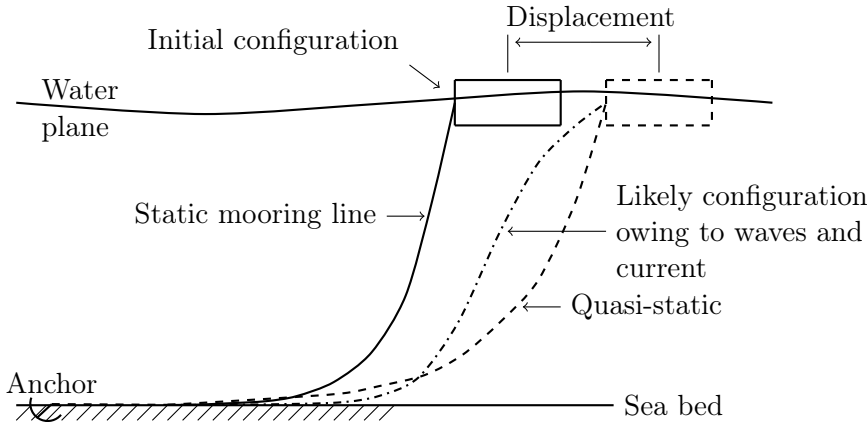


Figure 3.4: Differences of the mooring model types, adapted from Vickers (2012).

1. Definition of initial position of the semi-submersible floater and anchor position, which in turn defines the position of fairlead and touch down point.
2. Calculation of equilibrium configuration for each line with fixed ends.
3. Estimation of out-of-balance loads acting on the free floater and of the new position for the bodies assuming that the shape of the mooring line remains the same.

These steps are repeated until the out-of-balance loads are within a given tolerance. The results of this process yield the equilibrium position of the floating platform. Influencing parameters on the equilibrium position are the mooring line pretension, the amount of mooring lines, their orientation and material properties as well as the length and dimensions of the lines. This model is used mostly for the initial configuration of quasi-static and dynamic mooring models.

Quasi-static mooring model: The mooring solver offers the possibility to choose a quasi-static mooring model. The quasi-static approach assumes that the motions are linear between two static positions. The mooring line shape and tension follow from the catenary formulations based on the assumption that the line is in static equilibrium at each time step. Hence, the motion dependency of mass, damping and fluid acceleration is omitted for the mooring line. This approach disregards hydrodynamic and inertial forces on the line. These forces are important to predict the hydrodynamic damping of a moored floating platform.

Dynamic mooring model: Newton's second law of motion is used to formulate the dynamics of the mooring lines. The motions are a result of the forces acting on the mooring line. The motion equation cannot be solved directly. Therefore, numerical methods are needed. Dynamic mooring models are mostly based on finite element (FE), lumped mass (LM) or finite difference (FD) approaches for spatial discretisation. The lumped mass approach may be seen as a simplified version of the finite element method. Masciola et al. (2014) analysed the positive

and negative aspects of each discretisation method. Many codes based on FE or LM approaches may be found in the survey of Thomsen et al. (2017).

Dynamic models can better represent the likely mooring line configuration owing to waves and current. More details may be found in the literature by Davidson and Ringwood (2017) on the fundamentals of these mooring model types, in Thomsen et al. (2017) on properties of various dynamic mooring modelling codes, and in van den Berg and Pauw (2018) on the specific model and equations applied for the work in this thesis.

3.4.2 Dynamic mooring model

The mooring solver used for this thesis applies a quasi-static mooring model or a dynamic mooring model relying on a lumped mass approach. In both cases, Runge-Kutta schemes are used for time integration. The lumped mass approach divides the mooring line into an interconnected set of discrete elements. These elements are represented by nodes, at which the masses, external loads and internal reactions are lumped, and connectors are based on massless springs and dampers, see Figure 3.5. Each node possesses half of the mass of the previous and half of the subsequent mooring element. Thus, the top and bottom elements are by half an element weight too light. This may only be critical for floating platforms with relatively small own weight compared to the mooring line. This was not the case for the moored floating semi-submersible investigated. The nodal masses include structural and hydrodynamic added masses which are modelled. The spring constitutes the restoring force of the mooring line element and depends on the elastic modulus (axial stiffness) and cross sectional area. The damper element mimics the internal material damping in the line.

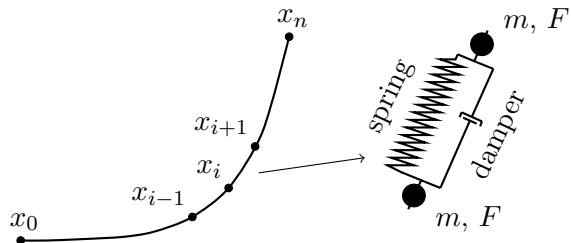


Figure 3.5: Principle of lumped mass model. It is a simplification of Figure 2.8. Internal stresses, external loads and masses are lumped at the nodes.

Equation of motion: The equation of motion for the LM model is obtained based on summation of forces at the nodes (Masciola et al., 2014):

$$\mathbf{M}_i \ddot{\vec{x}}_i = \vec{f}_{internal_i} + \vec{f}_{external_i} . \quad (3.56)$$

The mass matrix \mathbf{M} is strictly diagonal due to the characteristics of the LM approach. \vec{x}_i is the state vector with \vec{x}_i being the velocity and $\ddot{\vec{x}}_i$ the acceleration of

the i^{th} node. The internal and external forces are defined as follows:

$$\vec{f}_{\text{internal}_i} = \vec{f}_{st_i} + \vec{f}_{d_i} \quad \text{and} \quad (3.57)$$

$$\vec{f}_{\text{external}_i} = \vec{f}_{H_i} + \vec{w}_i . \quad (3.58)$$

Thus, the internal forces are a result of the mooring stiffness \vec{f}_{st} and internal damping \vec{f}_d , and the external forces of hydrodynamic loads \vec{f}_H and submerged weight \vec{w} . The internal forces depend on the position of the i^{th} node and its relative motion compared to the adjacent nodes $i - 1$ and $i + 1$. The top and bottom nodal motions require the boundary conditions given by the motion of the floater's fairlead at the top end and by a fixed point in the inertial reference frame, the anchor. This formulation disregards bending stiffness, which is valid for chain type mooring lines. Neglecting bending stiffness leads to a “low-order” LM formulation (Masciola et al., 2014) as presented in Equation (3.56). The hydrodynamic forces follow from a Morison type definition (Morison et al., 1950):

$$\vec{f}_H = \vec{f}_M + \vec{f}_{Dr} \quad \text{with:} \quad (3.59)$$

$$\vec{f}_M = \rho \pi \frac{D^2}{4} s C_M \vec{a} \quad \text{and} \quad (3.60)$$

$$\vec{f}_{Dr} = \frac{1}{2} \rho C_D D s |\vec{v}| \vec{v} . \quad (3.61)$$

The hydrodynamic force consists of an inertia \vec{f}_M and drag \vec{f}_{Dr} term. Possible lift forces are not included in the mooring solver at hand. The inertia term depends on the element length s , the diameter D , the inertia coefficient C_M , the acceleration of the fluid relative to the segment \vec{a} and the fluid density ρ . The inertia coefficient includes the added mass coefficient C_A in the form (van den Berg and Pauw, 2018): $C_M = 1 + C_A$. The hydrodynamic drag force f_D is also depending on the fluid density, and the mooring line element diameter and length. In addition, the magnitude and direction of the force is related to the non-linear velocity term $|\vec{v}| \vec{v}$. Here, \vec{v} is a relative velocity between fluid and mooring line segment. Its value depends on the orbital wave velocities, the current velocities, and the motions of the element. The element motions are a consequence of the floater motions given by the 6 DOF rigid body motion solver. The wave and current velocities need to be specified in the mooring solver and are not part of the coupling. These two velocity components were not used for the coupled decay simulations. The equations above are written in the element reference frame with a tangential and normal direction. Thus, inertia and drag coefficients in normal and tangential direction need to be defined.

The submerged weight \vec{w} is a force per meter line length in gravity direction and influenced by the buoyancy and mass of the mooring element. It is the net weight of the node in fluid. The internal loads, owing to mooring stiffness \vec{f}_{st} and damping \vec{f}_d , are given by the line material as damping percentage and axial stiffness.

Numerical integration: In a similar way as was done in Section 2.5.1, the equation of motion for a mooring node may be reformulated to obtain an initial

value problem, which is generally written as:

$$\dot{\vec{y}} = f(t, \vec{y}(t)) \quad \text{with} \quad \vec{y}(t_0) = \vec{y}_0 . \quad (3.62)$$

For a 1D problem, \vec{y} reads:

$$\vec{y} = \begin{bmatrix} \kappa \\ \dot{\kappa} \end{bmatrix} \quad \text{with} \quad \kappa = \dot{x} . \quad (3.63)$$

The integration methods available are part of the explicit Runge-Kutta schemes. The second-order scheme (RK2) is defined as (van den Berg and Pauw, 2018):

$$\vec{k}_1 = f(t_n, \vec{y}(t_n)) \quad (3.64)$$

$$\vec{k}_2 = f(t_{n+1}, \vec{y}(t_n) + \Delta t \vec{k}_1) \quad (3.65)$$

$$\vec{y}(t_{n+1}) = \vec{y}(t_n) + \frac{\Delta t}{2} (\vec{k}_1 + \vec{k}_2) \quad (3.66)$$

This scheme is second-order accurate. It is a two-stage approach also called Heun's method. In addition, there are two other integration schemes: the Runge-Kutta fourth-order and a Cash-Karp approach. The fourth-order method requires four stages and Cash-Karp six stages for solution of the next time step (van den Berg and Pauw, 2018). Thus, computationally these methods are more expensive, but they are also higher-order accurate. The RK2 scheme requires smaller time steps to achieve similar results than e.g. the Cash-Karp integration scheme. For completeness, the Cash-Karp scheme is given with (van den Berg and Pauw, 2018):

$$\vec{k}_1 = f(t_n, \vec{y}(t_n)) \quad (3.67)$$

$$\vec{k}_2 = f\left(t_{n+\frac{1}{5}}, \vec{y}(t_n) + \frac{\Delta t}{5} \vec{k}_1\right) \quad (3.68)$$

$$\vec{k}_3 = f\left(t_{n+\frac{3}{10}}, \vec{y}(t_n) + \Delta t \left[\frac{3}{40} \vec{k}_1 + \frac{9}{40} \vec{k}_2 \right] \right) \quad (3.69)$$

$$\vec{k}_4 = f\left(t_{n+\frac{3}{5}}, \vec{y}(t_n) + \Delta t \left[\frac{3}{10} \vec{k}_1 - \frac{9}{10} \vec{k}_2 + \frac{6}{5} \vec{k}_3 \right] \right) \quad (3.70)$$

$$\vec{k}_5 = f\left(t_{n+1}, \vec{y}(t_n) + \Delta t \left[-\frac{11}{54} \vec{k}_1 + \frac{5}{2} \vec{k}_2 - \frac{70}{27} \vec{k}_3 + \frac{35}{27} \vec{k}_4 \right] \right) \quad (3.71)$$

$$\begin{aligned} \vec{k}_6 &= f\left(t_{n+\frac{7}{8}}, \vec{y}(t_n) + \Delta t \left[\frac{1631}{55296} \vec{k}_1 + \frac{175}{512} \vec{k}_2 + \frac{575}{13824} \vec{k}_3 \right. \right. \\ &\quad \left. \left. + \frac{44275}{110592} \vec{k}_4 + \frac{253}{4096} \vec{k}_5 \right] \right) \end{aligned} \quad (3.72)$$

$$\vec{y}(t_{n+1}) = \vec{y}(t_n) + \Delta t \left(\frac{37}{378} \vec{k}_1 + \frac{250}{621} \vec{k}_3 + \frac{125}{594} \vec{k}_4 + \frac{512}{1771} \vec{k}_6 \right) . \quad (3.73)$$

This scheme is three times slower than the RK2 but also fifth-order accurate. For fine temporal discretisation, the differences of the solution between the Cash-Karp and second-order Runge-Kutta become negligible. As these schemes are explicit, fine temporal discretisation should always be considered for stability reasons.

3.4.3 Coupling of fluid and mooring equations

Figure 3.6 presents the schematic of the coupling procedure for the numerical simulation of a moored floating vessel using ReFRESCO and aNySIM-XMF. The dashed box represents the solution algorithm within the CFD solver including the 6 DOF rigid body motion solver and the dotted box the one within the mooring solver. At the beginning of each time step, the floater position calculated by the corrector step is transmitted to the mooring solver. Then, the mooring model (quasi-static or lumped-mass) calculates the total mooring forces and moments on the structure and passes them back to the 6 DOF solver within the CFD code. Hence, the coupling with the mooring solver is explicit and requires small time steps for numerical stability reasons. The time-steps used for the CFD simulations are usually small enough. If the iteration error calculated by the mooring model exceeds a user defined tolerance given in absolute values, the internal time step of aNySIM-XMF is adapted until the tolerance is met. Thus, the mooring model iterates on this error estimate.

The information exchange between fluid and rigid body motion equations in the corrector step occurs several times within a time step. The interval can be specified by the user, i.e. a value between each outer-loop iteration and once per time step may be selected. The information exchange with the mooring solver, however, occurs once per time step (in the predictor step), whereas the motions of the floater are updated in the predictor and corrector steps. Thus, there is a difference of one time step between mooring loads and motions. As damping is a consequence of a phase shift between body and fluid motions, this difference also contributes to the total damping of the moored system. However, as very small time steps were chosen this additional damping was regarded negligible for the work of this thesis.

3.5 Verification and Validation

According to Roache (2009), verification is primarily a mathematical exercise and validation an engineering activity. Verification checks the methods used to solve the equations, and validation scrutinises the choice of the mathematical model.

Verification is composed of code and solution verification. Code verification means to demonstrate that a computer code contains the correct implementation of the system of equations. Error and/or uncertainty estimation of a numerical simulation for a case, in which the exact solution is not known, is part of solution verification. Code verification must be done before solution verification.

Validation means the comparison of simulation and experiment in order to estimate the modelling error/uncertainty. It requires experimental data and should be done after solution verification. Validation is applied to the mathematical model and done for selected flow quantities. It also requires the experimental errors/uncertainties.

The numerical prediction of hydrodynamic damping and loads on ships and offshore structures using CFD suffer from large dependencies on the spatial and temporal discretisation. Coarse CFD simulations include large numerical diffusion. This diffusion acts as additional damping and might lead to a good agreement with the

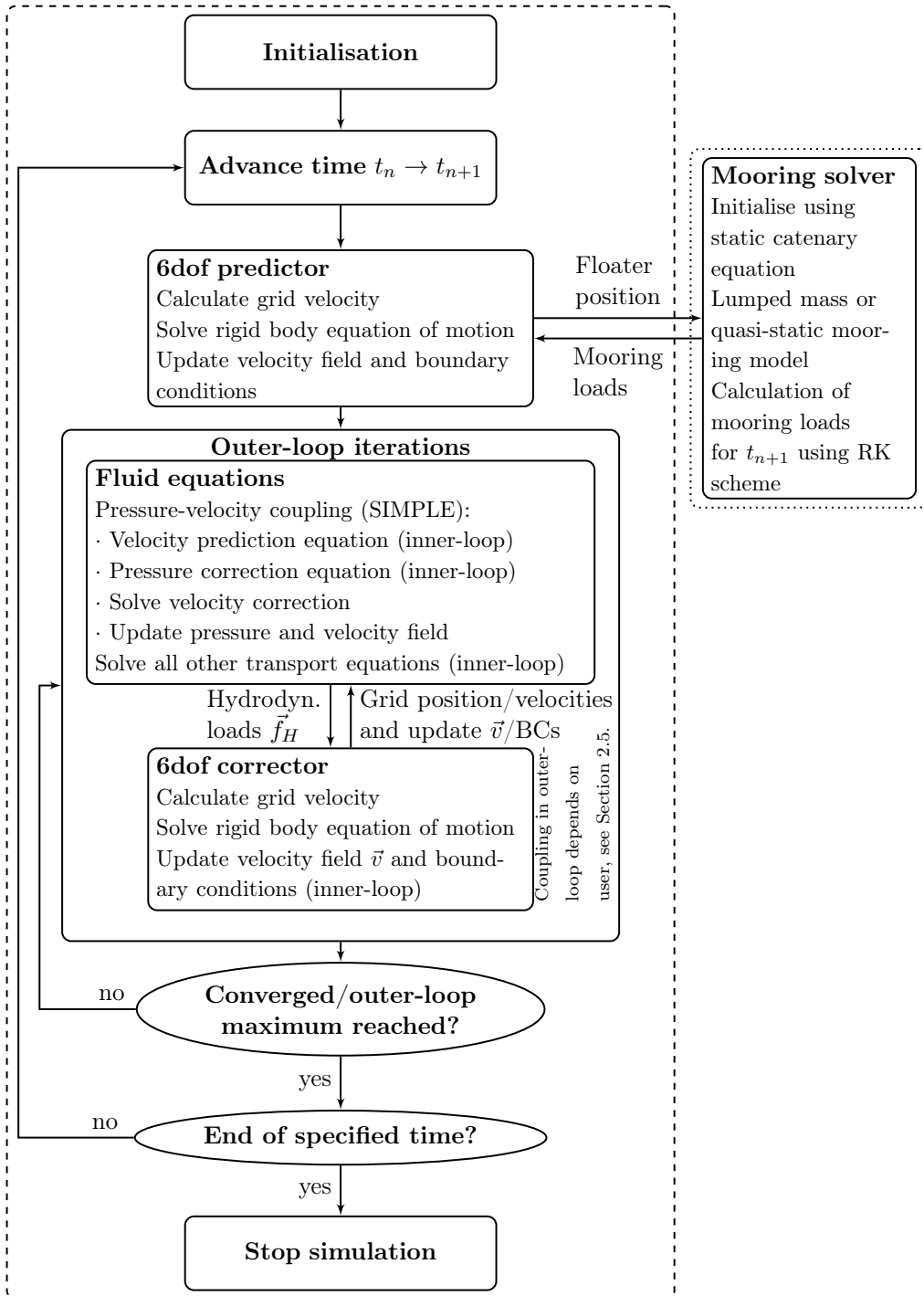


Figure 3.6: General simulation procedure of a moored floating structure with moving grids. The dashed box represents the steps for ReFRESCO and the dotted for aNySIMxml (xsimulation/4.1).

measured data which is misleading as large numerical errors remain. Therefore, verification and validation studies are important to reduce these errors.

3.5.1 Numerical Errors and Uncertainties

Errors and uncertainties arise in numerical simulations. Their quantification are both part of validation and verification. These errors may be distinguished in modelling ϵ_M , discretisation ϵ_d , iterative ϵ_{it} , input ϵ_I , round-off errors ϵ_{ro} , and statistical errors ϵ_{st} . Then, the total computational error ϵ_T of a quantity reads:

$$\epsilon_T = \epsilon_M + \epsilon_I + \epsilon_{NS} . \quad (3.74)$$

Where, the numerical simulation error ϵ_{NS} follows as:

$$\epsilon_{NS} = \epsilon_{it} + \epsilon_{ro} + \epsilon_d + \epsilon_{st} . \quad (3.75)$$

For validation purposes, the modelling errors ϵ_M are the important quantities, while for verification, these are the numerical simulation errors ϵ_{NS} . The modelling error defines the difference between the numerical and exact solution of the mathematical model. It can be quantified by comparison of numerical and experimental data, if numerical and experimental errors and uncertainties are assessed. The round-off error describes the difference between the calculated approximation of a number and its exact mathematical value. In calculations with double precision, i.e. 16 digits, the round-off error may be neglected (Eça and Hoekstra, 2009). The discretisation error denotes the difference between the exact solution of the conservation equations and the solution of the algebraic system of equations obtained by their discretisation (spatial and temporal). The iterative error is the difference between the iterative and exact solutions of the system of algebraic equations. The residual level obtained controls the iterative error. For residual levels of two orders of magnitude below the discretisation error, the iterative error may be considered small enough so that the discretisation error follows as major source of numerical errors (Eça and Hoekstra, 2009). The input error arises because of differences between the physical and numerical problem, such as insufficient experimental information or large numerical demands. Two examples are the dimensions of the computational domain and the characteristics of the turbulent flow field at the inlet boundary condition (Pereira, 2018). For unsteady flow problems, the statistical errors ϵ_{st} are also important. This error originates because of the finite length of the test domains and the duration of simulation time. This uncertainty could be reduced by repeated simulations and averaging the results. However, reliable error estimates without these expensive repetitions are needed for engineering approaches (Brouwer et al., 2015).

Definition of errors and uncertainties: The difference between the solution of a given quantity ϕ_i and its exact value ϕ_0 defines the error δ mathematically:

$$\delta = \phi_i - \phi_0 . \quad (3.76)$$

Uncertainties give an interval around the exact solution. This interval contains the exact solution with a certain degree of confidence. The uncertainty U_{ϕ_i} is defined as:

$$\phi_i - U_{\phi_i} \leq \phi_0 \leq \phi_i + U_{\phi_i} . \quad (3.77)$$

Equation (3.76) is the starting point for the estimation of the discretisation error/uncertainty.

The quantification errors/uncertainties requires usually a set of results obtained by different simulations. These sets are part of a convergence study. For the discretisation error/uncertainty, this study might include investigations on the spatial and temporal discretisation level. The type of convergence, identified by determination of the convergence ratio, defines the error estimation method. With three solutions, the convergence ratio R may be estimated with:

$$R = \frac{\phi_2 - \phi_1}{\phi_3 - \phi_2} . \quad (3.78)$$

The input parameters ϕ_1 , ϕ_2 and ϕ_3 correspond to solutions with fine, medium, and coarse grid spacing, respectively. ITTC (2017), Oberhagemann and el Moctar (2019) and Eça and Hoekstra (2014) present the convergence conditions as:

- Monotonic convergence: $0 < R < 1$
- Monotonic divergence: $R > 1$
- Oscillatory convergence: $R < 0$ and $|R| < 1$
- Oscillatory divergence: $R < 0$ and $|R| > 1$

Discretisation error and uncertainty: The discretisation error is seen as largest source of numerical simulation error, if the residuals drop below a certain limit (two orders below the discretisation error), the code is written in double precision, and the statistical oscillations are small. There are many different discretisation error estimation methods. Therefore, two methods to estimate discretisation errors and uncertainties were applied in order to assess the differences between these methods. The two discretisation error estimation techniques are the approaches by Eça and Hoekstra (2014) and by Oberhagemann and el Moctar (2019). For comparison purposes, the formulation proposed by Xing and Stern (2010) was added. The methods by Xing and Stern (2010) and Eça and Hoekstra (2014) are also widely used in the research community. As Oberhagemann and el Moctar (2019) do not provide an estimate for the discretisation uncertainty while the other approaches do, an attempt for an uncertainty estimate is developed in this thesis to overcome this disadvantage.

3.5.2 Approach by Eça and Hoekstra

Using Richardson extrapolation, as proposed by Eça and Hoekstra (2014), Equation (3.76) can be extended to:

$$\epsilon_d \approx \delta_{RE} = \phi_i - \phi_0 = \alpha h_i^{\eta_{ob}} . \quad (3.79)$$

Here, η_{ob} denotes the observed order of convergence, h the relative grid spacing, and α a coefficient related with the error level. The relative grid spacing h_i of a given grid depends on the typical grid spacing Δx_i . As shown by Crepier (2017), defining a typical grid spacing is not straightforward for trimmed unstructured grids as also used in this thesis. The grids are not necessarily geometrical similar and need to follow strict guidelines. The guidelines followed here are detailed for each test case in the following sections. Then, there are three unknowns in Equation (3.79), i.e. at least three solutions ϕ_i are needed to estimate the error. For unstructured grids (as used in this thesis), the relative and typical grid spacing are estimated by (Eça, 2016):

$$\Delta x_i = \left(\frac{1}{N_{cells_i}} \right)^{\frac{1}{n_d}}, \quad h_i = \frac{\Delta x_i}{\Delta x_1}. \quad (3.80)$$

N_{cells_i} is the number of cells of grid i , and n_d stands for the dimension of space, i.e. $n_d = 3$ for three-dimensional simulations. The subscript 1 denotes the solution of the finest grid and time step.

For unsteady calculations, both, spatial and temporal discretisation, play a role. Therefore, Equation (3.79) may be extended to:

$$\delta_{RE} = \phi_i - \phi_0 = \alpha_x h_i^{\eta_{ob,x}} + \alpha_t t_i^{\eta_{ob,t}}. \quad (3.81)$$

The subscripts x and t stand for space and time dependent values. t_i is the relative time step and is estimated by:

$$t_i = \frac{\Delta t_i}{\Delta t_1} = \frac{N_{t_1}}{N_{t_i}}. \quad (3.82)$$

The number of time steps for a certain time interval is denoted by N_{t_i} for a given simulation and Δt_i the corresponding time step size. Thus, the finest grid and time step are represented with $h_1 = 1$ and $t_1 = 1$.

In Equation (3.81), there are five unknowns. Thus, at least five solutions with both, variation in time and space resolution, for monotonic convergent data are required to solve this equation.

For simplification, Equation (3.79) for steady simulations is used to explain the procedure for the error and uncertainty estimation.

If Equation (3.79) does not deliver reliable output or the output is impossible to determine, then three other error estimators may be used, i.e. the observed order of grid convergence η_{ob} is either very small or very large (outside of the range $0.5 \leq \eta_{ob} \leq 2.0$). The three estimators are:

$$\delta_1 = \phi_i - \phi_0 = \alpha h_i, \quad (3.83)$$

$$\delta_2 = \phi_i - \phi_0 = \alpha h_i^2, \quad (3.84)$$

and

$$\delta_{12} = \phi_i - \phi_0 = \alpha_1 h_i + \alpha_2 h_i^2. \quad (3.85)$$

While Equation (3.83) and (3.84) are suitable for monotonic converging solutions, Equation (3.85) can be applied also to non-monotonic converging data.

Three simulations are deemed not reliable, since the error estimation with Richardson extrapolation depends highly on the observed order of convergence η_{ob} , the equations might be ill-conditioned for small data ranges, the data can contain noise, and the grids can be dissimilar. Therefore, Eça and Hoekstra (2014) recommend to use at least one data point more than unknowns, so the error estimation may be done in a least-squares sense. As an example, just the least-squares formulation for Equation (3.79) is regarded (the same as for Equation (3.83), (3.84), and (3.85)). ϕ_0 is determined from the minimum of the function:

$$S_{RE}^w(\phi_0, \alpha, \eta_{ob}) = \sqrt{\sum_{i=1}^{n_g} w_i (\phi_i - (\phi_0 + \alpha h_i^{\eta_{ob}}))^2}. \quad (3.86)$$

The least-squares are summed over the number of grids n_g . The procedure may be weighted with w_i in case more weight should be given to the finer grid solutions. Otherwise, the weights w_i equal 1 for all grids. In addition, the standard deviations are defined with:

$$\sigma_{RE}^w = \sqrt{\frac{\sum_{i=1}^{n_g} n_g w_i (\phi_i - (\phi_0 + \alpha h_i^{\eta_{ob}}))^2}{n_g - 3}}. \quad (3.87)$$

In case of a non-weighted approach as for this work, $n_g w_i$ is replaced by $n_g w_i = 1$. Once the error estimation is completed, the uncertainty can be obtained. A data range parameter Δ_ϕ is introduced to judge the quality of the data fit:

$$\Delta_\phi = \frac{\max(|\phi_i - \phi_j|)}{n_g - 1} \quad \text{with } 1 \leq i \leq n_g \quad \text{and } 1 \leq j \leq n_g. \quad (3.88)$$

A reliable error estimation is available, if the solution is monotonically convergent with $0 \leq \eta_{ob} \leq 2$ and if $\sigma < \Delta_\phi$ is true (σ replaces σ_{RE} or σ_{RE}^w). Furthermore, a safety factor can be chosen according to Roache (2009). This safety factor is $F_s = 1.25$ for a reliable error estimate and $F_s = 3$, otherwise. Then, the uncertainty is estimated for two cases:

- Reliable error estimation, i.e. $\sigma < \Delta_\phi$:

$$U_\phi(\phi_i) = F_s \epsilon_d(\phi_i) + \sigma + |\phi_i - \phi_{fit}|. \quad (3.89)$$

- Not reliable error estimation, i.e. $\sigma \geq \Delta_\phi$:

$$U_\phi(\phi_i) = F_s \frac{\sigma}{\Delta_\phi} (\epsilon_d(\phi_i) + \sigma + |\phi_i - \phi_{fit}|). \quad (3.90)$$

The uncertainty estimation has three components: the absolute value of the discretisation error times a safety factor, the standard deviation of the fit, and the absolute difference of the real data point ϕ_i and the value obtained from the fit for the same grid density ϕ_{fit} . More details may be found in Eça and Hoekstra (2014) and Eça and Hoekstra (2008).

3.5.3 Approach by Oberhagemann and el Moctar

The method by Oberhagemann and el Moctar (2019) is also published in Oberhagemann (2016). It requires uniform refinement in all spatial dimensions as well as time to achieve constant Courant numbers (definition see Equation (3.22)). Oberhagemann and el Moctar (2019) propose to use a Taylor series expansion similar to Equation (3.85). A non-dimensional scalar grid refinement ratio Υ is defined with:

$$\begin{aligned}\Upsilon_i &= \sqrt{\frac{1}{3} \left[\left(\frac{\Delta x_i}{\Delta x_1} \right)^2 + \left(\frac{\Delta y_i}{\Delta y_1} \right)^2 + \left(\frac{\Delta z_i}{\Delta z_1} \right)^2 \right]} \\ &= \sqrt{\frac{1}{3} \left[\left(\frac{1}{r_x} \right)^{2(i-1)} + \left(\frac{1}{r_y} \right)^{2(i-1)} + \left(\frac{1}{r_z} \right)^{2(i-1)} \right]}\end{aligned}\quad (3.91)$$

The spacing for a reference grid is indicated with subscript 1. Potentially, it is possible to refine the grid differently per spatial direction. Therefore, Υ consists of Δx , Δy , and Δz as the grid spacing in x , y , and z , respectively. The individual refinement factors are defined with

$$r_x = \frac{\Delta x_{i+1}}{\Delta x_i} , \quad r_y = \frac{\Delta y_{i+1}}{\Delta y_i} \quad \text{and} \quad r_z = \frac{\Delta z_{i+1}}{\Delta z_i} . \quad (3.92)$$

In case the refinement factors are kept constant for each spatial dimension as proposed by Oberhagemann and el Moctar (2019), the non-dimensional grid refinement ratio simplifies to:

$$\Upsilon_i = \frac{\Delta x_i}{\Delta x_1} = \left(\frac{1}{r} \right)^{(i-1)} \quad (3.93)$$

Here, Δx and r represent the typical grid spacing and general refinement factor, respectively. Contrary to Eça and Hoekstra, Oberhagemann and el Moctar define the coarse grid as the reference grid. Thus, for the coarse grid, i.e. $i = 1$, the scalar grid refinement ratio becomes $\Upsilon_1 = 1$. Then, the discretisation error δ_D is estimated with:

$$\epsilon_d \approx \delta_D = \phi_i - \phi_0 = a_1 \Upsilon_i + a_2 \Upsilon_i^2 + \dots . \quad (3.94)$$

a , a_1 , and a_2 are error coefficients related with the error level. The truncation of this polynomial “should be chosen so that the expected order of grid convergence can be replicated” (Oberhagemann, 2016). Thus, this method uses a theoretical η_{th} instead of an observed order of convergence. Again, for each unknown at least one grid solution is needed, i.e. for second order approximations, a minimum of three grids are required.

In case of scatter in the data, the approach by Oberhagemann and el Moctar follows the proposed least-squares minimisation by Eça and Hoekstra (2014), e.g.:

$$S_1(\phi_0, a) = \sqrt{\sum_{i=1}^{n_g} (\phi_i - (\phi_0 + a \Upsilon_i))^2} \quad (3.95)$$

for first order convergence and

$$S_2(\phi_0, a_1, a_2) = \sqrt{\sum_{i=1}^{n_g} (\phi_i - (\phi_0 + a_1 \Upsilon_i + a_2 \Upsilon_i^2))^2} \quad (3.96)$$

for second order grid convergence. More details may be found in the publications by Oberhagemann (2016), and by Oberhagemann and el Moctar (2019).

In contrast to the other two methods, the approach by Oberhagemann and el Moctar does not provide an estimation of the discretisation uncertainty. This would be useful in order to validate the numerical simulation with experimental data. Therefore, an attempt for an uncertainty estimation is given in this thesis. In a similar way as for the approach by Eça and Hoekstra, the safety factors may be used as defined by Roache (2009). For the proposed method, a safety factor of $F_s = 1.25$ is applied for monotonic convergent data with an observed order of convergence in a similar range as the theoretical order of convergence, i.e. their ratio should be $P \approx 1$. The safety factor is increased to $F_s = 3$, otherwise. Hence, the discretisation uncertainty may be written as:

$$U_{LSQth}(\phi_i) = F_s \delta_D(\phi_i) \quad \text{with} \quad F_s = \begin{cases} 1.25 & 0.8 < P < 1.2 \quad \text{and} \quad 0 < R < 1 \\ 3.0 & \text{otherwise} \end{cases}. \quad (3.97)$$

P is the convergence ratio and defined in Equation (3.101). It reflects the ratio between theoretical and observed order of convergence. The smaller safety factor is applied only if the theoretical and observed order of convergence are equal within a 20% margin. If the method should be used also for oscillatory convergent data, an additional factor is required to account for the loss of certainty in the data.

3.5.4 Approach by Xing and Stern

The formulation by Xing and Stern (2010) is named factors of safety method. The observed order of convergence follows from:

$$\eta_{ob} = \frac{\ln \left(\frac{\phi_3 - \phi_2}{\phi_2 - \phi_1} \right)}{\ln(r)}. \quad (3.98)$$

In accordance with Eça and Hoekstra, Xing and Stern (2010) define the fine grid as the reference grid. Thus, ϕ_1 , ϕ_2 , and ϕ_3 denote the fine, medium and coarse grid solutions. With the grid spacing Δx_i the refinement factor r reads:

$$r = \frac{\Delta x_2}{\Delta x_1} = \frac{\Delta x_3}{\Delta x_2}. \quad (3.99)$$

Following ITTC (2008), the error estimate is defined as:

$$\delta_{RE} = \frac{\phi_2 - \phi_1}{r^{\eta_{ob}} - 1}. \quad (3.100)$$

Xing and Stern (2010), however, recommend to multiply δ_{RE} with the ratio of convergence P :

$$P = \frac{\eta_{ob}}{\eta_{th}} . \quad (3.101)$$

P gives the ratio between the observed order of convergence η_{ob} and the theoretical order of convergence η_{th} limited by the discretisation schemes. A P value of close to one, i.e. $\eta_{ob} \approx \eta_{th}$, represents grids in the asymptotic region. Following the work of Phillips and Roy (2014), the estimated minimum observed order of accuracy is limited to $\eta_{ob} \geq 0.5$. The new error estimate becomes $\epsilon_d \approx P\delta_{RE}$. This error estimate takes into account the distance to the asymptotic region. Then, the discretisation uncertainty is given by (Xing and Stern, 2010):

$$U_{FS}(\phi) = FS(P) |\delta_{RE}(\phi)| = \begin{cases} (2.45 - 0.85P) |\delta_{RE}(\phi)| , & 0 < P \leq 1 \\ (16.4P - 14.8) |\delta_{RE}(\phi)| , & P > 1 . \end{cases} \quad (3.102)$$

A set of three grids is required to solve the errors and uncertainties using this method. As this approach is also widely used, its formulation and results were added to this thesis for comparison purposes.

3.5.5 Validation uncertainty

For independent values of the uncertainty estimates, the validation uncertainty U_V is defined as (ITTC, 2017):

$$U_V(\phi) = \sqrt{(U_{NS}(\phi))^2 + (U_{EXP}(\phi))^2 + (U_{INP}(\phi))^2} . \quad (3.103)$$

Assuming the other error components to be small enough, the discretisation uncertainty is approximately equal to the numerical simulation uncertainty, i.e. $U_{NS} \approx U_D$. In addition to the experimental U_{EXP} and numerical U_{NS} estimates, there are uncertainties of the input data U_{INP} . This equation shows that validation can only be done, if errors and uncertainties of the physical and numerical model are assessed. The validation uncertainty provides an interval around the modelling error ϵ_M :

$$\epsilon_{CO} - U_V(\phi) \leq \epsilon_M(\phi) \leq \epsilon_{CO} + U_V(\phi) \quad (3.104)$$

ϵ_{CO} denotes the comparison error between the experimental data ϕ_{EXP} and the numerical solution ϕ_{NS} , $\epsilon_{CO} = \phi_{EXP} - \phi_{NS}$. Validation is not a pass and fail exercise as it provides an interval around the modelling error. Therefore, validation of a given quantity is obtained depending on the decision of the analyst. The analyst has to decide whether the relation between $U_V(\phi)$ and ϵ_{CO} is acceptable. In case $U_V(\phi) \gg \epsilon_{CO}$, the validation study might be inconclusive. Then, the validation exercise provides details on the uncertainty contributions to be reduced. For $\epsilon_{CO} \gg U_V(\phi)$, the modelling error is well defined with $\epsilon_M \approx \epsilon_{CO}$.

4. Wave Propagation and Loads

Verification studies applying the three discretisation error techniques as defined in Section 3.5 were conducted for a wave propagation and a wave load test case. These test cases and their results, such as time traces, flow solution, and errors, are presented in this chapter. Moreover, two wave absorption functions were investigated to estimate the optimum for the smallest wave reflection.

4.1 Wave Propagation

Free surface and waves are encountered in many maritime flow problems. At first, accurate wave propagation has to be ensured. This section deals with a typical wave propagation test case.

4.1.1 Test case description and numerical setup

The input parameters for the wave generation and propagation simulations were previously used for tests in basins at MARIN and DST. The wave characteristics were as shown in Table 4.1.

Table 4.1: Wave characteristics.

Property	Size
Period, T_p	1.711 s
Height, H_w	0.142 m
Water depth, h	2.3 m

Following the applicability range defined by Lé Méhauté (1976), this wave corresponds to a deep water wave that can be modelled with Stokes theory for 3rd order or higher. In this case, the wave was modelled with the 5th order theory following definitions and implementations by Skjelbreia and Hendrickson (1960) and Lin (2008).

The wave basin at DST is 60 m long, 3 m wide and for propagating waves 2.3 m deep.

For cases with regular non-breaking waves and no fluid-structure interaction, the solution is pressure dominated. Therefore, wave simulations do not require a turbulence model. In fact, turbulence models might even penalise the accuracy of the

wave signal as there is an over-production of turbulent kinetic energy (Larsen and Fuhrman, 2018). Therefore, these simulations were conducted without turbulence model.

The two-dimensional computational domain for this case possessed the dimensions as specified in Table 4.2. For the coordinate system used in the 2D simulations, x is defined for the wave propagation direction and z for the vertical direction. The wave boundary condition (*BCWave*) was used at inlet and outlet, and a non-reflecting boundary condition (*NRBC*) was specified at outlet. More details on these boundary conditions are given in Section 2.4. The specified wave frequency at *BCWave* equalled the initial (theoretical) wave frequency. The sides were modelled as a symmetry plane. Thus, reflection at the outlet can occur only owing to a frequency change during the wave propagation and to numerical artefacts.

Table 4.2: Computational domain for wave propagation test case.

Property	Size
Wave length (Stokes 5 th order)	$\lambda_w \approx 4.5548 \text{ m}$
Length	$22.8 \text{ m} \approx 5 \cdot \lambda$
Water depth	2.3 m
Height	$4.6 \text{ m} \approx 1 \cdot \lambda$

To reduce the difference between initial and actual wave, and to reduce reflections, an absorption zone was applied at beginning and end of the domain. The absorption zones were one wave length long. This leads to a distance of three wave lengths between the inlet and outlet absorption zones. The domain, including absorption zones, wave probe location and refinement boxes, is presented in Figure 4.1.

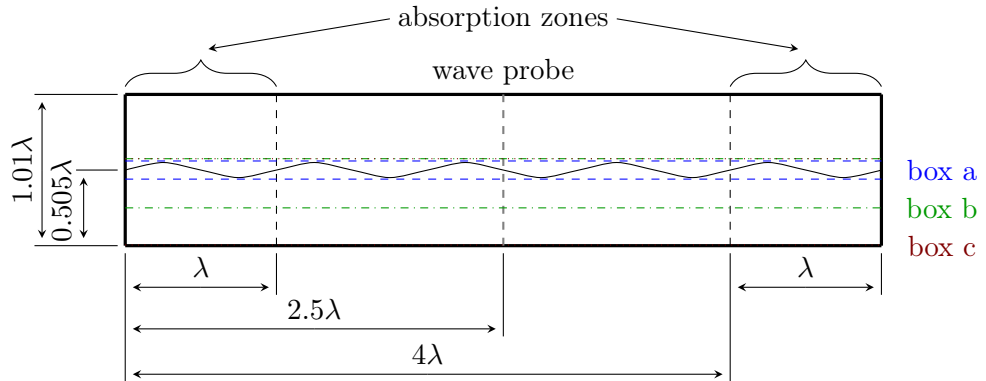


Figure 4.1: Grid and domain setup for the wave propagation test case including refinement boxes and absorption zones used. The definitions are given in terms of wave length λ .

The grids were generated with an unstructured hexahedral grid generator software following the topology guidelines by Rapuc et al. (2018). They proposed to refine the grid according to the kinetic wave energy. The first refinement box (box a)

covered the wave elevation with a 20 % margin above and below the wave. The following two boxes (box b and c) captured 90 % and 99.9 % of the wave energy, respectively. In Figure 4.2, the grid is shown stretched by a factor of three in vertical direction, for visualisation purposes. Four different grids were generated with the same topology. They are listed in Table 4.3.

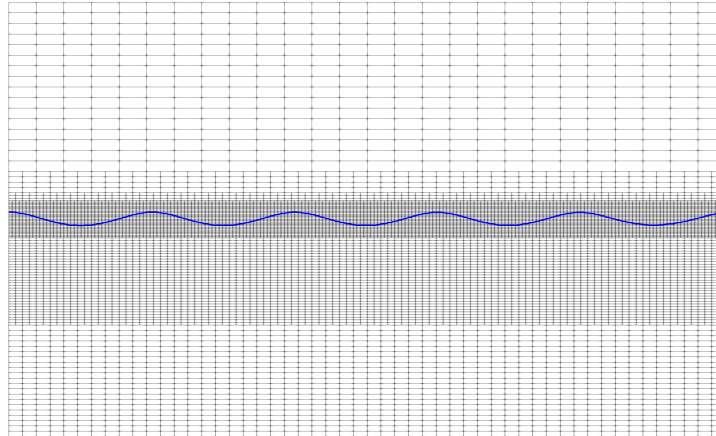


Figure 4.2: Grid topology of a coarse grid with wave elevation in blue for the wave propagation test case. For visualisation purposes, the vertical direction was scaled by a factor of 3.

Table 4.3: Grid definitions for test case one. The values tabulated are valid for refinement box A relative to the wave.

Grid name	# cells/wave height	# cells/wave length	total # of cells
Grid A	7	28	6 650
Grid B	10	40	11 284
Grid C	15	60	22 074
Grid D	20	80	36 618
Grid E	30	120	72 197

The time steps studied were defined as a multiple of the wave period T_p : $\Delta t_1 = T_p/280$, $\Delta t_2 = T_p/400$, $\Delta t_3 = T_p/600$, $\Delta t_4 = T_p/800$, and $\Delta t_5 = T_p/1200$. Between each grid and each time step constant refinement ratios were applied. This corresponds to the recommendations of ITTC (2008). The theoretical CFL numbers for each calculation are summarised in Table 4.4. These numbers are based on the theoretical orbital velocity in x of the wave, the grid spacing in x at the free surface and the time step size. CFL numbers below $\frac{1}{6}$ are required to be TVD when using the implicit second order backward scheme for time integration (Klaij et al., 2018). Achieving low CFL numbers leads also to better iterative convergence. This strict TVD constraint does not exist for first order time integration.

Table 4.4: Theoretical CFL numbers for test case one. The time steps are defined as a ratio of the wave period $T_p = 1.711\text{ s}$, i.e. $T_p/280$ is a coarse and $T_p/1200$ a fine time step.

Grids / Time steps Δt	$T_p/280$	$T_p/400$	$T_p/600$	$T_p/800$	$T_p/1200$
Grid A	0.14	0.09	0.06	0.05	0.03
Grid B	0.19	0.14	0.09	0.06	0.05
Grid C	0.28	0.19	0.14	0.09	0.06
Grid D	0.39	0.28	0.19	0.14	0.09
Grid E	0.56	0.39	0.28	0.19	0.14

4.1.2 Absorption zones

The optimum of body force function f_b and size of the absorption coefficient f_{max} needed to be found. The wave reflection coefficient C_r was taken as a quality measure. The reflection coefficient is defined as:

$$C_r = \frac{H_{w_{max}} - H_{w_{min}}}{H_{w_{max}} + H_{w_{min}}} . \quad (4.1)$$

$H_{w_{max}}$ and $H_{w_{min}}$ are the largest and smallest wave height, respectively. For this investigation, 15 consecutive waves were taken to estimate the reflection coefficient. These waves were recorded at the wave probe. Waves could have been travelled back from the outlet in the time frame selected for this estimation. The reflection coefficient was plotted against the absorption coefficient for two different body force functions (see Figure 4.3). This figure represents the results of 16 simulations for the cosine and 11 for the exponential function in the absorption zone, see Equations (3.37) and (2.92).

Figure 4.3 shows minima for the reflection coefficient at $f_{max} = 5$ for the cosine, and at $f_{max} = 15$ for the exponential function. The cosine function with $f_{max} = 5$ showed the lowest wave reflection. Thus, this body force function and coefficient was applied for all wave propagation simulations hereinafter.

4.1.3 Wave propagation results

The wave elevation was recorded with a wave probe located at 2.5 wave lengths from the inflow boundary condition, and thus in the centre of the domain (Figure 4.1). Figure 4.4 presents the result for the wave elevation.

The wave elevations of the different simulations agreed well with each other. In particular, the zero crossings of the signal overlapped for each of the simulations. Figure 4.4 depicts an overshoot and several non-regular waves at the beginning of the simulation. After about 10 wave periods, the wave profile stabilised and became regular. These two phenomena can be explained by the following reasons:

- At the inflow boundary condition, the wave kinematics were computed according to Stokes 5th order theory. The wave kinematics need to be fully developed in the domain to obtain a regular wave. As fluid in the domain

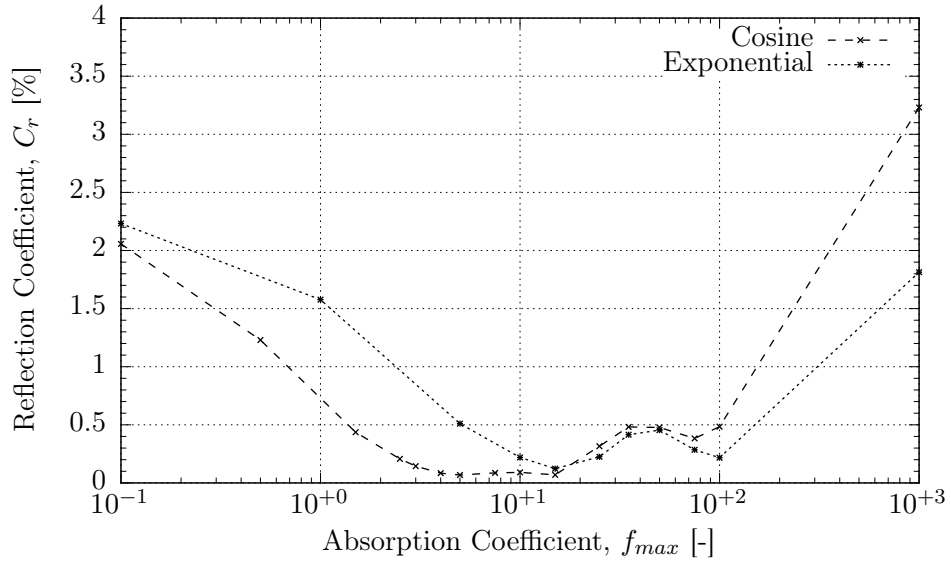


Figure 4.3: Wave reflection coefficient C_r as a function of the absorption coefficient f_{max} for an exponential and a cosine trend of the body force function f_b . The simulations were conducted with grid E and time step $\Delta t_5 = T_p/1200$.

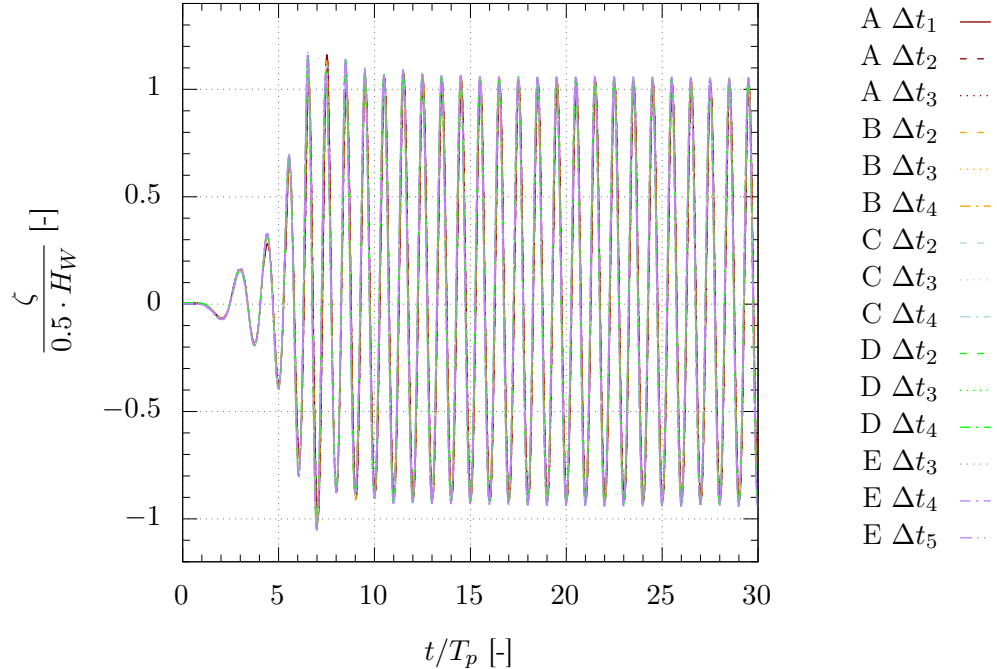


Figure 4.4: Wave elevation ζ for a selection of 15 simulations with different grids and time steps. The wave elevation is normalised by half of the theoretical wave height $0.5 \cdot H_w$ and the time by the period T_p .

was at rest at the beginning of the simulation, a couple of wave periods were needed to reach a fully developed stage.

- In addition, a small ramp-up function was implemented to ensure a smooth start of the simulations. This ramp-up resulted in small waves in the beginning. These small waves propagated slower and were eventually overtaken by the defined regular wave as longer waves also propagate faster. Consequently, superposition occurred and resulted in larger waves, which is presented as an overshoot in this figure.

As the differences between the lines are hardly noticeable in Figure 4.4, just the wave heights of the same selection of results are shown in Figure 4.5.

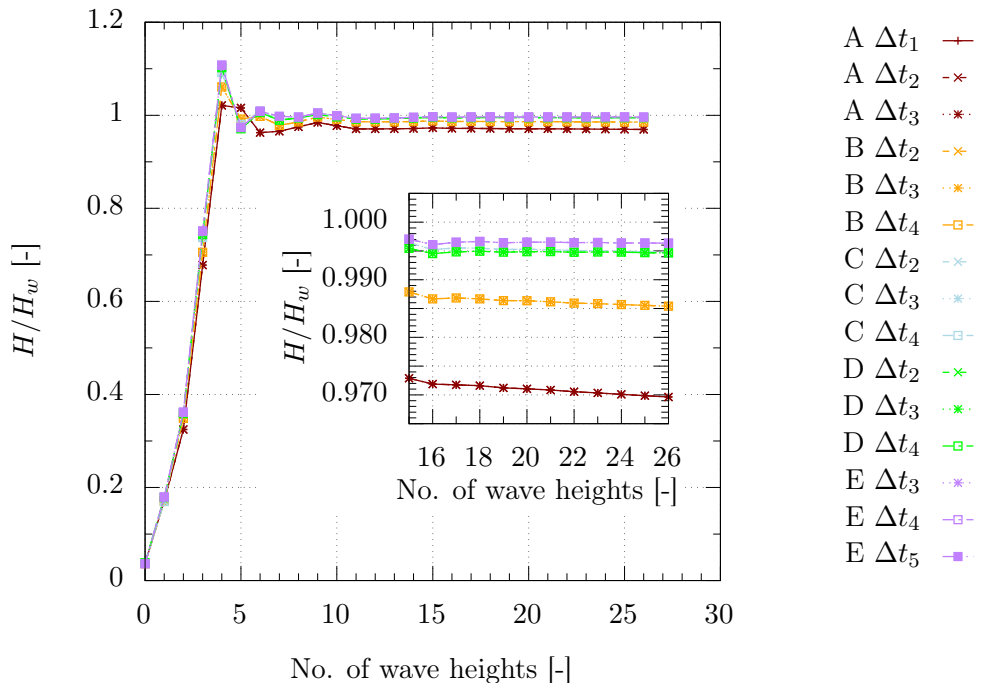


Figure 4.5: Wave heights for a selection of 15 simulations with different grids and time steps. In addition, a zoom on the last 11 wave heights is shown.

The mean and standard deviation of the wave height obtained for the last 10 wave periods for the finest grid and time step are: $0.141463 \text{ m} \pm 0.000042 \text{ m}$. The zoom in Figure 4.5 shows these 10 wave heights indicated with 16 – 26. The wave heights for the coarsest grid simulations are significantly smaller than the wave heights obtained on finer grids. Moreover, as the spatial resolution increases, the wave height values become steadier. This leads to smaller standard deviations. Although not quantified, this may be seen as an indication for smaller statistical uncertainty.

Figure 4.6 presents the air volume fraction c in the whole domain for six consecutive time instances. Volume fraction values of $c = 0$ mark cells filled by water (absence

of air) and $c = 1$ filled by air. The results are displayed for the finest grid and time step, i.e. Grid E and $\Delta t = T_p/1200$.

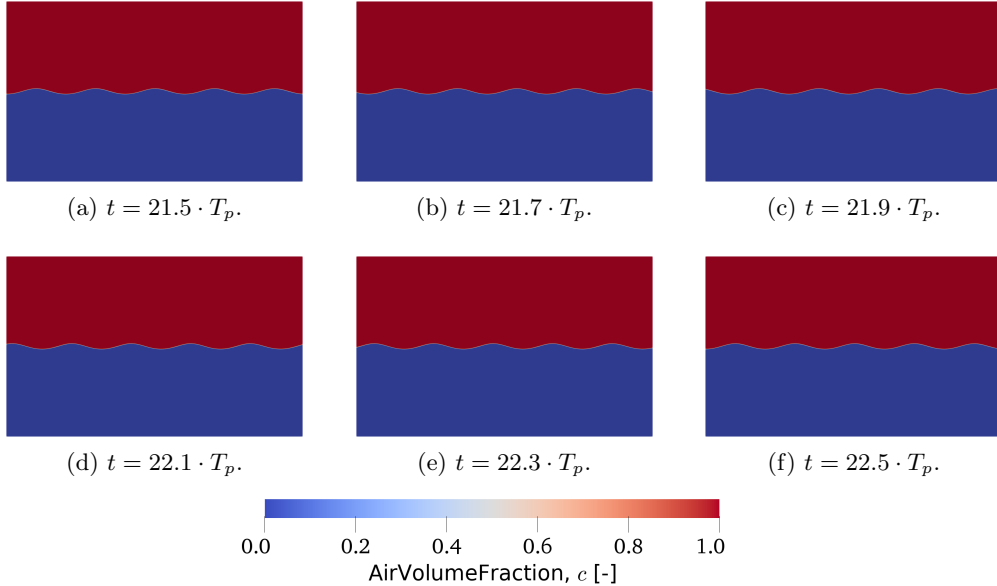


Figure 4.6: Air volume fraction for wave propagation at different time instances for wave period 22. The vertical coordinate is scaled by 3 in the figures for visualisation purposes.

In this figure, the wave progresses from left to right. As the differences between the computed wave and the analytical Stokes 5th order wave are small, a perfectly regular wave profile may be seen also near the absorption zones at the right end of the domain in Figure 4.6.

4.1.4 Iterative convergence

Owing to the iterative solution process of the system of algebraic equations, residuals remain at the end of each time step. These residuals should decrease down to a predefined convergence criterion or until the predefined maximum number of outer-loop iterations is reached. Most publications targeting CFD topics do not show iterative convergence of the solution. However, if large residuals remain at the end of a time step, they cannot be neglected for the verification study. Eça and Hoekstra (2009) and Eça (2016) proposed to achieve a residual level of two orders of magnitude below the discretisation error. Computational time can also be reduced with fast iterative convergence. Figure 4.7 shows the normalised residuals in L_2 and L_∞ norm, i.e. the root mean square of all residuals and the largest residual in the computational domain.

Figure 4.7 shows results for the smallest (grid A and $\Delta t = T_p/1200$), the medium (grid C and $\Delta t = T_p/600$), and the largest theoretical CFL number (grid E and $\Delta t = T_p/280$) of this test case. The representation in L_∞ norm provides the largest residuals in the domain, while the L_2 norm is a root mean square of all residuals.

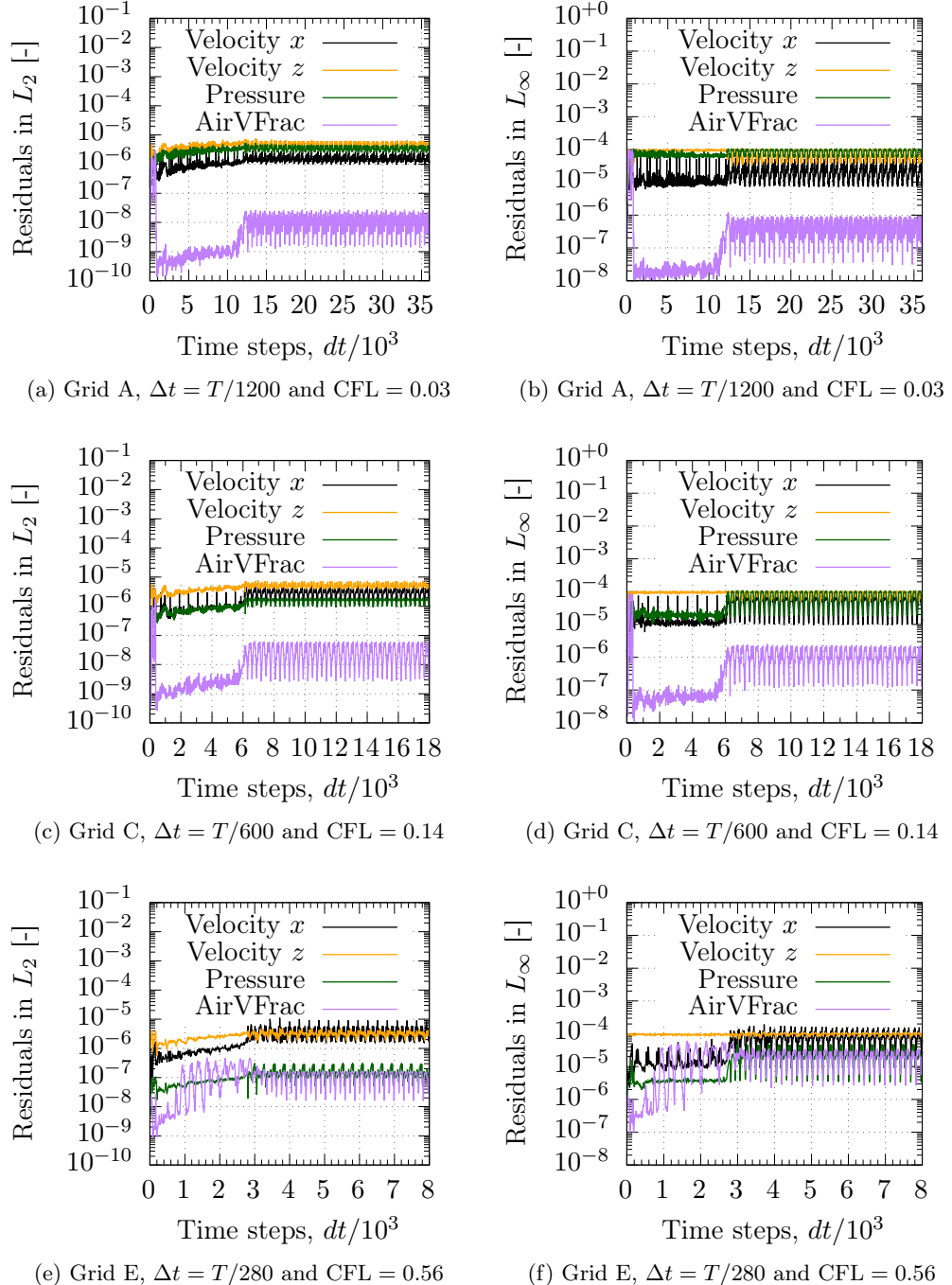


Figure 4.7: Residuals for the wave propagation test case at the end of each time step for three grids with stopping criteria $L_\infty < 10^{-4}$. The normalised residuals are visualised in L_2 and L_∞ norm on the left and right hand side, respectively.

The largest residuals are generally more difficult to converge for capturing schemes than values represented in L_2 norm, because errors of order one are always present

at jumps (Klaij et al., 2018). In this case, the higher residuals are located at the interface between air and water. A flow visualisation of the residuals for the vertical velocity component (Velocity z) for the simulation with the largest theoretical CFL number ($CFL = 0.56$) is presented in Figure 4.8. A threshold was applied to blank residuals below 10^{-5} , for visualisation purposes. The highest residuals are present at the free surface on the up- and downstream side of a wave trough when vertical velocities are largest.

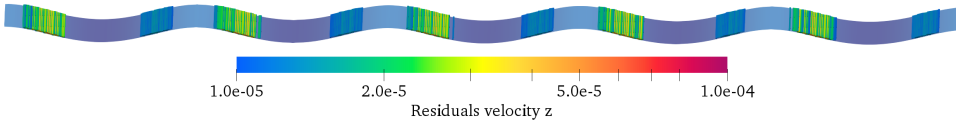


Figure 4.8: Residuals of the vertical component of the velocity in the domain for the wave propagation test case. A threshold is used to blank residuals below 10^{-5} . The colouring uses a logarithmic scale. The free surface is presented in blue for reference.

$L_\infty < 10^{-4}$ was applied as the convergence criteria for this test case. According to Eça and Hoekstra (2009), the residual norms L_2 and L_∞ of the variable change between consecutive iterations may be used as an iterative error estimate. Both residual norms were two orders of magnitude below the expected range of the discretisation error (10^{-4} to 10^{-2}). However, this iterative error estimate is not seen very reliable (Eça and Hoekstra, 2009). The residual convergence was consistent with the wave propagation. When the wave reached the outlet boundary and a regular wave was established in the whole computational domain, the residual convergence stabilised at a certain level. This level increased with higher CFL numbers.

The assessment of iterative errors would require simulations converged to machine accuracy. This is very difficult and expensive for numerical simulations of complex engineering applications. Here, an attempt to asses the influence of the iterative convergence is made by comparing the results of simulations with three different convergence criteria, i.e. $L_\infty < 10^{-4}$, $L_\infty < 10^{-5}$, and $L_\infty < 10^{-6}$. The averaged residuals in L_2 and L_∞ -norm are presented in Figure 4.9.

Figure 4.9 demonstrates the compliance with the respective convergence criterion of each simulation and the large difference between the residual norms. The residuals are highest for the vertical velocity (Velocity z) and lowest for the air volume fraction. Spurious velocities, as discussed by Klaij et al. (2018), may be responsible for these higher residual values. Decreasing the residuals by one order of magnitude in L_∞ norm does result in a similar reduction of residuals in L_2 norm. More important for an engineer is the behaviour of the wave height with increased restriction of the iterative convergence. Therefore, Table 4.5 lists the mean wave height and the standard deviation of the mean for each convergence criterion.

The mean wave height increases slightly by 0.04% from simulations with a convergence criteria of $C_{it_{10^{-4}}}$ to simulations with $C_{it_{10^{-6}}}$. This small difference is

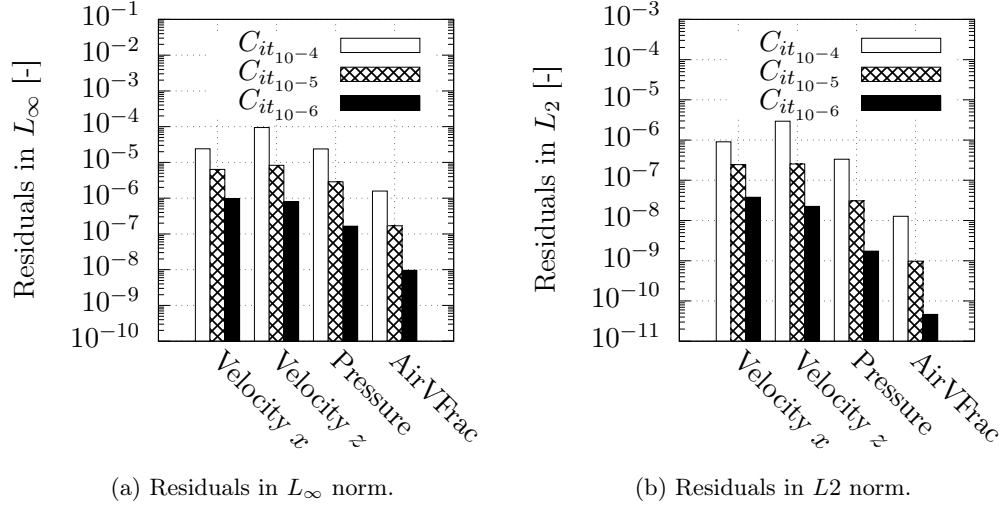


Figure 4.9: Residuals averaged over time for different convergence criteria, i.e. $L_\infty < 10^{-4}$, $L_\infty < 10^{-5}$, and $L_\infty < 10^{-6}$. The simulations were conducted with grid E and $\Delta t = T/1200$.

Table 4.5: Influence of the iterative convergence criterion on the wave propagation. The standard deviation of the mean quantities are below 0.1%.

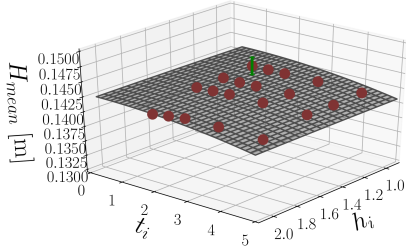
Simulation	Mean wave height H [m]	Mean wave period T [s]
$C_{it} \times 10^{-4}$	0.14146	1.7111
$C_{it} \times 10^{-5}$	0.14152	1.7110
$C_{it} \times 10^{-6}$	0.14152	1.7110

accompanied with an increase of 3.3% in standard deviation. Both, the size of the standard deviation, < 0.1%, and the difference of the mean wave height, are negligible compared with the discretisation error.

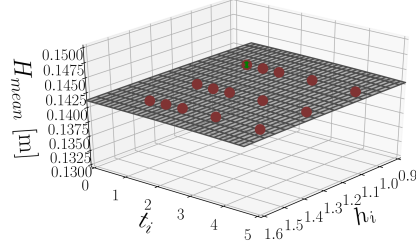
4.1.5 Discretisation errors

The error and uncertainty estimation for the wave propagation test case was performed on the wave characteristics, i.e. the wave height and period. These characteristics were taken from the results recorded by the wave probe monitor and presented in Figure 4.4. Because of the irregular wave behaviour at the beginning of the simulation, the wave analysis started when the first 10 waves had passed the observed location. At this point in time, possible wave reflections would be back from the outflow boundary condition. In total 15 consecutive waves were analysed per simulation. The differences in wave period were very small (< 0.05%). Therefore, results for the error and uncertainty estimations are exhibited just for the wave height.

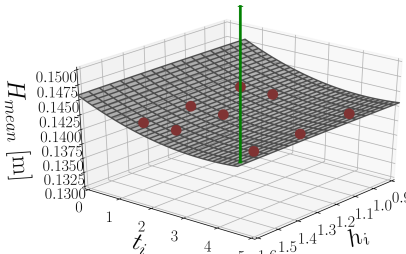
Eça and Hoekstra approach: Different data sets were selected for this approach to investigate the dependence of the error and uncertainty estimation on the combination of spatial and temporal discretisation. Figure 4.10 shows the results for the mean wave height per simulation (red dots), the fitted plane, and an uncertainty bar for the finest grid and time step.



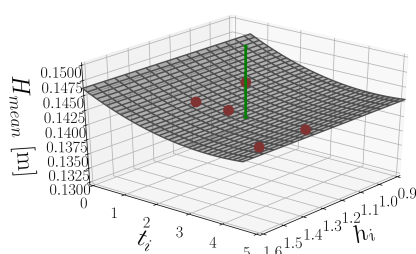
(a) Result for 20 simulations without grid A: $\phi_0 = 0.14193 \text{ m}$.



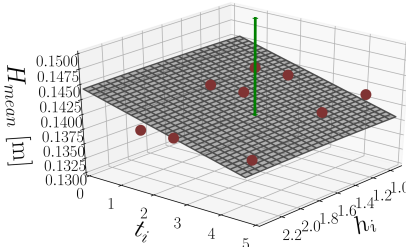
(b) Result for 15 simulations without grids A and B: $\phi_0 = 0.14132 \text{ m}$.



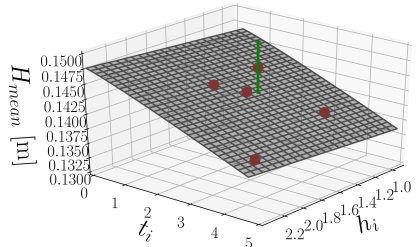
(c) Result for 9 simulations using grids C, D and E with Δt_1 , Δt_3 and Δt_5 : $\phi_0 = 0.14598 \text{ m}$.



(d) Result for 5 simulations using grids C, D and E with Δt_1 , Δt_3 and Δt_5 : $\phi_0 = 0.14648 \text{ m}$.



(e) Result for 9 simulations using grids A, C and E with Δt_1 , Δt_3 and Δt_5 : $\phi_0 = 0.14417 \text{ m}$.



(f) Result for 5 simulations using grids A, C and E with Δt_1 , Δt_3 and Δt_5 : $\phi_0 = 0.14498 \text{ m}$.

Figure 4.10: Discretisation error and uncertainty estimation using the approach by Eça and Hoekstra (2014) for the mean wave height H_{mean} with different data sets selected. Each data point is defined with non-dimensional grid h_i and time step t_i spacing.

The results shown in these figures confirm the observation that wave heights fitted well with each other. The error and uncertainty estimation, following the procedure of Eça and Hoekstra (2014), revealed different results for the extrapolated grid and

time step independent solution ϕ_0 depending on the selected sets of grids and time steps. In each case, the same finest solution was taken. The results are listed in Table 4.6.

Table 4.6: Results for discretisation error and uncertainty estimation by Eça and Hoekstra (2014) for different data sets for H_{wmean} . The errors are given in percentage based on the extrapolated value.

Data set	Extrapolated value ϕ_0 , [m]	Solution of finest grid and time step ϕ_1 , [m]	Error ϵ_ϕ , [%]	Uncertainty U_ϕ , [%]
Without A	0.14193	0.141463	0.3	1.0
Without AB	0.14132	0.141463	0.1	0.3
9 solutions, CDE	0.14598	0.141463	3.1	9.6
5 solutions, CDE	0.14648	0.141463	3.4	4.4
9 solutions, ACE	0.14417	0.141463	1.9	5.9
5 solutions, ACE	0.14498	0.141463	2.4	3.1

Depending on the selected data sets, a difference of $\approx 3.5\%$ for the extrapolated value can be obtained and between $0.3 - 9.6\%$ for the estimated uncertainty. The differences in uncertainty arose owing to scatter in the data. This scatter was more pronounced for results of simulations with coarser temporal and spatial resolution. For finer spatial resolution, however, oscillatory convergence was observed. In addition, the data points also included simulations with larger CFL numbers than required to be TVD. Thus, the code switches to a lower order interface capturing scheme to ensure stability. Eça et al. (2019) demonstrated that discretisation errors are not independent from iterative errors. As the convergence criteria and number of outer loop iterations was kept constant, the influence of the iterative error increased with spatial and temporal discretisation. In addition, Klaij et al. (2018) stated that CFD simulations with interface capturing schemes have problems to converge to low levels in L_∞ - norm because of their step function behaviour at the interface. Hence, oscillatory convergence in the data cannot be omitted for engineering applications and could be observed for solutions of the finer grids, e.g. for grids C, D and E. Furthermore, the free surface should be defined based on kinematic and dynamic boundary conditions. Instead, common procedure (also applied in this work) is to define the free surface at a volume fraction of $c = 0.5$ which does not fulfil the kinematic and dynamic boundary conditions. Thus, Eskilsson et al. (2017) took into account a dispersion of volume fraction values. The estimated order of convergence increased. The error and uncertainty estimation, however, lead to increased values which suggest further grid refinement. Moreover, Eskilsson et al. (2017) performed simulations with at least three times smaller CFL numbers than used in this work. Smaller CFL numbers also help to converge residuals faster and to lower residual levels which in turn helps to reduce oscillatory convergent behaviour (Eça et al., 2019). These small CFL numbers ($CFL \leq 0.01$) are rather difficult to achieve for the complex simulations of the dynamics of FOWTs. Therefore, these fine temporal discretisations were not considered here. Nevertheless, these studies reveal that wave computations with

Navier-Stokes equations solvers are difficult and associated with more uncertainties than one might expect.

Comparison: The approach by Oberhagemann and el Moctar requires constant CFL numbers and a constant refinement ratio. This was achieved for the grids A, C, and E with the time steps $\Delta t_1 = T_p/280$, $\Delta t_3 = T_p/600$ and $\Delta t_5 = T_p/1200$, i.e. for $CFL = 0.14$. The results showed monotonic convergence and were refined with a refinement factor of $r \approx 2$. Figure 4.11 presents the results for the Oberhagemann and el Moctar (OeM) approach compared to the method by Eça and Hoekstra (EH), and Xing and Stern (XS). For the comparison, the notation of Oberhagemann and el Moctar was adopted. The results of the CFD simulations are indicated with black circles and presented as a function of the non-dimensional grid refinement factor Υ . The extrapolated values, using Equations (3.95) and (3.96), are indicated with S1 and S2, respectively. As comparison, the results of the method by Eça and Hoekstra were utilised for nine and five solutions which correspond to the data set selected for the approach by Oberhagemann and el Moctar. In addition, the results of Eça and Hoekstra for 20 simulations and of Xing and Stern are given as reference.

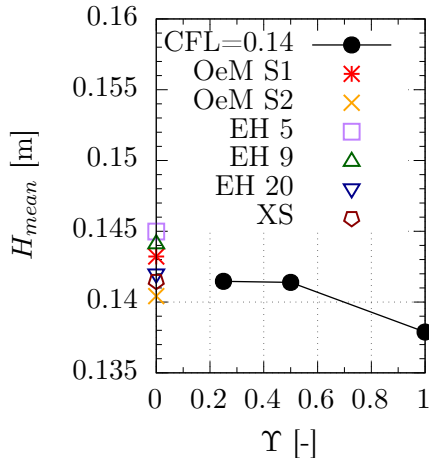


Figure 4.11: Comparison of results for extrapolated grid and time step independent solution of the mean wave height H_{wmean} using the approach by Oberhagemann and el Moctar (OeM), Eça and Hoekstra (EH), and Xing and Stern (XS). The CFD results show the solution for grids A, C, and E. Υ is the non-dimensional grid spacing.

Figure 4.11 and Table 4.7 show a distribution of the results between 0.14042 and 0.14322 for Oberhagemann and el Moctar. These results are very close to the input wave height of $H_w = 0.142$ m, to the mean wave height extrapolated with 20 solutions using the method by Eça and Hoekstra ($H_{wmean} = 0.14193$ m), and to the result using the formulation by Xing and Stern ($H_{wmean} = 0.14147$ m). The results for the finest grid and time step differ less than < 1.2% from S1 and S2, and 0.38% from the input wave height. The results of the method by

Table 4.7: Results for discretisation error and uncertainty estimation of one data set for H_{wmean} using the approach by Oberhagemann and el Moctar (2019). The errors are given in percentage based on the extrapolated value.

Data set	Result with $S1$ [m]	Result with $S2$ [m]	Solution of finest grid [m]	Error ϵ_ϕ $S1, S2$ [%]	Uncertainty $S1, S2$ [%]
ACE, CFL = 0.14	0.14322	0.14042	0.141463	-1.2, 0.7	3.7, 2.2

Eça and Hoekstra with the same grids and time steps revealed larger differences. These values are, however, also within 2.1% from the input wave height. The result of Xing and Stern matches well with the solution of Eça and Hoekstra for 20 solutions and possesses less conservative values than for Eça and Hoekstra with 5 and 9 solutions. Moreover, the results of Eça and Hoekstra were more conservative than of Oberhagemann and el Moctar, and the results became less conservative for estimates with larger amount of solutions. The results tabulated in Table 4.8 present very small error and uncertainty estimates, which indicate a converged solution for this test case when using grid E and Δt_5 . The values for the uncertainty estimates are smallest for the approach by Xing and Stern, small for the new uncertainty estimate for the approach by Oberhagemann and el Moctar, and spread between small and moderate numbers depending on the data set used for the method by Eça and Hoekstra. Nevertheless, the very small values for the approach by Xing and Stern and for the approach by Eça and Hoekstra for the data set “Without AB” do not seem very realistic for this test case. A smaller error estimate for the Xing and Stern method than for the other two methods is to be expected as long as the observed order of convergence is smaller than the theoretical order. Moreover, the approach by Eça and Hoekstra takes convergence along other CFL numbers and the data quality into account. These differences in the formulations result in different error and uncertainty estimates.

Table 4.8: Results for discretisation error and uncertainty estimation of one data set for H_{wmean} using the approach by Xing and Stern (2010). The errors are given in percentage based on the extrapolated value, and multiplied by the convergence ratio.

Data set	Extrapolated value ϕ_0 , [m]	Solution of finest grid and time step ϕ_1 , [m]	Error ϵ_ϕ , [%]	Uncertainty U_{FS} , [%]
ACE, CFL = 0.14	0.14147	0.141463	0.003	0.03

4.1.6 Stokes 5th order

The wave signal, recorded by the probe, was compared with the analytical Stokes 5th order solution. Figure 4.12 presents this comparison. The uncertainty bar represents the discretisation uncertainty for 20 simulations, obtained with the approach by Eça and Hoekstra for H_{wmean} .

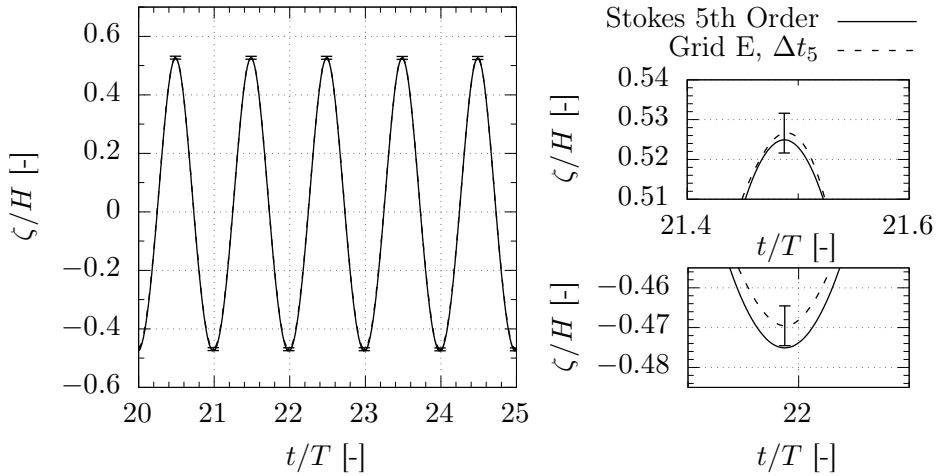


Figure 4.12: Comparison of numerical with analytical result for test case one. Presented are the wave elevations ζ normalised by the theoretical wave height H . The numerical result is the solution with finest grid and time step. A zoom in on one wave crest and trough is shown on the right.

Despite the small uncertainty of 1%, the bar overlaps the difference between the analytical and the numerical wave elevation. Moreover, the zoom depicts a vertical shift of the numerical simulation compared to the analytical solution. This shift is about 1/10th of the size of the grid cell at free surface. This might arise because of the finite discretisation around the free surface. If this different mean value would be subtracted in the plot, the differences would decrease further. Therefore, the numerical simulation represented the theoretical input wave for fine spatial and temporal discretisation. Although line-by-line comparison seemed very good, there were uncertainties and differences between the simulations.

4.2 Wave Loads

If the representation of the wave signal is deemed accurate enough, wave loads on maritime structures may be investigated with confidence. Wave load computations are more complex than wave propagation studies as it involves good modelling of the waves and their loads on the structure owing to pressure and friction. Wave-structure interaction might also include wave run up and reflections from the structure. These effects are higher-order and difficult to capture accurately with numerical simulations using coarse discretisations (space and time) or applying lower-fidelity methods.

4.2.1 Test case description and numerical setup

The wave loads on vertical surface piercing cylinder test case was analysed by the OC5 consortium (Robertson et al., 2015) using mostly potential flow solvers, and by Burmester and Guerin (2016) comparing potential flow and viscous flow

solvers. The test case consisted of a regular wave modelled with Stokes 5th order theory. The calibration for this case resulted in the wave parameters as summarised in Table 4.9.

Table 4.9: Wave characteristics for the wave load test case as in the experiments (Robertson et al., 2015).

Property	Size
Period, T_p	2.114 s
Height, H_w	0.5343 m
Water depth, h	10.0 m

The vertical cylinder, placed as an obstacle in the wave propagation direction, had a diameter of $D = 0.327$ m and a draft below the free surface of 1.44 m. In the model tests, the cylinder was mounted to a carriage above the free surface. Thus, the cylinder was restrained from motions. The water depth was 10 m in the basin.

As in the previous test case, no turbulence model was applied, since the wave loads are pressure dominated (see e.g. Burmester and Guerinel (2016)). Furthermore, they showed that the wave load results were slightly smaller with turbulence model than without. But the difference was insignificant.

The computational domain was a three-dimensional box and was generated with the dimensions listed in Table 4.10. This domain was defined for one symmetrical half of the cylinder. As investigated by Burmester and Guerinel (2016), the loads on the same half cylinder in waves resulted in almost identical values for a full cylinder simulation. The water depths was reduced compared to the experiments still ensuring deep water conditions. These two assumptions were made to lower computational costs. The right-handed coordinate system was chosen to be as follows: x points in wave propagation direction, y horizontally transverse to it, and z vertically upwards.

Table 4.10: Computational domain for test case two.

Property	Size
Wave length (Stokes 5 th order)	$\lambda_w \approx 6.97737$ m
Length	35 m $\approx 5 \cdot \lambda$
Water depth	6.5 m $\approx 1 \cdot \lambda$
Height	10 m
Width	1.635 m $\approx 5 \cdot D$

The boundary conditions for inlet, top, bottom, outlet, and symmetry plane were the same as for the previous test case. The free side was modelled with a slip-wall boundary condition and the cylinder with a no-slip condition. The former boundary restrains normal velocities, while the latter restrains also those in tangential direction. More details may be found in Section 3.1.7. The absorption zones at inlet and outlet were one wave length long. The same body force function and

absorption coefficient as in the wave propagation test case were selected, i.e. a cosine function with $f_{max} = 5$.

In addition to the grid topology guidelines followed in the previous case, extra refinement around the cylinder was achieved to capture wave diffraction effects. The ratio between wave length and cylinder diameter is $\lambda/D \approx 21.34$. Thus, the grid around the cylinder requires further refinement. The computational domain and three different perspectives on the grid are shown in Figure 4.13.

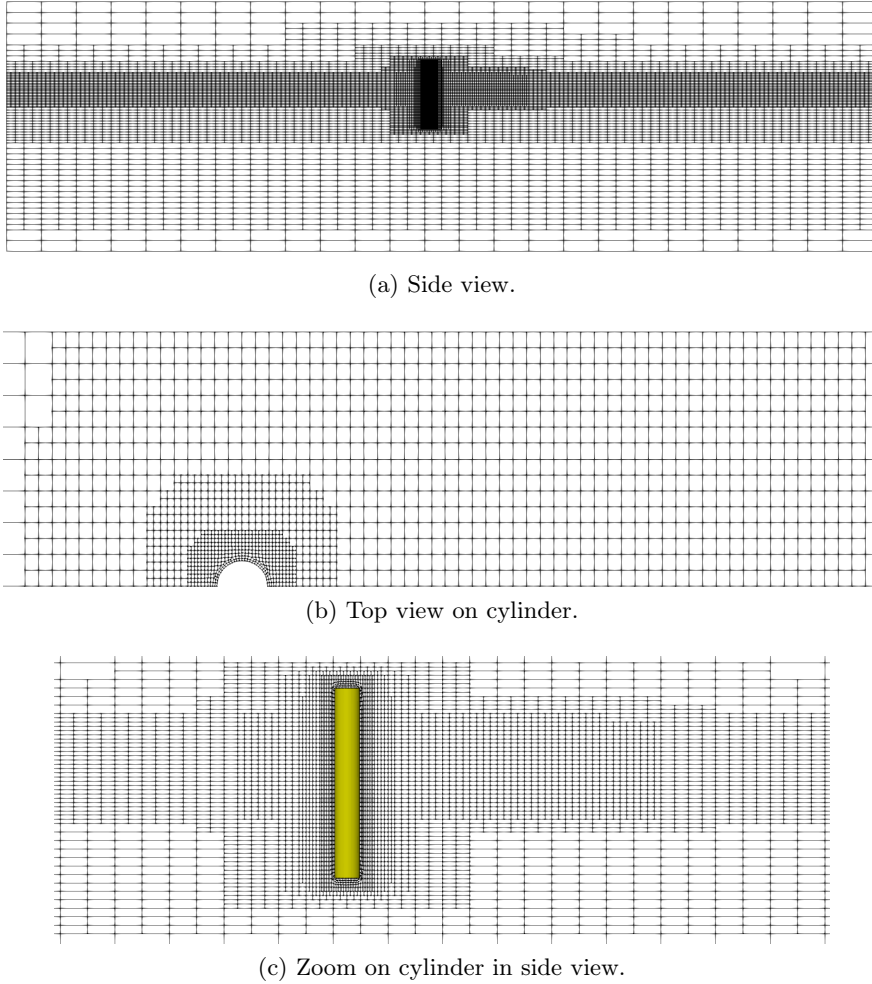


Figure 4.13: Computational domain for test case two with grid in a side view (a), a horizontal slice of the grid at still water line with zoom to refined region (b), and a zoom on the cylinder refinement in side view (c).

As shown in these figures, the extra refinement boxes resolve the domain at free surface in horizontal directions only. The cell sizes in vertical direction were kept constant around the free surface to avoid disturbance of the flow due to grid refinement. Following this procedure, five different grids were generated. Table 4.11 lists the grid characteristics. The cells per wave height and length refer to the

outer free surface refinement box. Hence, one refinement level more was obtained in the vicinity and wake, and two levels more directly on the surface of the cylinder. As turbulent effects were seen negligible, the boundary layer did not receive additional refinement. These grids follow the proposed refinement ratio guideline of the ITTC, i.e. $r = \sqrt{2}$.

Table 4.11: Grid definitions for test case two. The values tabulated show the amount of cells relative to the wave for refinement box A and the total amount of cells. One refinement level more was obtained in the vicinity and wake, and two levels more directly on surfaces of the cylinder than for box A.

Grid name	# cells/wave height	# cells/wave length	total	# of cells
Grid A	20	80		105 382
Grid B	28	113		321 303
Grid C	40	160		796 476
Grid D	56	226		1 828 088
Grid E	80	320		4 087 614

The time steps were defined as a ratio of the wave period T_p : $\Delta t_1 = T_p/400$, $\Delta t_2 \approx T_p/565$, $\Delta t_3 = T_p/800$, $\Delta t_4 \approx T_p/1131$, $\Delta t_5 = T_p/1600$, $\Delta t_6 \approx T_p/2263$, and $\Delta t_7 = T_p/3200$. The time steps follow exactly the same refinement ratio as the grids. Table 4.12 summarises all simulations and tabulates their theoretical CFL numbers.

Table 4.12: Theoretical CFL numbers for test case two. The time steps are defined as a ratio of the wave period $T_p = 2.114\text{s}$, i.e. $T_p/400$ is a coarse and $T_p/3200$ a fine time step.

Grids / Δt	Δt_1 $T_p/400$	Δt_2 $T_p/565$	Δt_3 $T_p/800$	Δt_4 $T_p/1131$	Δt_5 $T_p/1600$	Δt_6 $T_p/2263$	Δt_7 $T_p/3200$
Grid A	0.21	0.15	0.11	0.07	0.05	0.04	-
Grid B	-	0.21	0.15	0.11	0.07	0.05	-
Grid C	-	-	0.21	0.15	0.11	0.07	-
Grid D	-	-	-	0.21	0.15	0.11	0.07
Grid E	-	-	-	-	0.21	0.15	0.11

4.2.2 Wave load results

Figure 4.14 presents the results of the wave load test case for 22 simulations. This figure shows the 27th wave load period of in total 30 waves generated. The results revealed that the loads increase with level of discretisation. Certainly, differences between the coarsest and finest grid are small (5% difference in height of wave load cycle) and are visible only around maxima and minima. This indicates that the influence of the discretisation on the solution is small for the period and important for the wave load peaks.

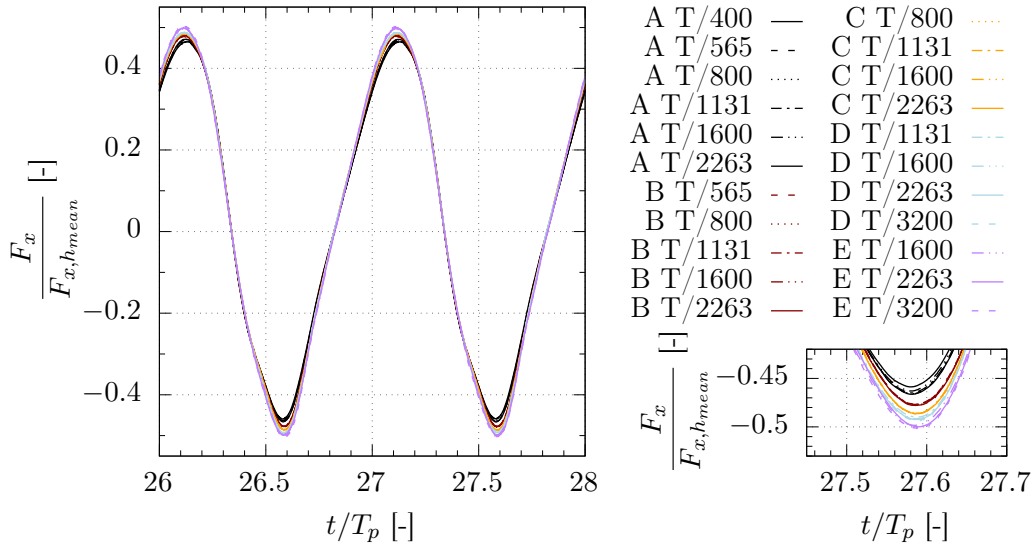


Figure 4.14: Wave loads F_x on the cylinder for 25 simulations with different grids and time steps. The loads are normalised by the mean oscillation height $F_{x,hmean}$ of the finest grid and time step, and the time by the wave period T_p . On the bottom right, a zoom is shown for one negative peak.

The mean oscillation height of the wave load in x direction $F_{x,hmean}$ was determined for the last 10 wave load cycles. The value for the mean oscillation height was 640.320 N and for the corresponding standard deviation 1.6041 N obtained from the simulation with the finest grid and time step. In general, the wave load increases and the standard deviation decreases for finer spatial and temporal discretisation.

The wave load time history presents one way to analyse the results of the numerical simulations. Another way is the visualisation of the flow field around the cylinder. Then, the differences in flow solution and their influence on the computed wave load may be discussed in more detail. Figure 4.15 presents the free surface around the cylinder for three different grids and at five different time instances. The solution is mirrored at the xz plane for visualisation purposes.

The wave propagates from left to right and advances in time from top to bottom for each grid in Figure 4.15. The solution of the finest grid revealed more disturbances in the flow than the solution of the other two simulations. This disturbance influenced the upstream wave profile. Moreover, after the wave passed the cylinder, backflow from the wave may be observed at first downstream of the cylinder. This backflow eventually collapsed upstream of the cylinder when the following wave trough arrived. These small phenomena may be observed in detail on the fine grid and were almost smoothed out for the coarsest grid.

Figure 4.16 visualises the flow velocities in x (wave propagation from left to right) direction at the free surface in top view. The same time instances for the same three grids were taken as in Figure 4.15.

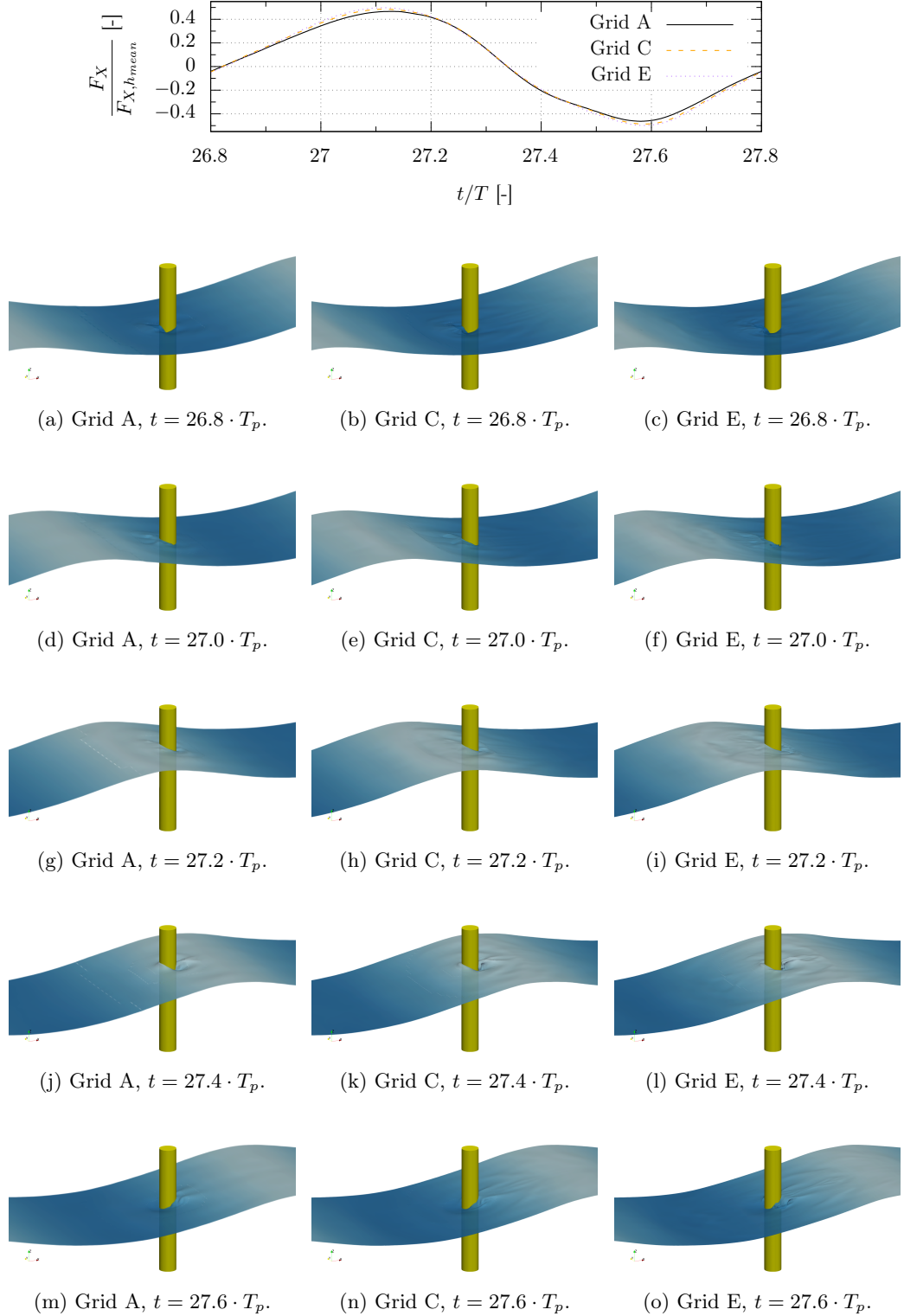


Figure 4.15: Free surface around cylinder (volume fraction of $c = 0.5$) for three different grids with the same time step, i.e. $\Delta t = T_p/1600$.

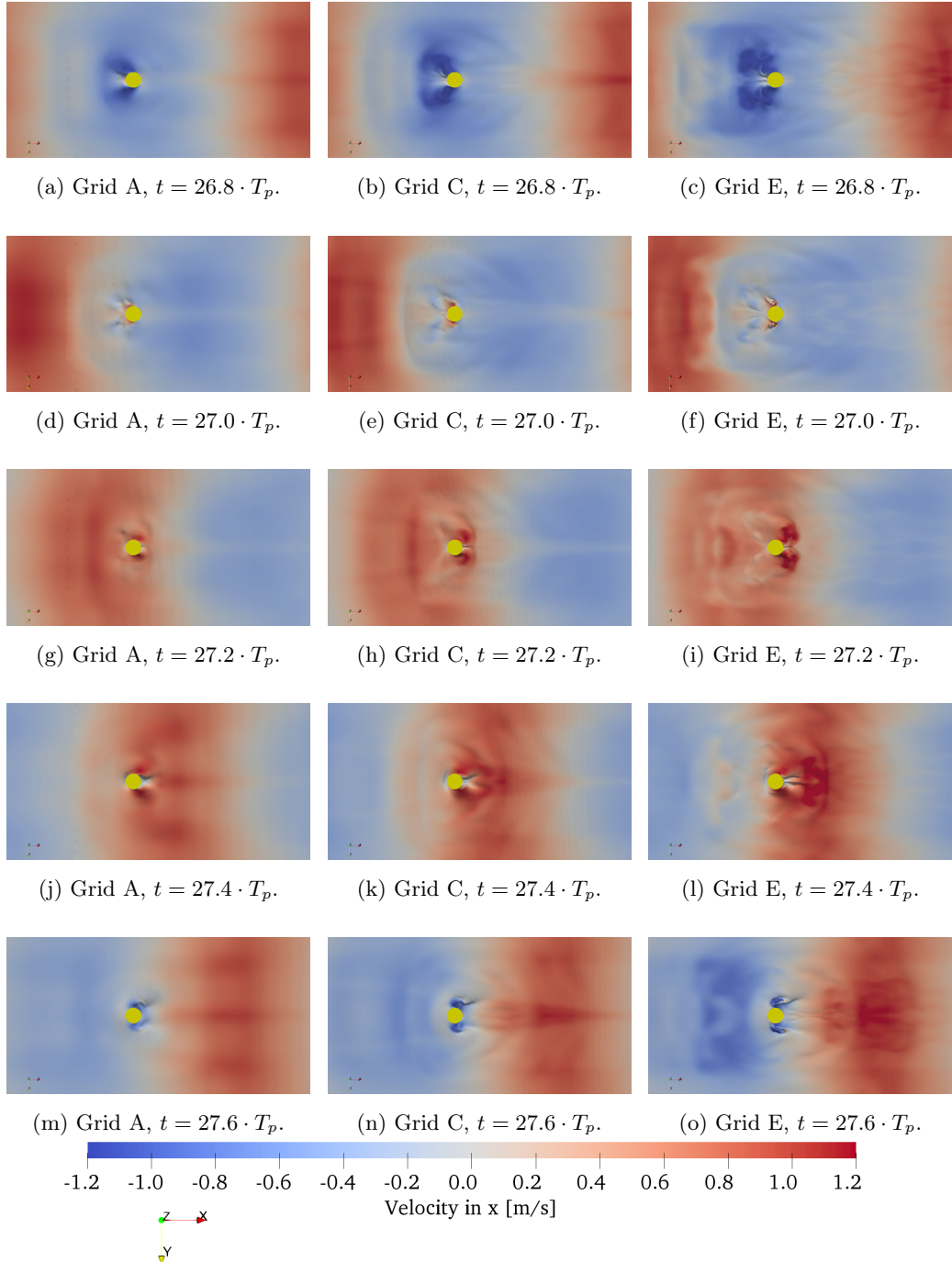


Figure 4.16: x component of velocity at free surface around cylinder (volume fraction of $c = 0.5$) for three different grids with the same time step, i.e. $\Delta t = T_p/1600$. The corresponding CFL numbers are 0.05, 0.11, and 0.21 from left to right, respectively.

The differences in wave elevation, seen in the previous figure, are also present in the flow velocities. At the first and last time instance, the backflow is clearly visible and enhanced for finer grid solution. At $t = 27.2 \cdot T_p$ and $t = 27.4 \cdot T_p$, the flow disturbance accompanied with larger flow velocities clearly differs between the three simulations. Thus, finer spatial and temporal discretisation yielded also smaller modelling errors.

4.2.3 Iterative convergence

Figure 4.17 exhibits the residual convergence at the end of each time step for two examples of the wave load test case. These two examples represent the simulations with the smallest and largest CFL number. The residuals in L_2 norm are plotted for each of these examples.

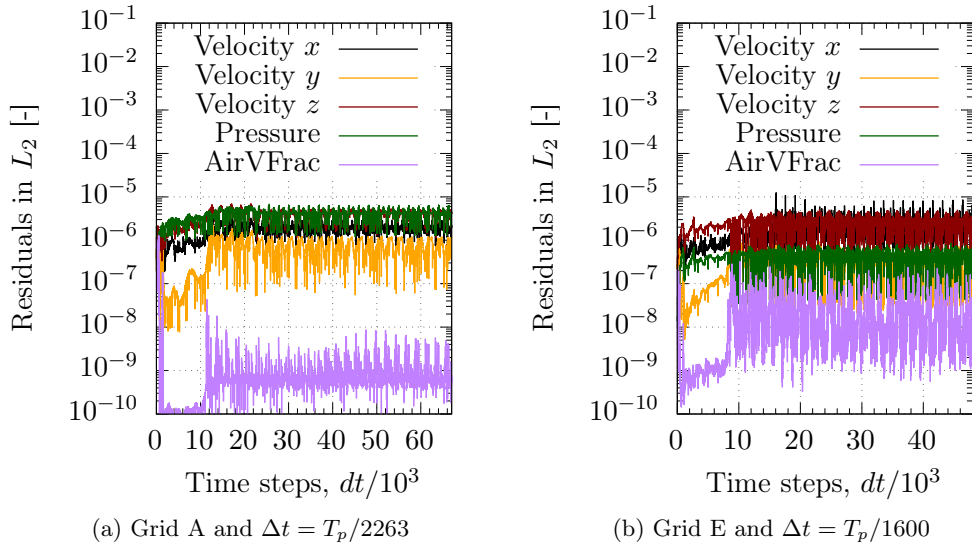


Figure 4.17: Example of iterative convergence for test case two. The normalised residuals are presented in L_2 norm.

Residuals larger than the results presented in these figures are possible. Hence, the residuals are analysed and quantified in Figure 4.18.

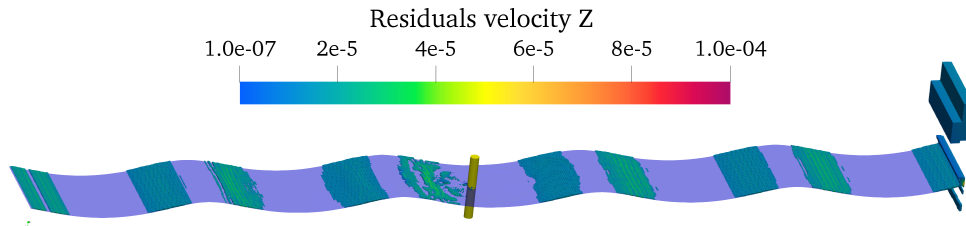


Figure 4.18: Velocity residuals in z direction in the domain for test case two.

Figure 4.18 shows the free surface in light blue and the highest residuals with rainbow colours. The residuals were largest for the vertical velocity v_z , at the free surface, at the outlet boundary condition and around the cylinder. The residuals in the other control volumes converged below 10^{-7} and are blanked for visualisation purposes.

Simulations with $L_\infty < 10^{-4}$, $L_\infty < 10^{-5}$, and $L_\infty < 10^{-6}$ were performed using the finest grid and time step (grid E and $\Delta t_7 = T_p/2263$) to quantify the influence of different iterative convergence criteria. Figure 4.19 exhibits the averaged residuals in L_∞ and L_2 norm.

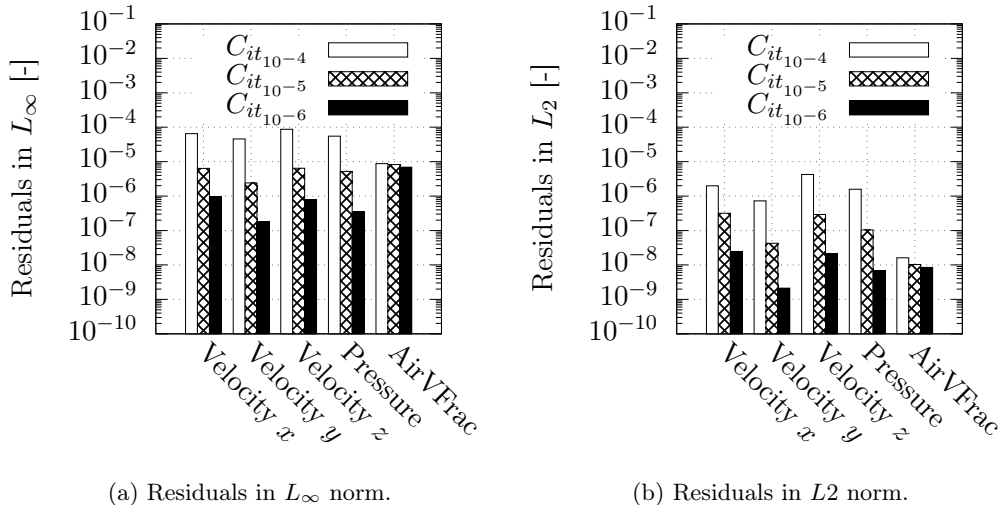


Figure 4.19: Residuals averaged over time for different convergence criteria, i.e. $L_\infty < 10^{-4}$, $L_\infty < 10^{-5}$, and $L_\infty < 10^{-6}$.

Apart from the residuals for the air volume fraction of $L_\infty < 10^{-6}$, all residual quantities converged below the criterion specified. The most critical quantities are the air volume fraction and the vertical velocity. The influence on the mean horizontal wave load heights in-line with the wave propagation $F_{x,h_{mean}}$ is studied as well. The results are summarized in Table 4.13 for the wave load oscillation height, i.e. the difference between maximum and minimum of one zero-upcrossing period. The wave loads are averaged over time as in the previous test case for the wave height after the first 15 waves passed and the first reflected waves could be back from the outflow boundary.

The results depict monotonic convergence with differences between simulation $C_{it}10^{-4}$ and $C_{it}10^{-6}$ of 0.7%.

4.2.4 Discretisation errors

The mean oscillation height of the wave loads were employed to estimate the discretisation error and uncertainty for test case two. These loads are a sum of all loads acting on the cylinder in x direction.

Table 4.13: Influence of the iterative convergence criterion on the mean wave load heights using grid E and $\Delta t_7 = T_p/2263$. The standard deviation of the mean quantities are below 0.3%.

Simulation	Mean wave load height $F_{x,h_{mean}}$ [N]	Mean wave load period $T_{LP_{mean}}$ [s]
$C_{it_{10^{-4}}}$	621.426	2.1142
$C_{it_{10^{-5}}}$	625.863	2.1136
$C_{it_{10^{-6}}}$	625.887	2.1136

Eça and Hoekstra approach: The approach by Eça and Hoekstra was also applied using different data sets for this test case. The sensitivity on the data set selected can be analysed in this way. As a reference solution, a result is given for all 22 simulations. 30 wave periods were simulated of which the last 15 waves were analysed. Figure 4.20 visualises the results.

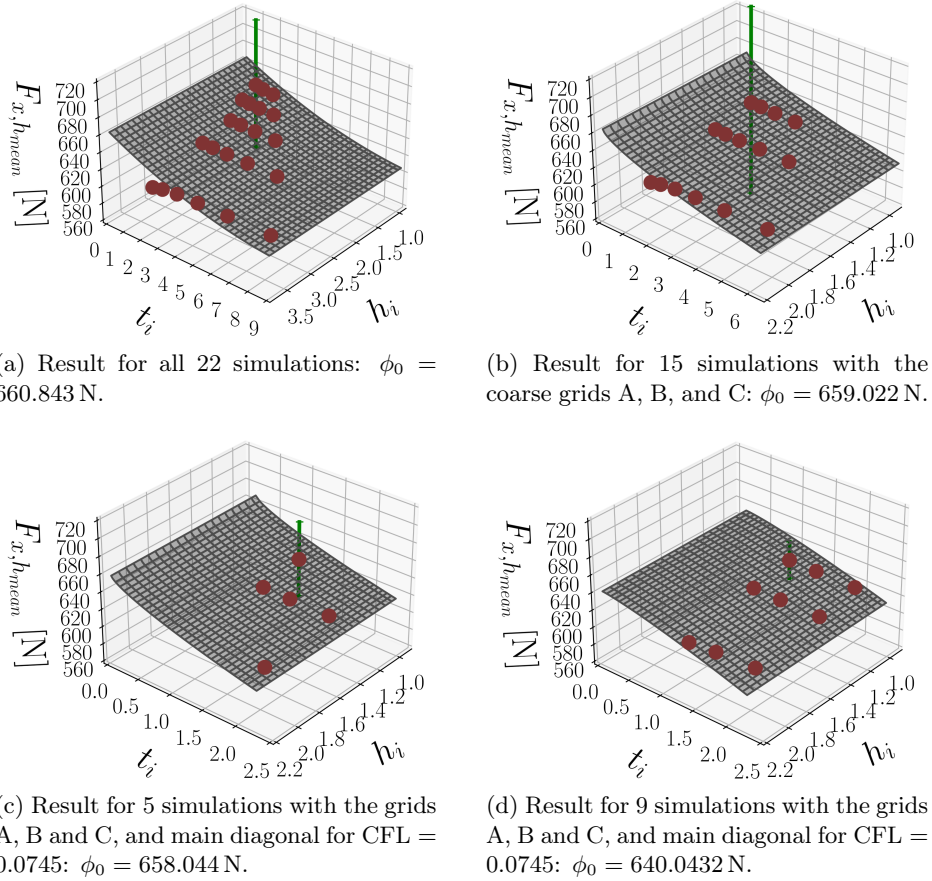


Figure 4.20: Discretisation error and uncertainty estimation using the approach by Eça and Hoekstra (2014) for the mean of the wave load height $F_{x,h_{mean}}$ with different data sets. Each data point is defined with non-dimensional grid h_i and time step t_i spacing.

The results of Figure 4.20 exhibit larger differences between each other than for test case one. The shape of the fitted surface also changes depending on the selected cases. The results of the error and uncertainty estimation are summarised in Table 4.14.

Table 4.14: Results for discretisation error and uncertainty estimation for different sets of grids and time steps for the mean oscillation height of the wave load $F_{x,h\text{mean}}$ using the approach by Eça and Hoekstra (2014). The errors are given in percentage based on the extrapolated value.

Data set	Extrapolated value ϕ_0 , [N]	Solution of finest grid and time step ϕ_1 , [N]	Error ϵ_ϕ , [%]	Uncertainty U_ϕ , [%]
22 solutions, ABCDE	660.843	640.320	3.1	12.0
15 solutions, ABC	659.022	623.082	5.5	18.1
11 solutions, CDE	686.426	640.320	6.7	22.7
16 solutions, BCDE	671.451	640.320	4.9	15.8
9 solutions, ABC	640.432	623.082	2.7	3.5
5 solutions, ABC	658.044	623.082	5.3	7.0
9 solutions, BCD	661.216	630.391	4.7	6.2
5 solutions, BCD	665.308	630.391	5.3	6.9

For this test case, a difference of 6.7% for the extrapolated grid and time step independent value of the mean oscillation height of the wave load $F_{x,h\text{mean}}$ was found depending on the data set selected. The estimated uncertainty ranges from 3.5 – 22.7%. This value has a larger difference from the estimated error for oscillatory convergent data and is closer to the solution of the finest grid and time step for monotonic convergent data. Monotonic convergence on the diagonal was achieved for the four results with five and nine grid sets. For these data sets, uncertainties were lower than for oscillatory data. Thus, scatter in the data and too coarse discretisation penalise the uncertainty U_ϕ . Moreover, reflections from the side boundaries occur as no absorption zone and Sommerfeld boundary condition were defined. These reflections might influence the wave load results and involve scatter.

Oberhagemann and el Moctar approach: Figure 4.21 shows the results with the approach by Oberhagemann and el Moctar. These are the data sets that produced monotonic convergence.

Ten data sets could be found with monotonic convergent data. Eight of these sets are visualised in Figure 4.21. The results are also summarised in Table 4.15.

The results obtained with the approach by Oberhagemann and el Moctar for these ten data sets showed a distribution of extrapolated values for ϕ_0 ranging from 613.169 N to 663.282 N. This is a difference of about 7.6%. Apart from two cases, the linear method by Oberhagemann and el Moctar, $S1$, produced lower results for ϕ_0 than the results including a second order term, $S2$. The results with the first order term were also closer to the finest grid solution apart from the same two cases. Therefore, the errors listed in Table 4.15 were smaller for the first

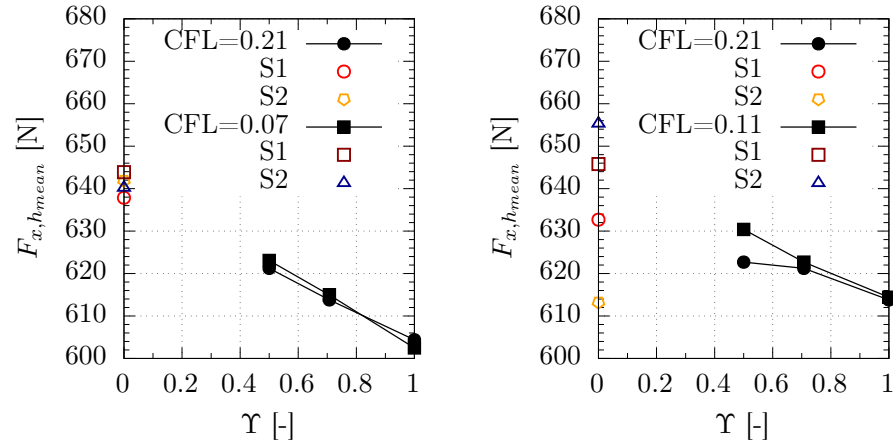
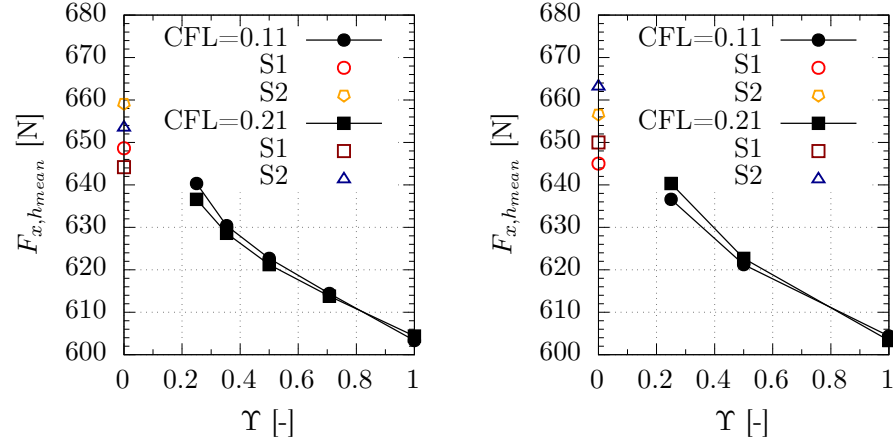


Figure 4.21: Comparison of results for extrapolated grid and time step independent solution for the mean oscillation height of the wave load $F_{x,h_{mean}}$ using the method by Oberhagemann and el Moctar. The results are presented as a function of the non-dimensional grid spacing Υ .

order than the first plus second order solution. The data sets BCD with $CFL = 0.21$ and ABC $CFL = 0.07$ are different and result in lower discretisation errors for $S2$. This demonstrates that the observed order of convergence is closer to the theoretical order of convergence for second order schemes. The estimated uncertainties, however, suggest present results of three times the error estimate. Thus, the results are not within 20% of the theoretical order of convergence. As these simulations were conducted with second order approximations, the results for $S2$ are seen more reliable and taken for comparison with the results of the other two methods.

Table 4.15: Results for discretisation error and uncertainty estimation for different data sets for the mean oscillation height of the wave load $F_{x,h_{mean}}$ using the approach by Oberhagemann and el Moctar (2019). The errors are given in percentage based on the extrapolated value.

Data set	Result with $S1$ [N]	Result with $S2$ [N]	Solution of finest grid [N]	Error ϵ_ϕ $S1, S2$ [%]	Uncertainty $S1, S2$ [%]
ABCDE, CFL = 0.11	648.613	659.091	640.320	1.3, 2.8	3.8, 8.5
ABCDE, CFL = 0.21	644.169	653.614	636.588	1.2, 2.6	3.5, 7.8
ABCD, CFL = 0.07	646.244	650.935	631.585	2.3, 3.0	6.8, 8.9
ABC, CFL = 0.21	637.838	641.846	621.227	2.6, 3.2	7.8, 9.6
ABC, CFL = 0.11	641.895	643.977	622.675	3.0, 3.3	3.7, 9.9
ABC, CFL = 0.07	643.877	640.340	623.081	3.2, 2.7	9.7, 8.1
BCD, CFL = 0.11	645.804	655.447	630.391	2.4, 3.8	7.2, 11.5
BCD, CFL = 0.21	632.673	613.169	622.675	1.6, 1.6	4.8, 4.8
ACE, CFL = 0.11	649.990	663.282	640.320	1.5, 3.5	4.5, 10.4
ACE, CFL = 0.21	645.008	656.576	636.588	1.3, 3.0	3.9, 9.1

Comparison: A comparison between the results for the three discretisation error estimation methods was done for this test case. Figure 4.22 visualises the results. The solutions of the grids A, B, C, D, and E for CFL numbers between 0.11 and 0.21 are presented in these figures as solid black markers. Their extrapolated values using five solutions for the method by Eça and Hoekstra (EH 5) or nine (EH 9) or 22 (EH 22), the corresponding results by Oberhagemann and el Moctar (OeM), and Xing and Stern (XS) are exhibited for $\Upsilon = 0$.

The results of Figure 4.22 indicate that the solutions with the method by Eça and Hoekstra were more conservative than those by Oberhagemann and el Moctar, and both more conservative than Xing and Stern. The solution obtained by Eça and Hoekstra for 22 simulations was closest to the solution by Oberhagemann and el Moctar for CFL = 0.11 and five grids. For this test case, the results of Xing and Stern, listed in Table 4.16, revealed very small discretisation errors. The uncertainties, however, are in a similar range as the values estimated using the approach by Eça and Hoekstra. The uncertainties for the method by Oberhagemann and el Moctar tend to possess lower values than the other two methods.

For cases with a lower observed order than theoretical order of convergence, the error estimate of Xing and Stern reduces compared to the other methods as the estimate is multiplied by the convergence ratio. The uncertainty estimate, how-

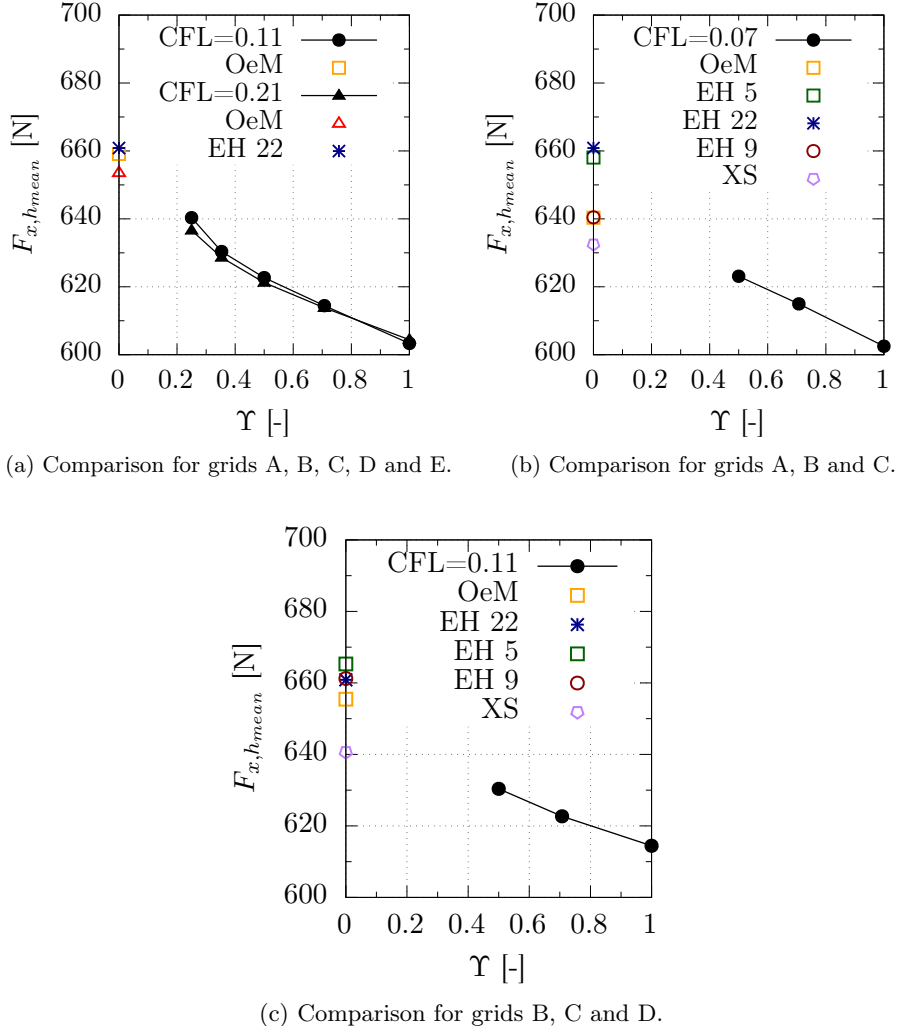


Figure 4.22: Comparison of results for extrapolated grid and time step independent solution using the approaches by Oberhagemann and el Moctar (OeM), by Eça and Hoekstra (EH), and by Xing and Stern (XS) for test case two. The results of the mean wave load heights $F_{x,h_{mean}}$ are shown with non-dimensional grid spacing factor Υ .

ever, accounts for the discrepancy in the order of convergence. The error estimate of the approach by Oberhagemann and el Moctar relies on a least-squares fit of the data and is not reduced by the convergence ratio. It solely relies on the theoretical order of convergence. The discrepancy, however, is accounted for in the uncertainty estimate by a step function of the safety factor. These differences lead to smaller error estimates for the approach by Xing and Stern and similar uncertainty values compared to the approach by Oberhagemann and el Moctar. The method by Eça and Hoekstra relies on different CFL numbers, and hence, allows for a convergence outside of the main CFL number. This explains the small

differences in the error estimate and extrapolated value when compared with the approach by Oberhagemann and el Moctar. Moreover, the data quality and the type of convergence is reflected in the uncertainty estimate. This method may also be applied to non-monotonic convergent data. The data quality measure (see Equation (3.88)) reduces for more data points. Therefore, the uncertainty estimates for more data points are smaller than for less data. This procedure also results in slightly different uncertainty values than the other two methods.

Table 4.16: Results for discretisation error and uncertainty estimation of different data sets for the mean of the wave load height $F_{x,h,mean}$ using the approach by Xing and Stern (2010). The errors are given in percentage based on the extrapolated value, and multiplied by the convergence ratio.

Set combination	Extrapolated value ϕ_0 , [N]	Solution of finest grid and time step ϕ_1 , [N]	Error ϵ_ϕ , [%]	Uncertainty U_{FS} , [%]
ACE, CFL = 0.11	650.970	640.320	1.6	13.9
ACE, CFL = 0.21	645.859	636.588	1.4	12.3
ABC, CFL = 0.07	632.473	623.081	1.5	4.6
BCD, CFL = 0.11	640.586	630.391	1.5	13.6

4.2.5 Validation

The aim of such a large study should be to validate the numerical simulations with experimental data. Experimental data were available from the OC5 study Robertson et al. (2017b). Figure 4.23 presents the comparison of the numerical simulations with experimental data. The uncertainty bars plotted in this figure represent the discretisation uncertainty of the finest grid and time step for 22 simulations obtained by the method of Eça and Hoekstra (Table 4.14).

No errors and uncertainties of the experiment were available. Thus, no formal validation of the numerical simulations can be done for this test case. The time trace and the uncertainty bars presented in Figure 4.23, however, showed a good match with the experimental results. The mean and standard deviation of the wave load heights, $F_{x,h}$, obtained after 10 wave periods for the finest grid and time step were: $640.320 \text{ N} \pm 1.6041 \text{ N}$ (0.25%). The corresponding values for the experiment for the last 28 waves were: $672.108 \text{ N} \pm 12.9296 \text{ N}$ (1.92%). The comparison error between the experiment and the numerical simulation (= 4.96%) was also smaller than the discretisation uncertainty for the statistical values.

4.3 Concluding Remarks on Waves and Wave Loads

The work of this chapter included simulations for wave propagation and loads on a cylinder for several different grids and time steps to estimate the discretisation errors and uncertainties. For the wave propagation and wave load simulations the discretisation error estimation approaches developed by Eça and Hoekstra (2014), Oberhagemann and el Moctar (2019), and Xing and Stern (2010) were

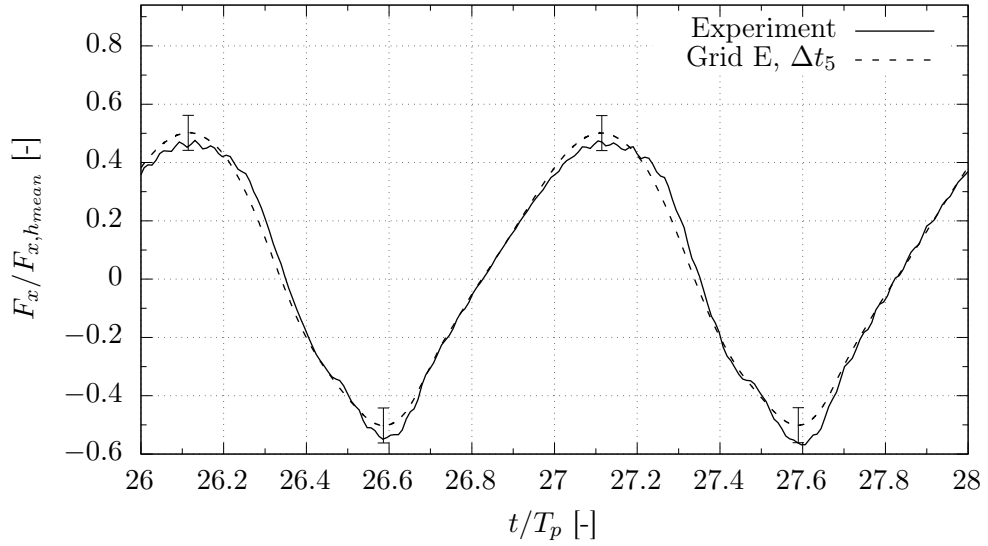


Figure 4.23: Comparison of numerical and experimental results of wave loads F_x for test case two, including uncertainty bars obtained with the method by Eça and Hoekstra for 22 simulations. The experimental data was taken from Robertson et al. (2015). The wave loads are normalised by the mean oscillation height $F_{x,h,mean}$ of the numerical simulation.

compared. Details on the numerical settings, the computational setup, and the iterative convergence were also given. In addition, the difference of two wave absorption functions were studied and their optimum found. Finally, the results of each test case were compared either to the analytical solution (wave propagation) or to available experimental data (wave loads).

The step-by-step approach, with increasing complexity in the test cases and the comparison of three different methods to estimate the discretisation error, provide a way towards increased credibility for numerical simulations of waves and fixed objects in waves.

From this extensive study, the following conclusions may be drawn:

- Guidelines for the grid generation exist to perform CFD simulations of waves. Applying these guidelines provides a safe method to obtain accurate results. Nevertheless, these guidelines might need revision for simulations with wave structure interaction. This is important in particular for simulations with significant differences between the dimensions of wave and structure as shown in this wave load study.
- Spatial and temporal discretisation also determines the level of modelling accuracy as certain effects are smoothed out by too coarse resolution.
- The outcome of these two test cases, wave propagation and wave load, were very close to the analytical and experimental result: 0.4% and 4.96%, respectively. Therefore, it may be assumed that the choice of spatial and temporal

discretisation was sufficiently accurate for typical engineering applications.

- The three discretisation error techniques revealed consistent output for the two test cases. The difference of the extrapolated grid and time step independent solutions for the different methods was always less than 10%.
- For most of the data sets, the method by Eça and Hoekstra resulted in more conservative (larger) discretisation errors than the approach by Oberhagemann and el Moctar, and both were larger than the results using the formulation by Xing and Stern. In addition, the uncertainty estimation by Eça and Hoekstra takes scatter in the data into account. The technique by Eça and Hoekstra, however, requires at least five solutions to estimate an error while the methods of Oberhagemann and el Moctar, and of Xing and Stern can yield reliable estimates with three solutions once the data is monotonic convergent.
- The approach by Oberhagemann and el Moctar is less robust for more data, against scatter, and if the results are non-monotonic. On the other hand, this method is faster and reduces computational costs.
- Additionally to the discretisation errors, the approaches by Eça and Hoekstra, and Xing and Stern provide uncertainty estimates. The uncertainty estimates of Xing and Stern rely on just three solutions but yielded similar results compared with the results of the formulation by Eça and Hoekstra.
- In this thesis, a new uncertainty formulation was proposed to compensate for this disadvantage of the method by Oberhagemann and el Moctar compared to the other two methods. The new uncertainty estimate includes the quality of the simulation data by changing the safety factor as a function of the convergence ratio. In general, this method predicted slightly lower values for the uncertainty than the other two approaches. Very large discrepancies between theoretical and observed order of convergence do not result in larger uncertainties. Very poor quality of the data is accounted for using the other two uncertainty estimates. Therefore, more investigation is required to optimise the uncertainty estimation method.
- The iterative convergence of the numerical equations was studied by comparing the residuals in L_∞ and L_2 norm. In addition, the results for different convergence criteria were compared to each other. For periodic simulations such as waves, the influence of the iterative convergence criterion is not significant.
- Experimental data including errors and uncertainties are important to formally perform validation. Errors and uncertainties for model test data are seldom provided and were not available here. Nevertheless, the uncertainty bars for the solution with the finest grid and time step overlapped the experimental result for the wave load test case. The results for errors and uncertainties of the wave propagation test case also overlapped the analytical solution.

Chapter 5 provides further work on verification and validation as well as hydrodynamic damping using the OC5 semi-submersible floating platform.

5. Hydrodynamic Damping

This chapter is dedicated to investigations of a moored semi-submersible floating wind turbine in surge decay. The investigations were conducted in order to obtain the numerical and physical ingredients of accurate floating wind turbine simulations using CFD. These ingredients involve the discretisation errors and uncertainties of the viscous-flow simulations and of the dynamic mooring model, different input parameters such as initial displacement, release time and restoring stiffness, and several models, e.g. turbulence models, free surface, and mooring models.

5.1 Test Case Description

The semi-submersible and the mooring system described in this section were used for the work of this chapter. At first, the semi-submersible and mooring layout are described as given by the experiments. Then, the numerical setup is detailed including boundary conditions, domain dimensions, and grid generation.

5.1.1 Semi-submersible and mooring layout

The surge decay simulations were performed with the OC5 DeepCwind semi-submersible floating wind turbine (Robertson et al., 2017b). Work with the same floater was also published in Burmester et al. (2017, 2020c,b), and Robertson et al. (2017b). Solely the floater geometry was simulated, but the mass properties of the whole system including floater, tower, nacelle, and rotor were used.

Semi-submersible and coordinate system: The floater geometry and the coordinate system are presented in Figure 5.1.

A right-handed coordinate system was adopted in this work: the x coordinate pointed in forward (surge) direction, the y coordinate in transverse (sway) direction, and the z coordinate vertically upwards (heave). The system's origin was set to the centre of gravity of the floating structure (see Table 5.1).

The decay tests were performed with an initial displacement of 0.167 m in surge. The computations were performed at model scale with a scaling factor of 50.

The main particulars of the floating system and the stiffness properties are summarised in Table 5.1 and Table 5.2, respectively. The stiffness properties are the diagonal values of the linear mooring restoring matrix.

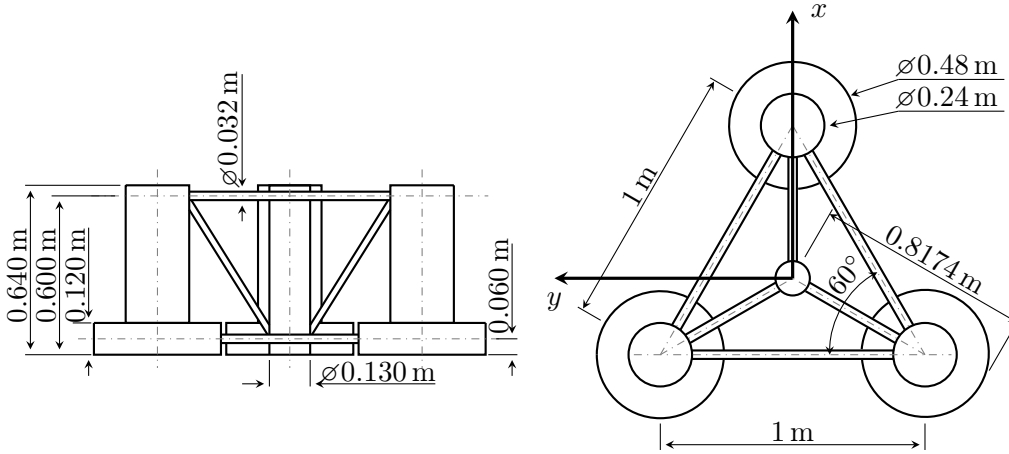


Figure 5.1: Drawing of the OC5 DeepCwind semi-submersible (Robertson et al., 2017b) at model scale (scaling factor of 50) including dimensions and coordinate system as simulated, adapted from Burmester et al. (2020b).

Table 5.1: Main particulars of the floating wind turbine system.

Designation	Value
Draft	0.4 m
Mass	111.664 kg
Centre of gravity above keel	0.2386 m
Roll radius of gyration	0.6526 m
Pitch radius of gyration	0.6676 m
Yaw radius of gyration	0.6264 m

Table 5.2: Linearised stiffness properties of the mooring system. The values are given with respect to the centre of gravity.

Designation	Value
Surge	33.84 N/m
Sway	29.4 N/m
Heave	7.76 N/m
Roll	12.21 Nm/rad
Pitch	16.96 Nm/rad
Yaw	19.168 Nm/rad

Mooring layout and characteristics: The experiments of the OC5 semi-submersible were performed with a catenary mooring system for station keeping. The mooring setup replaces the restoring stiffness given in Table 5.2 and contains an external damping description, i.e. the mooring loads replace \vec{f}_C and \vec{f}_D in Equation (2.102). The moorings were placed 120° apart from each other: one in front and two to the sides (starboard and portside). The anchors were located horizontally at 16.76 m from the centre column and at a depth of 4.0 m below the still water line. A mooring line with a length of 16.71 m connects each anchor to the fairlead. Figure 5.2 illustrates a schematic setup with semi-submersible floater in a top view.

Table 5.3 lists the mooring line characteristics as calibrated by Gueydon (2016) for the OC5 semi-submersible. The drag and inertia coefficients as well as the element diameter were used to calculate the hydrodynamic forces induced on the mooring lines. The axial damping is given relative to the critical damping $B_{crit} = 2\sqrt{MC}$. In this equation, M is the mass and C the stiffness. The term submerged

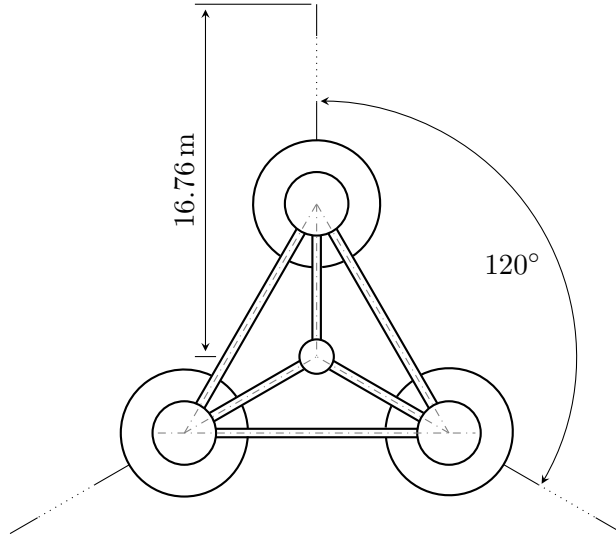


Figure 5.2: Mooring setup for OC5 DeepCwind semi-submersible (Robertson et al., 2017b) at model scale (scaling factor of 50).

weight means the mass reduced by the buoyancy of the element. As the mooring lines are totally submerged between anchor and fairlead, the submerged weight is distributed uniformly along the line and lumped at the nodes between the spring and damper elements, see Figure 3.5 for further explanation.

Table 5.3: Mooring characteristics as given by Gueydon (2016).

Designation	Value	Units
Length	16.71	[m]
Mass/meter	0.05024	[kg/m]
Submerged weight/meter	0.431917	[N/m]
Axial stiffness	5989.0666	[N/m]
Element diameter	0.00277372	[m]
Axial damping ratio	5.0	[%]
Normal drag coefficient, C_{D_n}	2.4	[\cdot]
Tangential drag coefficient, C_{D_t}	0.8	[\cdot]
Normal inertia coefficient, C_{M_n}	3.1	[\cdot]
Tangential inertia coefficient, C_{M_t}	1.7	[\cdot]

The initial state of the mooring line shape was calculated by the catenary equations (Section 2.6). Figure 5.3 shows the resulting configuration for the present case. For visualisation purposes, a simplified floater geometry and a coordinate system were added to the drawing. Parts of the mooring lines laid on the seabed. The touch down point was variable and calculated for each time step. The end of each line marks the anchor position.

This mooring layout was used for simulations coupled with the quasi-static and the dynamic mooring model. All other simulations were performed with the linearised

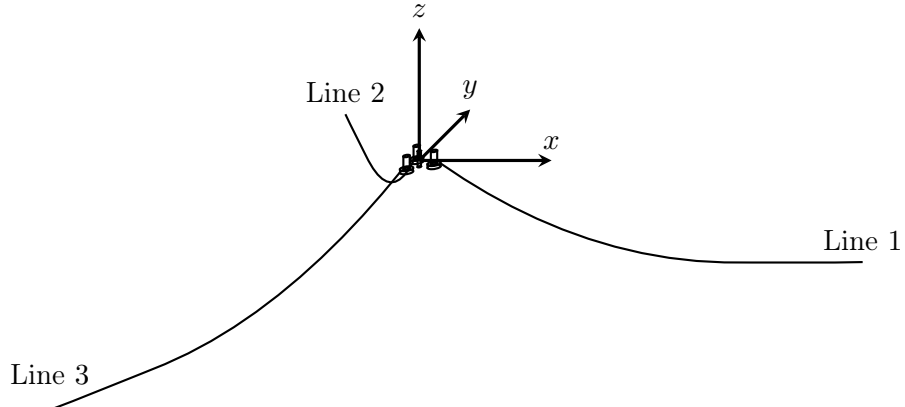


Figure 5.3: Initial mooring line configuration for lines 1, 2 and 3 connected to a simplified model of the semi-submersible.

stiffness properties as listed in Table 5.2.

5.1.2 Numerical Setup

Two computational domains were created and employed for the numerical simulations of this work. The domains had a symmetric half and a full cylinder shape. The dimensions, boundary conditions and grid topology are detailed next.

Computational domains and boundary conditions: The computational domain for parts of the simulations was modelled as a semi-cylinder in such a way that it forms a symmetric half with respect to the xz plane. The domain had a total height of 4.6 m, a water depth of $h = 4.0$ m, and a radius of 4.9 m. The radius corresponds to six times the characteristic radius of the semi-submersible, 0.8174 m. The water depth was adopted from the experiments. The computational domain is illustrated in Figure 5.4.

At the bottom and top of the domain, a static pressure was prescribed. The boundaries of the semi-submersible were represented with no-slip conditions. For the xz plane, a symmetry condition was applied for the half domain simulations. The curved surface area was modelled as a non-reflecting boundary condition of Sommerfeld type (Sommerfeld, 1949), see also Section 2.4.3. In contrast to the wave propagation and wave load cases, no waves were generated, and therefore no absorption zones were used for most of the simulations. The benefit of using absorption zones for surge decay simulations is addressed in Section 5.4.2. Subsequently, wave absorption is applied to simulations with full domain configuration. Furthermore, the KSKL turbulence model (see Section 2.3) was applied for the numerical simulations, if it is not stated otherwise. The flow in the domain was assumed laminar at the initial condition. Therefore, a turbulent viscosity ratio was specified initially with $\mu_t/\mu = 0.01$ in the domain.

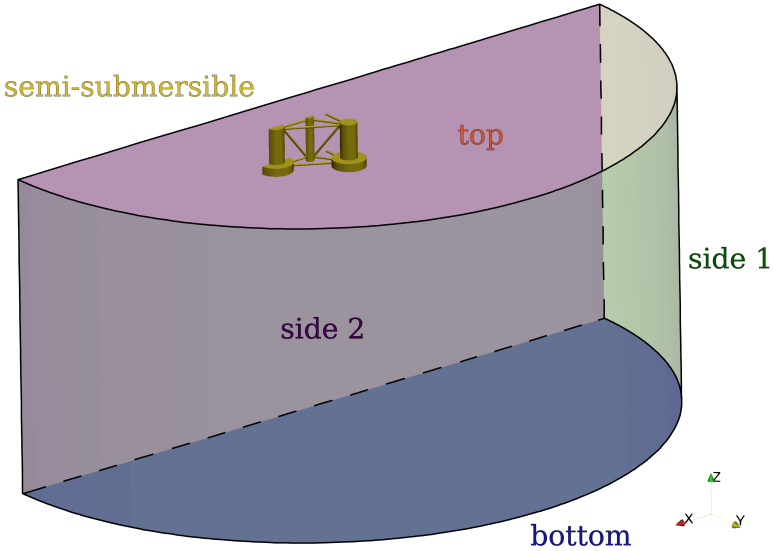


Figure 5.4: Computational half domain including boundaries for the surge decay simulations (Burmester et al., 2020c).

Grid topology: The grid topology was chosen in such a way that the cell size reduces towards the semi-submersible floater and towards the free surface. At the free surface, the refinement in vertical direction was kept constant to reduce the amount of hanging nodes in this direction. The grid was also refined on the curves and surfaces of the semi-submersible. The hull above water was refined as much as needed to cover curves and surfaces. At critical geometrical points, more refinement was needed to capture the contour of the geometry (see Figure 5.5).

Table 5.4 summarises the size, location, and level of refinement of each refinement box. The boxes are formed according to the domain shape as a cylinder with radius and height. The refinement diffusion was kept constant with 3 cells as transition between refinement regions. The surfaces above water were refined with a level of 2 and below water with 4. The edges of the geometry were refined with a refinement level of 5 and at the three pipe connector on the centre column of 7. In addition, an internal surface was defined at the location of the free surface. This internal surface refined the grid in x and y with a level of 3, and in z with a level of 4. Due to the internal surface and the cell sizes, the cell faces were aligned with the initial location of the free surface. These refinement proportions were kept constant for all grids, i.e. just the initial cell size was adjusted. This procedure follows in principle the guideline given by Crepier (2017).

For all grids, viscous layer cells were generated to guarantee a non-dimensional wall distance value of $y_{max}^+ < 1.5$. This goal was achieved regardless of the total grid size. For full domain simulations, the grid was mirrored at the xz plane to ensure geometrically similar grids.

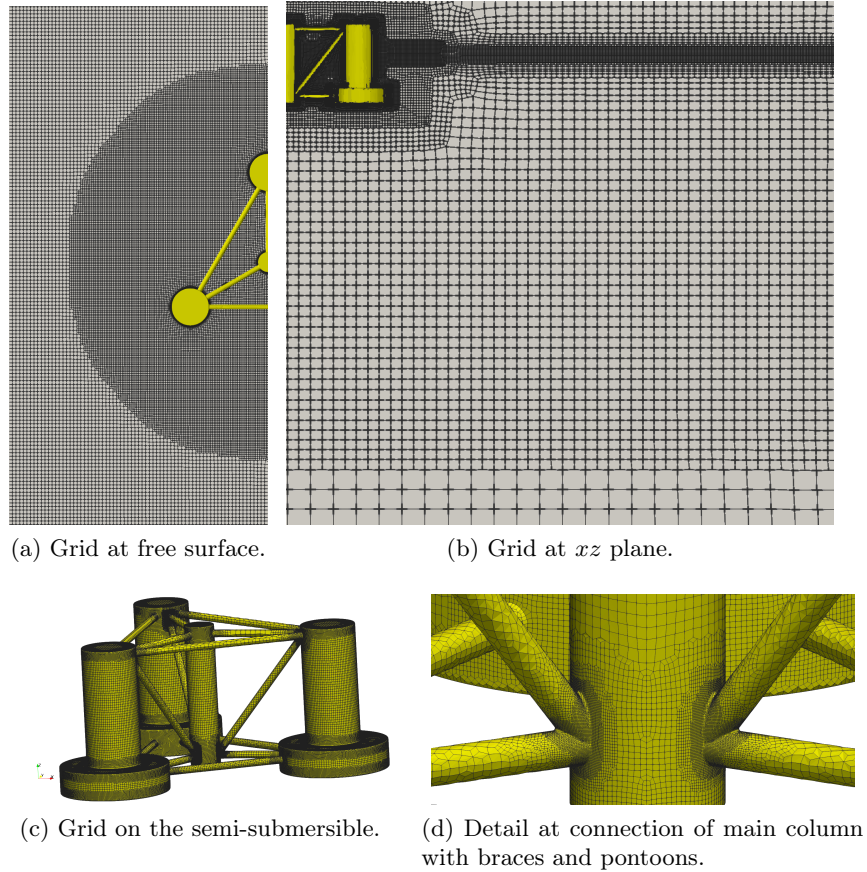


Figure 5.5: Grid topology for surge decay simulation presented for the coarse grid.

Table 5.4: Grid topology for the surge decay simulations. Presented is each refinement box in cylindrical form with origin, height and radius. Each box has a certain degree of refinement ($2^{\text{Refinement level}}$ per coordinate direction).

Region	Origin, [m]	Radius, [m]	Height, [m]	Refinement level
Domain	(0, 0, -4.0000)	4.9	4.60	0
Box 1	(0, 0, -2.5000)	4.9	3.25	1
Box 2	(0, 0, -0.2800)	1.0	0.70	3
Box 3	(0, 0, 0.1264)	1.2	0.07	4

5.2 Discretisation Errors and Uncertainties

In this section, the results of the verification studies are analysed for the OC5 semi-submersible in surge decay motions using a linearised stiffness matrix and for the dynamic mooring model decoupled from the CFD solver. These two sets of simulations were performed individually to estimate their influence on the total discretisation error and uncertainty. The accurate prediction of the hydrodynamic

loads form the basis for simulations with floating structures. Therefore, the influence of the spatial and temporal discretisation are investigated in this section.

5.2.1 Viscous-flow simulations

Because of the complex geometry of the floater, more complex grids and numerical settings are required than for the wave propagation and wave load simulations. Thus, more sources of uncertainty are present and higher values are expected.

Numerical simulations: Different grids were generated with the topology guidelines given in Section 5.1.2. These grids are listed in Table 5.5.

Table 5.5: Grid definitions for surge decay simulations. The table presents the refinement factors of the base cell size w.r.t. the previous grid and the total amount of cells.

Grid name	Refinement factor	Total # of cells
Grid A	-	3 425 233
Grid B	1.333	5 609 092
Grid C	1.333	9 900 573
Grid D	1.333	17 836 326

The time steps were defined as a ratio of the oscillation period, $T_p \approx 15.5563$ s: $\Delta t_1 = T_p/3200$, $\Delta t_2 = T_p/4800$, $\Delta t_3 = T_p/6400$, $\Delta t_4 \approx T_p/8533$, $\Delta t_5 = T_p/12800$. These small time steps were required to decrease the theoretical CFL numbers below 1 and into the TVD stable region. The simulations are summarised in Table 5.6 with the theoretical CFL numbers obtained. The theoretical CFL number was calculated based on the smallest cell size outside of the viscous layer in x direction, the maximum surge decay velocity, and the time step. There is a set of three grids that can be employed for the Oberhagemann and el Moctar approach. In addition, results of all 18 simulations are suited for the approach by Eça and Hoekstra.

Table 5.6: Theoretical CFL numbers for surge decay simulations. The time steps are defined as a ratio of the oscillation period $T_p \approx 15.5563$ s, i.e. $T_p/3200$ is a coarse and $T_p/12800$ a fine time step.

Grids / Δt	Δt_1	Δt_2	Δt_3	Δt_4	Δt_5
	$T_p/3200$	$T_p/4800$	$T_p/6400$	$T_p/8533$	$T_p/12800$
Grid A	0.23	0.15	0.11	0.08	0.06
Grid B	0.30	0.21	0.15	0.11	0.08
Grid C	0.40	0.27	0.21	0.15	0.10
Grid D	0.53	-	0.27	-	0.13

Some of the simulations with larger theoretical CFL numbers exceed the constraint for TVD (see Section 3.1.5). Figure 5.6 presents the semi-submersible with Courant

numbers above the TVD constraint, i.e. $CFL > \frac{1}{6}$, for the simulation with the largest theoretical CFL number listed in Table 5.6. A time instance is chosen at which the largest CFL numbers were observed, i.e. at $t = 18.667\text{s}$. As Figure 5.6 shows, Courant numbers exceeding the TVD constraint are present mostly at the pipe connections and heave damping plates away from the free surface. However, there are also a few CVs with larger CFL numbers around the diagonal pipes. Nevertheless, the figure depicts that the TVD constraint is met by almost the entire domain and apart from a few time steps also for the entire simulation.

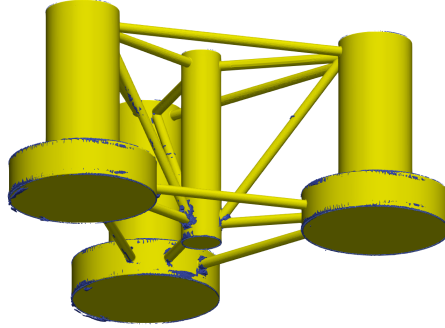


Figure 5.6: Courant numbers around the floater for the finest grid and coarsest time step, i.e. theoretical $CFL = 0.53$. A time instance is chosen at which the largest CFL numbers were observed ($t = 18.667\text{s}$). CFL numbers below $\frac{1}{6}$ are blanked using a threshold.

Surge decay and numerical damping results: In Figure 5.7, the 18 simulations are presented as decaying oscillations in surge over time.

Because the difference of the solutions for different time steps was too small, only four different lines can be seen in Figure 5.7. Hence, the solutions of these simulations were more grid than time step size dependent. The difference between the grids increases with progressing simulation time. Applying the optimised motion PQ method to the surge decay time history for a selection of nine simulations delivers the results presented in Figure 5.8.

Figure 5.8 reveals an increase of linear damping for grid coarsening. The quadratic damping generally increases for finer spatial resolution and reduces for finer temporal resolution. The change of damping for finer spatial and temporal discretisation is a result of reduced numerical diffusion, and better resolved geometry and viscous effects (Burmester et al., 2020a). As presented in Burmester et al. (2020c), linear damping is dominated by wave radiation. More spatial refinement leads to better resolved curvatures of the geometry, and consequently, less radiated waves, but it resolves the velocity field, vortices and eddies better. The former decreases linear damping and the latter increases quadratic damping. Reduced numerical diffusion owing to finer temporal and spatial discretisation decreases the damping as less energy is dissipated. This may also be seen by the slight decrease of critical damping ratio due to finer discretisation.

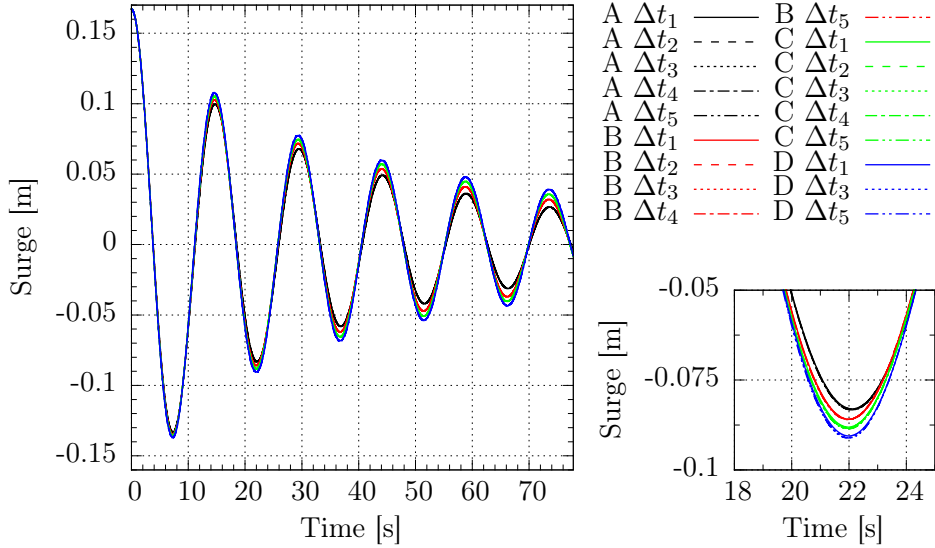


Figure 5.7: Surge decay motion x for 18 simulations with four different grids and five different time steps. On the bottom right, a zoom is shown for the second negative oscillation peak.

Iterative convergence: Figure 5.9 exhibits the iterative convergence at the end of each time step for the simulation with the largest and the smallest theoretical CFL number.

The residuals converge below 10^{-4} for each simulation in L_2 and 10^{-2} in L_∞ norm. A finer grid lowers the residual level in L_2 norm. Higher CFL numbers lead to higher residuals in L_∞ norm. Therefore, Figure 5.10 presents the residuals for the simulation with the largest CFL number, i.e. grid D with $\Delta t = T_p/3200$.

The highest residuals were found for the air volume fraction. They were in the viscous layer cells at free surface. Residuals in the range of 10^{-8} to 10^{-7} can be found at the outlet boundary condition and around the floater at the height of the free surface as well as at wave fronts and backs. Hence, all other locations converged well below 10^{-8} . This shows that it is important to look into the locations of residual convergence.

Different convergence criteria were also investigated for this case. Figure 5.11 presents the results of the effective residuals obtained for the following convergence criteria: $L_2 < 10^{-4}$, $L_2 < 10^{-5}$, and $L_\infty < 10^{-5}$. The criteria are more loosely chosen than in the previous wave propagation and wave load cases as good convergence is difficult to achieve. The reasons for the less good convergence are larger CFL numbers, and the more complex geometry leading to less good grid quality.

The convergence criterion is met by the simulation for $L_2 < 10^{-4}$. However, the criterion $L_2 < 10^{-5}$ could not be held even with up to 500 outer loop iterations per time step as the residual convergence stagnates. The simulation with the iterative convergence criterion $L_\infty < 10^{-5}$ was restricted to 60 outer loop iterations. This simulation achieved similar average residuals in L_2 and L_∞ norm, but never reaches

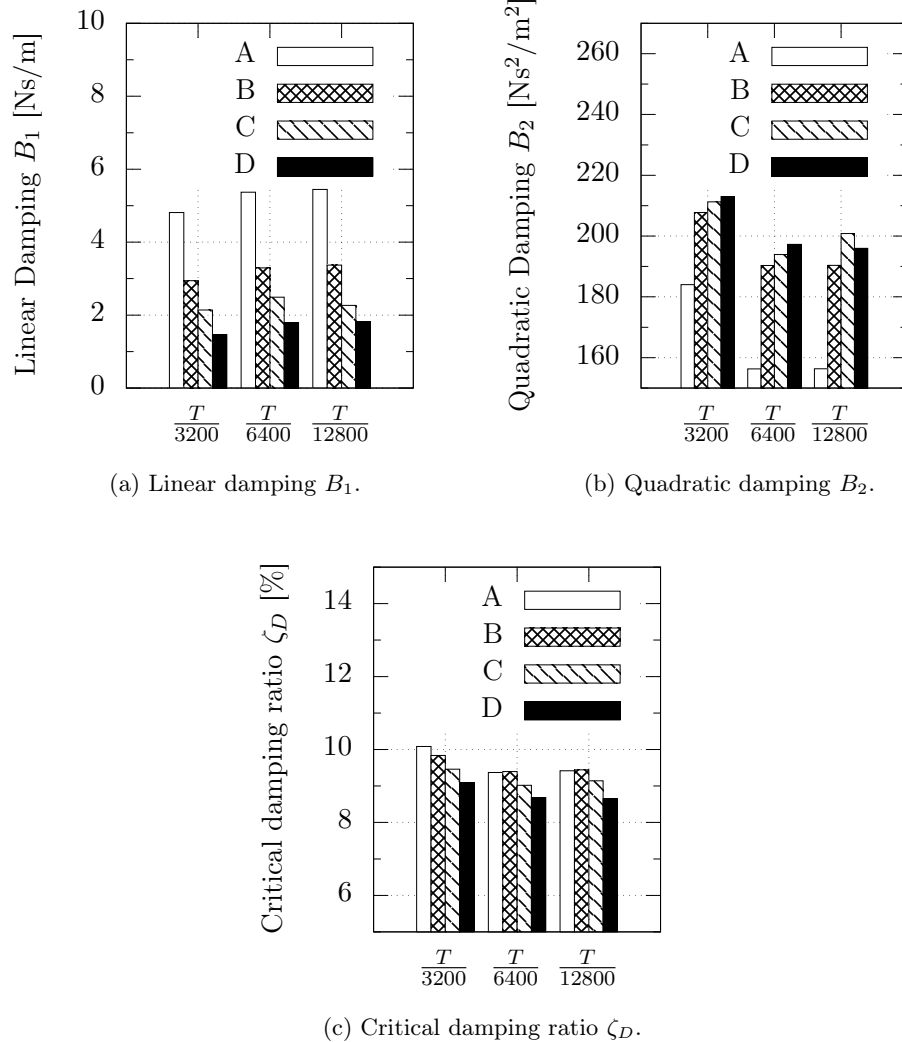


Figure 5.8: Results of the hydrodynamic damping analysis using the optimised motion PQ method for different grids and time steps. A is the coarsest and D the finest grid.

the convergence criterion. Figure 5.12 presents the surge decay time history for each criterion.

The surge decay time history is very similar between the simulation for $L_2 < 10^{-5}$ and $L_\infty < 10^{-5}$. As the criterion $L_2 < 10^{-5}$ together with 500 outer loop iterations was very time consuming, the simulation was not completed. Nevertheless, it can be seen that the results overlap the results using $L_\infty < 10^{-5}$ and 60 outer loop iterations. The results for $L_2 < 10^{-4}$ are significantly different in oscillation amplitude and period. Shortly after the start of the simulation, the differences are already noticeable. They increased with progressing time. Larger residuals, and thus, a larger imbalance of the equations system, at the end of a time loop

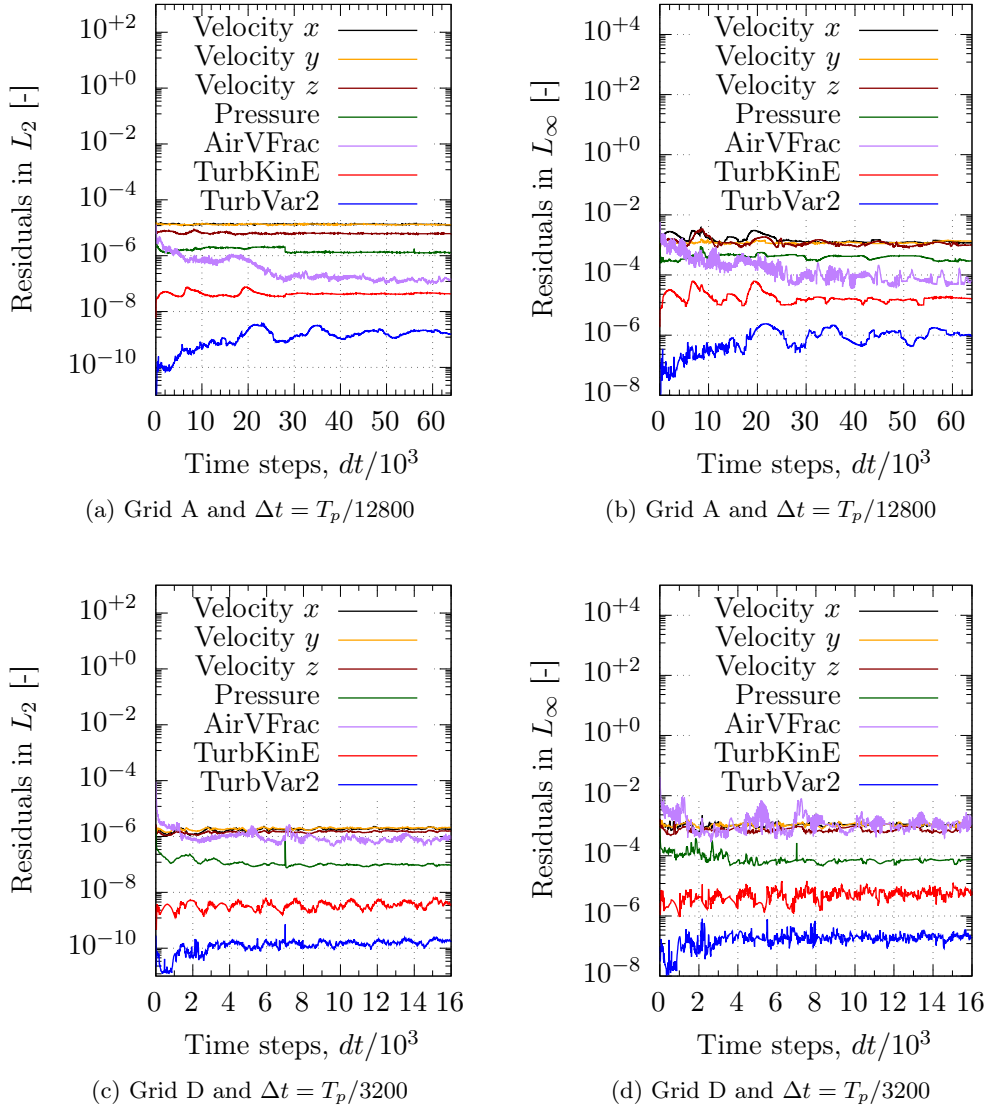


Figure 5.9: Examples of iterative convergence for the surge decay simulations. On the left, the normalised residuals in L_2 , and on the right, in L_∞ norm are presented for two different simulations.

are propagated to the next time loop. This leads to very different flow characteristics (velocity and pressure) compared to simulations with iterative convergence at lower levels. These differences in flow characteristics influence the equation of motion, and hence, the motions of the floater. Thus, the iterative convergence of complex simulations has to be investigated if lower levels can be reached. In surge decay simulations, the computed conditions do not repeat periodically. Then, errors because of the initial conditions are very dramatic as they are propagated. Therefore, low residual levels need to be reached in the first time steps.

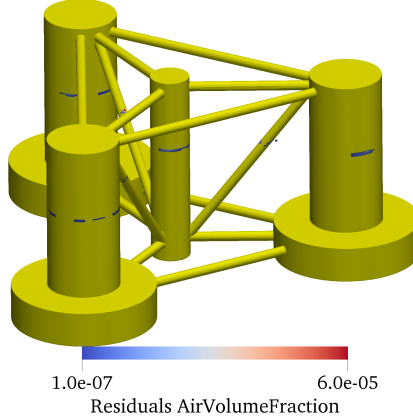


Figure 5.10: The residuals for air volume fraction are shown for the surge decay simulations at $7000 \cdot \Delta t$ using grid D and $\Delta t = T_p/3200$, i.e. for the largest CFL number.

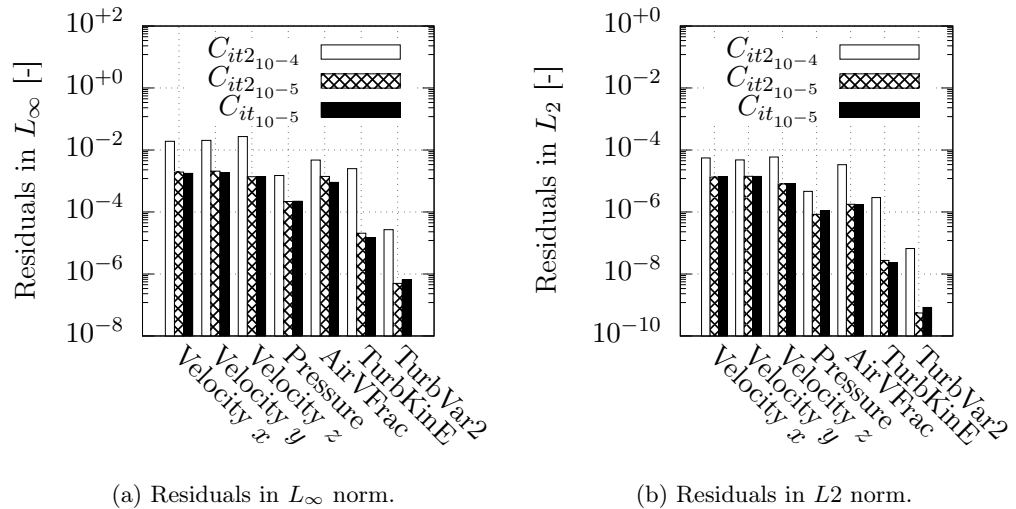


Figure 5.11: Residuals averaged over time for different convergence criteria, i.e. $L_2 < 10^{-4}$, $L_2 < 10^{-5}$, and $L_\infty < 10^{-5}$.

Discretisation errors and uncertainties: Initially, the error and uncertainty estimation for these simulations was performed on linear and quadratic damping coefficients. These coefficients are post-processed values of the decay results shown in Figure 5.7. Applying the method by Eça and Hoekstra, however, results in uncertainties of $U_\phi = 421.7\%$ for the linear and $U_\phi = 87\%$ for the quadratic coefficient using the solution of the finest grid and time step. Similarly, integration to estimate the area enclosed by the surge decay motion graph leads to uncertainties of $U_\phi = 40.8\%$. Consequently, the quantities chosen for the estimation of errors and uncertainties need to be as least post-processed as possible. Then, the errors and uncertainties obtained are a result of the numerical simulations and not of

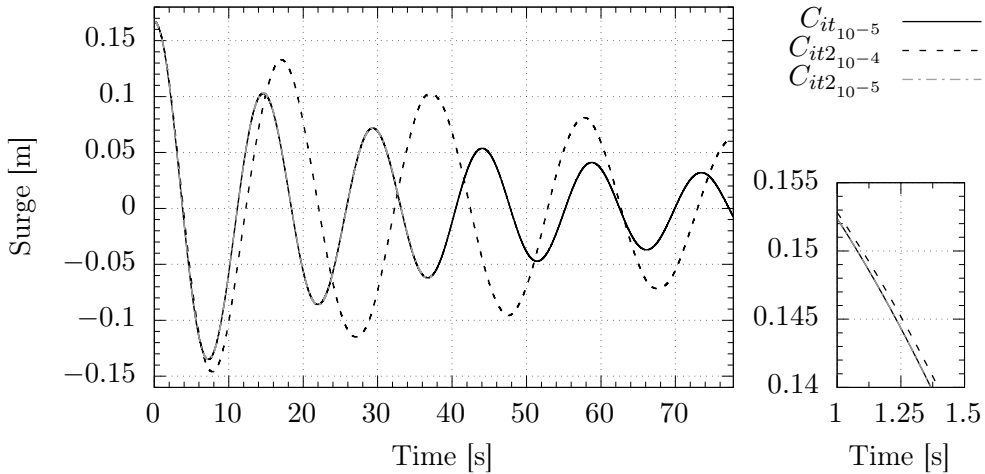


Figure 5.12: Comparison of results for different convergence criteria: $L_2 < 10^{-4}$, $L_2 < 10^{-5}$, and $L_\infty < 10^{-5}$. On the bottom right, a zoom into the start of the simulation is shown.

the post-processing technique. In the above examples, the hydrodynamic damping analysis and the trapezoidal rule for integration in itself possess uncertainties which lead to unrealistic error/uncertainty estimation. Therefore, the discretisation error estimation was performed on the oscillation range, i.e. the difference between one maximum and the following minimum of one oscillation. The differences between the results increase with simulation time.

Eça and Hoekstra approach: The oscillation height of the second zero-upcrossing cycle H_2 was calculated for each simulation. The solution of H_2 is given for each normalised time step t_i and grid size h_i , see Figure 5.13. The solution of the finest data set is presented with ϕ_1 and the extrapolated value with ϕ_0 in Table 5.7.

Table 5.7: Results for discretisation error and uncertainty estimation using the approach by Eça and Hoekstra (2014) for different data sets for H_2 of the surge decay simulations. The errors are given in percentage based on the extrapolated value.

Set combination	Extrapolated value ϕ_0 , [m]	Solution of finest grid and time step ϕ_1 , [m]	Error ϵ_ϕ , [%]	Uncertainty U_ϕ , [%]
18 solutions, ABCD	0.21888	0.19900	9.1	31.0
12 solutions, ABCD	0.22400	0.19900	11.2	16.1
9 solutions, ABC	0.20766	0.19377	6.7	21.8
5 solutions, ABC	0.20924	0.19377	7.4	10.0

The form of the fitted plane changes from an almost straight to a curved shape. The results for the error and uncertainty estimation scatter as in the previous wave cases. The extrapolated value differs by 7.3% and the uncertainty lays in

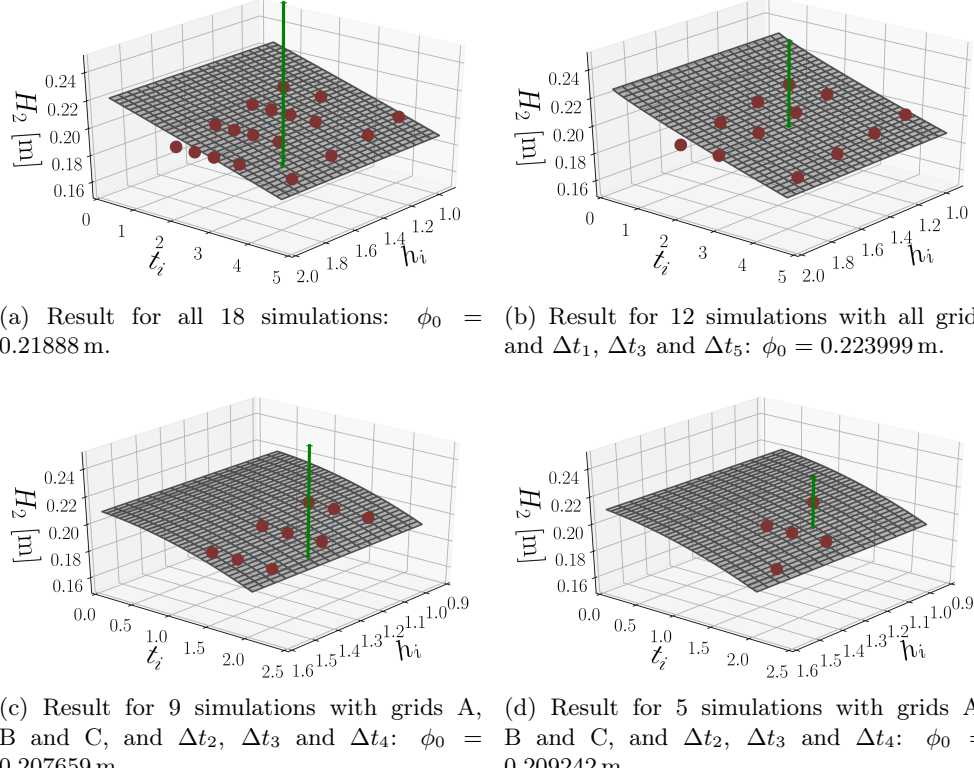


Figure 5.13: Discretisation error and uncertainty estimation using the approach by Eça and Hoekstra (2014) for the oscillation height of the second cycle H_2 with different grids and time steps selected. The data points are defined with the non-dimensional grid h_i and time step t_i spacing.

a range of 10% to 31%. The uncertainties for 18 and 9 data points were larger as the results of these simulations were more oscillatory. The result for 12 data sets was obtained with larger temporal discretisation steps. The differences of the solutions increased and led to monotonic convergence, and consequently, smaller uncertainties.

Comparison: There is exactly one data set resulting in constant CFL numbers (Table 5.6). Figure 5.14 shows a comparison between the three methods for this set.

The result using the approach by Oberhagemann and el Moctar (OeM) with linear extrapolation is closer to the grid solutions. Thus, the result with quadratic extrapolation obtained larger errors, and is, therefore, more conservative. This demonstrates that the observed order of convergence is closer to the linear than the second order approach. Hence, also large uncertainties are estimated using a safety factor of $F_s = 3$. Despite the choice of second order approximation schemes for the simulations, a different observed order of convergence may arise due to complex flow problems and grids. Table 5.8 presents results for the extrapolated

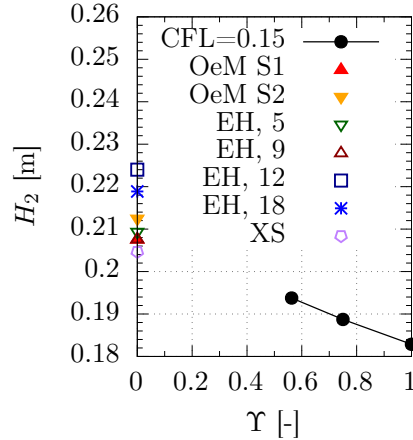


Figure 5.14: Comparison of results for extrapolated grid and time step independent solution for second oscillation height H_2 using the Oberhagemann and el Moctar (OeM) approach, the method by Eça and Hoekstra (EH), and the formulation by Xing & Stern (XS) for the surge decay simulations. The results are given as a function of the non-dimensional grid spacing factor Υ using data for grids A, B, and C.

solutions, and their errors and uncertainties.

Table 5.8: Results for discretisation error and uncertainty estimation of one data set for H_2 using the approach by Oberhagemann and el Moctar (2019). The errors are given in percentage based on the extrapolated value.

Data set	Result with S1 [m]	Result with S2 [m]	Solution of finest grid [m]	Error ϵ_ϕ S1, S2 [%]	Uncertainty S1, S2 [%]
ABC, CFL = 0.15	0.207612	0.212355	0.19377	6.7, 8.7	20.0, 26.2

Table 5.9: Results for discretisation error and uncertainty estimation of one data set for H_2 using the approach by Xing and Stern (2010). The errors are given in percentage based on the extrapolated value, and multiplied by the convergence ratio.

Set combination	Extrapolated value ϕ_0 , [m]	Solution of finest grid and time step ϕ_1 , [m]	Error ϵ_ϕ , [%]	Uncertainty U_{FS} , [%]
ABC, CFL = 0.15	0.20464	0.193774	4.8	30.6

The three methods produce remarkably similar results for these surge decay simulations and for the same data set. Nevertheless, the data set selected was not in the asymptotic range. Therefore, the method by Xing and Stern results in smaller errors than the other two methods, see Table 5.9. The uncertainties estimated are

higher and fit well to the ones estimated by Eça and Hoekstra for 18 data points. Thus, the error estimation using the approach by Oberhagemann and el Moctar, and Eça and Hoekstra yielded more conservative values than the method by Xing and Stern. The estimated uncertainties for the method by Oberhagemann and el Moctar fit well in the overall range given by the methods of Eça and Hoekstra and Xing and Stern.

The numerical simulations of this thesis were conducted with grid B and $\Delta t = T/6400$ unless stated explicitly otherwise. This simulation has a 81.7% higher linear damping, a 2.9% lower quadratic damping, and about 8.5% larger equivalent linear damping than the simulation with finest spatial and temporal refinement.

5.2.2 Dynamic mooring model

The OC5 DeepCwind semi-submersible was experimentally tested with catenary mooring lines. Numerically, the mooring system was modelled using the lumped-mass mooring model, see Section 3.4.2. This mooring model uses a finite number of evenly sized elements for spatial discretisation. Temporal discretisation is achieved using constant time steps. As a consequence, verification studies may be conducted to investigate the discretisation error of the mooring model. In this section, the discretisation error on the mooring model was calculated without coupling to the CFD solver. The simulations were conducted with a model as given by Gueydon (2016). The mooring layout may be found in Section 5.1.1.

Numerical simulations: The semi-submersible model was represented in aNySIM by hydrostatics and hydrodynamics calculated with DIFFRAC in frequency domain and calibrated against experimental data (Gueydon, 2016). DIFFRAC is a frequency domain potential-flow code developed and maintained by MARIN (MARIN, 2017). DIFFRAC provides hydrodynamic damping assuming linear mooring restoring forces and neglecting viscosity on the basis of the Green Function. In aNySIM, viscous damping and non-linear moorings may be added. The mooring model was calibrated against model test data for surge motion by Gueydon (2016). The hydrodynamic damping was estimated from the experiments. The results were added to the aNySIM model. Additional Morison type drag elements for the heave damping plates complemented the time domain model. In the mooring study, the floater model was not changed. Table 5.10 summarises the floater model values as documented by Gueydon (2016).

This study was intended to investigate the mooring system parameters. The mooring system properties were quantified based on their effects on the motions of the floater and the mooring loads computed at the fairleads.

For this investigation, the mooring line was discretised with 10, 20, 40, 80, 160, and 320 elements. The total length of the mooring lines did not change. The time steps used were defined as a function of the oscillation period, $T_p \approx 15.5563\text{ s}$: $\Delta t_1 = T_p/800$, $\Delta t_2 = T_p/1600$, $\Delta t_3 = T_p/3200$, $\Delta t_4 = T_p/6400$, and $\Delta t_5 = T_p/12800$. These small time steps were taken as the final mooring model was coupled to the

Table 5.10: Semi-submersible model in aNySIM as given by Gueydon (2016).

Designation	Value	Units
Linear damping in surge, B_{111}	3.0943	[Ns/m]
Linear damping in sway, B_{122}	1.2558	[Ns/m]
Linear damping in heave, B_{133}	3.8749	[Ns/m]
Linear damping in roll, B_{144}	2.1813	[Nm s]
Linear damping in pitch, B_{155}	2.1926	[Nm s]
Linear damping in yaw, B_{166}	1.8238	[Nm s]
Quadratic damping in surge, B_{211}	409.56	[Ns ² /m ²]
Quadratic damping in sway, B_{222}	529.44	[Ns ² /m ²]
Quadratic damping in heave, B_{233}	0.00	[Ns ² /m ²]
Quadratic damping in roll, B_{244}	0.00	[Nm s ²]
Quadratic damping in pitch, B_{255}	0.00	[Nm s ²]
Quadratic damping in yaw, B_{266}	24.32	[Nm s ²]
Heave damping plate, C_{D_n}	3.9	[\cdot]
Heave damping plate, C_{D_t}	0.0	[\cdot]
Heave damping plate, C_{M_n}	1.0	[\cdot]
Heave damping plate, C_{M_t}	1.0	[\cdot]
Floater mass, m	108.94	[kg]
Radius of gyration, r_{xx}	0.6526	[m]
Radius of gyration, r_{yy}	0.6676	[m]
Radius of gyration, r_{zz}	0.6264	[m]
Water depth, h	4.0	[m]

CFD solver. Thus, 30 simulations were conducted in total and the refinement factor equalled always 2. This means that the three discretisation error estimation methods may be applied also to the mooring model.

Line dynamics results: The comparison as a time history plot is presented in Figure 5.15 for selected simulations. The complete surge motion of the experimental campaign is replicated using a force time history to move the floater to a desired location. This location is reached at the negative maximum. Then, the force time history ends and the floater oscillates owing to the mooring restoring forces. Damping of the system arises due to the drag coefficients of the heave damping plates and mooring lines, and the provided linear and quadratic damping values of the floater (see Table 5.3 and 5.10).

The results in this figure demonstrate a small influence of the discretisation on the peak values and periods of the motion signal.

Discretisation errors and uncertainties: The discretisation errors were estimated using the surge decay motion time history. The three discretisation error estimation methods were applied for the mean oscillation period T_{pmean} , the mean

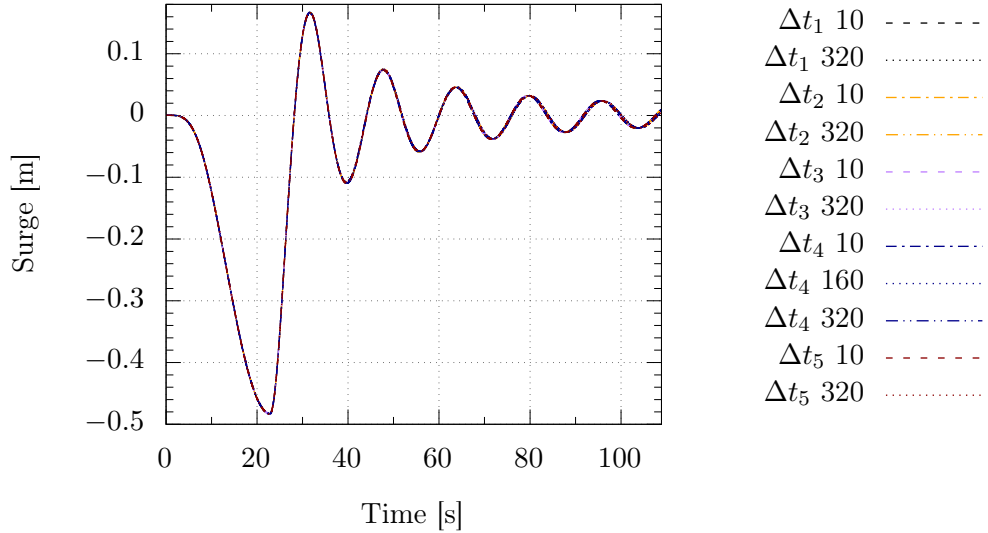


Figure 5.15: Time history of 11 selected surge decay simulations with different time steps and amount of elements.

of the logarithmic decrement of the positive Λ_{pmean} and negative Λ_{nmean} peaks and the oscillation range for the second H_2 and third H_3 cycle. The logarithmic decrement is defined in Equation (2.17).

Eça and Hoekstra approach: Table 5.11 summarises the results using the approach by Eça and Hoekstra (2014) for the complete data set and for five different parameters of the mooring simulations.

Table 5.11: Results for discretisation error and uncertainty estimation using the approach by Eça and Hoekstra (2014) for the complete data set and for five different parameters of the mooring simulations. The errors are given in percentage based on the extrapolated value.

Set, parameter	Extrapolated value ϕ_0	Solution of finest number of elements and time step ϕ_1	Error $\epsilon_\phi, [\%]$	Uncertainty $U_\phi, [\%]$
30 solutions, H_2	0.10468 m	0.10468 m	0.00	0.0
30 solutions, H_3	0.06609 m	0.06609 m	0.00	0.0
30 solutions, Λ_{pmean}	0.42778	0.427805	0.00	0.0
30 solutions, Λ_{nmean}	0.37404	0.374062	0.00	0.0
30 solutions, T_{mean}	16.0789 s	16.0727 s	-0.04	0.7

The largest uncertainty for the finest element and time step combination was achieved for the mean oscillation period, $U_\phi = 0.7\%$. The uncertainty for the simulation with the coarsest resolution (time and space) was $U_\phi = 2.6\%$. The uncertainties for the other quantities were in the range of $U_\phi \leq 1.2\%$ for the coarsest resolved mooring lines. The finest data set for H_2 , H_3 , Λ_{pmean} , and Λ_{nmean} resulted

in $U_\phi = 0.0\%$.

Comparison: The results for the approaches by Oberhagemann and el Moctar (2019) and Xing and Stern (2010) are listed in Table 5.12 and 5.13. In both tables, the results for the same data are presented. The data point in the middle of the set in combination with the parameter investigated gives its name to the entry in the tables, e.g. 160 elements with $T_p/6400$. The two different simulation sets are refined with a ratio of 2, i.e. the set “ $T_p/6400$, 160elts” (elts = elements) includes data for the following simulations: $\Delta t = T_p/3200$ and 80 elements, $\Delta t = T_p/6400$ and 160 elements, and $\Delta t = T_p/12800$ and 320 elements.

Table 5.12: Results for discretisation error and uncertainty estimation of one data set for different parameters using the approach by Oberhagemann and el Moctar (2019) for the mooring simulations. The errors are given in percentage based on the extrapolated value.

Data set	Result with S2	Solution of finest number of elements	Error ϵ_ϕ S2 [%]	Uncertainty U_{LSQth_2} [%]
$T_p/6400$, 160elts, H_2	0.10468 m	0.10468 m	0.00	0.0
$T_p/6400$, 160elts, H_3	0.06609 m	0.06609 m	0.00	0.0
$T_p/6400$, 160elts, Λ_{nmean}	0.37404	0.374062	0.00	0.01
$T_p/3200$, 40elts, H_2	0.10467 m	0.10469 m	0.01	0.02
$T_p/3200$, 40elts, Λ_{nmean}	0.37412	0.373944	-0.02	0.02

Table 5.13: Results for discretisation error and uncertainty estimation of one data set for different parameters using the approach by Xing and Stern (2010). The errors are given in percentage based on the extrapolated value, and multiplied by the convergence ratio.

Set combination	Extrapolated value ϕ_0	Solution of finest number of elements ϕ_1	Error ϵ_ϕ , [%]	Uncertainty U_{FS} , [%]
$T_p/6400$, 160elts, H_2	0.10468 m	0.10468 m	0.0	0.0
$T_p/6400$, 160elts, H_3	0.06609 m	0.06609 m	0.00	0.0
$T_p/6400$, 160elts, Λ_{nmean}	0.37406	0.374062	0.00	0.0
$T_p/3200$, 40elts, H_2	0.10468 m	0.10469 m	0.00	0.00
$T_p/3200$, 40elts, Λ_{nmean}	0.37409	0.374051	0.00	0.00

The results in these tables present negligible or zero error and uncertainty values. However, these values increase for coarser discretisation. Thus, there are discretisation errors present in lumped mass mooring simulations and they can be assessed. They are, however, small for the level of discretisation chosen. The results for other simulation sets and parameters resulted also in oscillatory convergence, i.e. not all parameters can be shown using the methods by Oberhagemann and el Moctar (2019) and Xing and Stern (2010). As the errors are very small, an illustration is not deemed to provide an added value to the comparison.

The coupled CFD dynamic mooring model simulations were performed with a temporal discretisation of $\Delta t = T_p/6400$ and a spatial discretisation of 160 mooring line elements.

5.3 Input Sensitivity

The input values to the numerical simulations need to be as accurate as possible to replicate the decay tests performed experimentally. This section deals with the sensitivity to different input parameters on the estimated hydrodynamic damping. These parameters are the point in time of the release, the value of the initial displacement, and modelling of the restoring stiffness. In addition, the influence of small temperature changes was investigated and may be found in Appendix B.

5.3.1 Initial displacement and release time

Release time: The initial displacement for the experimental surge decay test was obtained by an operator moving the semi-submersible floating wind turbine in negative x direction. As the floater's release point in time was not clearly defined, the numerical simulations were started when the decay motion reached the furthest positive x position, i.e. $x = 0.167$ m at model scale. This leads to a couple of input differences between simulations and experiment. The flow at the moment in time when the floater reaches 0.167 m in x is disturbed for the experiment and at rest for the numerical simulation. Moreover, the coupling between different DOFs is more pronounced for the experiment owing to the larger initial displacement. A simulation with an earlier release, and hence, large negative initial displacement (RT) in 1 DOF was conducted to be compared with the 1 DOF simulation with the initial displacement of $x = 0.167$ m and the experiment. Figure 5.16 displays the comparison. The 1 DOF RT simulation starts approx. 7.18 s (slightly less than $0.5 \cdot T_p$) before the other numerical simulation.

The results summarised in Table 5.14 were obtained by applying the PQ analysis from the same starting value, i.e. $x = 0.167$ m. The linear damping is largely reduced, the quadratic damping increased, and the period was almost unchanged compared to the standard initial displacement. The relative differences of the results between the two simulations was a 35.9% smaller linear and a 31.4% larger quadratic damping, and therefore, a 14.1% larger critical damping ratio. Thus, the different initial release time leads to disturbance in the flow which reduces the wave radiation component but increases the viscous damping components resulting in larger total damping.

Applying the PQ method to the start of the simulation, i.e. with large negative initial displacement, leads to increased linear and decreased quadratic damping. The relative differences between the two starting values of the PQ method of the same simulation are 19.9% in linear and 8.4% in quadratic damping. This example reveals that linear damping has the largest contribution for the start of the simulation. When the fluid and the floater are in motion, the importance of

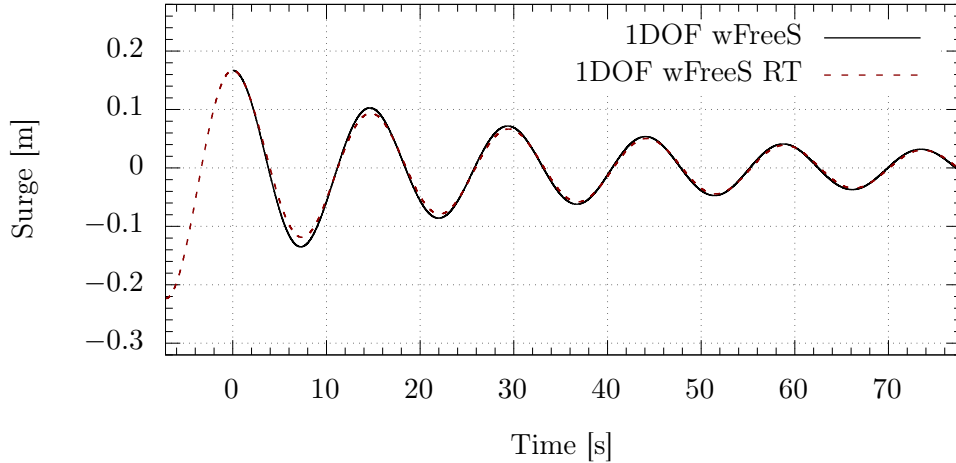


Figure 5.16: Surge decay time history for 1 DOF simulations with different initial release time instances.

linear damping reduces compared to the quadratic term. Besides, larger initial displacement also leads to higher motion velocities, and hence, the radiated waves increase.

Table 5.14: Hydrodynamic damping comparison of simulations with different input parameters for 1 DOF and 3 DOF, for increased and decreased initial displacements, for different release time (RT), 10 times larger pitch stiffness ($10 \cdot C_{55}$), and with quasi-static non-linear mooring model (QSM).

Simulation name	Lin. damping B_1 [Ns/m]	Quad. damping B_2 [Ns ² /m ²]	Critical damping ratio ζ_D [%]	Oscillation period T_n [s]
1 DOF	3.2955	190.6071	9.4048	14.6736
1 DOF RT	2.1139	250.4511	10.9478	14.6790
1 DOF 0.207 m	2.4659	232.1091	10.4690	14.6772
1 DOF 0.127 m	4.1858	142.2807	8.0800	14.7085
3 DOF C_{55}	3.2445	227.7145	10.3511	15.0203
3 DOF $10 \cdot C_{55}$	3.4431	197.8283	9.6651	14.7678
3 DOF QSM	2.9660	210.5389	9.9766	14.6615

Sensitivity on the initial displacement value: The sensitivity to the initial displacement may also be studied by varying the input value. The standard displacement used throughout the work of this thesis is 0.167 m. For two simulations, this value was changed to 0.127 m and 0.207 m, i.e. +0.04 m and -0.04 m with respect to the original initial displacement. The simulations are indicated with their initial displacements in Table 5.14 and Figure 5.17.

The results depict significant differences in the damping terms between these calculations. Whereas, the periods were again almost the same. A smaller initial

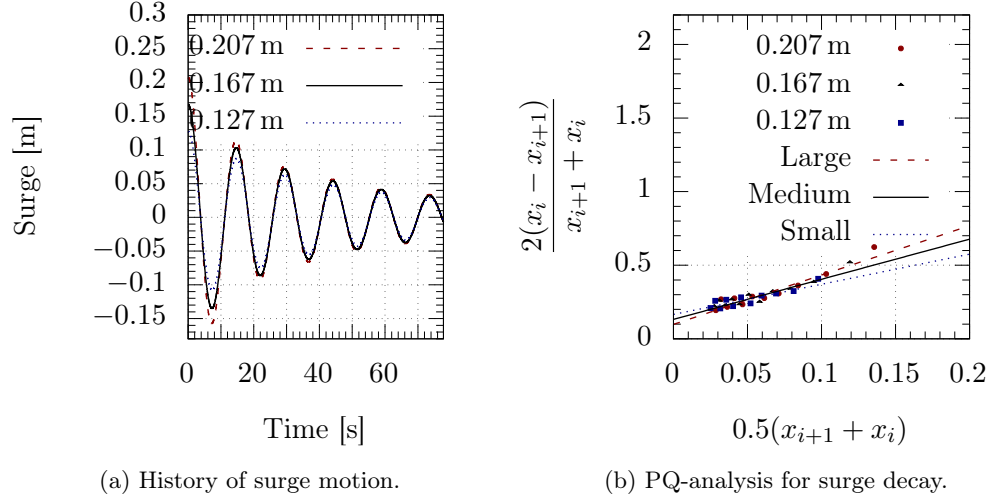


Figure 5.17: Surge decay time history and PQ analysis diagram for 1 DOF simulations with different initial displacements, i.e. $x = 0.207\text{ m}$, $x = 0.167\text{ m}$, and $x = 0.127\text{ m}$. The corresponding fits are indicated with ‘‘Large’’, ‘‘Medium’’, and ‘‘Small’’.

displacement yields larger linear and smaller quadratic damping. A larger initial displacement results in the opposite, i.e. smaller linear and larger quadratic damping. Using the 1 DOF simulation with standard initial displacement as a base, the range of differences for linear and quadratic damping are -25.2% to $+27.0\%$ and $+21.8\%$ to -25.4% for the 0.04 m larger and smaller initial displacements, respectively. The values for the equivalent linear damping range between $+11.9\%$ and -13.4% for the larger and smaller initial displacements. Thus, a larger initial displacement also results in larger hydrodynamic damping of the floater. Even though such a large difference in initial displacement is unlikely for the experiments (measurement uncertainties were not assessed), this study depicts an influence of the value for the initial displacement on the hydrodynamic damping. Larger initial displacements increase the relative velocities between floater and fluid. This increases the pressure drag and skin friction damping component as well as wave radiation, and eddy and lift damping. The results presented in Figure 5.17(b) also reveal that the first oscillation, represented by the largest two values on the abscissa, has a large contribution to the overall shape of the fitting. The other values in the PQ diagram are closer to each other for all three simulations. As a result, for the same oscillation amplitudes more similar hydrodynamic damping values are likely, if the first oscillation peaks are neglected in the damping estimation. Furthermore, the spatial and temporal discretisation was optimised for the initial displacement of $x = 0.167\text{ m}$. This might lead to larger and/or smaller discretisation errors for the other two initial displacements.

5.3.2 Restoring stiffness

The oscillation frequency (and period) is influenced by the floating system's mass and stiffness (see Equation (2.10)). Increasing the stiffness leads to shorter periods but also to different floater velocities. Thus, the stiffness of the mooring system also has an effect on the hydrodynamic damping. This was investigated by a simulation with non-linear mooring restoring forces and a simulation with 10 times larger pitch stiffness. Non-linear restoring forces are important mainly for large oscillations when the linear assumption of the restoring forces is not valid anymore. A 10 times larger pitch stiffness shows also the influence of surge-pitch coupling on the surge damping. The non-linear mooring restoring forces were achieved by coupling of ReFRESCO with a quasi-static mooring model (QSM) as part of aNySIMxmf. Details of the coupling and mooring model may be found in Section 3.4 and of catenary equations solved in Section 2.6.

Surge decay time history and hydrodynamic damping values: The results for the surge decay time history of the stiffness variation are presented in Figure 5.18 in comparison with the other simulations. The respective hydrodynamic damping values are summarised in Table 5.14.

Figure 5.18 displays also the heave and pitch motion. The differences in surge time history are small between the simulations. The simulations with increased pitch stiffness and the non-linear mooring model possessed shorter oscillation periods. Increasing the stiffness leads to smaller quadratic damping because the pitch motion amplitudes are significantly reduced. Then, the trajectory of the floater in pitch and the viscous damping components are smaller. The same reason for increased quadratic damping applies to the simulation with a non-linear quasi-static mooring model. The heave motion of the QSM simulation is larger than for the other numerical simulations. The simulations with linear stiffness applied a vertical force on the centre of gravity to mimic the weight of the mooring lines. The applied force was calibrated to achieve heave motions around zero. The QSM simulation used the mooring characteristics as reported without additional adjustments. Nevertheless, the heave offset was less than 0.5 mm which corresponds to 0.125% of the floater's draught. Hence, the heave motion is wrong but might be neglected. The simulation with increased stiffness had a 6% larger linear damping, a 13% smaller quadratic damping, and a 6.6% smaller critical damping ratio compared to the normal 3DOF simulation with linear stiffness. The QSM simulation had a 8% smaller linear damping, a 7% smaller quadratic damping, and a 3.6% smaller total damping than the standard computation with linear stiffness. Accordingly, the stiffness of the moored floating system clearly influences the hydrodynamic damping.

Flow characteristics: The velocity field and vortices around the floater are important factors for the hydrodynamic damping. They mainly influence the viscous dependent damping components. Therefore, the flow solutions for the 3DOF simulations with different restoring stiffness are presented in Figure 5.19 for the velocity field and in Figure 5.20 for the Q criterion. The time instances were chosen di-

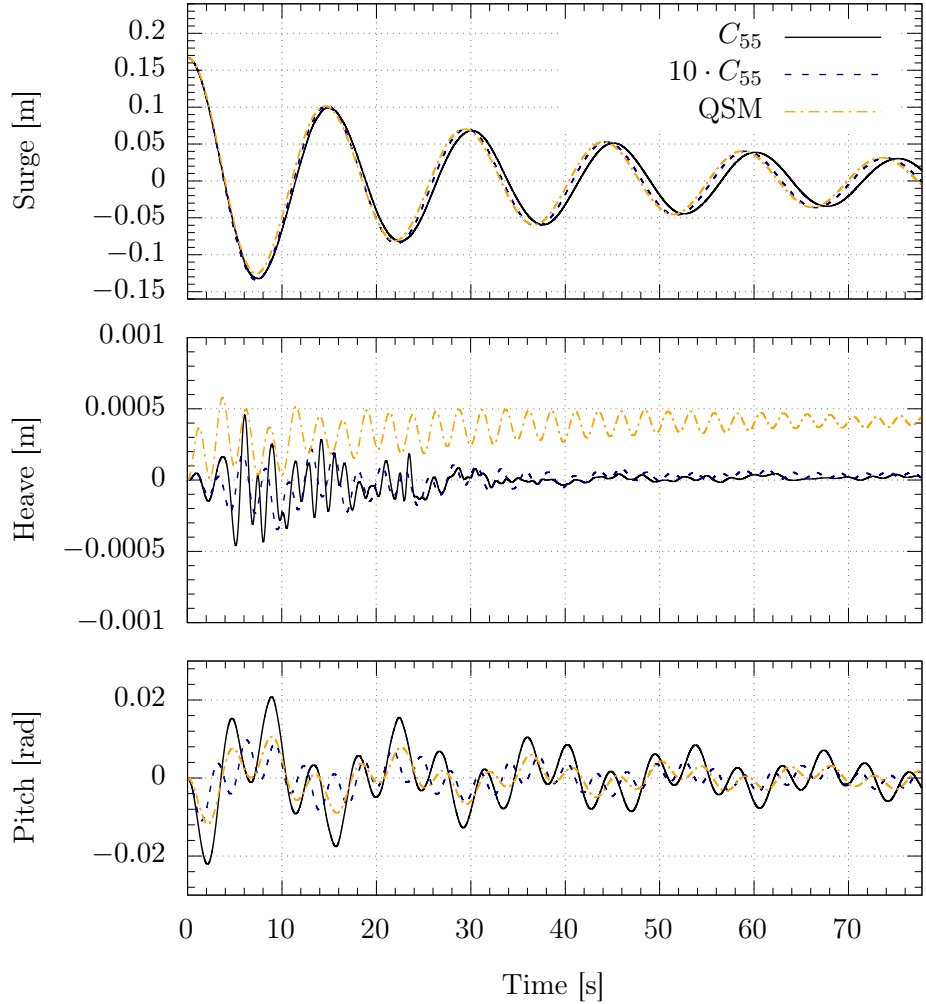


Figure 5.18: Surge decay time history for 3DOF of simulations with different stiffness properties: $10C_{55}$ denotes 10 times larger pitch stiffness, C_{55} pitch stiffness as reported and QSM non-linear quasi-static mooring model.

rectly after the first negative and until after the first positive peak, i.e. $t \approx 0.51T_p$, $t \approx 0.72T_p$, $t \approx 0.93T_p$ and $t \approx 1.14T_p$. These time instances are marked on the surge decay time history presented in Figure 5.19. Figure 5.19 shows the magnitude of the velocities at the height of the centre of gravity (COG) in a horizontal plane. A dark blue colour corresponds to 'zero' velocities and red to $v_M \geq 0.1 \text{ m/s}$. For visualisation purposes, the flow solution was mirrored at the symmetry plane, i.e. at $y = 0$.

The skin friction component is closely related to the velocities around the floater. Figure 5.19 reveals an increase of the size of the high velocity regions with time from $t = 7.7782 \text{ s}$ to $t = 10.8894 \text{ s}$. Then, these regions decreased again. This corresponds to the velocity of the floater. The largest velocity values were present for the first two instances. The largest flow velocities were present at $t = 7.7782 \text{ s}$

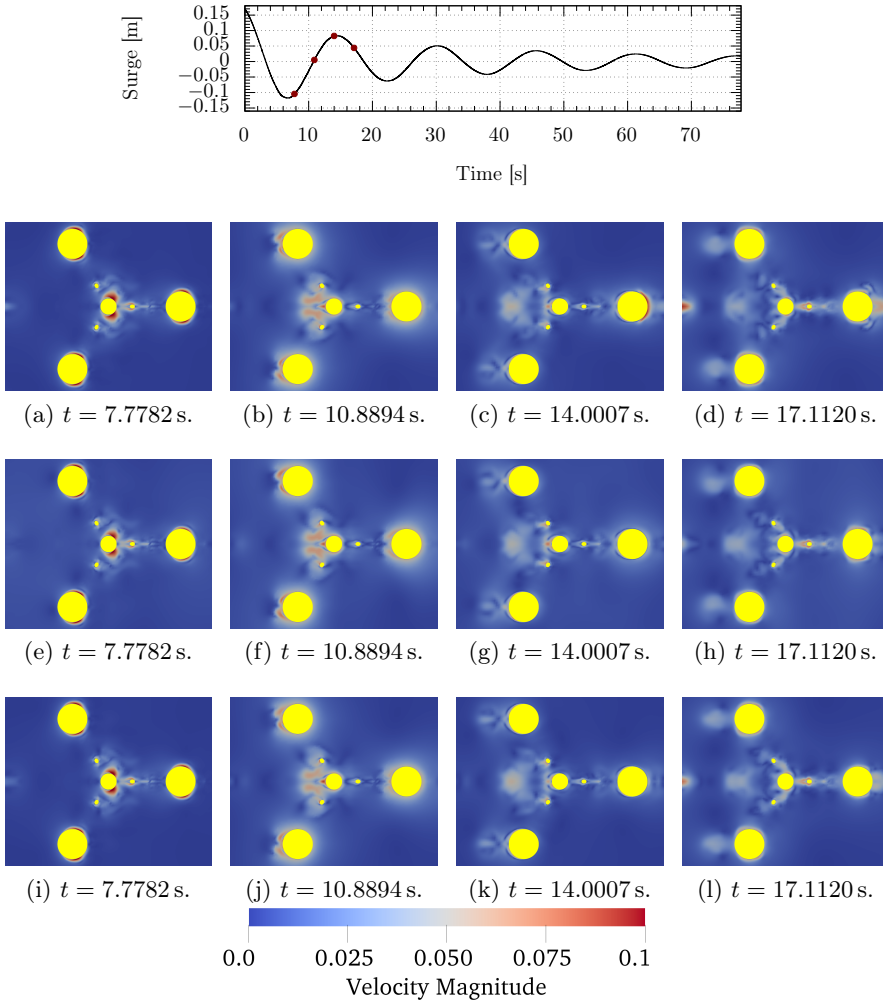


Figure 5.19: Velocity magnitude [m/s] of several numerical simulations with symmetric domain and different restoring stiffness for different time instances shown at the height of the centre of gravity (Burmester et al., 2020c). The 3 DOF simulation with linear moorings and $10C_{55}$ is presented in the first row (a-d), the 3 DOF simulation with linear moorings and C_{55} in the second row (e-h), and the 3 DOF simulation with a quasi-static mooring model in the third row (i-l).

for all three simulations. This flow observation does not correspond to the motion velocities of the floater. The largest motion velocities of the floater within this cycle were present at $t = 10.8894\text{s}$. However, it corresponds to the point in time at which the floater has just changed the motion direction. Thus, the relative velocity between floater and fluid are highest.

The largest difference may be observed for the third time instance ($t = 14.0007\text{s}$) at the front corner column. At this time, the simulation with increased pitch stiffness reveals large velocities while the velocity magnitude for the other two simulations is small. This could be related to the different pitch motion due to the

larger stiffness. Apart from this observation, the velocity field is very similar for the three simulations.

The eddy making and lift damping components depend on the amount and form of vortices in the flow around the floater. As discussed later in Section 5.4.1, the Q criterion is a good measure to give a quantitative idea on the amount and form of vortices in the flow. A value of $Q = 0.5 \text{ s}^{-2}$ was taken for comparison of the 3 DOF simulations with linear moorings, increased pitch restoring, and non-linear mooring model. Figure 5.20 shows the Q -contours coloured with the y component of the velocity for four time instances of each simulation.

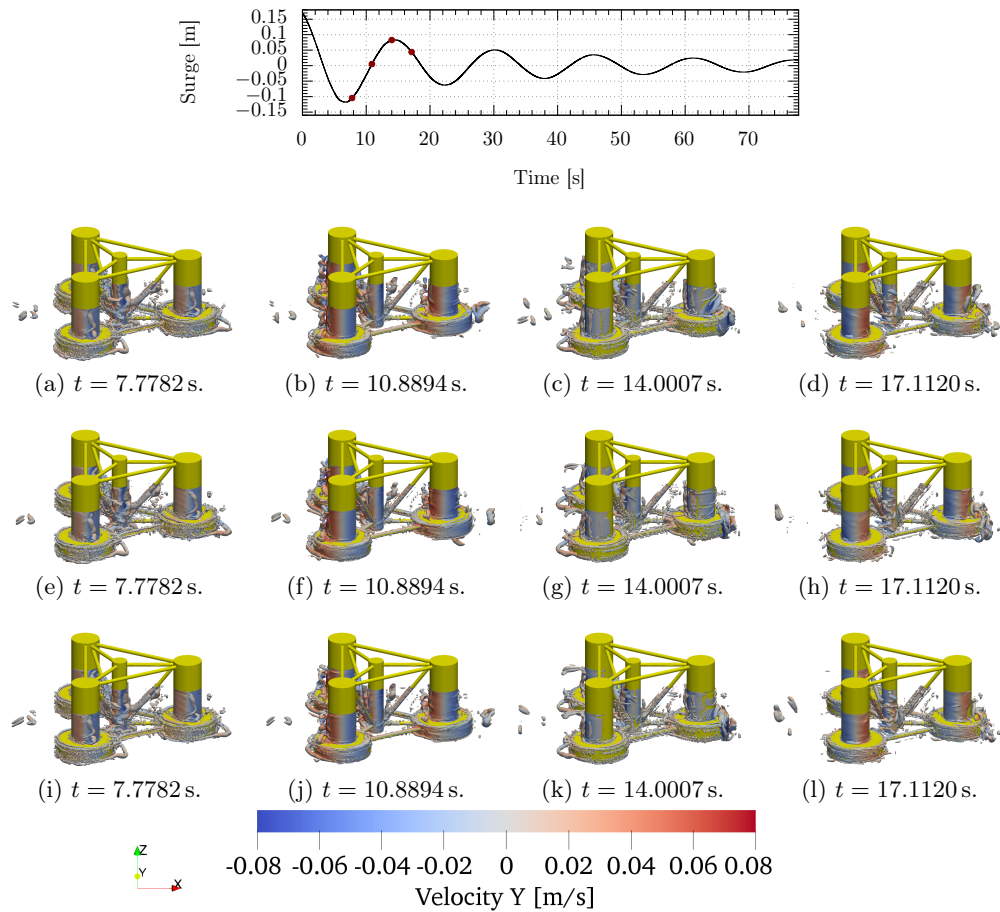


Figure 5.20: Contour of $Q = 0.5 \text{ s}^{-2}$ around the floater and coloured with the y component of the velocity vector for several numerical simulations with symmetric domain. The 3 DOF simulation with linear moorings and $10C_{55}$ is presented in the first row (a-d), the 3 DOF simulation with linear moorings and C_{55} in the second row (e-h), and the 3 DOF simulation with a quasi-static mooring model in the third row (i-l).

The largest cross-wise velocities and coherent vortical structures were exhibited for large floater velocities, i.e. at $t = 10.8894 \text{ s}$. The vortices are generated mainly at the vertical sides of the heave damping plates, the vertical columns, and at the

cross braces. The largest differences may be observed for the second, third, and fourth time instances, and on the right-hand side of the right corner column. The differences in vortical structures between the 3 DOF simulations with increased pitch stiffness and the other two simulations are larger than between the simulations with linear and non-linear mooring restoring forces. At the third time instance, a large vortex is visible on the right-hand side of the upper right column. For the other two simulations, the large vortex is located at the height of the heave damping plates. This is in-line with the largest velocity field observed around the height of the COG in the same location. This is an indication for the larger pitch restoring stiffness when compared to the other two simulations. Hence, the correct restoring stiffness values are important also for the flow characteristics around the floater.

5.4 Modelling Influence

Several sources of modelling errors exist. In this section, the sources originating from turbulence modelling, the free surface, motion coupling, domain restrictions, and mooring modelling are addressed.

5.4.1 Turbulence modelling

The eddy and lift damping component is a result of vortex creation resulting in local pressure changes. The creation and size of eddies depends on the turbulence model. Therefore, three turbulence models, the KSKL, SST 2003 and EARSM, were compared to a laminar and an inviscid (Euler) simulation to investigate their influence on the hydrodynamic damping. The simulation setup was the same as given in Section 5.2, i.e. a symmetric domain including free surface modelling and with linear restoring stiffness. The symmetry plane might restrict the vorticity created at the centre elements of the floater and might lead to underestimation of the eddy and lift damping component compared to a simulation with full domain. The largest Reynolds number reached is in the order of 31 000 and is inside the turbulent region. Consequently, transition between laminar and turbulent flow might occur in several oscillation cycles. Figure 5.21 presents the results of the surge decay motion time history for each of the simulations and Table 5.15 gives the corresponding values for damping and period.

The results depict large differences between the inviscid flow simulation and the other four simulations. In particular, the oscillation peaks differ from each other. The quadratic damping term reduces to very small values and the linear damping increases. Moreover, the equivalent linear damping, a measure for the total damping and represented as ratio to the critical damping, is just half of the damping estimated for the other simulations. The periods, however, are almost unaffected as expected by the definition given in Equation (2.13). The largest influences on the periods are owing to the mass and stiffness of the oscillating system. These quantities were kept constant. The inviscid simulation cannot account for the skin friction damping component. Vortices can be generated because of numerical errors such as by the lower grid quality, and at sharp edges of the geometry such as

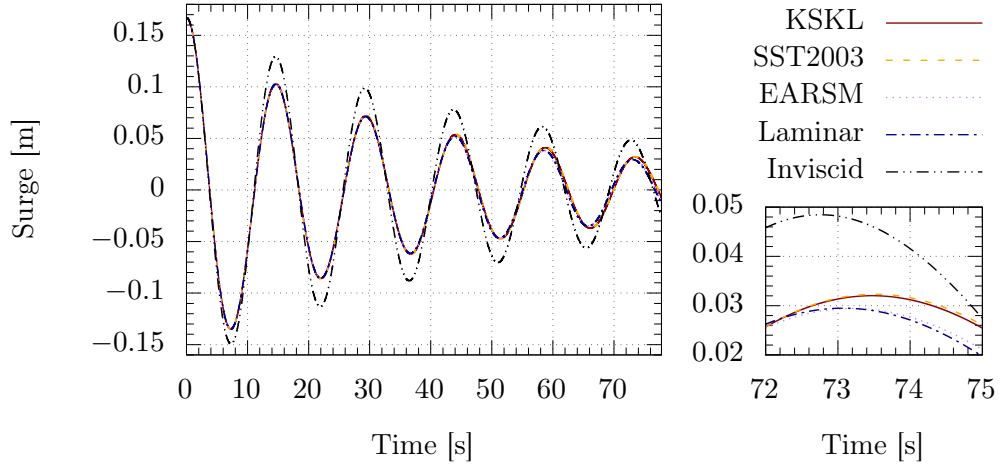


Figure 5.21: Surge decay time history of simulations with different turbulence modelling approaches. On the bottom right, a zoom into an oscillation peak at the end of the simulation is shown.

Table 5.15: Hydrodynamic damping values for simulations with different turbulence modelling approaches. Each surge decay simulation was performed for 1 DOF and with free surface.

Simulation name	Lin. damping B_1 [Ns/m]	Quad. damping B_2 [Ns ² /m ²]	Critical damping ratio ζ_D [%]	Oscillation period T_n [s]
KSKL	3.2955	190.6071	9.4048	14.6736
SST 2003	3.5243	182.7695	9.2370	14.6841
EARSM	4.6397	155.2600	8.9432	14.6289
Laminar	4.3820	160.6033	9.0099	14.6061
Inviscid	5.1097	30.1017	4.4401	14.5393

at connection points and the heave damping plates. Vortices may also be given at the inlet boundary condition and propagate towards the floater. Furthermore, the simulation with inviscid flow has smaller numerical diffusion than the RANS simulations. This leads to larger wave radiation and, hence, the linear damping increases. Figure 5.22 shows the wave elevation measured at a wave probe $x = 0.9$ m upstream of the centre of gravity of the floater for the different turbulence modelling approaches. At the start of the simulation the radiated waves are similar for each simulation. The largest radiated waves are visible shortly after the largest oscillation velocity is reached. As the decay motion progresses in time and the oscillations become smaller, the radiated waves from simulations with the SST 2003, KSKL, EARSM and Laminar also decrease. This, however, is not the case for the inviscid flow simulation and represented by a larger linear damping coefficient in Table 5.15.

The simulation with viscosity and without turbulence model is called laminar in the

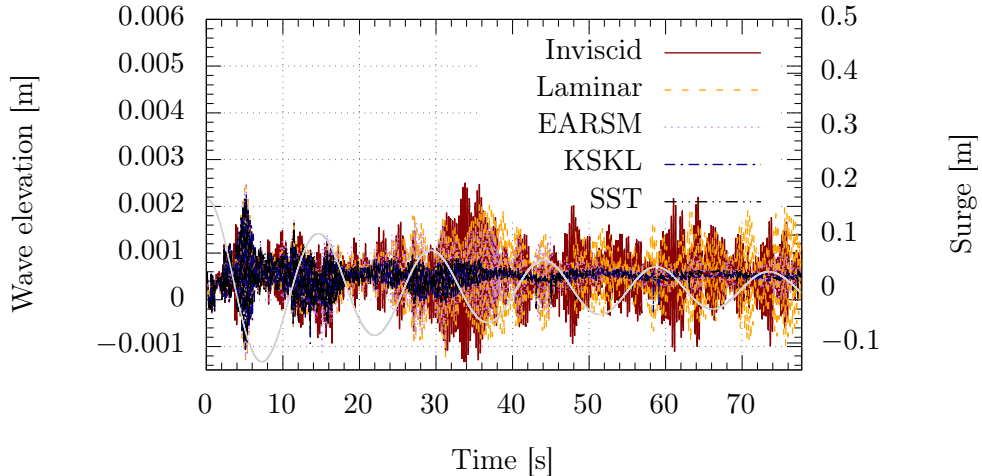


Figure 5.22: Wave elevation as a function of time at $x = 0.9$ m upstream of the centre of gravity for different turbulence modelling approaches. The corresponding surge decay motion is plotted on top in grey as a reference.

above figures and tables. The results of the laminar simulation and the EARSM are very similar, i.e. the linear damping is slightly increased and the quadratic damping decreased compared to the results using KSKL and SST 2003 turbulence models. Because of the too coarse discretisation, smaller turbulent scales are not resolved and not modelled (absence of a turbulence model) and their influence is reduced compared to the RANS simulations. Thus, the eddy and lift damping component is smaller than for the RANS computations. As a result of the absence of a turbulence model, the numerical diffusion is reduced and larger waves are radiated, see Figure 5.22.

The EARSM simulation takes the anisotropy of turbulence into account. This influences the eddy and lift damping. Compared to the simulations with KSKL and SST 2003, the EARSM computation has larger linear damping and smaller quadratic damping associated with a slight decrease of skin friction and increase of eddy, lift, and wave radiation damping. The differences in vorticity may be seen in Figure 5.23 for these simulations at different points in time ($\approx 0.51T_p$, $0.72T_p$, $0.93T_p$ and $1.14T_p$).

In general, the vorticity shown in Figure 5.23 is larger for time instances with larger motion velocities of the floater, i.e. $0.72T_p$ and $0.93T_p$. The largest difference in vorticity can be noted for the inviscid simulation. For these figures, the vorticity in the wake of the centre and front column is significantly smaller than for the other results. The other results depict only minor differences in the form or amount of vorticity. These observations are also represented in the estimated damping values listed in Table 5.15.

As discussed in Jeong and Hussain (1995) vorticity may not be the best representation of vortical structures. The flow immediately near the wall is characterised by shear. No vortical motion is exhibited by the flow in the near wall region.

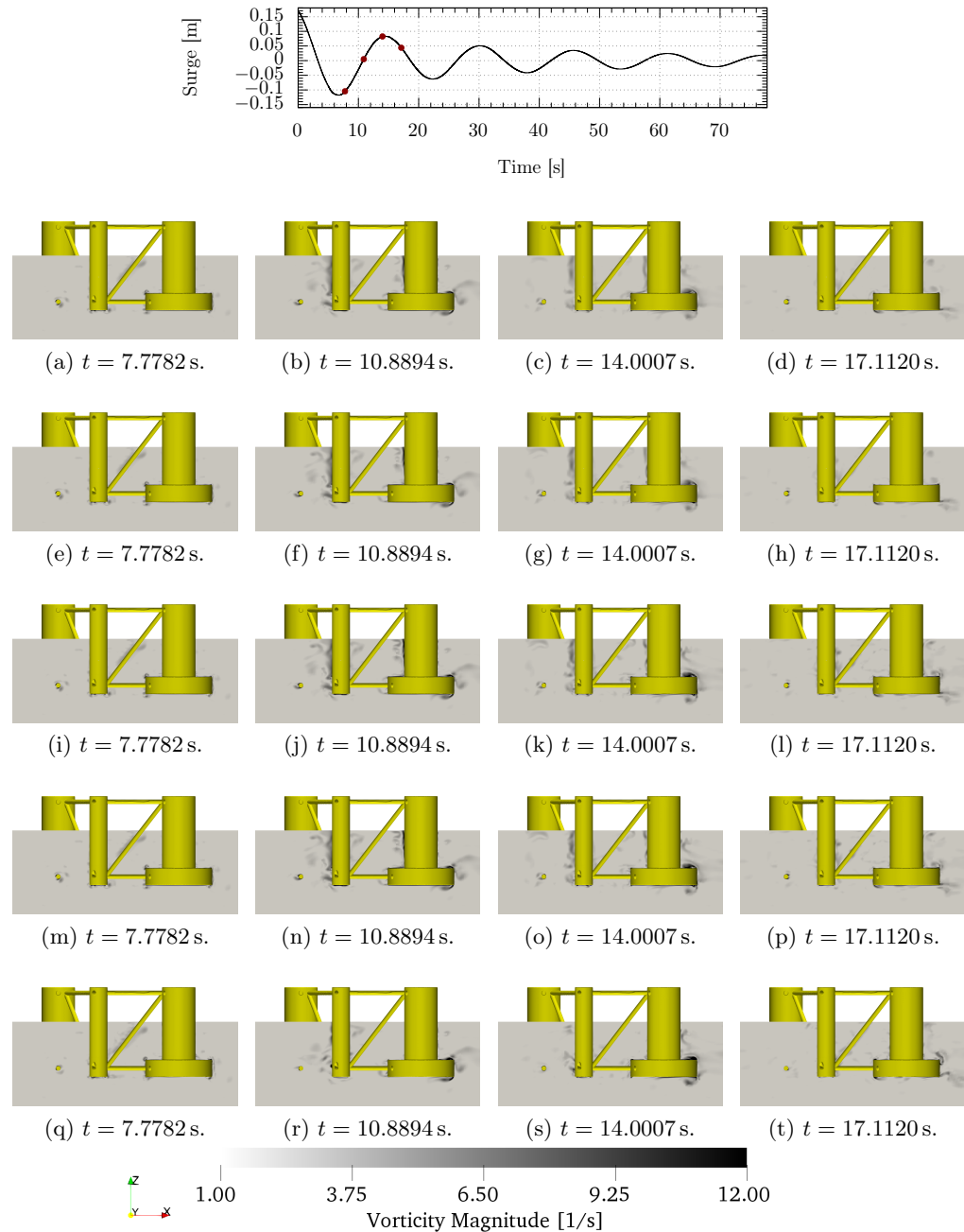


Figure 5.23: Vorticity around the floater at $y = 0.04$ m from the symmetry plane for different turbulence modelling approaches. Top row (a) - (d) shows the KSKL, second row (e) - (h) the SST 2003, and third row (i) - (l) the EARSM turbulence models. Fourth row (m) - (p) is the laminar and the last row (q) - (t) the inviscid simulation. The time instances from left to right are approximately at $0.51T_p$, $0.72T_p$, $0.93T_p$ and $1.14T_p$ (T_p is the oscillation period).

Vorticity, however, shows largest values close to the wall. Therefore, Hunt et al. (1988) provided the Q criterion for the identification of a vortex structure. In this work, the Q criterion was used to investigate the differences between different computations. Decomposing the velocity gradient in strain rate and vorticity tensor by $\nabla \vec{v} = \mathbf{S}_t + \boldsymbol{\Omega}_v$ leads to the definition of the Q criterion for incompressible flows as (Haller, 2005):

$$Q = \frac{1}{2} (\|\boldsymbol{\Omega}_v\|^2 - \|\mathbf{S}_t\|^2) \quad , \text{ where} \quad (5.1)$$

$$\mathbf{S}_t = \frac{1}{2} (\nabla \vec{v} + (\nabla \vec{v})^T) \quad \text{and} \quad \boldsymbol{\Omega}_v = \frac{1}{2} (\nabla \vec{v} - (\nabla \vec{v})^T) \quad . \quad (5.2)$$

Q describes the imbalance between the magnitude of vorticity $\boldsymbol{\Omega}_v$ and shear strain rate \mathbf{S}_t tensor, i.e. between the asymmetric component of the velocity gradient and the symmetric component. According to Jeong and Hussain (1995) vortices occur, if the value of this criterion is positive, i.e. $Q > 0$. This means that the vorticity is larger than the shear strain rate. Besides, it is proposed to use a small positive number. Hence, the selection of a Q value is very subjective and is the responsibility of the researcher/engineer. The value chosen is $Q = 0.5 \text{ s}^{-2}$ (see Figure 5.24). The results need to be taken with care as a different value would lead to a different amount and shape of the vortical structures in the flow. The vortical structures are coloured by the y component of the velocity vector.

The differences in vortical structures is more evident from Figure 5.24 than from 5.23. In particular, the simulation with inviscid flow exhibits fewer coherent structures around the floater, i.e. the eddy damping component is smaller for this simulation. The results for simulations with EARSM and without turbulence (laminar) are more chaotic, i.e. there are smaller but more structures and in more directions than for the results of the other two models. This influences the eddy making damping component.

The results of the simulations with the KSKL and SST 2003 turbulence models are very similar for motion time history, damping values and flow solution. The KSKL model was chosen for the numerical simulation of the OC5 DeepCwind semi-submersible, since the EARSM model requires more computational resources and underestimates the skin friction damping component, and the SST2003 model converges less good for free surface simulations.

5.4.2 Free surface and motion coupling

This section is dedicated to the investigation of wave radiation, and motion coupling up to 3 DOF. Wave radiation is investigated by the comparison of simulations with and without free surface, and with and without wave absorption. Simulations with 1 DOF (surge only) and with 3 DOF (surge, heave, and pitch) were performed to investigate the effect of motion coupling up to 3 DOF. The diagonal of the linear restoring matrix is given by Table 5.2.

Wave radiation: A double-body (DB) simulation and a simulation with free surface (wFreeS) and for 1 DOF were performed to study the influence of the free

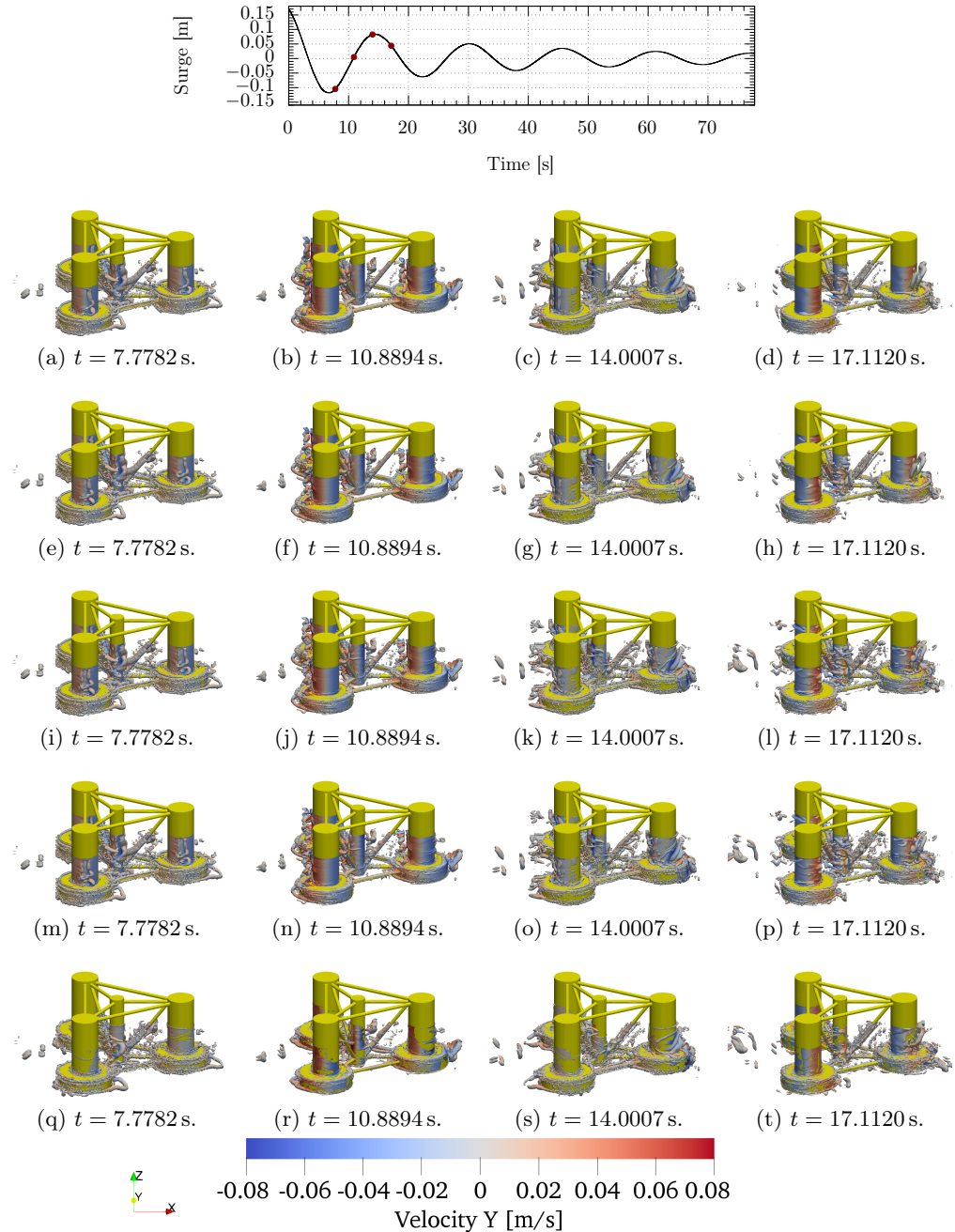


Figure 5.24: Contour of $Q = 0.5 \text{ s}^{-2}$ around the floater coloured with y component of the velocity vector for different turbulence modelling approaches. Top row (a) - (d) shows the KSKL, second row (e) - (h) the SST 2003, and third row (i) - (l) the EARSM turbulence models. Fourth row (m) - (p) is the laminar and the last row (q) - (t) the inviscid simulation. The time instances from left to right are approximately at $0.51T_p$, $0.72T_p$, $0.93T_p$ and $1.14T_p$ (T_p is the oscillation period).

surface on the hydrodynamic damping. For simulations with free surface and wave radiation, wave reflections may occur at the domain boundaries. The effect of wave reflections is observed with another simulation including absorption zones. Figure 5.25 presents the result for these three simulations. The corresponding hydrodynamic damping values are tabulated in Table 5.16.

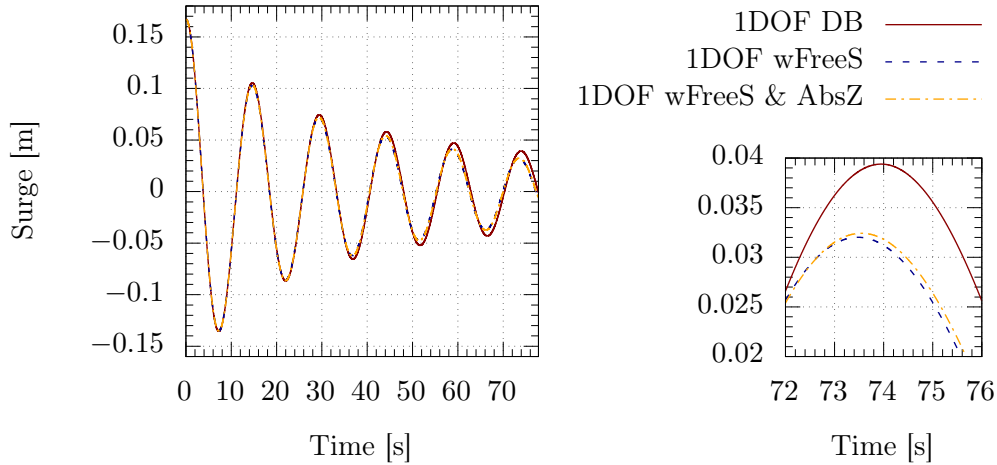


Figure 5.25: Surge decay time history of simulations with (1DOF wFreeS) and without (1DOF DB) free surface, and with wave absorption (1DOF wFreeS & AbsZ). On the right hand side, a zoom on the last oscillation peak is shown.

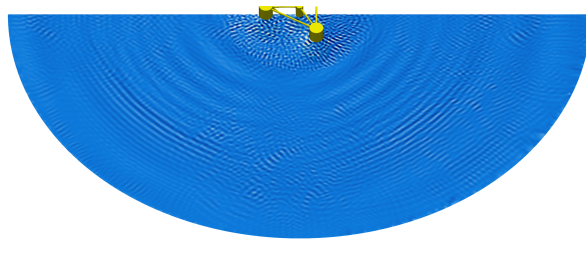
The difference between the 1 DOF wFreeS and the 1 DOF DB simulation is the additional free surface. In Figure 5.25, the differences in oscillation amplitude are hardly noticeable in the beginning of the simulation. After about 30 s, these differences increase. The PQ analysis revealed a significant increase of linear damping for the simulation with free surface (see Table 5.16). This supports the hypotheses that the damping owing to wave radiation is a linear damping. The quadratic damping is decreased for free surface simulations. Thus, interaction between the different damping components occurs due to the additional disturbance of the flow by radiated waves. The altered velocity field influences the skin friction, pressure drag, and the eddy and lift damping components. This is also addressed in the paragraph on flow characteristics below. These flow differences result in a 7.9% lower critical damping ratio for the simulation with free surface.

The radiated waves can be reflected by the outer boundaries of the computational domain if no damping or absorption methods are applied. Reflected waves interact with the floater and influence the hydrodynamic damping. The surge decay simulations were computed without and with absorption zones to investigate the influence of wave reflection. The absorption zone was located in a ring with inner radius 3.0 m and outer radius of 4.9 m coinciding with the outer domain radius. The absorption function and coefficient were adopted from the investigations of Chapter 4, i.e. a cosine function with an absorption coefficient of 5. Further details on wave absorption may be found in Section 2.4.2. The results presented

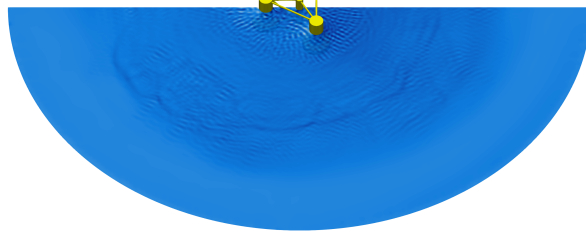
Table 5.16: Hydrodynamic damping comparison of simulations with and without free surface (DB), for 1 DOF and 3 DOF, for increased and decreased initial displacements, for different release time (LID), 10 times larger pitch stiffness ($10 \cdot C_{55}$), and with quasi-static non-linear mooring model (QSM).

Simulation name	Lin. damping B_1 [Ns/m]	Quad. damping B_2 [Ns ² /m ²]	Critical damping ratio ζ_D [%]	Oscillation period T_n [s]
1 DOF DB	0.2787	266.7257	10.2166	14.7771
1 DOF	3.2955	190.6071	9.4048	14.6736
1 DOF AbsZ	3.3246	189.0627	9.3436	14.6916
3 DOF C_{55}	3.2445	227.7145	10.3511	15.0203
3 DOF QSM	2.9660	210.5389	9.9766	14.6615

in Figure 5.25 demonstrate small influence for 1 DOF surge decay simulations. The zoom on the oscillation peak at the fifth cycle enables distinguishing the two simulations.



(a) Without absorption zone.



(b) With absorption zone.

Figure 5.26: Surface elevation in the domain for two simulations with and without absorption zone at $0.51T_p$.

Hydrodynamic damping estimation reveals 0.89% larger linear, 0.81% smaller quadratic damping, and 0.53% smaller equivalent linear damping compared with the simulation without absorption zones. These numbers confirm the observation of the surge decay time history. Yet, the more realistic surface elevation in the domain is important for trustworthy results. The coloured surface elevation for the two simulations is shown in Figure 5.26.

The absorption function reduces the wave heights to negligible sizes in the absorption zone around the outer domain boundaries and even reduces the wave heights

in the vicinity of the floater (see Figure 5.26). However, the influence on the floater motions is small. Absorption zones were disregarded for the simulations with symmetric domain and included for those with a complete computational domain.

Flow characteristics: The flow solutions for the double body, the 1DOF with free surface, and the 1DOF with free surface and absorption zone simulation are presented in Figure 5.27 and 5.28. The time instances were chosen directly after the first negative and until after the first positive peak as before, i.e. $t \approx 0.51T_p$, $t \approx 0.72T_p$, $t \approx 0.93T_p$ and $t \approx 1.14T_p$. Figure 5.27 shows the magnitude of the velocities at the height of the centre of gravity (COG) in a horizontal plane. A dark blue colour corresponds to 'zero' velocities and red to $v_M \geq 0.1$ m/s. For visualisation purposes, the flow solution was mirrored at the symmetry plane, i.e. at $y = 0$.

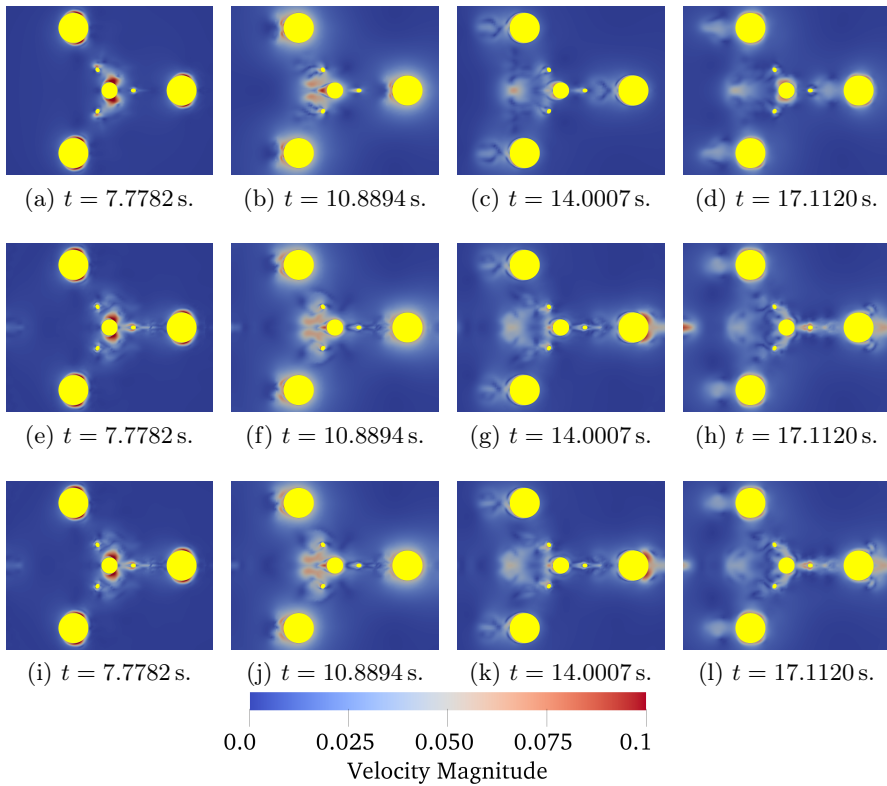


Figure 5.27: Velocity magnitude [m/s] of several numerical simulations with symmetric domain for investigations of the wave radiation effects at different time instances shown at the height of the centre of gravity (Burmester et al., 2020c). The 1 DOF double body simulation is presented in the top row (a-d), the 1 DOF with free surface in the second row (e-h), the 1 DOF simulation with absorption zones in the third row (i-l).

As before, Figure 5.27 reveals an increase of the size of the high velocity regions with time from $t = 7.7782$ s to $t = 10.8894$ s. Then, these regions decreased again.

The largest velocities of all results are shown for the double body simulation. This coincides with the largest quadratic damping which may be a result of the increased skin friction damping component. After $t = 10.8894\text{s}$, the velocity regions for the simulations with free surface were larger than those for the double body simulation. In particular, the velocity regions around the front corner column increased. The increased regions of flow velocities around the floater correlate with an increase of linear damping.

The skin friction component is closely related to the velocities around the floater. Furthermore, the eddy making and lift damping components depend on the amount and form of vortices in the flow around the vessel. As discussed in Section 5.4.1, the Q criterion is a good measure to give a quantitative idea on the amount and form of vortices in the flow. Thus, a value of $Q = 0.5 \text{ s}^{-2}$ was taken for comparison of the different 1 DOF simulations with and without free surface and with and without wave absorption. Figure 5.28 shows the Q -contours coloured with the y -component of the velocity for different time instances of the described simulations.

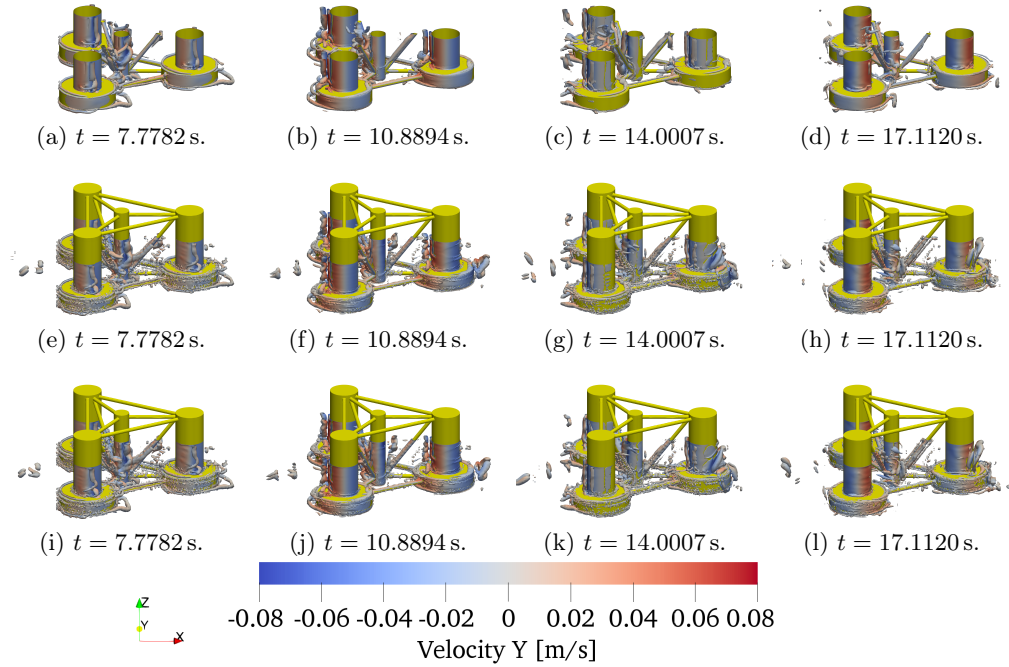


Figure 5.28: Contour of $Q = 0.5 \text{ s}^{-2}$ around the floater and coloured with the y component of the velocity vector for several numerical simulations with symmetric domain. The 1 DOF double body simulation is presented in the top row (a-d), the 1 DOF with free surface in the second row (e-h), the 1 DOF simulation with absorption zones in the third row (i-l).

A more general disturbance of the flow, and therefore, more vortex distribution was present in the far field for simulations including a free surface. For these results, more vortices were also present at the upstream corner column. The vortical structures shown for the double body simulation are less chaotic, more coherent,

and mostly horizontal.

Large velocity values were present for the double body simulation, the simulations with free surface possessed larger vortical structures. This indicates interaction between the wave radiation, the skin friction, and the eddy making and lift damping components.

Motion coupling up to 3 DOF: The experimental decay tests were performed for each degree of freedom individually. However, the floater was always able to move in all six degrees-of-freedom. As there is strong coupling between surge, heave and pitch for a semi-submersible floating wind turbine, it is important to enable these DOFs also for the numerical simulations. This was done for the 3DOF simulation. The effect of the motion coupling on the dynamic behaviour, i.e. time history and damping values, in surge was investigated and the results are presented in Figure 5.29 and Table 5.16. The 3DOF simulation used a linear stiffness matrix. Hence, the weight of the mooring lines accounted for by the non-linear mooring models, was missing in these simulations. Therefore, simulations with enabled heave motion were performed with an additional vertical force applied on the centre of gravity to account for the missing weight of the mooring lines.

The 3DOF surge decay simulation with enabled heave and pitch motion leads to longer periods and increased quadratic damping of the floater. Due to the motions in heave and pitch, energy is dissipated in these directions. This leads to an increase in damping represented by an increase of 9.1% in critical damping ratio for the 3DOF simulation compared to the 1DOF simulation. The differences between the simulations presented in Figure 5.29 increase with time. Motion coupling up to 3DOF influences mostly the quadratic damping with an increase of 16.3%. The oscillation period increased by 2.3%. Thus, the influences of motion coupling up to 3DOF and the free surface are important to model the total hydrodynamic damping of the semi-submersible floater.

5.4.3 Complete domain and motions

In this section, the influence of the complete computational domain and motion coupling up to 6DOF are analysed. The complete computational domain enables realistic non-symmetric vortex creation and the motion coupling increases the floater trajectory about the other cross-wise degrees-of-freedom. These components are more complex and require more computational resources than the previous investigations. Figure 5.30 shows two full domain simulations with 3 and 6DOF motions compared to a 3DOF simulation with symmetric domain. Each RANS simulation was coupled to the non-linear quasi-static mooring model (QSM).

The time history plots displayed in Figure 5.30 present only one line as the difference between the numerical simulations is marginal. The lines are almost on top of each other. Nevertheless, slightly different hydrodynamic damping parameters may be obtained using the PQ method. Table 5.17 lists the damping estimation results. Figure 5.31 presents the corresponding PQ diagram for each of the

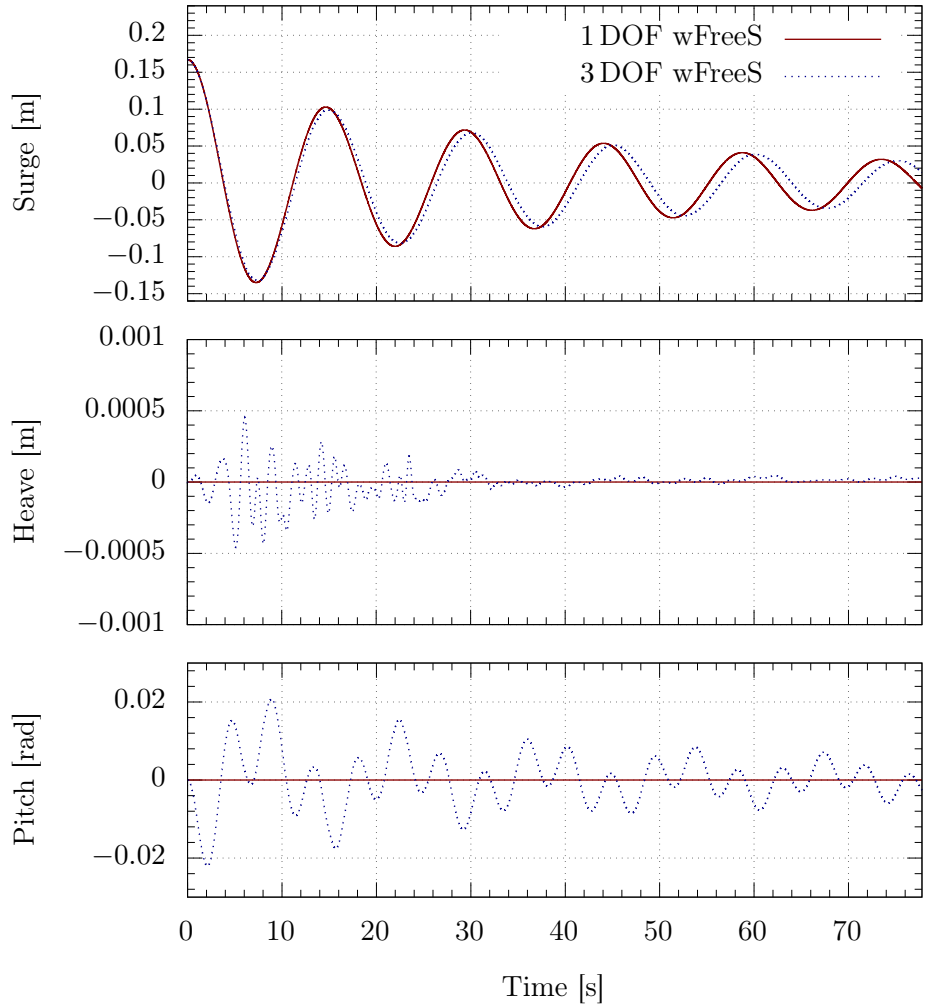


Figure 5.29: Surge decay time history of simulations with motion coupling up to 3 DOF (surge, heave, and pitch).

three computations. Hardly any differences are visible. The differences in critical damping ratio are also of less than 2%.

The quadratic damping increases slightly with complexity of the simulations and the linear damping decreases. A complete domain enables vortices to interact with each other and they are not symmetric. This influences the eddy and lift damping component. The former contributes to an increase in quadratic damping. Moreover, the radiated waves are able to travel in all directions. The wave energy of these waves is smaller than for radiated waves using a symmetric domain. This reduces the linear damping.

Figure 5.32 shows a comparison between the 3 DOF surge decay simulations for a symmetric and a full domain. Vortical structures are represented using the Q-criterion with $Q = 0.5 \text{ s}^{-2}$. At the chosen point in time, the surge motion is positive, i.e. from left to right. The coherent structure just upstream of the

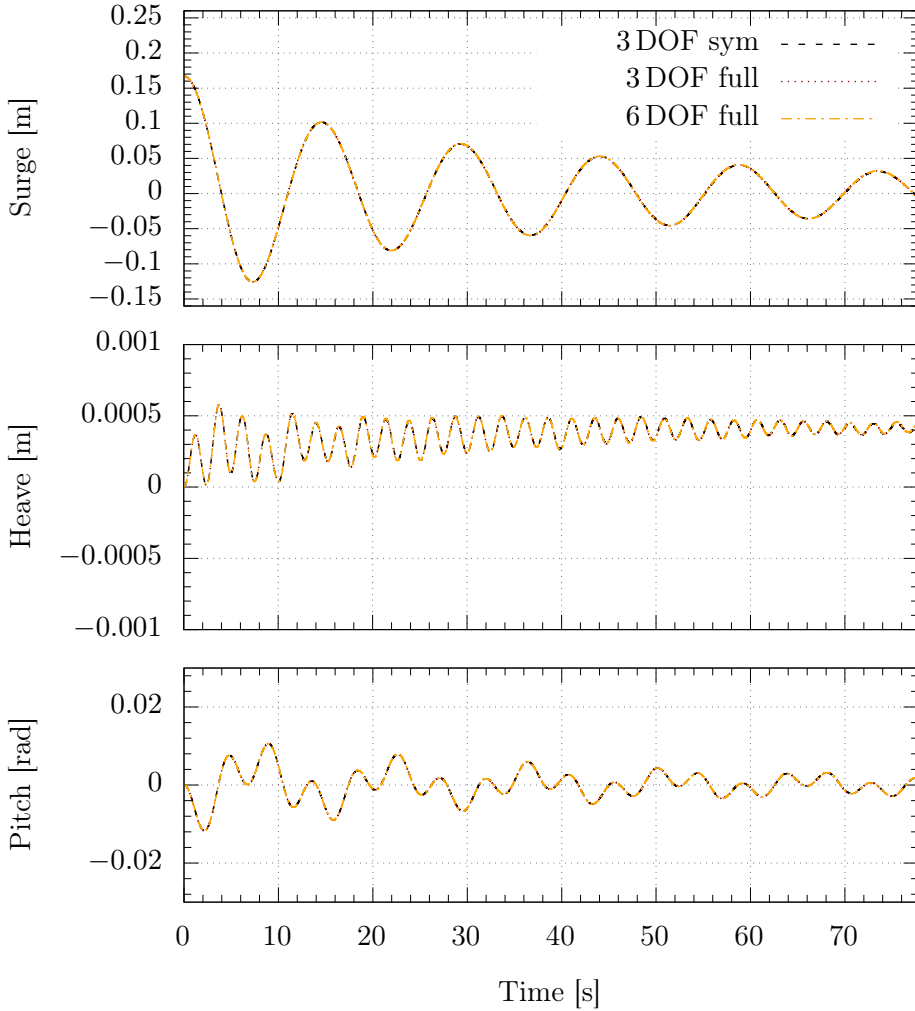


Figure 5.30: Results for surge decay time history of simulations with a quasi-static mooring model and different computational domains: 3 DOF simulation with symmetric domain, 3 DOF simulation with complete domain, and 6 DOF simulation with complete domain

right corner column differs slightly between the two simulations. In addition, the vortices in the wake of the semi-submersible (left of the floater in the figure) show a different shape. However, the differences between the two simulations were marginal. Therefore, the influence of the symmetry boundary condition on the eddy and lift damping component of the OC5 semi-submersible in surge decay may be neglected.

The trajectory of the floater for the 6 DOF simulation is larger as the semi-submersible's motions are extended to sway, roll, and yaw. Energy is then dissipated also in these degrees-of-freedom. Thus, the skin friction is increased, and hence, also the quadratic damping. The motions in the other DOFs are very small (shown later in the next subsection) and have less influence than the coupling of

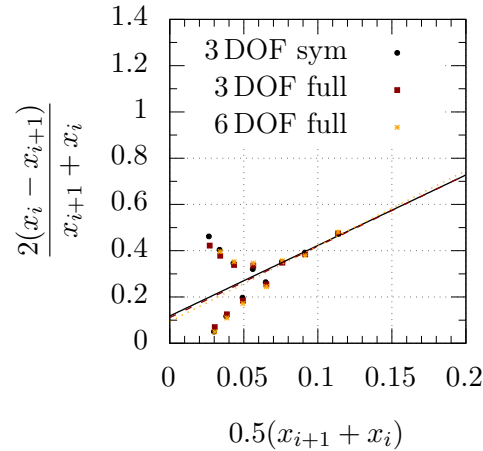


Figure 5.31: PQ diagram for simulations with a quasi-static mooring model and different computational domains: 3 DOF simulation with symmetric domain, 3 DOF simulation with complete domain, and 6 DOF simulation with complete domain

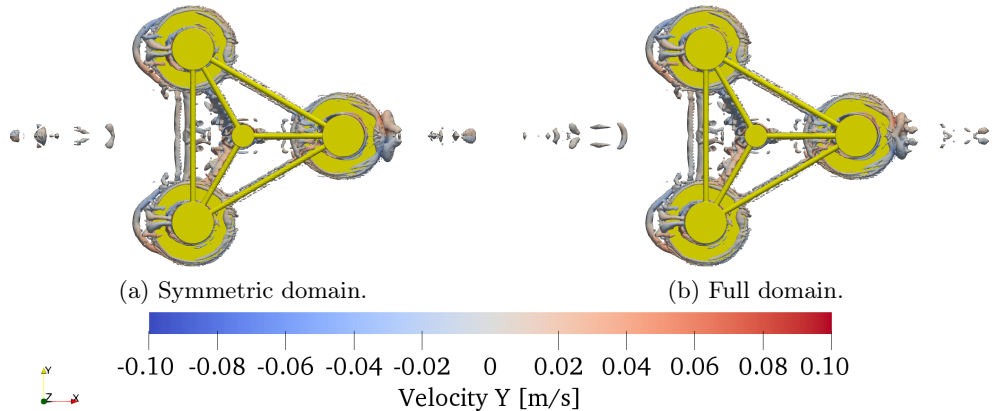


Figure 5.32: Vortices around the floater for symmetric and full domain displayed using $Q = 0.5 \text{ s}^{-2}$ and coloured with the y component of the velocity vector. The simulations enable 3 DOF motions (surge, heave, yaw) and include a non-linear quasi-static mooring model. The chosen time instance is at $t = 12.4451 \text{ s} \approx 0.8 \cdot T_p$. For visualisation purposes, the flow is mirrored at the xz plane for the symmetric domain simulation.

surge with heave and pitch. Summarised, the effect of each modelling influence studied here is minor compared to turbulence and free surface modelling as well as coupling of up to 3 DOF.

5.4.4 Dynamic mooring model

In the experiments used for this thesis, a catenary mooring system was adopted. These mooring lines were towed along by the motions of the floater and interacted

Table 5.17: Hydrodynamic damping comparison of 3 and 6 DOF simulations with a quasi-static mooring model (QSM) and with symmetric (sym.) and full domain (full).

Simulation name	Lin. damping B_1 [Ns/m]	Quad. damping B_2 [Ns ² /m ²]	Crit. damping ratio ζ_D [%]	Oscillation period T_n [s]
3 DOF sym.	2.9660	210.5389	9.9766	14.6615
3 DOF full	2.7891	213.0239	9.9662	14.6567
6 DOF full	2.3610	225.0683	10.1661	14.6509

with the surrounding flow. Hence, the mooring line shape differs from the pure catenary solution as shown in Figure 3.4. Due to the different mooring line shape, the line tension and the restoring loads change compared to the prediction by the catenary mooring equations. Moreover, the moorings create additional damping originating from the components pressure drag, skin friction as well as eddy making. Therefore, a dynamic mooring model using lumped-mass discretisation was coupled to the 6 DOF solver to investigate the effect of the mooring lines on the dynamic behaviour of the floating system. More details regarding the mooring model may be found in Section 3.4.

In Section 5.2.2, a meticulous verification study on the dynamic mooring model was performed. It revealed negligible but quantifiable discretisation errors and uncertainties. Oscillatory convergence was observed for coarser spatial and temporal discretisation. Fine resolution of the mooring model was selected for this reason and the time step sizes investigated in Section 5.2.2 were similar to the time step size used in the CFD solver. Because of the lower computational costs and the good accuracy of the results, the combination of 160 elements and a time step of $\Delta t_4 = T_p/6400$ was chosen for the final simulations. Besides, this combination possessed the same discretisation uncertainties as for the finest data set.

The coupled simulations were performed with a 2nd order Runge-Kutta scheme to save computational time. A comparison of the results between the Cash-Karp and 2nd order scheme may be found in Appendix A. The results show negligible motion differences but significant improvements in computational time. Furthermore, the mooring characteristics used for the verification study in Section 5.2.2 were taken from Gueydon (2016) and were obtained by a previous version of the aNySIM-XMF code. The mooring loads did not replicate the experimental data. Therefore, further sensitivity studies were conducted to improve the mooring tension-surge-motion relation. The detailed results of the simulations may be found in Appendix A. The final mooring model is summarised in Table 5.18. This mooring setup differs from the original by Gueydon (2016) in the mass and submerged weight per meter and in the normal drag coefficient.

The results of the mooring system investigations revealed the largest contribution to the dynamics of the floater by the normal drag coefficient and the weight of the mooring lines. Thus, two drag coefficients and two submerged weight values were applied to study their influence on the hydrodynamic damping of the moored OC5 semi-submersible. These two conditions are the values as reported by Gueydon

Table 5.18: Characteristics of the final mooring system.

Designation	Old values	New values	Units
Length	16.71	16.71	[m]
Mass/meter	0.05024	0.0594	[kg/m]
Submerged weight/meter	0.431917	0.5086	[N/m]
Axial stiffness	5989.0666	5989.0666	[N/m]
Element diameter	0.00277372	0.00277372	[m]
Axial damping	5.0	5.0	[%]
Normal drag coefficient, C_{D_n}	2.4	1.5	[\cdot]
Tangential drag coefficient, C_{D_t}	0.8	0.8	[\cdot]
Normal inertia coefficient, C_{M_n}	3.1	3.1	[\cdot]
Tangential inertia coefficient, C_{M_t}	1.7	1.7	[\cdot]

(2016) and the new values obtained as part of this thesis. In Figure 5.33, the results using different dynamic mooring models with lumped-mass discretisation (LM) are shown and compared to the 6 DOF simulation with a quasi-static mooring model (QSM).

Figure 5.33 presents the motions in all 6 degrees-of-freedom for each simulation. As the geometry in the CFD simulations was perfectly symmetric and the surge decay was performed with initial displacement in x only, the figure reveals negligible motions in sway, roll, and yaw. The choice of mooring model influences the oscillation peaks and periods. Increased submerged weight leads to smaller heave motion, and shorter surge oscillation periods. The pitch and surge oscillation peaks, and hence the hydrodynamic damping, are significantly affected by the normal drag coefficient. This observation is confirmed by the hydrodynamic damping values listed in Table 5.19 and the PQ diagram shown in Figure 5.34.

Table 5.19: Hydrodynamic damping comparison of 6 DOF surge decay simulations with lumped mass mooring model compared for different line stiffness (C_{new} and C_{old}) and normal drag coefficient (C_{D_n}) to the experimental data.

Simulation name	Lin. damping B_1 [Ns/m]	Quad. damping B_2 [Ns ² /m ²]	Crit. damping ratio ζ_D [%]	Oscillation period T_h [s]
$C_{old}, C_{D_n} = 2.4$	4.8866	604.5238	20.9387	16.5720
$C_{old}, C_{D_n} = 1.5$	4.9168	481.0330	17.2256	16.5782
$C_{new}, C_{D_n} = 2.4$	4.7240	497.4867	19.9976	15.4807
$C_{new}, C_{D_n} = 1.5$	4.5685	406.4866	16.7392	15.4935

The dynamic mooring model has the largest influence on quadratic damping. Relative differences of about 48.6% in quadratic damping may be determined between the simulation with C_{old} and $C_{D_n} = 2.4$ and the one with C_{new} and $C_{D_n} = 1.5$. These two simulations also possess a 25% relative difference in the total damping. Compared to the quasi-static mooring model, these differences increase further. Moreover, the linear damping increases slightly for simulations with smaller sub-

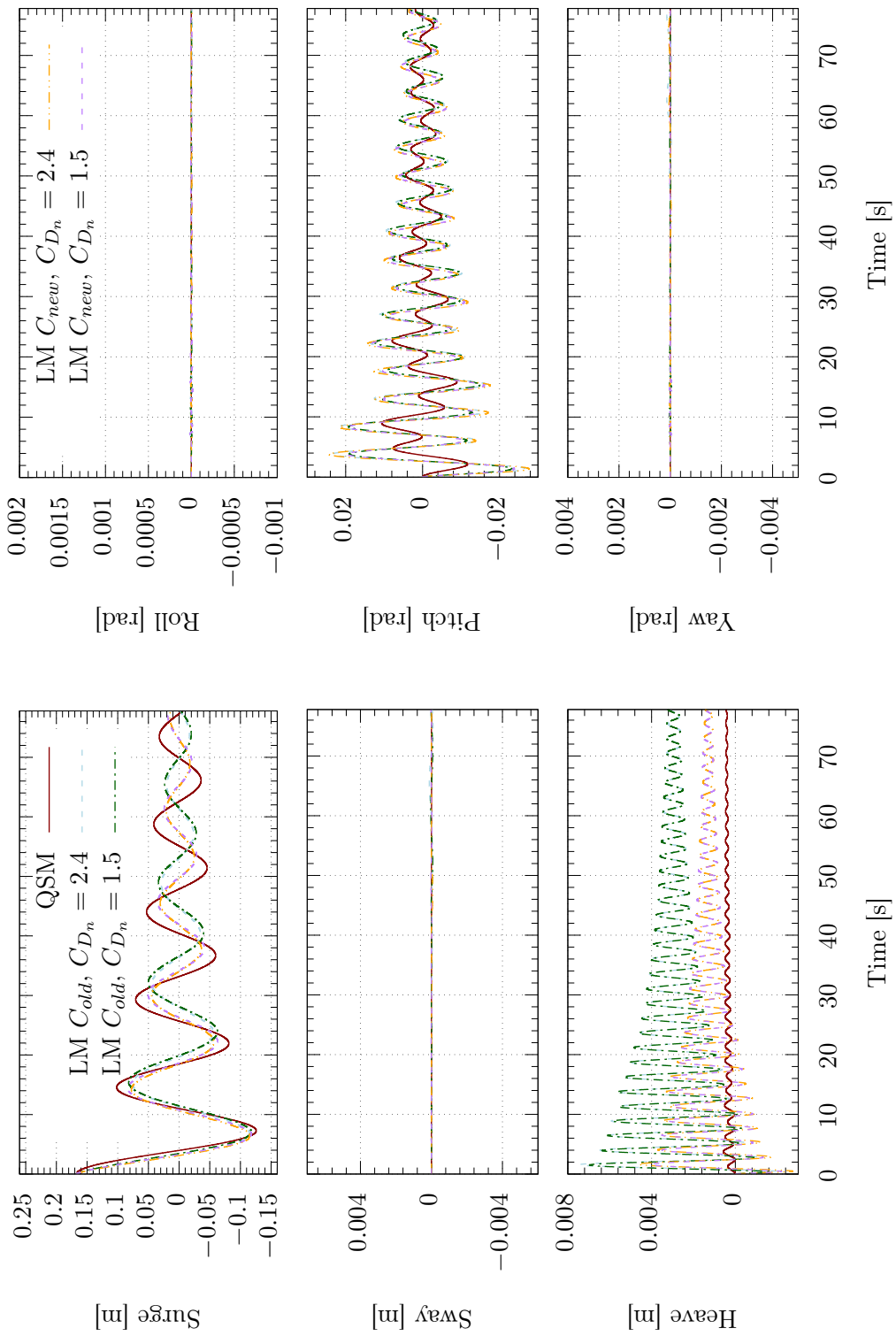


Figure 5.33: Results for 6 DOF surge decay simulations with different mooring models and characteristics.

merged weight, and consequently, larger heave motion. The results presented in Figure 5.34 indicate that the main influence of the mooring model on the quadratic damping (represented by the slope of the fitted lines) originates from the submerged weight. The large differences in hydrodynamic damping between the simulations with the various mooring models show the importance of well calibrated mooring parameters.

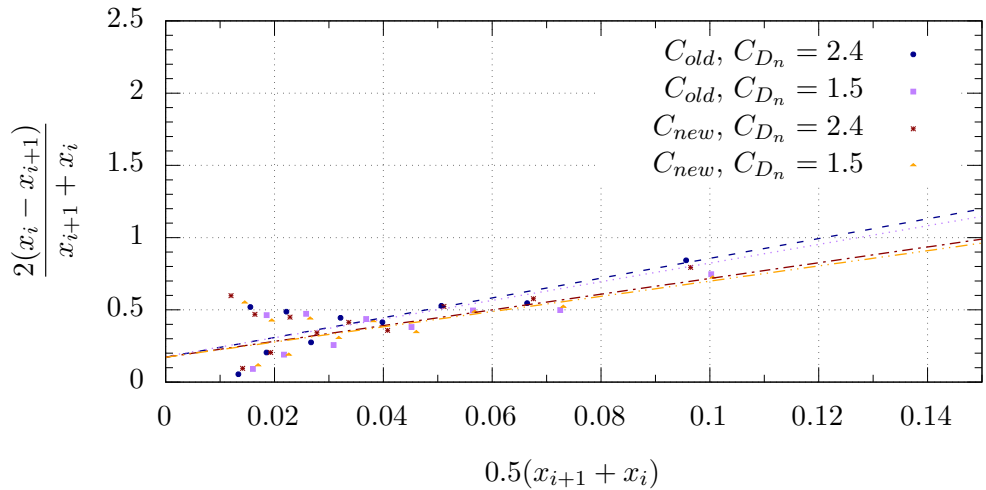


Figure 5.34: PQ diagram for simulations with different characteristics in the dynamic mooring model.

5.5 Validation

The displacement values of the experiment in all 6 DOF are applied as initial conditions to replicate the model tests as close as possible. The influence of this improvement and the comparison to the experiment including a validation uncertainty bar are presented in this section.

5.5.1 Initial six DOF displacement

As the experiments were conducted with initial displacements in all 6 degrees-of-freedom, the cross-wise motions (sway, roll, and yaw) are not represented well by the numerical simulations. This discrepancy alters the damping of the floater. An indication of the changes may be found from the large initial displacement simulation of Section 5.3. Therefore, another simulation with the settings of the best fit of the previous section, i.e. LM C_{sb} , $C_{Dn} = 1.5$, was conducted to investigate the influence of an initial displacement in all 6 DOF. The initial displacement values were taken from the experimental data but without initial velocities or accelerations and without initial flow disturbance around the structure. The results of this simulation are shown in Figure 5.35 and listed in Table 5.20.

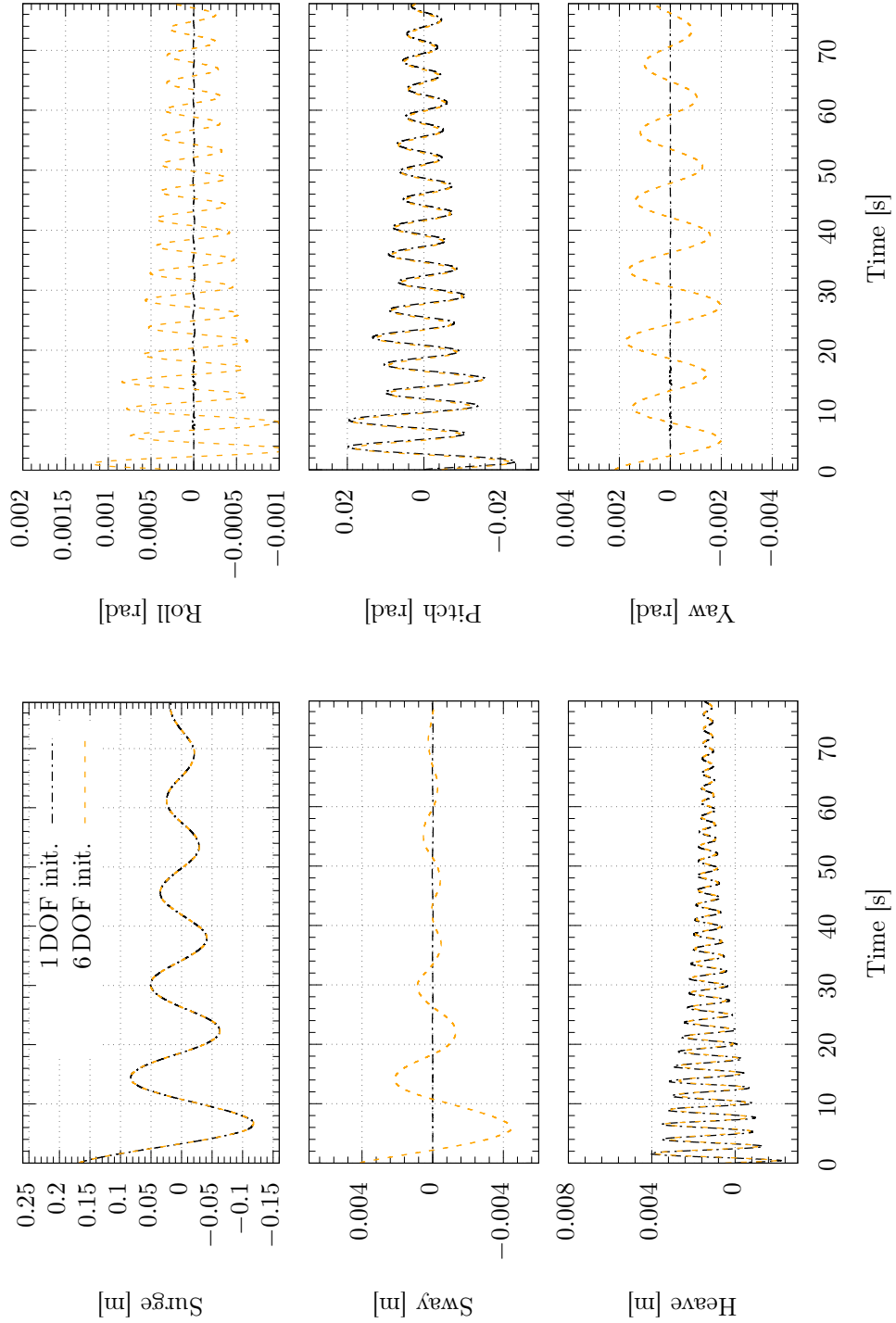


Figure 5.35: Results for 6 DOF surge decay simulations with initial displacements for surge (1 DOF init.) and for each DOF (6 DOF init.).

The difference in surge motion between the two numerical simulations is hardly visible. Thus, the effect of the initial displacements in the other degrees-of-freedom

is minor. Nevertheless, sway, roll, and yaw motions are visible for the whole time history recorded. Sway decays faster than surge. The oscillation amplitudes of sway, roll and yaw are about 1 – 2 orders of magnitude below the surge and pitch motions. The linear and quadratic damping values are influenced slightly.

5.5.2 Comparison with experiment

Figure 5.36 presents the results of the numerical simulation with 6 DOF displacement compared to the experimental data. This figure also presents an uncertainty bar based on the results of Section 5.2.1 and 5.2.2 using the approach by Eça and Hoekstra (2014). As the two discretisation uncertainty results were independent from each other, the new discretisation uncertainty, U_ϕ , may be obtained by:

$$U_\phi = \sqrt{U_{\phi_{LM}}^2 + U_{\phi_{RANS}}^2} . \quad (5.3)$$

In this equation, $U_{\phi_{LM}}$ denotes the discretisation uncertainty determined for the lumped-mass model and $U_{\phi_{RANS}}$ the value for the RANS simulations of Section 5.2.1. For the oscillation height of the second cycle, an uncertainty of $U_\phi = 45.8\%$ was estimated. This uncertainty bar represents the confidence interval, in which the exact solution is to be found with a 95% coverage (Eça and Hoekstra, 2014).

The motion results in surge and pitch were similar between experiment and numerical simulation. In sway and yaw, the differences were larger. This indicates non-symmetric execution of the experiments, non-symmetric setup of the mooring system and/or non-symmetric geometry of the floater. Moreover, there are a larger mean offset and larger oscillations in heave for the numerical simulation. The difference might be a result of a mismatch in floater mass, mooring weight and/or water density between experiment and numerical simulation. Admittedly, the mean could also have been zeroed in the experiments as a post-processing step. This mismatch of heave motion contributes to the hydrodynamic damping as discussed in Section 5.4.2. Nevertheless, this contribution is expected to be small as the motions are small.

The hydrodynamic damping of the numerical simulation has a 17.25% larger linear damping, a 5.16% larger quadratic damping, and a 1.26% larger critical damping ratio than the experiment (Burmester et al., 2021). The discretisation uncertainty estimated overlaps the difference between numerical simulation and experiment. The modelling differences such as a perfect and smooth floater model for the numerical simulations (not possible for experiments), and the missing tower, cable and turbine interactions contribute to motion and damping differences which were not studied in this work. Moreover, the input differences and the spatial discretisation are a major part of the hydrodynamic damping. The remaining input differences are a large negative initial displacement for surge, the corresponding displacements in the other degrees-of-freedom, initial accelerations and velocities of the floater, and initial disturbance of the surrounding flow due to previous motions of the floater. Furthermore, formal validation as defined in Equation (3.103) is not possible as experimental uncertainties were not available.

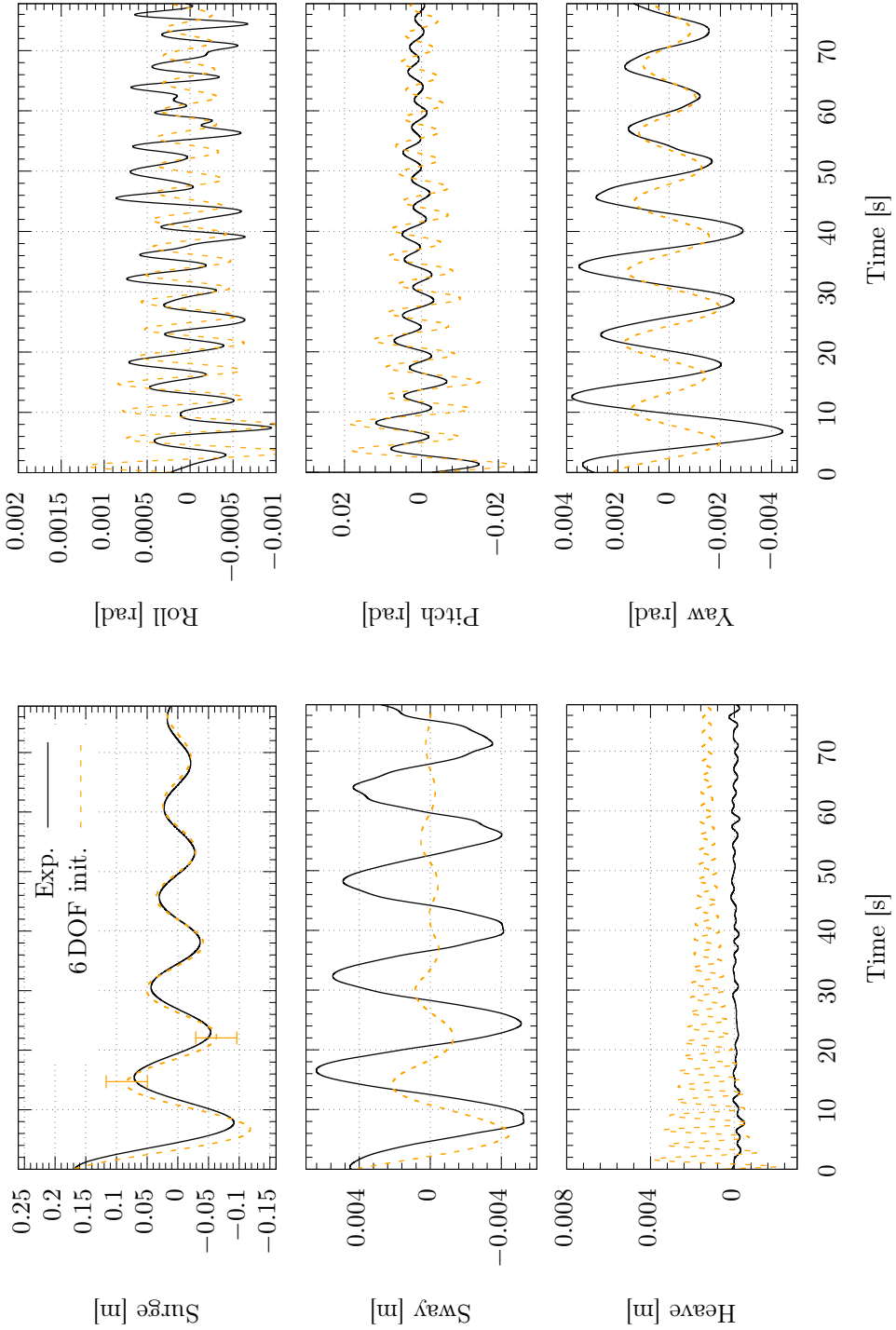


Figure 5.36: Results for 6 DOF surge decay simulation with initial displacements for each DOF compared with the experiment. The discretisation uncertainty bar resulted from the method by Eça and Hoekstra (2014) for the independent RANS and dynamic mooring simulations.

Table 5.20: Hydrodynamic damping comparison of 6 DOF surge decay simulations with to the experimental data.

Simulation name	Lin. damping B_1 [Ns/m]	Quad. damping B_2 [Ns ² /m ²]	Crit. damping ratio ζ_D [%]	Oscillation period T_n [s]
C_{new} , $C_{D_n} = 1.5$ 6 DOF init. displ.	4.5941	401.2189	16.5797	15.4901
Experiment	3.9181	381.5233	16.3731	15.0359

5.6 Concluding Remarks

The work for this chapter included the surge decay simulations of the OC5 DeepCwind semi-submersible floater with CFD and with coupled mooring models. A solution verification study was performed to quantify the numerical errors on the viscous-flow and on the dynamic mooring model simulations. In addition, the influence of different models (turbulence and mooring), different numerical schemes, free surface, motion coupling, different input data, and computational domain configuration on the surge decay motion and hydrodynamic damping were studied and analysed. Taking the numerical errors and all modelling and input influences into account, the final numerical simulation was compared to the experiments, for validation purposes. From these studies, the following conclusions may be drawn:

- Spatial refinement significantly influences the hydrodynamic damping. Grid refinement increases quadratic damping and decreases linear damping of the semi-submersible floater as more eddies are resolved and numerical diffusion is decreased. Moreover, temporal discretisation had a small impact on the hydrodynamic damping at least for the small time steps investigated.
- The influence of increased outer-loop iterations and of the two second-order semi-implicit coupling schemes (see appendix) on the motions may be neglected. The former is a result of stagnation of the residual convergence.
- Involving the free surface in the numerical simulations allows waves to be radiated. This wave radiation damping component is the major contribution to linear damping. It also influences the vortex creation and the skin friction, and thereby affects the quadratic damping. As a result, the hydrodynamic damping components may not be determined independently. Applying wave absorption zones helps to improve the flow solution appearance but it has minor contribution to the hydrodynamic damping (< 1%).
- Because of motions in the other directions during the decay test, kinetic energy of the floater may be dissipated in these directions resulting in more damping of the system. As motion coupling influences the skin friction, this component contributes mainly to quadratic damping. Motion coupling is important up to 3 DOF (surge, heave and pitch coupling).

- The viscous effects largely contribute to quadratic damping and have small influence on the linear damping. The skin friction, pressure drag, and the eddy and lift damping components are reduced for simulations without turbulence models and almost negligible for inviscid flow. Simulations with the turbulence models SST and KSKL showed very similar damping of the system. The hydrodynamic damping results of the EARSM simulation, however, revealed results close to those of the simulation without turbulence model. Compared to the laminar simulation, fewer waves are radiated and more eddies shed. Additionally, the skin friction damping component is reduced using EARSM, and thus, the quadratic damping coefficient.
- Viscous effects do not play a major role for the oscillation period, i.e. it does not influence the added mass of the floater.
- The mooring modelling has a significant influence on the hydrodynamic damping of the platform. The stiffness controls the velocities of the floater affecting the skin friction, eddy creation and wave radiation of the platform. More importantly, the drag coefficient and the submerged weight of the mooring lines contributes directly to quadratic damping. Larger drag coefficients and submerged weight result in increased damping and decreased oscillation period of the floating system. Hence, correct mooring modelling for catenary line systems is crucial to determine the dynamic behaviour of the moored floating platform.
- The input data, such as value of initial displacement, initial displaced degrees-of-freedom, initial velocities and accelerations, initial disturbances of the flow, and point in time of release, influence hydrodynamic damping. Thus, accurate simulation of the surge decay motion requires accurately reported experimental data and good adaptation by the simulation engineer. Nevertheless, accurate 1 DOF initial displacement without excitation of the other degrees-of-freedom is very difficult for experimental tests.

Sarpkaya (2010) states: “The damping is affected by everything and anything that one can possibly imagine”. The results of this chapter are in accordance with this statement and quantify many influencing factors. Many more factors, such as wave reflections, aerodynamic damping due to turbine and tower, connected power cable, surface roughness and flexibility of the floating system, mooring system layout, open windows or doors, external vibrations, post-processing of the data, etc., are possible and could increase this study to infinity. The largest factors from numerical simulation point of view may be the spatial discretisation, the free surface, turbulence and mooring models, the allowable degrees-of-freedom, and correct input data. These factors were studied and their influence shown.

6. Conclusions and Outlook

The work of this thesis is aimed at reliable and accurate numerical predictions of hydrodynamic damping and loads on floating offshore wind turbines. Therefore, three different verification procedures were investigated for four aspects of floating wind turbine simulations: wave propagation, wave loads on a cylinder, surge decay, and a dynamic mooring model. Moreover, the influence of different models (turbulence models, mooring models) and parameters on hydrodynamic damping was analysed using the OC5 semi-submersible floating wind turbine. The numerical simulations were also compared to experimental data, for validation purposes. In this final chapter, the thesis is summarised, conclusions are drawn, and an outlook for further work is provided.

6.1 Summary

The thesis starts with background information on hydrodynamic damping of floating wind turbines and its determination followed by governing equations of fluid flow, their Reynolds averaging, on water wave theories, rigid body motions and the catenary mooring line equations. This theoretical background is given in Chapter 2.

Details on numerical methods used are provided in Chapter 3 with a focus on wave loads and decay simulations of a moored semi-submersible floating wind turbine. At first, methods are specified for the numerical discretisation of the governing equations and the treatment of the pressure and velocity coupling. In addition, wave generation and absorption methods are given as well as specifications on the coupling between fluid flow equations and the rigid body motion equations. Subsequently, formulations for the dynamic mooring model are provided and complemented by the coupling to the viscous-flow solver. These equations are followed by definitions of verification, validation, and numerical error and uncertainty quantification. To estimate discretisation errors, three approaches are introduced: the formulation by Eça and Hoekstra (2014), Oberhagemann and el Moctar (2019), and Xing and Stern (2010). As part of this thesis, the approach by Oberhagemann and el Moctar (2019) was extended with an expression for the discretisation uncertainty.

Numerical computations using the described approaches were conducted for a wave

propagation test case and for wave loads on a surface piercing cylinder. In these studies, iterative convergence was monitored in terms of residual norms, and regions with larger residuals were analysed and discussed. Furthermore, two absorption functions were compared in terms of wave reflection and their optimum settings were found. The three introduced discretisation error and uncertainty approaches were applied to these two cases and compared to each other. In Chapter 4, the results of the wave load case are compared to experimental data, for validation purposes, and of the wave propagation case to the analytical solution. Moreover, wave elevation, wave load, and flow field data were analysed and discussed.

The three discretisation error approaches were also applied to surge decay simulations with a linear stiffness matrix and to the stand-alone simulations of a dynamic mooring model. The results of the different approaches were compared to each other, and a combined uncertainty value based on the viscous-flow and dynamic mooring model simulations was estimated. Moreover, several surge decay simulations were conducted to investigate the influence of different models and input parameters on damping and on the flow characteristics. To ensure comparability of the results, the same damping estimation method was applied to the same number of oscillation cycles for each simulation. The computations involved different spatial and temporal discretisation, initial displacements in space and time, different linear restoring stiffness values, and turbulence modelling approaches. Additionally, simulations with and without free surface as well as with and without wave absorption methods were conducted. The effect of motion coupling for up to 6 DOF, full and half domain computations, and different mooring models were investigated systematically. In Chapter 5, the results of these investigations are presented and discussed in detail.

6.2 General Conclusions

Simpler physical and numerical problems yield smaller discrepancies to the analytical or experimental result and have smaller discretisation uncertainties. This was demonstrated by different investigations on viscous-flow simulations for wave propagation, wave loads on a cylinder, and surge decay of a floating wind turbine with linear restoring stiffness and a dynamic mooring model. For complex flow problems, more input parameters and models are used which lead to larger discrepancies. Accordingly, the verification study on viscous-flow simulations resulted in the largest uncertainty estimates for the surge decay test case.

The three error and uncertainty estimation techniques revealed similar values for the four different verification cases. The approach by Eça and Hoekstra seems to be the most robust method but also the most demanding as it requires at least five data points of five calculations. The estimates of Xing and Stern for the wave propagation test case may be too small. Yet, for all other test cases, this method led to trustworthy results in a similar range as the approach by Eça and Hoekstra. The results for the method by Oberhagemann and el Moctar provided similar estimates as the approach by Eça and Hoekstra. Nevertheless, the approaches by

Xing and Stern as well as by Oberhagemann and el Moctar are less demanding as both rely on data of just three simulations with constant CFL numbers. These data points, however, require to be monotonic convergent in space and time.

In this thesis, a new uncertainty formulation was proposed for the method by Oberhagemann and el Moctar. The new uncertainty estimate includes the quality of the simulation data by changing the safety factor as a function of convergence ratio. In general, this new method predicted slightly lower values for the uncertainty than the other two approaches. Very large discrepancies between theoretical and observed order of convergence did not result in larger uncertainties. Yet, poor quality of the data is accounted for using the uncertainty estimates by Eça and Hoekstra as well as by Xing and Stern.

For periodic simulations such as waves, the influence of the iterative convergence criterion is not significant. The choice of the criterion, however, becomes crucial, if simulations are transient, non-periodic, and grids complex, such as for the surge decay test case. The initial iteration error is propagated and may cause large discrepancies in the results. Therefore, demanding iterative convergence criteria should be selected for transient, non-periodic simulations to achieve time accurate solutions. This will increase computational costs. Thus, investigating the influence of this criterion is recommended to obtain an optimum setting in terms of accuracy and feasibility.

Experimental data including errors and uncertainties are important to formally perform validation. Errors and uncertainties for model test data are seldom provided and were not available for the experimental data underlying this thesis. Nevertheless, the uncertainty bars of the numerical simulations overlapped the experimental result for both, the solution with the finest grid and time step of the wave load simulations, and for the solution of the final coupled surge decay simulation. The results for errors and uncertainties of the wave propagation case also overlapped the analytical solution. Moreover, the verification study on the stand-alone dynamic mooring model simulations exhibited convergence for finer spatial and temporal discretisation of the mooring lines.

In the investigations, spatial refinement significantly influenced hydrodynamic damping. Quadratic damping was increased and linear damping of the semi-submersible floater decreased. Grid refinement led to more accurately resolved viscous effects, finer surface resolution of the floater geometry, and decreased numerical diffusion. As a result, the total hydrodynamic damping decreased for finer grids reducing numerical damping of the simulations. This means, however, that simulations with coarse discretisation might provide good agreement with physical data of hydrodynamic damping. Thus, grid refinement studies are obligatory to accurately capture hydrodynamic damping and to improve reliability of the simulations.

The temporal discretisation was chosen to be very fine, and therefore, its influence on damping and the oscillation period was found negligible. Nevertheless, the Courant numbers affected iterative convergence and the accuracy of numerical schemes such as the interface capturing schemes used to discretise the convection term in the volume fraction transport equation.

Involving free surface in the numerical simulations allowed waves to be radiated. This wave radiation damping component is the major contribution to linear damping of the OC5 semi-submersible. Additionally, this component also influences vortex creation and skin friction, and thereby affects the quadratic damping. Thus, the hydrodynamic damping components may not be determined independently as they are coupled.

Viscous effects largely contribute to quadratic damping and have small influence on linear damping. The skin friction and the eddy and lift components were reduced for simulations without turbulence models, and non-existent (skin friction) or almost negligible (eddy and lift) for inviscid flows. The EARSM model reduces the skin friction component, and therefore, the quadratic damping coefficient was smaller compared to the KSKL and SST model. The viscosity and turbulence model have a minor influence on the oscillation period.

Coupling of different degrees-of-freedom during decay motions are important as kinetic energy is dissipated in the other directions. For the surge decay simulations of the OC5 DeepCwind semi-submersible, motion coupling up to 3 DOF (surge, heave and pitch) increased hydrodynamic damping. Because of additional skin friction and eddies, motion coupling contributes to the quadratic damping of the system. Motion coupling including the other degrees-of-freedom seems to be negligible.

The mooring model had a significant impact on hydrodynamic damping of the platform. The stiffness controlled motion velocities of the floater, and hence, affected skin friction, eddy creation, and wave radiation. Moreover, the drag coefficient defined for dynamic mooring models contributes directly to quadratic damping. Larger drag coefficients resulted in increased damping and larger stiffness in decreased oscillation period of the floating system. Thus, correct mooring modelling for catenary line systems is crucial to determine the dynamic behaviour of the moored floating platform.

The input data, such as value of initial displacement and point in time of release, have an influence on hydrodynamic damping. An earlier time of release leads to disturbances of the flow around the structure, and in turn, to lower linear damping. This contribution is not negligible. Therefore, accurate simulation of the surge decay motion also requires accurately reported experimental data and good adaptation by the simulation engineer. As this was one of the critical issues with the experimental data underlying this thesis and provided to the OC5 consortium, experiments for the succeeding OC6 project were simplified and the effects of input data uncertainty investigated (Robertson et al., 2020b,a).

6.3 Outlook

Future work requires experimental data with estimated errors and uncertainties to formally validate numerical simulations of floating wind turbines.

The turbulence modelling approaches could be extended to hybrid or bridging methods using full domain simulations to assess the influence of a variety of more accurate turbulence models on hydrodynamic damping.

Investigations on the mooring induced hydrodynamic damping could be extended to different solvers using different discretisation approaches, input parameters, etc. A list of suitable solvers was given by Thomsen et al. (2017). Moreover, the coupling could include the local velocity and pressure field to improve the accuracy of the considered hydrodynamic loads on the lines.

The next step in the investigation of the hydrodynamics of floating wind turbines should be the simulation of moored semi-submersible floaters in regular waves, in bi-chromatic waves, and eventually, in irregular sea states. At first, wave propagation for the respective wave parameters needs to be verified followed by further verification of floater motions. A start in this direction is given by Wang et al. (2020b).

Further investigations should include the assessment of the aerodynamic behaviour of the turbine and tower. Subsequently, coupled simulations on floating wind turbines with rotating turbine and moving floater are possible. In an extended step, wind turbine control algorithms could be added to increase comparability to full scale devices and to study its effects on the dynamic behaviour of the floating system. Each step requires verification and validation. Finally, structural elasticity needs to be included in the CFD simulations and verified to complete the assessment of CFD credibility for floating wind turbines (see Figure 1.2).

A. Mooring Calculations

This appendix is dedicated to investigations with the dynamic mooring model. Several studies are detailed to show the procedure to obtain improved mooring characteristics. These studies include analysis of the considered hydrodynamic coefficients, and the influence of a different Runge-Kutta type integration scheme. The original mooring simulations were setup and performed by Gueydon (2016) using a previous version of aNySIM. The input data was calibrated against the experimental data used for the OC5 project. These characteristics were also applied for the verification studies of this thesis. Simulations with the aNySIMxml version of this thesis (aNySIMxml v12.2 or xsimulation v4.1.4), however, did not replicate the experimental results. Moreover, the mooring lines modelled with the lumped-mass model were well refined as the results in Chapter 5 revealed. More refinement lead to more computing time, and therefore, faster time integration schemes of second order were considered for the final coupled viscous-flow and dynamic mooring simulations.

A.1 Time integration schemes

The mooring solver allows the use of several different explicit time integration schemes of the Runge-Kutta (RK) type. These schemes range from the second-order accurate Runge-Kutta (RK2) scheme to the fifth-order accurate Cash-Karp scheme (RK45). A sensitivity study on these two methods is conducted for a time step of $\Delta t_4 = T_p/6400$ as the time step size is determined by the RANS simulations, approved by the mooring solver verification study, and in the stability region of both explicit time integration schemes provided van den Berg and Pauw (2018). The RK2 scheme has three times less derivative functions to solve, and therefore, this scheme is expected to be three times faster than the RK45 method. In this study, the two schemes were compared in terms of absolute difference of oscillatory motion values and computing time. The time history with both schemes produced the result as shown in Figure A.1.

The two simulations are on top of each other with a difference of $\leq 0.02\%$ in motion amplitude for this particular case (160 elements and $\Delta t_4 = T/6400$). The computational time for RK2 was reduced about 20% compared to the simulation with RK45. Each of these simulations was conducted on a laptop (Intel Core i7 6700-HQ processor with 2.6GHz and 16GB memory). The impact of this time reduction on the coupled computation time is expected to be small as most of

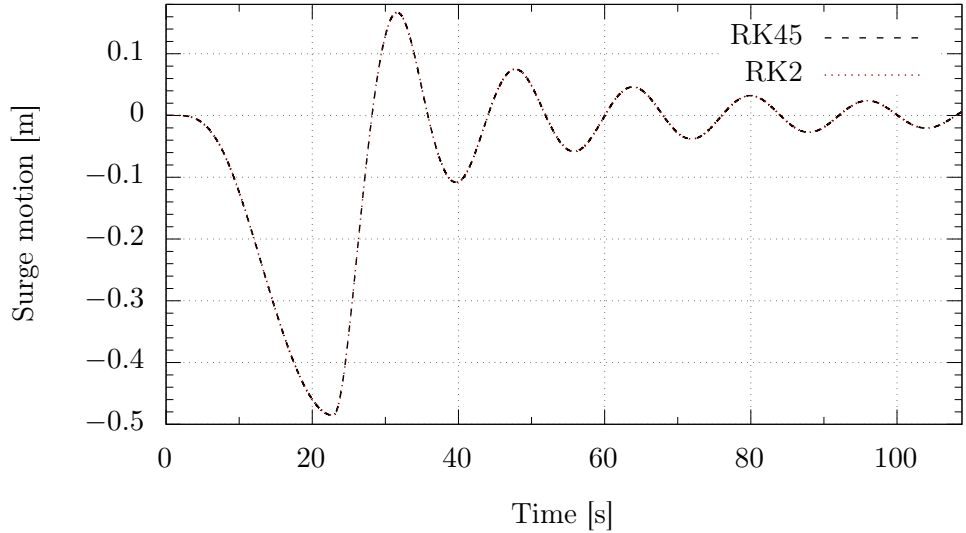


Figure A.1: Time history second-order Runge-Kutta (RK2) and fifth-order Cash-Karp (RK45) scheme. The simulation results were obtained with 160 elements and a time-step of $\Delta t_4 = T/6400$.

the computations take place on the RANS side. Nevertheless, the following investigations and the coupling with the RANS solver were conducted with the RK2 time discretisation scheme as there was no significant loss of accuracy and the computations were significantly faster than using the higher-order RK45 scheme.

A.2 Drag and inertia on the mooring lines

The hydrodynamic loads induced on the mooring lines are computed by an empirical Morison type formulation. These loads are composed of a drag and inertia term. They are estimated using dimensionless and empirically determined coefficients defined in the mooring line coordinate system as normal and tangential to the line. Thus, two drag and two inertia coefficients were calibrated by Gueydon (2016) and are listed in Table 5.3. The hydrodynamic forces on the line are essential for the mooring loads at the fairleads which in turn influences the motions of the floater. To analyse the influence of different drag and inertia coefficients on the mooring loads, the tension of the dynamic mooring lines at the fairleads were computed and compared to the experiment. Therefore, the motions of the experiment were imposed on the numerical model. In other words, the numerical model followed exactly the motions of the experiment. The results for different normal drag coefficients are presented for the front line, line 1, in Figure A.2. The line with normal drag coefficient of $C_{D_n} = 2.4$ represents the result as given by Gueydon (2016). Assuming no dynamic effects in the lines are present, the tension at zero surge motion is the pretension of the mooring line. The tension plot starts around zero x motion and reaches the top tension load at the negative maxima

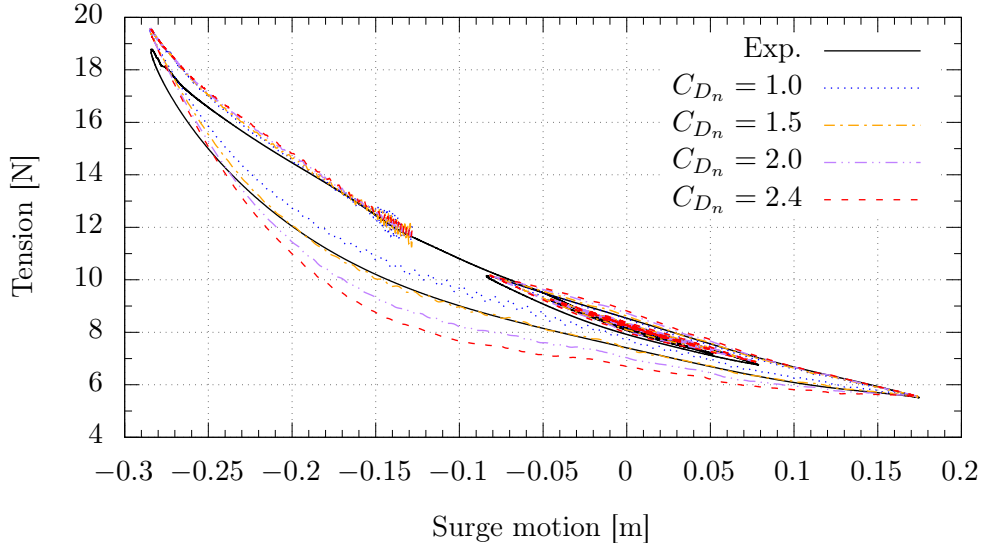


Figure A.2: Mooring tension in the front line, line 1, as a function of surge displacement during decay simulations for different normal drag coefficients C_{D_n} . The tension values of the experiment are shifted by -1.04 N , for visualisation purposes.

of the surge motion. Then, the tension reduces with the floater approaching the positive maximum surge position. The decrease of tension does not follow the rising curve owing to dynamic effects in the mooring line. The difference between tension increase and decrease curve becomes larger for larger normal drag coefficients. The difference between these plotted lines represents a loss of energy in the oscillating system. Thus, it shows the mooring induced damping on the floater. The tension-motion curve of the numerical simulations is closer to the experiment for smaller tension. In the coupled RANS simulations, the maximum tension values of the presented results were never reached as the simulated surge decay motions were in the range between -0.15 m to 0.167 m . In this range, the simulation with $C_{D_n} = 1.5$ shows the best match of the experimental results. Therefore, the following simulations were conducted with this normal drag coefficient.

The tension-motion results for different tangential drag coefficients are presented for the front line, line 1, in Figure A.3.

The results shown in Figure A.3 reveal no significant influence of the tangential drag coefficient on the mooring line load. As the motion, and therefore, the fluid velocities in surge motion are normal to the mooring line coordinate system, negligible influence of the tangential drag coefficient was expected. Decreasing the tangential drag coefficient to zero lead to small tension oscillations. These were reduced for larger coefficients. Hence, the value of the tangential drag coefficient applied to the following simulations remained at $C_{D_t} = 0.8$ as documented by Gueydon (2016).

Figure A.4 shows the mooring tension results as a function of the surge motion for different normal inertia coefficients C_{M_n} .

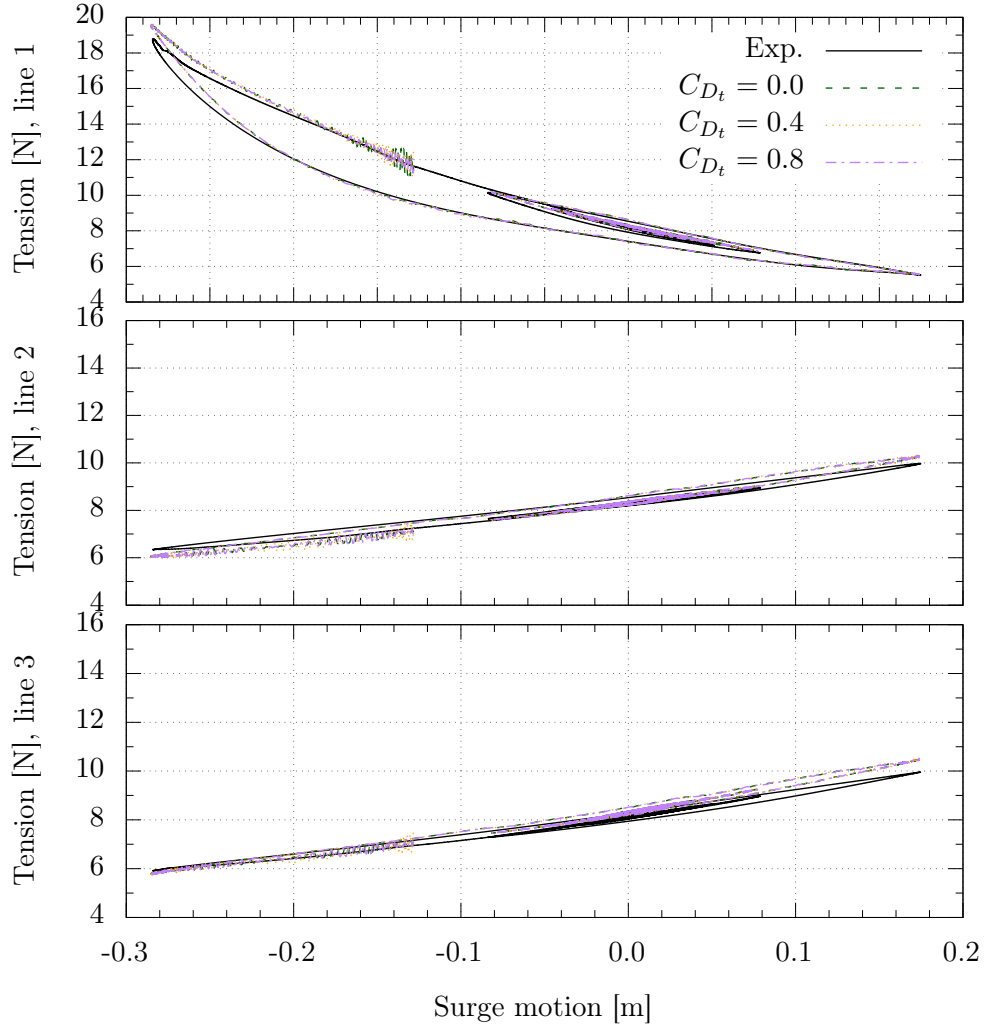


Figure A.3: Mooring tension in line 1, 2 and 3 as a function of surge displacement during surge decay simulations for different tangential drag coefficients C_{Dt} . For visualisation purposes, the tension values of the experiment are shifted by -1.04 N and -0.52 N for the upstream (line 1) and downstream (line 2 and 3) mooring lines, respectively.

No significant influence of different inertia coefficients on the mooring line tension is visible in Figure A.4. The results for different tangential inertia coefficients is identical to the normal inertia coefficient study. Therefore, the values of the inertia coefficients were not changed and used as calibrated by Gueydon (2016). The last investigation focuses on the submerged weight of the mooring lines which influences the pretension. The different pretension was the reason for shifted tension values of the experiment in these investigations.

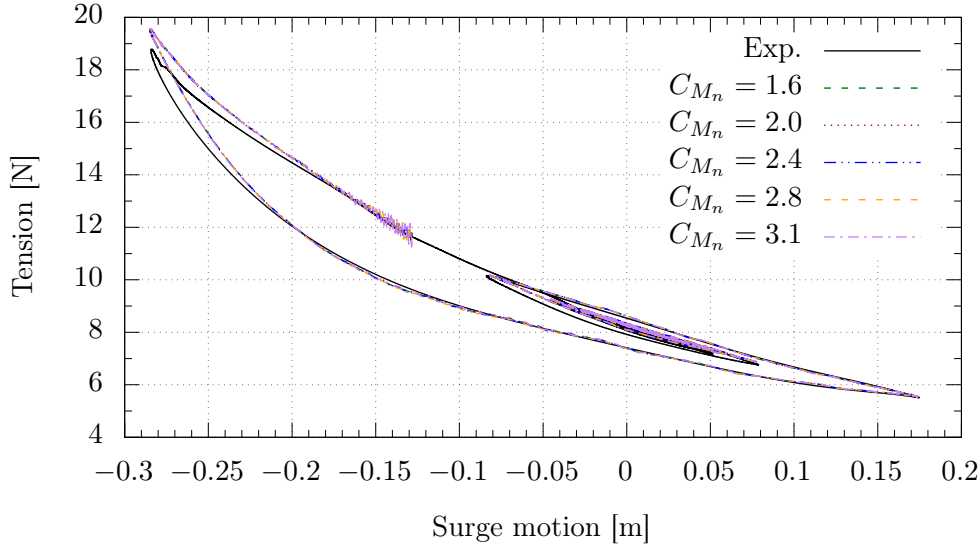


Figure A.4: Mooring tension in line 1 as a function of surge displacement during surge decay simulations for different normal inertia coefficients C_{M_n} . The tension values of the experiment are shifted by -1.04 N , for visualisation purposes.

A.3 Mooring characteristics

The zero-crossing tension values are comparable to the pretension of the mooring system. The pretension of the mooring system depends on the axial stiffness, the mass, and the submerged weight of each line. The axial stiffness is a property of the line easily proved by displacement tests in dry conditions. The mass of the line is only important for mooring systems with parts above the free surface. However, the mass and submerged weight are linked to each other and should not be changed independently. Thus, the submerged weight was altered to fit the experimental tension-motion curve. The result for an increase of submerged weight by 19.3% was compared to a simulation with the original value given by Gueydon (2016). Figure A.5 shows this comparison for the three mooring lines.

Both numerical results, the original and the new, were obtained with the normal drag coefficient, i.e. $C_{D_n} = 1.5$. The comparison of the three plots shows that line 1 experienced the largest loads and the loads on line 2 and 3 were not symmetric during this simulation/experiment. Owing to the imposed motion of the experiment on the numerical simulation, similar mooring load behaviour for the numerical simulation and the experiment may be observed. The surge decay was not a pure one DOF motion. Sway, heave, roll, pitch, and yaw motions were observed and recorded during this experimental test (see Figure 5.33). If the test is not pure symmetric, the mooring lines cannot be loaded symmetrically. This difference was also present in the numerical simulations. The original submerged weight of the mooring lines by Gueydon (2016) reveals better results for the tension-motion relation of line 2 and 3. Nevertheless, the new values match the characteristics of line 1 better. Furthermore, the slope of the tension-motion lines for the numer-

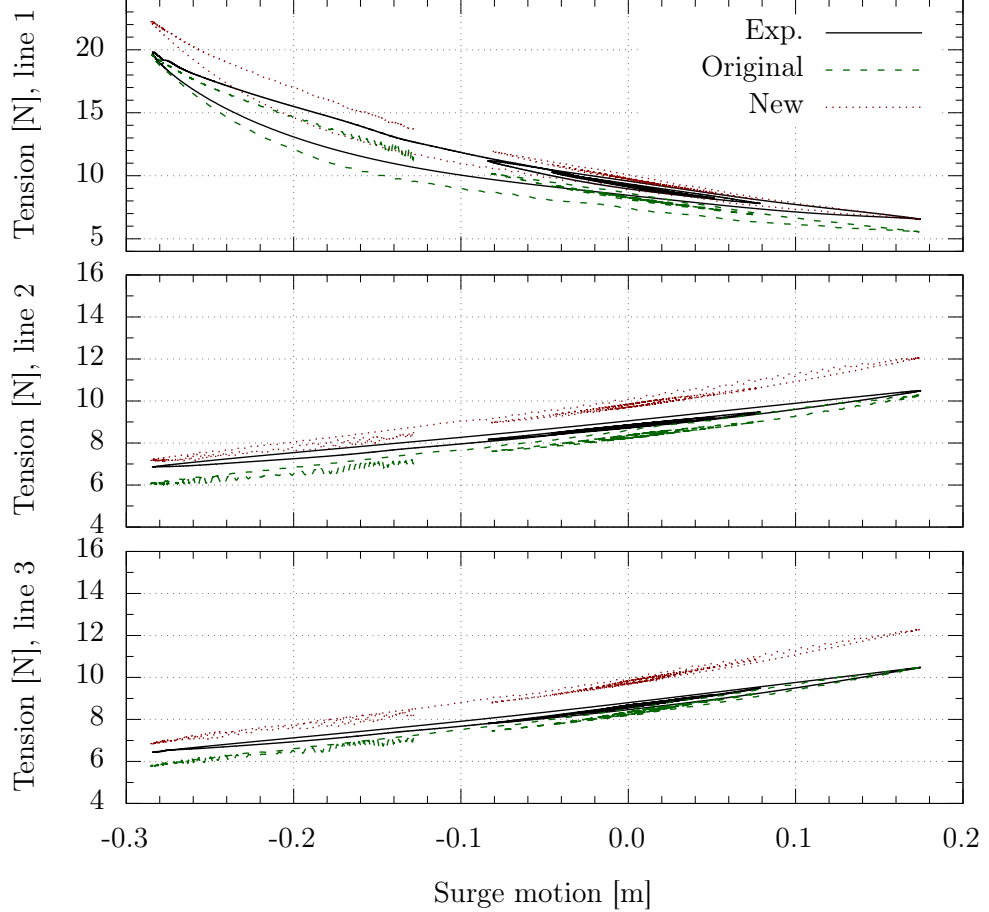


Figure A.5: Mooring tension in line 1, 2 and 3 as a function of surge displacement during decay simulations for different submerged weight values.

ical results are steeper than of the experiment. Thus, the axial stiffness of the numerical simulations was not correct and needs further investigations. However, the characteristics of the mooring lines influence each other. The axial stiffness, axial damping, drag and inertia coefficients, and the submerged weight change the shape of the tension-motion curve. The difference between numerical simulation and experiment is acceptable. The characteristics of the new mooring system are summarised in Table A.1. This mooring setup differs from the original by Gueddon (2016) in the mass and submerged weight per meter and in the normal drag coefficient (see Table 5.3).

Table A.1: Characteristics of the new mooring system.

Designation	Value	Units
Length	16.71	[m]
Mass/meter	0.0594	[kg/m]
Submerged weight/meter	0.5086	[N/m]
Axial stiffness	5989.0666	[N/m]
Element diameter	0.00277372	[m]
Axial damping	5.0	[%]
Normal drag coefficient, C_{D_n}	1.5	[\cdot]
Tangential drag coefficient, C_{D_t}	0.8	[\cdot]
Normal inertia coefficient, C_{M_n}	3.1	[\cdot]
Tangential inertia coefficient, C_{M_t}	1.7	[\cdot]

B. Further Hydrodynamic Damping Investigations

In this chapter, a couple of additional investigations are presented. These investigations are aimed at additional influencing factors on the hydrodynamic damping. These factors are different second order coupling schemes between the rigid body motion and viscous-flow solver, and discrepancies in the input data for the temperature and viscosity. Furthermore, details on the motion coupling for different 6 DOF simulations are presented.

B.1 Coupling schemes

The coupling between the rigid-body motion solver and the viscous-flow solver was done with Adams-Bashforth-Moulton (ABM) as implemented by Rosetti (2015), Rosetti and Vaz (2017), Vaz (2014) or with the second-order backward differencing (BDF2) scheme. Figure B.1 shows a comparison of the surge decay results using these two schemes for a 1 DOF simulation with symmetric domain and linear stiffness matrix. In the two cases, the numerical settings, such as outer-loop coupling frequency, were the same.

The results reveal no differences between the two schemes. The oscillation peaks differ by less than $10^{-3}\%$ from each other. Thus, the results are independent on either of the two coupling schemes investigated. For all other simulations in the thesis, the BDF2 scheme was used.

The accuracy of the coupling depends on the outer-loop coupling frequency defined by the user, which is set to each 10th outer-loop iteration for the simulations of this thesis. At each 10th outer-loop, the information is transferred between structural and fluid equations. Two further simulations were performed using a frequency of each outer-loop iteration with the same maximum number of outer-loop iterations and with 200 outer-loop iterations. The results are presented in Figure B.2 and in Table B.1.

The figures depict no significant differences. Applying the motion optimised PQ method, however, reveals small differences between the three simulations, see Table B.1. The largest differences occur between the simulation using coupling at each 10th outer-loop iteration and the simulation with a coupling frequency of 1 and a maximum of 200 outer-loops per time step. The relative difference is of $< 0.8\%$ in linear and of $< 0.4\%$ in quadratic damping. The periods differ by

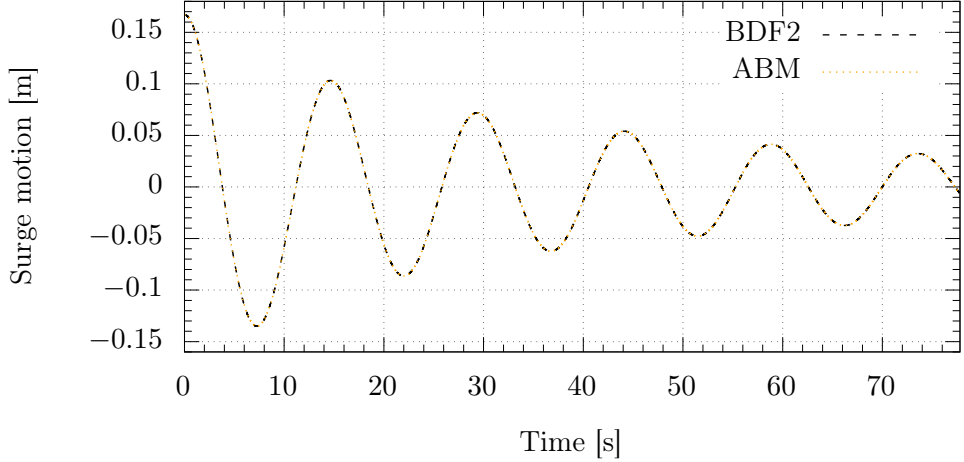


Figure B.1: Comparison of results for two different coupling schemes, the Adams-Basforth-Moulton (ABM) and the second-order backward differencing (BDF2) scheme.

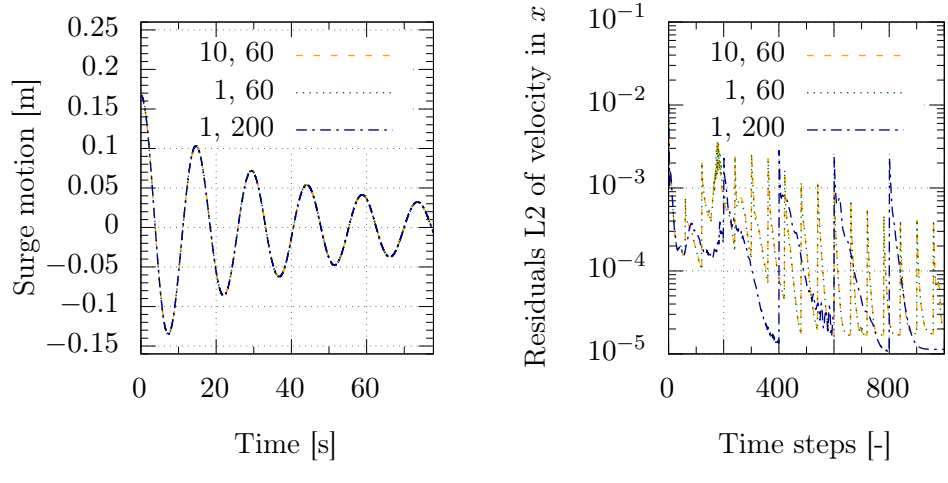


Figure B.2: Comparison of results for two different coupling frequencies and two different maximum outer-loop iterations. The simulation numbers mean the following: 10, 60 - coupling at each 10th outer iteration with a maximum of 60 iterations per time step, 1, 60 - coupling at each outer iteration with max. 60 iterations, 1, 200 - coupling at each outer iteration and max. 200 iterations per time step.

< 0.01% from each other. These differences are marginal and do not justify the additional computational time. Moreover, the residual convergence stagnates and never reaches the demanding criteria specified as discussed in Section 5.2.1. Therefore, all simulations were conducted with coupling at each 10th outer-loop and a

Table B.1: Damping differences between two different coupling frequencies and two different maximum outer-loop iterations.

Simulation	Linear damp. term B_1 [Ns/m]	Quadratic damp. term B_2 [Ns ² /m ²]	Natural period T_n [s]
Each 10 th it., max. 60	3.3246	189.0627	14.6916
Each it., max. 60	3.3245	188.4251	14.6911
Each it., max. 200	3.3501	188.3963	14.6927

maximum of 60 outer-loops per time step.

B.2 Influence of Temperature

The temperature was not documented during the experiments but a posteriori determined as 16.5° C. Thus, there might have been a relatively large discrepancy between each day of measurement. For the numerical simulations, the dynamic viscosity and density of water and air at 16.5° C were fixed. Yet, the viscosity influences the quadratic damping as analysed in Section 5.4.1. Therefore, the influence of viscosity corresponding to 1° C warmer and colder than the temperature determined was investigated with a simulation for 15.5° C and for 17.5° C. The results revealed small differences of 0.77% in linear damping to the standard 1 DOF simulation with free surface. The quadratic damping differed by 0.57% to the simulation at 16.5° C. These differences are below 1 %. Thus, small deviations in the reported temperature will not influence the results significantly.

B.3 Motion coupling

Figure B.3 presents different views on the motion coupling. The top left plot represents the surge decay comparison between the experiment and three simulations. The simulations differ by their mooring model and initial displacement, i.e. a lumped mass (LM) mooring model, quasi-static moorings (QSM), initial displacement in surge (1 DOF init) and initial displacement in all directions (6 DOF init). The results were already presented in Section 5.4.4. The other plots in Figure B.3 display sway, heave, roll, pitch, and yaw as a function of the surge decay motion. Each of the motion trajectories starts at the maximum surge displacement on the right. As the initial velocity of the floater was zero for the numerical simulations and non-zero for the experiment, the path trace shown in the plots is very different. Nevertheless, the simulation with initial displacement in all 6 DOF shows motion results in the same order as the experiment. The maxima in sway, roll, pitch and yaw coincide with the maxima of surge for both, the experiment as well as the numerical simulation. The heave motion is larger for the numerical simulation due to the small mismatch of the hydrostatics, i.e. the mass of the floating system and the weight of the mooring lines do not equal the buoyancy. However, all differences are very small. The strongest coupling exists between surge and pitch motion. This

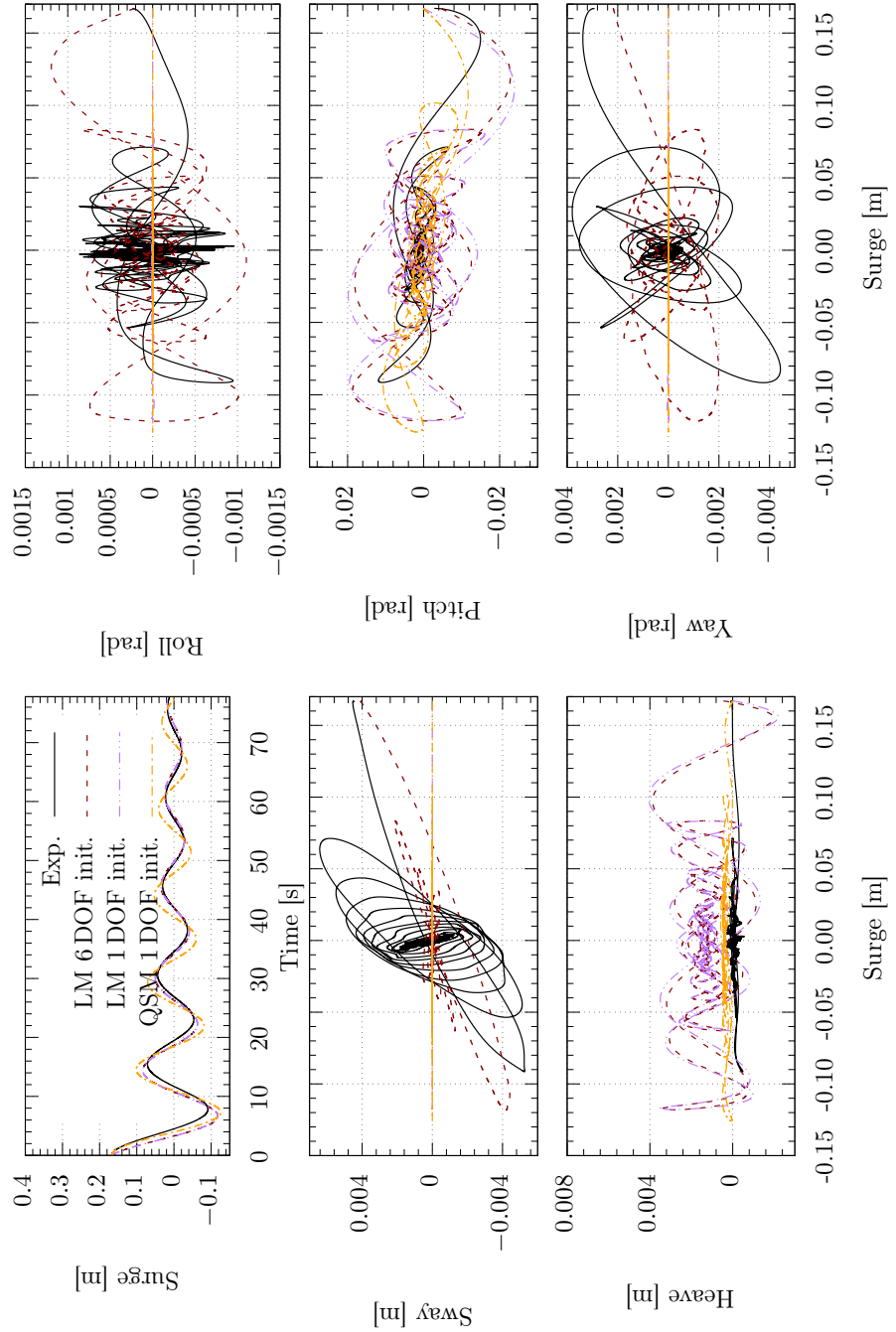


Figure B.3: Surge decay simulations allowing for 6 DOF motions. Visualising each DOF as a function of the surge motion

coupling is also present for the simulations with 1 DOF initial displacement, which proofs small influence from the initial conditions. The motions in sway, roll and yaw, however, are a result of the not perfect execution of the experiments, and a not perfectly shaped geometry, distributed mass, and mooring setup. Nevertheless, a perfect execution for 1 DOF, and a perfect geometry, and mooring setup are currently impossible in model tests.

C. Interface Capturing Schemes

ReFRESCO's interface capturing scheme (Refrics) was used for all simulations in this thesis. In this chapter, the differences to other interface capturing schemes are highlighted in terms of wave elevation, loads on cylinder, and flow solution for the wave load test case.

C.1 Numerical Simulations

From the simulations summarised in Table 4.12, Grid C was used together with the time steps: Δt_3 , Δt_4 and Δt_5 , i.e. $\text{CFL} = 0.21$, $\text{CFL} = 0.15$, and $\text{CFL} = 0.11$. Each of these cases was computed with the following interface capturing schemes:

- Refrics (ReFRESCO's interface capturing scheme): More details on the theory and implementation can be found in Klaij et al. (2018)
- QUICK (Quadratic Upwind Interpolation for Convective Kinematics): More details are given in e.g. Ferziger and Perić (2002).
- HRIC (High Resolution Interface Capturing): This scheme was introduced by Muzaferija et al. (1999).
- SuperBee: Roe (1985) gave name to this scheme.

Thus, twelve simulations were performed to investigate the influence of these schemes for different CFL numbers on the results.

C.2 Iterative Convergence

The iterative convergence tolerance was set to $L_\infty \leq 10^{-4}$ for each simulation. The maximum number of outer-loop iterations was set to 100. In Figure C.1, the iterative convergence levels reached for the air volume fraction c are presented in L_2 norm.

Figure C.1 shows small influence of the time step size on the residual levels reached at the end of each time step. The average number of outer loop iterations per time step are presented in Table C.1 based on 30 wave periods.

The results in Table C.1 show a decrease of outer-loops per time step needed for larger temporal discretization. The influence of the time step size is larger for Refrics and SuperBee than for HRIC and QUICK. In general, QUICK is the fastest scheme and SuperBee the slowest of these four.

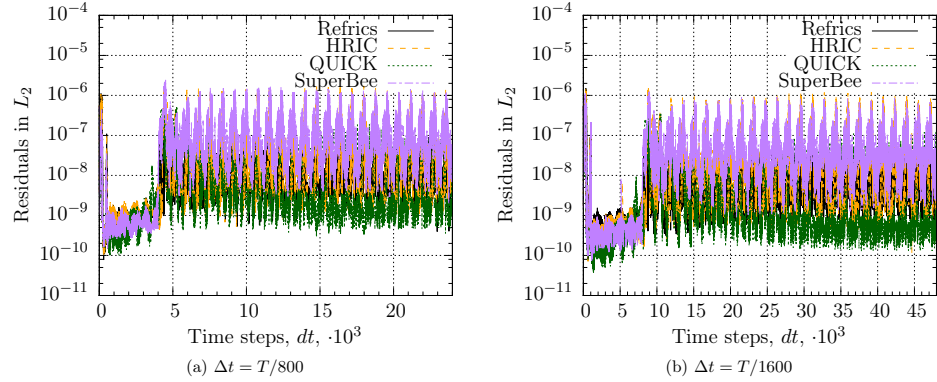


Figure C.1: Residuals for the volume fraction c in L_2 norm of the different interface capturing schemes. The residuals are presented at the end of each time step.

Table C.1: Average amount of outer-loop iterations per time step needed to reach convergence limit per interface capturing scheme.

Schemes / Δt	$T/800$	$T/1131$	$T/1600$
Refrics	72	64	58
HRIC	70	64	59
QUICK	54	50	46
SuperBee	75	68	62

C.3 Wave Elevation and Loads

The wave elevation at the end of the simulation for two time steps is shown in Figure C.2.

The wave elevation at inlet, $x = 0.0$ m, and outlet, $x = 35.0$ m, was forced to the Stokes 5th order solution by the absorption zones. Therefore, the results differ mostly in the centre of the domain. Here, large differences between QUICK and the other three results may be observed. The height and period of the wave was captured similarly by Refrics, HRIC and SuperBee. The difference of these schemes may be seen in the wave crest shape. The steepest shape is visible for Refrics and SuperBee.

The wave elevation influences the wave loads on the cylinder. Therefore, the wave loads are presented in Figure C.3. This figure shows that larger waves cause larger wave loads on the cylinder. Thus, QUICK also results in smaller wave loads than the other three.

C.4 Flow Solution

The air volume fraction at the centre line $y = 0.0$ m is shown in Figure C.4 just upstream of the cylinder.

The shape of the air volume fraction presented in this figure differs between these

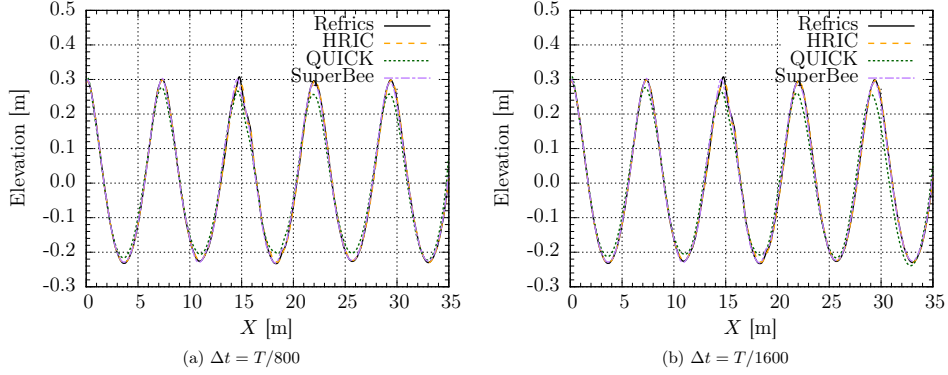


Figure C.2: Wave elevation along the x axis for the different interface capturing schemes. The elevation is measured $y = 0.5$ m from the centre line of the cylinder.

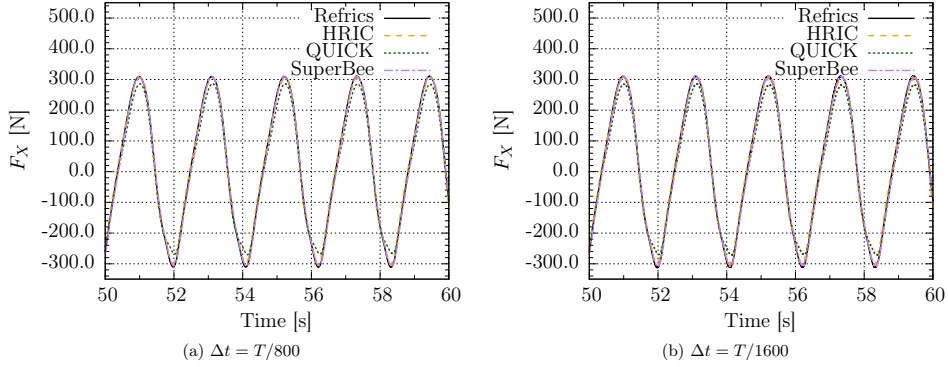


Figure C.3: Wave loads on the cylinder for the different interface capturing schemes.

simulations. Refrics and HRIC present a sharp interface within three cells in vertical direction. The solution of these two interface capturing schemes for the wave further away from the cylinder, however, starts to differ notably. The interface for the simulation using SuperBee is distributed over five cells and using QUICK about ten cells.

C.5 Remarks

For the investigated wave load case, it is not recommended to use QUICK to capture the interface between water and air for such wave load cases. HRIC and Refrics were both satisfying in terms of computational costs and accuracy. SuperBee provides satisfying results for the wave elevation and loads but delivers different results for the flow solution.

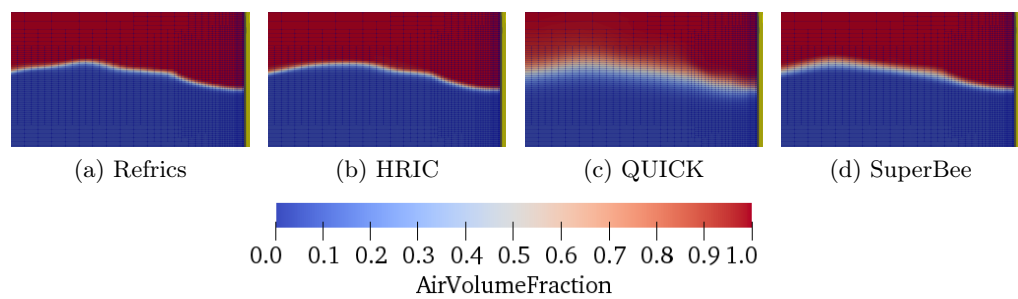


Figure C.4: Air volume fraction of the wave at $t = 59.192\text{ s}$ for four different interface capturing schemes upstream of the cylinder.

Bibliography

- Adam, F., Myland, T., Dahlhaus, F., and Großmann, J.
2014. Scale tests of the GICON-TLP for wind turbines. In *Proc. of the 33rd International Conference on Ocean, Offshore and Arctic Engineering, OMAE*, San Francisco, CA, USA.
- Aloisio, G. and Di Felice, F.
2006. PIV analysis around the bilge keel of a ship model in free roll decay. In *Proc. of the 14th National Meeting of the Italian Association of LASer VElocimetry and non invasive diagnostics*, Rome, Italy. AIVELA.
- Andersen, M. T.
2016. *Floating Foundations for Offshore Wind Turbines*. PhD thesis, Aalborg University, Denmark.
- Azcona, J., Bouchotrouch, F., González, M., Garciandía, J., Munduate, X., Kelberlau, F., and Nygaard, T. A.
2014. Aerodynamic thrust modelling in wave tank tests of offshore floating wind turbines using a ducted fan. *Journal of Physics: Conference Series*, 524.
- Bak, C., Zahle, F., Bitsche, R., Kim, T., Yde, A. Henriksen, L. C., Natarajan, A., and Hansen, M.
2013. Description of the DTU 10 MW Reference wind turbine. Technical Report Energy Report-I-0092, DTU - Technical University of Denmark, Roskilde, Denmark.
- Bauer, M., Gylstorff, S., Bargmann Madsen, E., and Mejlgård, N.
2018. The Fukushima accident and public perceptions about nuclear power around the globe - A challenge & response model. *Environmental Communication*, 13.
- Bayati, I., Facchinetti, A., Fontanella, A., Giberti, H., and Belloli, M.
2018. A wind tunnel/HIL setup for integrated tests of floating offshore wind turbines. *Journal of Physics: Conference Series*, 1037.
- Bearman, P. and Russel, M.
1997. Measurements of hydrodynamic damping of bluff bodies with application to the prediction of viscous damping of TLP hulls. In *Twenty-First Symposium on Naval Hydrodynamics*, Washington, DC, USA.

- Benitz, M.
2016. *Simulating the Hydrodynamics of Offshore Floating Wind Turbine Platforms in a Finite Volume Framework*. PhD thesis, University of Massachusetts - Amherst, Amherst, MA, USA.
- Benitz, M. A., Schmidt, D. P., Lackner, M. A., M. Stewart, G., Jonkman, J., and Robertson, A.
2015. Validation of hydrodynamic load models using CFD for the OC4-DeepCwind semisubmersible. In *Proc. of the 34th International Conference on Ocean, Offshore and Arctic Engineering, OMAE*, St. John's, Canada.
- Bertram, V.
2012. *Practical Ship Hydrodynamics*, 2nd edition. London, UK: Butterworth-Heinemann, Elsevier.
- Beyer, F., Arnold, M., and Cheng, P. W.
2013. Analysis of floating offshore wind turbines hydrodynamics using coupled CFD and multibody methods. In *Proc. of the 23rd International Offshore and Polar Engineering Conference, ISOPE*, Anchorage, AK, USA.
- Beyer, F., Choisnet, T., Kretschmer, M., and Cheng, P. W.
2015. Coupled MBS-CFD simulation of the IDEOL floating offshore wind turbine foundation compared to wave tank model test data. In *Proc. of the 25th International Offshore and Polar Engineering Conference, ISOPE*, Kona, HI, USA.
- Borg, M., Shires, A., and Collu, M.
2014. Offshore floating vertical axis wind turbines, dynamics modelling state of the art. part I: Aerodynamics. *Renewable and Sustainable Energy Reviews*, 39:1214–1225.
- Borisade, F., Choisnet, T., and Cheng, P.
2016. Design study and full scale MBS-CFD simulation of the IDEOL floating offshore wind turbine foundation. *Journal of Physics: Conference Series*, 753:092002.
- Bozonnet, P. and Emery, A.
2015. CFD simulations for the design of offshore floating wind platforms encompassing heave plates. In *Proc. of the 25th International Offshore and Polar Engineering Conference, ISOPE*, Kona, HI, USA.
- Bredmose, H., Lemmer, F., Borg, M., Pegalajar-Jurado, A., Mikkelsen, R., Larsen, T. S., Fjelstrup, T., Yu, W., Lomholt, A., Boehm, L., and Armendariz, J. A.
2017. The triple spar campaign: Model tests of a 10MW floating wind turbine with waves, wind and pitch control. *Energy Procedia*, 137:58–76.
- Brouwer, J., Tukker, J., and van Rijsbergen, M.
2015. Uncertainty analysis and stationarity test of finite length time series signals. In *Proc. of the 4th International Conference on Advanced Model Measurement Technology for the Maritime Industry, AMT*, Istanbul, Turkey.

- Burmester, S. and Guerinel, M.
2016. Calculations of wave loads on a vertical cylinder using potential-flow and viscous-flow solvers. In *Proc. of the 35th International Conference on Ocean, Offshore and Arctic Engineering, OMAE*, Busan, Korea.
- Burmester, S., Gueydon, S., and Make, M.
2016. Determination of scaled wind turbine rotor characteristics from 3 dimensional RANS calculations. *Journal of Physics: Conference Series*, 753.
- Burmester, S., Vaz, G., and el Moctar, O.
2020a. Towards credible CFD simulations for floating offshore wind turbines. *Ocean Engineering*, 209:107237.
- Burmester, S., Vaz, G., and el Moctar, O.
2021. On the hydrodynamic damping and analysis of a moored floating offshore wind turbine using cfd. *To be submitted to: Renewable Energy*, -:-.
- Burmester, S., Vaz, G., el Moctar, O., Gueydon, S., Koop, A., Wang, Y., and Chen, H.-C.
2020b. High-fidelity modelling of floating offshore wind turbine platforms. In *Proc. of the 39th International Conference on Ocean, Offshore and Arctic Engineering, OMAE*, Fort Lauderdale, FL, USA.
- Burmester, S., Vaz, G., Gueydon, S., and el Moctar, O.
2017. Surge decay simulations of a semi-submersible floating offshore wind turbine. In *20th Numerical Towing Tank Symposium, NuTTS*, Wageningen, The Netherlands.
- Burmester, S., Vaz, G., Gueydon, S., and el Moctar, O.
2020c. Investigation of a semi-submersible floating wind turbine in surge decay using CFD. *Ship Technology Research*, 67:2–14.
- Burton, T., Jenkins, N., Sharpe, D., and Bossanyi, E.
2011. *Wind Energy Handbook*, 2nd edition. Chichester, UK: Wiley.
- Butterfield, S., Musial, W., Jonkman, J., and Sclavounos, P.
2005. Engineering challenges for floating offshore wind turbines. In *Proc. of the EWEA Offshore Wind Conference*, Copenhagen, Denmark.
- Cermelli, C., Roddier, D., and Aubault, A.
2009. WindFloat: A floating foundation for offshore wind turbines part II: hydrodynamics analysis. In *Proc. of the 28th International Conference on Ocean, Offshore and Arctic Engineering, OMAE*, Honolulu, HI, USA.
- Chakrabarti, S.
1998. Physical model testing of floating offshore structures. In *Proc. of the Dynamic Positioning Conference*, Houston, TX, USA. Marine Technology Society.
- Chillcce, G. and el Moctar, O.
2018. A numerical method for manoeuvring simulation in regular waves. *Ocean Engineering*, 170:434–444.

- Chujo, T., Minami, Y., Nimura, T., and Ishida, S.
2013. Experimental study for spar type floating offshore wind turbine with blade-pitch control. In *Proc. of the 32nd International Conference on Ocean, Offshore and Arctic Engineering, OMAE*, Nantes, France. ASME.
- Cordle, A. and Jonkman, J.
2011. State of the art in floating wind turbine design tools. In *Proc. of the 21st International Offshore and Polar Engineering Conference, ISOPE*, Maui, Hawaii, USA.
- Crepier, P.
2017. Ship resistance prediction: Verification and validation exercise on unstructured grids. In *Proc. of the 7th International Conference on Computational Methods in Marine Engineering, MARINE*, Nantes, France.
- Cruz, J. and Atcheson, M.
2016. *Floating offshore wind energy - The next generation of wind energy*, 1st edition. Switzerland: Springer.
- Davidson, J. and Ringwood, J. V.
2017. Mathematical modelling of mooring systems for wave energy converters - A review. *Journal of Energies*, 10.
- de Ridder, E.-J., Otto, W., Zondervan, G.-J., Huijs, F., and Vaz, G.
2014. Development of a scaled-down floating wind turbine for offshore basin testing. In *Proc. of the 33rd International Conference on Ocean, Offshore and Arctic Engineering, OMAE*, San Francisco, USA.
- Eça, L.
2016. Estimation of numerical uncertainties for steady and unsteady flows. Technical report, Instituto Superior Técnico, Lisbon, Portugal.
- Eça, L. and Hoekstra, M.
2008. Testing uncertainty estimation and validation procedures in the flow around a backward facing step. In *Proc. of the 3rd Workshop on CFD Uncertainty Analysis*, Lisbon, Portugal.
- Eça, L. and Hoekstra, M.
2009. Evaluation of numerical error estimation based on grid refinement studies with the method of the manufactured solutions. *Journal of Computers and Fluids, Elsevier*, 38:1580–1591.
- Eça, L. and Hoekstra, M.
2014. A procedure for the estimation of the numerical uncertainty of CFD calculations based on grid refinement studies. *Journal of Computational Physics, Elsevier*.
- Eça, L., Vaz, G., Toxopeus, S. L., and Hoekstra, M.
2019. Numerical errors in unsteady flow simulations. *Journal of Verification, Validation and Uncertainty Quantification*, 4.

- Eskilsson, C., Palm, J., and Bergdahl, L.
2017. On numerical uncertainty of VOF-RANS simulations of wave energy converters through V&V technique. In *Proc. of the 12th European Wave and Tidal Energy Conference, EWTEC*, Cork, Ireland.
- European Wind Energy Association
2011. Wind in our sails - The coming of Europe's offshore wind energy industry.
- Faltinsen, O.
1990. *Sea Loads on Ships and Offshore Structures*, 1st edition. Cambridge, United Kingdom: Cambridge University Press.
- Fenton, J.
1985. A fifth-order stokes theory for steady waves. *Journal of Waterway, Port Costal, and Ocean Engineering*, 3:216–234.
- Ferziger, J. H. and Perić, M.
2002. *Computational Methods For Fluid Dynamics*, 3rd edition. Berlin, Germany: Springer-Verlag.
- Goupee, A., Fowler, M. J., Kimball, R. W., Helder, J., and de Ridder, E.-J.
2014. Additional wind/wave basin testing of the DeepCwind semi-submersible with a performance-matched wind turbine. In *Proc. of the 33rd International Conference on Ocean, Offshore and Arctic Engineering, OMAE*, San Francisco, CA, USA.
- Goupee, A., Koo, B., Lambrakos, K., and Kimball, R.
2012. Model tests for three floating wind turbine concepts. In *Proc. of Offshore Technology Conference, OTC*, Houston, TX, USA.
- Gross, D., Hauger, W., Schröder, J., and Wall, W. A.
2006. *Technische Mechanik 3 - Kinetik*. Berlin, Germany: Springer.
- Gueydon, S.
2016. Aerodynamic damping on a semisubmersible floating foundation for wind turbines. *Energy Procedia*, 94:367–378.
- Gueydon, S., Bayati, I., and de Ridder, E.-J.
2020. Discussion of solutions for basin model tests of FOWTs in combined waves and wind. *Ocean Engineering*, 209:107288.
- Gueydon, S. and Fernandes, G.
2013. Scaling methodology for floating wind turbines. In *Proc. of the EWEA Offshore Conference*, Frankfurt, Germany.
- Guntur, S. and Sørensen, N.
2014. An evaluation of several methods of determining the local angle of attack on wind turbine blades. *Journal of Physics: Conference Series*, 555:012045.

- Hall, M. and Goupee, A. J.
2018. Validation of a hybrid modeling approach to floating wind turbine testing. *Wind Energy*, 21:391–408.
- Haller, G.
2005. An objective definition of a vortex. *Journal of Fluid Mechanics*, 525:1–26.
- Handscherl, S., Feder, D., and Abdel-Maksoud, M.
2015. Estimation of ship roll damping - a comparison fo the decay and the harmonic excited roll motion technique for a post Panamax container ship. In *Proc. of the 12th International Conference on the Stability of Ships and Ocean Vehicles, STAB*, Glasgow, UK.
- Hennig, J.
2005. *Generation and analysis of harsh wave environment*. PhD thesis, Technische Universität Berlin, Germany.
- Himeno, Y.
1981. Prediction of ship roll damping - state of the art. Technical Report 239, Department of Naval Architecture and Marine Engineering, University of Michigan, Ann Arbor, Michigan, USA.
- Hirt, C. and Nichols, B.
1981. Volume of Fluid (VOF) method for the dynamics of free boundaries. *Journal of Computational Physics*, 39:201–225.
- Huijs, F., de Ridder, E.-J., and Savenije, F.
2014. Comparison of model tests and coupled simulations for a semi-submersible floating wind turbine. In *Proc. of the 33rd International Conference on Ocean, Offshore and Arctic Engineering, OMAE*, San Francisco, CA, USA. ASME.
- Hunt, J., Wray, A., and Moin, P.
1988. Eddies, streams, and convergence zones in turbulent flows. In *Proc. of the Summer Program*, Pp. 193–208, Stanford, USA. Center for Turbulence Research.
- Irvine, M., Longo, J., and Stern, F.
2005. Towing-tank tests for surface combatant for free roll decay and coupled pitch and heave motions. In *Proc. of the 25th Symposium on Naval Hydrodynamics*, Washington, DC, USA. The National Academies Press.
- Israeli, M. and Orszag, S. A.
1981. Approximation of radiation boundary conditions. *Journal of Computational Physics*, 41:115–135.
- ITTC
2008. Recommended procedures and guidelines: Uncertainty analysis in CFD - Verification and validation methodology and procedures. 7.5-03-01-01.
- ITTC
2011. Recommended procedures and guidelines: Numerical estimation of roll damping. 7.5-02-07-04.5.

ITTC

2014. The ocean engineering committee - Final report and recommendations.
26th International Towing Tank Conference - Volume I.

ITTC

2017. Recommended procedures and guidelines: Uncertainty analysis in CFD - Verification and validation methodology and procedures. 7.5-03-01-01.

Jaouën, F., Koop, A., and Vatinel, L.

2019. URANS predictions of low-frequency damping of a LNGC. In *Proc. of the 38th International Conference on Ocean, Offshore and Arctic Engineering, OMAE*, Glasgow, Scotland, UK. ASME.

Jeong, J. and Hussain, F.

1995. On the identification of a vortex. *Journal of Fluid Mechanics*, 285:69–94.

Jiang, C., el Moctar, O., Moura Paredes, G., and Schellin, T.

2020. Validation of a dynamic mooring model coupled with a RANS solver. *Marine Structures*, 72:102783.

Jonkman, J., Butterfield, S., Musial, W., and Scott, G.

2009. Definition of a 5-MW reference wind turbine for offshore system development. Technical Report NREL/TP-500-38060, National Renewable Energy Laboratory (NREL), Boulder, CO, USA.

Journée, J. and Massie, W.

2001. *Offshore Hydromechanics*. Delft, The Netherlands: Delft University of Technology.

Karimirad, M. and Moan, T.

2010. Effect of aerodynamic and hydrodynamic damping on dynamic response of a spar type floating wind turbine. In *Proc. of the European Wind Energy Conference, EWEC*, Warsaw, Poland.

Klaij, C., Hoekstra, M., and Vaz, G.

2018. Design, analysis and verification of a Volume-of-Fluid model with interface-capturing scheme. *Computers and Fluids*, 170:324–340.

Klaij, C. and Vaz, G.

2017. *ReFRESCO theory manual*. Maritime Research Institute Netherlands (MARIN), Wageningen, The Netherlands.

Klaij, C. and Vuik, C.

2013. Simple-type preconditioners for cell-centered, colocated Finite Volume discretization of Reynolds-Averaged Navier-Stokes equations. *International Journal for Numerical Methods in Fluids*, 17:830–849.

Kok, J.

2000. Resolving the dependence on freestream values for the $k - \omega$ turbulence model. *AIAA Journal*, 38:1292–1295.

- Kölling, M., Resnik, B., and Sargsyan, A.
2014. Application of the random decrement technique for experimental determination of damping parameters of bearing structures. In *Proc. of the 8th International Conference on Material Technologies and Modeling, MMT*, Ariel, Israel.
- Komusanac, I., Brindley, G., and Fraile, D.
2020. Wind energy in Europe in 2019. Technical report, WindEurope.
- Koo, B., Goupee, A., Lambrakos, K., and Kimball, R.
2012. Model tests for a floating wind turbine on three different floaters. In *Proc. of the 31st International Conference on Ocean, Offshore and Arctic Engineering, OMAE*, Rio de Janeiro, Brazil.
- Larsen, B. E. and Fuhrman, D. R.
2018. On the over-production of turbulence beneath surface waves in Reynolds-averaged Navier-Stokes models. *Journal of Fluid Mechanics*, 853:419–460.
- Lé Méhauté, B.
1976. *An introduction to hydrodynamics and water waves*. New York, USA: Springer Science and Business Media.
- Lee, J. and Zhao, F.
2020. Global wind report 2019. Technical report, Global Wind Energy Council (GWEC).
- Lemmer, F.
2018. *Low-order modeling, controller design and optimization of floating offshore wind turbines*. PhD thesis, University of Stuttgart, Stuttgart, Germany.
- Li, Y., Paik, K.-J., Xiao, T., and Carrica, P. M.
2012. Dynamic overset CFD simulations of wind turbine aerodynamics. *Renewable Energy*, 37:285–298.
- Lin, P.
2008. *Numerical modeling of water waves*. London and New York: CRC Press, Taylor & Francis.
- Liu, Y. and Xiao, Q.
2019. Development of a fully coupled aero-hydro-mooring-elastic tool for floating offshore wind turbines. *Journal of Hydrodynamics*, 31:21–33.
- Liu, Y., Xiao, Q., A., I., Peyrard, C., and Wan, D.
2017. Establishing a fully coupled CFD analysis tool for floating offshore wind turbines. *Renewable Energy*, 112:280–301.
- Make, M. and Vaz, G.
2015. Analyzing scaling effects on floating offshore wind turbines using CFD. *Renewable Energy, Elsevier*.

- Make, M., Vaz, G., Fernandes, G., Burmester, S., and Gueydon, S.
2015. Analysis of aerodynamic performance of floating wind turbines using CFD and BEMT methods. In *Proc. of the 34th International Conference on Ocean, Offshore and Arctic Engineering, OMAE*, St. John's, Canada.
- MARIN
2017. *DIFFRAC - User Guide*. Wageningen, The Netherlands.
- Martin, H. R., Kimball, R. W., Viselli, A. M., and j. Goupee, A.
2012. Methodology for wind/wave basin testing of floating offshore wind turbines. In *Proc. of the 31st International Conference on Ocean, Offshore and Arctic Engineering, OMAE*, Rio de Janeiro, Brazil.
- Masciola, M., Robertson, A., and Jonkman, J.
2014. Extending the capabilities of the mooring analysis program: A survey of dynamic mooring line theories for integration into FAST. In *Proc. of the 33rd International Conference on Ocean, Offshore and Arctic Engineering, OMAE*, San Francisco, CA, USA.
- Menter, F.
1994. Two-equation eddy-viscosity turbulence models for engineering applications. *American Institute of Aeronautics and Astronautics Journal*, 32.
- Menter, F. and Egorov, Y.
2006. Revisiting the turbulent scale equation. In *Proc. of the Symposium on One Hundred Years of Boundary Layer. Solid mechanics and its applications, IUTAM*, volume 129, Pp. 279–290, Dordrecht, NL. Springer.
- Menter, F. and Egorov, Y.
2010. The scale-adaptive simulation method for unsteady turbulent flow predictions. part 1: Theory and model description. *Flow, Turbulence and Combustion*, 85:113–138.
- Menter, F., Kuntz, M., and Langtry, R.
2003. Ten years of industrial experience with the sst turbulence model. *Turbulence, Heat and Mass Transfer*.
- Miller, T. F. and Schmidt, F. W.
1988. Use of a pressure-weighted interpolation method for the solution of the incompressible Navier-Stokes equations on a nonstaggered grid system. *Numerical Heat Transfer, Part A: Applications*, 14.
- Morison, J., O'Brien, M., Johnson, J., and Schaaf, S. A.
1950. The force exerted by surface waves on piles. *Journal of Petroleum Technology*, 2.
- Moukalled, F., Mangnani, L., and Darwish, M.
2016. *The Finite Volume Method in Computational Fluid Dynamics*. Springer International Publishing.

- Müller, K., Sandner, F., Bredmose, H., Azcona, J., Manjock, A., and Pereira, R.
2014. Improved tank test procedures for scaled floating offshore wind turbines. In *Proc. of the 1st International Wind Engineering Conference, IWEC*, Hannover, Germany. Technische Informationsbibliothek und Universitätsbibliothek.
- Muzaferija, S., Perić, M., Sames, P., and Schellin, T.
1999. A two-fluid Navier-Stokes solver to simulate water entry. *Twenty-Second Symposium on Naval Hydrodynamics*, 22:638–651.
- Myhr, A., Maus, K., and Nygaard, T.
2011. Experimental and computational comparison of the OC3-HYWIND and Tension-Leg-Buoy (TLB) floating wind turbine conceptual design. In *Proc. of the 21st International Offshore and Polar Engineering Conference, ISOPE*, Maui, HI, USA.
- Nelder, J. A. and Mead, R.
1965. A simplex method for function minimization. *The Computer Journal*, 7:308–313.
- Nematbakhsh, A., Bachynski, E. E., Gao, Z., and Moan, T.
2015. Comparison of wave load effects on a TLP wind turbine by using computational fluid dynamics and potential flow theory approaches. *Applied Ocean Research*, 53:142–154.
- Oberhagemann, J.
2016. *On Prediction of Wave-Induced Loads and Vibration of Ship Structures with Finite Volume Fluid Dynamic Methods*. PhD thesis, University of Duisburg-Essen, Duisburg, Germany.
- Oberhagemann, J. and el Moctar, O.
2019. An extrapolation method for discretization independent solution of uncertainty quantification procedure for time domain CFD computations. *Submitted to: Ship Technology Research*.
- Owusu, P. A. and Asumadu-Sarkodie, S.
2016. A review of renewable energy sources, sustainability issues and climate change mitigation. *Cogent Engineering*, 3:1167990.
- Pereira, F., Eca, L., and Vaz, G.
2017. Verification and validation exercises for the flow around the KVLCC2 tanker at model and full-scale reynolds numbers. *Ocean Engineering*, 129:133–148.
- Pereira, F., Eca, L., Vaz, G., and Girimaji, S.
2021. Towards predictive RANS and SRS computations of turbulent external flows of practical interest. *Archives of Computational Methods in Engineering*.
- Pereira, F., Eca, L., Vaz, G., and Kerkvliet, M.
2019. Application of second-moment closure to statistically steady flows of practical interest. *Ocean Engineering*, 189:106372.

- Pereira, F. M. S.
2018. *Towards predictive Scale-Resolving Simulations of turbulent external flows*. PhD thesis, Universidade de Lisboa, Instituto Superior Técnico, Lisbon, Portugal.
- Perić, R. and Abdel-Maksoud, M.
2016. Reliable damping of free-surface waves in numerical simulations. *Ship Technology Research - Schiffstechnik*, 63.
- Perić, R. and Abdel-Maksoud, M.
2018. Analytical prediction of reflection coefficients for wave absorbing layers in flow simulations of regular free-surface waves. *Ocean Engineering*, 147:132–147.
- Phillips, T. S. and Roy, C. J.
2014. Richardson extrapolation-based discretization uncertainty estimation for computational fluid dynamics. *Journal of Fluids Engineering*, 136.
- Piehl, H. P.
2016. *Ship Roll Damping Analysis*. PhD thesis, Universität Duisburg-Essen, Duisburg, Germany.
- Pistidda, A., Ottens, H., and Zoontjes, R.
2012. Using CFD to assess low frequency damping. In *Proc. of the 31st International Conference on Ocean, Offshore and Arctic Engineering, OMAE*, Rio de Janeiro, Brazil.
- Pope, S. B.
2000. *Turbulent Flows*. Cambridge University Press.
- Quallen, S., Xing, T., Carrica, P., Li, Y., and Xu, J.
2014. CFD simulation of a floating offshore wind turbine system using a quasi-static crowfoot mooring-line model. In *Proc. of the 24th International Offshore and Polar Engineering Conference, ISOPE*, Anchorage, AK, USA.
- Ramírez, L., Fraile, D., and Brindley, G.
2020. Offshore Wind in Europe - Key trends and statistics 2019. Technical report, WindEurope.
- Rapuc, S., Creppier, P., Jaouen, F., and Regnier, P.
2018. Towards guidelines for consistent wave propagation in CFD simulations. In *Proc. of the 19th International Conference on Ship & Maritime Research, NAV*, Trieste, Italy.
- Rhie, C. M. and Chow, W. L.
1983. Numerical study of the turbulent flow past an airfoil with trailing edge separation. *AIAA Journal*, 21.
- Rivera-Arreba, I., Bruinsma, N., Bachynski, E. E., Viré, A., Paulsen, B. T., and Jacobsen, N. G.
2019. Modelling of a semisubmersible floating offshore wind platform in severe waves. *Journal of Offshore Mechanics and Arctic Engineering*, 141.

- Roache, P. J.
 2009. *Fundamentals of verification and validation*. Hermosa publ.
- Robertson, A., Bachynski, E., Gueydon, S., Wendt, F., and Schnünemann, P.
 2020a. Total experimental uncertainty in hydrodynamic testing of a semisubmersible wind turbine, considering numerical propagation of systematic uncertainty. *Ocean Engineering*, 195:106605.
- Robertson, A., Gueydon, E., Bachynski, E., Wang, L., Jonkman, J., Alarcon, D., Amet, E., Beardsell, A., Bonnet, P., Brun, C., Chen, Z., Feron, M., Forbush, D., Galinos, C., Galvan, J., Gilbert, P., Gomez, J., Harnois, V., Haudin, F., Hu, Z., Le Dreff, J., Leimeister, M., Lemmer, F., Li, H., McKinnon, G., Mendikoa, I., Moghtadaei, A., Netzbando, S., Oh, S., Pegalajar-Jurado, A., Nguyen, M., Ruehl, K., Schnünemann, P., Shi, W., Shin, H., Si, Y., Surmont, F., Trubat, P., Qwist, J., and Wohlfahrt-Laymann, S.
 2020b. OC6 phase I: Investigating the underprediction of low-frequency hydrodynamic loads and responses of a floating wind turbine. *Journal of Physics: Conference Series*, 1618:032033.
- Robertson, A., Jonkman, J., Masciola, M., Song, H., , Goupee, A., Coulling, A., and Luan, C.
 2014. Definition of the semisubmersible floating system for phase II of OC4. Technical Report NREL/TP-5000-60601, NREL, Golden, CO, USA.
- Robertson, A., Jonkman, J., Wendt, F., Goupee, A., and Dagher, H.
 2017a. Definition of the semisubmersible floating system for phase II of OC5. Technical report, IEA wind, Roskilde, Denmark.
- Robertson, A., Wendt, F., Jonkman, J., Popko, W., Dagher, H., Gueydon, S., Qvist, J., Vittori, F., Uzunoglu, E., Harries, R., Yde, A., Galinos, C., Hermans, K., de Vaal, J. B., Bozonnet, P., Bouy, L., Bayati, I., Bergua, R., Fernandez, J. G., Alonso, I. M., Sanchez, C. B., Shin, H., Oh, S., Molins, C., and Debruyne, Y.
 2017b. OC5 project phase II: Validation of global loads of the deepcwind floating semisubmersible wind turbine. *Energy Procedia*, 137:38–57.
- Robertson, A., Wendt, F., Jonkman, J., Popko, W., Vorpahl, F., Stansberg, C. T., Bachynski, E. E., Bayati, I., Beyer, F., de Vaal, J. B., Harris, R., Yamaguchi, A., Shin, H., Kim, B., van der Zee, T., Bozonnet, P., Aguilao, B., Bergua, R., Qvist, J., Qijun, W., Chen, X., Guerinel, M., Tu, Y., Yutong, H., Li, R., and Bouy, L.
 2015. OC5 project phase I: Validation of hydrodynamic loading on a fixed cylinder. In *Proc. of the 25th International Offshore and Polar Engineering Conference, ISOPE*, Kona, HI, USA.
- Roe, P. L.
 1985. Some contributions to the modelling of discontinuous flows. *Lectures in Applied Mathematics*, 22.

- Rosetti, G., Gonçalves, R., Fujarra, A., and Koop, A.
2016. CFD calculations of the vortex-induced motions of a circular-column semi-submersible. In *Proc. of the 35th International Conference on Ocean, Offshore and Arctic Engineering, OMAE*, Busan, South Korea.
- Rosetti, G. and Vaz, G.
2017. On the numerical simulations of captive, driven and freely moving cylinder. *Journal of Fluids and Structures*, 74.
- Rosetti, G. F.
2015. *Improvements in the Numerical Modeling of Turbulence and Fluid-Structure Interaction for the Vortex-Induced Vibrations of a Rigid Cylinder*. PhD thesis, Universidade de São Paulo, São Paulo, Brazil.
- Rummelhoff, I.
2017. *World's first floating wind farm has started production*. <https://www.equinor.com/en/news/worlds-first-floating-wind-farm-started-production.html>.
- Sarpkaya, T.
1976. In-line and transverse forces on cylinders in oscillatory flow at high Reynolds numbers. In *Proc. of the Offshore Technology Conference, OTC*, Dallas, TX, USA.
- Sarpkaya, T.
2010. *Wave forces on offshore structures*, 1st edition. New York, USA: Cambridge University Press.
- Sauder, T., Chabaud, V., Thys, M., Bachynski, E. E., and Saether, L. O.
2016. Real-time hybrid model testing of a braceless semi-submersible wind turbine: Part I - The hybrid approach. In *Proc. of the 35th International Conference on Ocean, Offshore and Arctic Engineering, OMAE*, Busan, Korea.
- Schmitke, R.
1978. Ship sway, roll, and yaw motions in oblique seas. *Transactions*, 86:26–46.
- Skjelbreia, L. and Hendrickson, J.
1960. Fifth order gravity wave theory. *Coastal Engineering Proceedings*, 7.
- Skopljak, N.
2020. *WindFloat Atlantic producing power*. <https://www.offshorewind.biz-/2020/01/03/windfloat-atlantic-producing-power/>.
- Sommerfeld, A.
1949. *Partial Differential Equations in Physics*, 4th edition. New York, USA: Academic Press.
- Stewart, G. and Muskulus, M.
2016. A review and comparison of floating offshore wind turbine model experiments. *Energy Procedia*, 94:227–231.

- Thomsen, J. B., Ferri, F., and Kofoed, J. P.
2017. Screening of available tools for dynamic mooring analysis of wave energy converters. *Energies*, 10(853).
- Tran, T., Kim, D., and Song, J.
2014. Computational fluid dynamic analysis of a floating offshore wind turbine experiencing platform pitching motion. *Energies*, 7(5011-5026).
- Tran, T. and Kim, D.-H.
2015. The coupled dynamic response computation for a semi-submersible platform of floating offshore wind turbine. *Journal of Wind Engineering and Industrial Aerodynamics*, 147:104–119.
- Tran, T. and Kim, D.-H.
2016. Fully coupled aero-hydrodynamic analysis of a semi-submersible FOWT using a dynamic fluid body interaction approach. *Renewable Energy*, 92:244–261.
- van den Berg, J. and Pauw, W.
2018. *aNySIM theory documentation*. Maritime Research Institute Netherlands (MARIN), Wageningen, The Netherlands.
- van der Vegt, J. J.
1984. Slinger gedrag van schepen.
- van Kuik, G. and Peinke, J.
2016. *Long-term Research Challenges in Wind Energy - A Research Agenda by the European Academy of Wind Energy*, volume 4 of *Research Topics in Wind Energy*. Cham, Switzerland: Springer International Publishing.
- Vaz, G.
2014. Equations-of-motion implementation in ReFRESCO. Technical report, Maritime Research Institute Netherlands (MARIN), Wageningen, The Netherlands.
- Vaz, G., Jaouen, F., and Hoekstra, M.
2009. Free-surface viscous flow computation - Validation of uRANS code FRESCO. In *Proc. of the 28th International Conference on Ocean, Offshore and Arctic Engineering, OMAE*, Honolulu, Hawaii, USA.
- Veldman, A., Luppkes, R., van der Plas, P., van der Heiden, H., Düz, B., Seubers, H., Helder, J., Bunnik, T., and Huijsmans, R.
2016. Free-surface flow simulations for moored and floating offshore platforms. In *Proc. of the European Congress on Computational Methods in Applied Sciences and Engineering, ECCOMAS*, Crete Island, Greece.
- Vickers, A. W.
2012. *Improve the Understanding of Uncertainties in Numerical Analysis of Moored Floating Wave Energy Converters*. PhD thesis, University of Exeter, Exeter, UK.

- Wallin, S. and Johansson, A.
2000. An explicit algebraic reynolds stress model for incompressible and compressible turbulent flows. *Journal of Fluid Mechanics*, 403:89–132.
- Wang, W., Wu, M., Palm, J., and Eskilsson, C.
2018. Estimation of numerical uncertainty in CFD simulations of a passively controlled wave energy converter. *Journal of Engineering for the Maritime Environment*, 232.
- Wang, Y., Chen, H.-C., Vaz, G., and Burmester, S.
2019. CFD simulation of semi-submersible floating offshore wind turbine under pitch decay motion. In *Proc. of the 2nd International Offshore Wind Technical Conference, IOWTC*, St. Julian's, Malta.
- Wang, Y., Chen, H.-C., Vaz, G., and Burmester, S.
2020a. CFD simulation of semi-submersible floating offshore wind turbine under regular waves. In *Proc. of the 30th (2020) International Ocean and Polar Engineering Conference, ISOPE*, Shanghai, China.
- Wang, Y., Chen, H.-C., Vaz, G., and Mewes, S.
2020b. Verification study of CFD simulation of semi-submersible floating offshore wind turbine under regular waves. In *Proc. of the 3rd International Offshore Wind Technical Conference, IOWTC*, Boston, MA, USA.
- Wassermann, S.
2017. *Estimation of ship roll damping for the investigation of extreme roll events*. PhD thesis, Technische Universität Hamburg, Hamburg, Germany.
- Webster, W. C.
1995. Mooring-induced damping. *Ocean Engineering*, 22:571–591.
- Wellens, P. R.
2012. *Wave simulation in truncated domains for offshore applications*. PhD thesis, Technische Universiteit Delft, Delft, The Netherlands.
- Weller, S.
2012. Analysis of the DeepCwind model tests and a first attempt to simulate a semi-submersible floating wind platform with aNySIM. Technical Report 24602-MSG-1, MARIN (Maritime Research Institute Netherlands, Wageningen, The Netherlands).
- Xing, T. and Stern, F.
2010. Factors of safety for Richardson extrapolation. *Journal of Fluids Engineering*, 132.
- Zhang, Y. and Kim, B.
2018. A fully coupled computational fluid dynamics method for analysis of semi-submersible floating offshore wind turbines under wind-wave excitation conditions based on OC5 data. *Applied sciences*, 8:2314.

DuEPublico

Duisburg-Essen Publications online

UNIVERSITÄT
DUISBURG
ESSEN

Offen im Denken

ub | universitäts
bibliothek

Diese Dissertation wird via DuEPublico, dem Dokumenten- und Publikationsserver der Universität Duisburg-Essen, zur Verfügung gestellt und liegt auch als Print-Version vor.

DOI: 10.17185/duepublico/76120

URN: urn:nbn:de:hbz:465-20220630-125542-4

Alle Rechte vorbehalten.